ON-STREAM ANALYSIS OF PARTICLE SIZE DISTRIBUTIONS

A thesis submitted for the degree of

Ph.D. in Engineering

in the University of London

Anthony Bertram Holland-Batt
B.Sc.(Eng.) A.R.S.M.

Department of Mining

and Mineral Technology,

Royal School of Mines,

London, S.W.7.

ABSTRACT

This Thesis describes the development and calibration of an On-Stream Particle Size Distribution Analyser, which operates by applying a centrifugal force field to a suspension of the particles in a fluid medium. The results obtained during the first stage of a programme of research into the method of operation of the Size Analyser are also described and analysed in detail. The progress made is reviewed and plans for future research are outlined.

CONTENTS

LIST OF FIGURES

LIST OF FIGURES (Continued)

LIST OF FIGURES (Continued)

LIST OF SYMBOLS

Symbol	Quantity	Units
a	Area of an elemental surface	$cm.^2$
A	Projected area ; a constant in equations	$cm.^2$/-
b	Velocity gradient	$sec.^{-1}$
B	A constant in equations	-
C	Drag Coefficient	-
C_V	Volume concentration of solids at (r,α)	-
C_{Vf}	Volume concentration at inlet to helix	-
C_W	Weight concentration of solids at (r,α)	-
d	Differential notation	-
D	Diameter of a spherical particle; particle size	cm.
$\check{D}$	Mean size defined by equation B.5.29	cm.
$\hat{D}$	Mean size defined by equation B.5.30	cm.
$\mathring{D}$	Mean Size defined by equation B.5.38	cm.
$\bar{D}$	Mean Size defined by equation B.5.40	cm.
e	Base of natural logarithms	-
ε_α	Tangential flux of particles = VC_V	$sec.^{-1}$
ε_r	Radial flux of particles	$sec.^{-1}$
E, E_o, E_1	Constants	-
F_A	Accelerative force	dynes
F_B	Shear(Bagnold)force	dynes
F_N	Net accelerative force (F_A-F_p)	dynes
F_p	Pressure gradient (displacement) force	dynes
G_L	Viscous drag force	dynes
G_T	Turbulent drag force	dynes
h	Increment in radius (r)	cm.
H	Total head in fluid/suspension	cm.
i	Number of particles of size D	-

LIST OF SYMBOLS (continued)

Symbol	Quantity	Units
k	Maximum size, Size Modulus of Gaudin-Schuhmann Distribution function	cm./μ
K_L	Defined as equal to $(\sigma-P)^6 D^2/18\,(\sigma-1)^5$	sec.
K_T	Defined as equal to $[10(\sigma-P)D/3P]^{\frac{1}{2}}$	cm.$^{\frac{1}{2}}$
L	Distance between centres of adjacent spheres; and	cm.
	Cross-sectional area of pipe ÷ Perimeter of cross-section	cm.
m	Error multiple	-
M	Volume/weight proportion of size D in a sample	-
M_F	Cumulative vol./wt. proportion finer than size D	-
n	Viscosity of fluid/suspension	poise
$\bar{n}$	Exponent characterising relationship between V and D in the transitional regime of motion	-
N	Distribution Modulus of the Gaudin-Schuhmann function.	-
p	Pressure in fluid/suspension	dynes/cm.^{2}
P	Density of suspension at (r,α)	gm./cm.^{3}
P_o	Density of suspension at inlet to helix	gm./cm^3
q	Ratio of particle diameter to radius of motion	-
Q	Exponent in velocity compensation equation	-
r	Radius of motion of fluid or particle	cm.
r_i	Radius of inner wall of helical channel	cm.
r_m	Radius of outer wall of helical channel	cm.
$\bar{r}$	Radius of curvature of axis of helical channel	cm.
R_F	Reynold's number for fluid in channel	-

LIST OF SYMBOLS (continued)

Symbol	Quantity	Units
R_p	Reynold's Number for radial motion of particle	-
R_s	Reynold's Number for suspension in channel	-
S	Density gauge reading	mV
t	Time	sec.
T	Square of the particle radial velocity (U^2)	cm.^{2}/sec.^{2}
u	Velocity of particle relative to fluid	cm./sec.
u_T	Tangential component of particle velocity u.	cm./sec.
U	Radial component of particle velocity u.	cm./sec.
U_{TER}	Terminal radial velocity component	cm./sec.
v	Axial velocity variation ~~accelleration~~ of fluid/suspension near outer wall	cm./sec./rad.
V	Axial velocity of fluid/suspension at (r,α)	cm./sec.
$\bar{V}$	Average axial velocity of fluid/suspension calculated from volume throughput	cm./sec.
W	Work done in shearing the suspension	ergs.
x	Distance between nearest points of adjacent spheres	cm.
X	Thickness of radiation absorber	cm.
y	Rectangular axis	-
Y	Dummy variable of integration	
z	Rectangular axis; 'apparent' value of T	
α	Angular position within helix	
β	Distance between centres of adjacent layers of particles	cm.
∂	Partial differential notation	-
δ	Notation for infinitesimal increment	-

LIST OF SYMBOLS (continued)

Symbol	Quantity	Units
ζ	Amplitude of shear velocity fluctuation	cm./sec.
θ	Angle of particle motion relative to radial direction	degrees
μ	Microns; mass absorption coefficient	cm.^{2}/gm.
λ	Linear particle concentration = D/(L - D)	-
ξ	Total instantaneous shear velocity	cm./sec.
ρ	Density of fluid	gm./cm.^{3}
σ	Density of solid particles	gm./cm.^{3}
τ	Instantaneous shear stress within suspension	dynes/cm.^{2}
$\bar{\tau}$	Time-average shear stress within suspension	dynes/cm.^{2}
ϕ	Dimensionless group characterising flow in curved pipes	-
exp	Denotes 'e raised to the power of'.	-
ln	Logarithm to base e	
log	Logarithm to base 10	

PART A

INTRODUCTION

The ideas forming the basis of this thesis were generated during the early stages of a grinding research project, when it was realised that the continuous analysis of a wet grinding circuit [1,2] could not be undertaken satisfactorily without frequent and rapid measurement of the size distribution of particles produced by the mill.

Various ways of obtaining this information were considered, ranging from turbidimitry, sedimentation, elutration or screening, conducted on intermittent batch samples, to continuous use of different sizes of D.S.M. screens, wet sieves or hydrocyclones in conjunction with flowrate and pulp density measurements.

The batch techniques, while capable of yielding full information concerning the size distribution of solid particles present, suffer from the disadvantages of being both intermittent in action and time consuming. Measurement and recording of the density and flowrate of the feed to and products from a wet screen or hydrocyclone can be made continuously, but the circuit is complex and considerable instrumentation is required.

A final disadvantage of the systems discussed above is that they involve physical interference with the pulp stream: either the removal of a portion or the division of the stream into subsidiary flows. Where the pulp is to undergo further treatment or analysis, this is a most undesirable feature.

The device subsequently described has been developed for the specific purpose of carrying out on-stream analysis of particle size distributions occuring as suspensions in fluid media. It has eliminated some, but not all, of the disadvantages of the alternatives mentioned above.

However, one great virtue of the device is that, potentially, it can be improved, and it may well be that the planned programme of research which follows on from the work described in this thesis will succeed in eliminating many of the technical drawbacks which still limit its usefulness.

The thesis is presented in two main sections. Part A describes the development of both the sizer itself and of a suitable calibration technique. Part B gives a detailed analysis of the particle-fluid behaviour within the sizer, aimed at providing some kind of theoretical framework within which the performance of the sizer may be evaluated. It also describes further testwork conducted on a more sophisticated version of the device using ideal spherical particles. This work was designed to establish the extent to which the conclusions drawn earlier could usefully be applied and to establish if possible a fundamental basis for the empirical calibration developed in the first part of the thesis. Finally, the progress achieved is reviewed and an outline of the further research deemed necessary is given.

2. PRELIMINARY TESTWORK.

2.1 Introduction and Basic Principles.

The purpose of the on-stream size analyser is to provide continuous information concerning the size distribution of particles present in suspensions of solids in fluid media.

The principle of the system is to apply a centrifugal force to the suspension so that particles of different masses attain different velocities in the direction of the force. When the force is applied at right angles to the direction of motion of a suspension flowing in an enclosed channel, the resulting concentration of particles across the channel is influenced by the size distribution of the solid particles. When the particles are of similar shape and density the pattern of concentration across the channel will be directly dependent on their size distribution. Hence, if the concentration profile can be measured and related to the size distribution causing it, the results may be used as the basis of a system of on-stream size analysis.

2.2 Mark 1 Cell

The first version of the sizer cell is shown in figure A.2.1. It consisted of half-inch diameter piping which changed in shape progressively from circular to flat rectangular to circular while turning through about 280°. Thin windows of Melinex were let into the sides of the channel at the midpoint of the turn to permit observation of any density effects created within the device.

The shape of the cell was determined by two requirements. The first was to allow centrifugal force to create a concentration gradient across the flow channel. The second was the

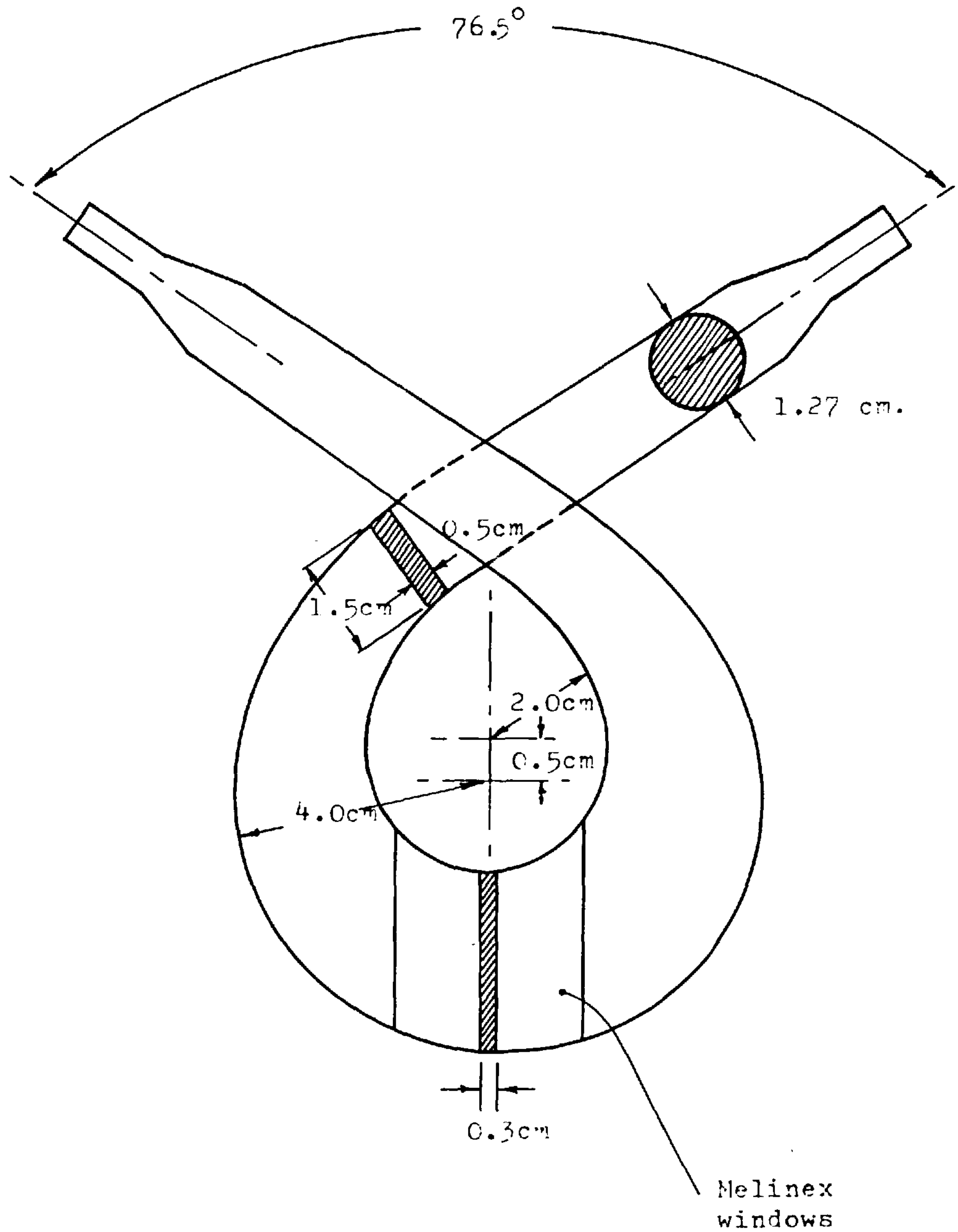

FIGURE A.2.1: Mark 1 Cell

necessity of dispersing the concentration spectrum over a reasonable width of channel for purposes of observation and measurement.

The dimensions of the Mark 1 and all subsequent sizer cells were selected with a particular application in mind.[1,2] The total supply of suspension was to be about 1 litre/min. of a pulp containing of the order of 70% by weight of quartz particles. This pulp could be diluted, but the requirements of the system restricted the permissible dilution to a certain range. The sizer feed had to be sufficiently dilute to permit a useful degree of radial motion for the individual particles. It had also to be dense enough to allow changes in particle concentration to be measured in a thin layer of material. A dilution to 20% solids by weight was chosen initially, giving a total flow of 90 c.c./sec. With this feedrate, the internal dimensions of the Mark 1 cell gave an average flow velocity of 120cm./sec. It was hoped that this would be adequate.

2.2.1 <u>Testwork Using the Mark 1 Cell.</u>

The first tests were designed to establish by means of visual observation whether or not the chosen cell dimensions and feed conditions gave any detectable density gradient across the channel.

The circuit used is shown in Figure A.2.2. It consists of a small variable speed centrifugal pump equipped with a feed hopper, feed and return lines for the cell, and a light source for illuminating the windows from below.

Various size fractions of quartz sand were made up as suspensions containing 20% solids by weight and pumped through the cell at several different flowrates.

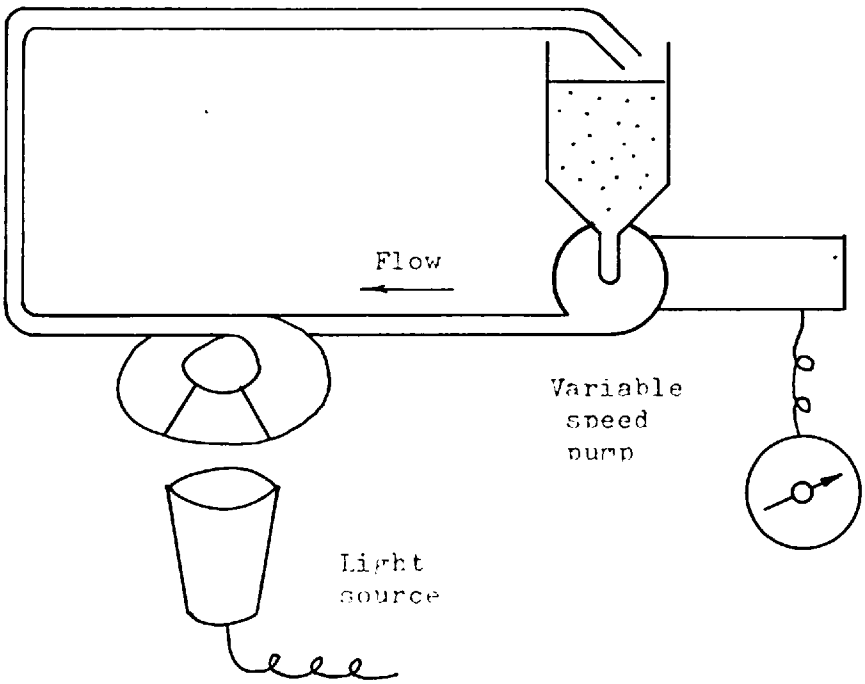

FIGURE A.2.2: Test Circuit for Mark 1 Cell

Moderate concentration gradients were observed with the coarser particle sizes when the pump was run at full speed. (Approximately 120 c.c./sec.)

No observable gradient was found for sizes finer than 72 mesh B.S. At all pump speeds, moreover, considerable flexing of the Melinex windows occurred, resulting in a high degree of local turbulence. The flow patterns observed within the window zone are shown in Figure A.2.3.

It was obvious that even if the design of the windows was altered the Mark 1 cell would be unable to create an effective concentration gradient at a flowrate of 90 c.c./sec. unless the suspensions contained substantial amounts of material coarser than 72 mesh B.S. Since the size distributions which the instrument would be required to measure were unlikely to be of this type, testwork using the Mark 1 cell was discontinued and a new cell was designed.

2.3 Mark 2 Cell

The second version of the cell is shown in Figure A.2.4. The cross-sectional area of the flow channel was reduced by approx. a third, so that for a feed rate of 90 c.c/sec the average flow velocity in the cell would be increased from 120cm./sec. to 200cm./sec. The 280° turn of changing radius used in the Mark 1 was replaced by a full helical turn. Other changes include the use of perspex as the constructional material for the entire cell and the provision of an extended lead-out from the helix: these modifications were introduced to eliminate window flexure and to enable the action of the sizer to be observed both within and downstream of the helix.

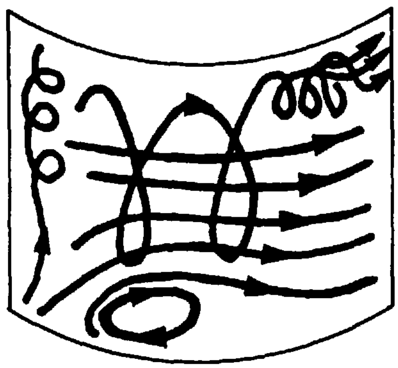

Solids: −36 +52 #

Flowrate: 120 c.c./sec.

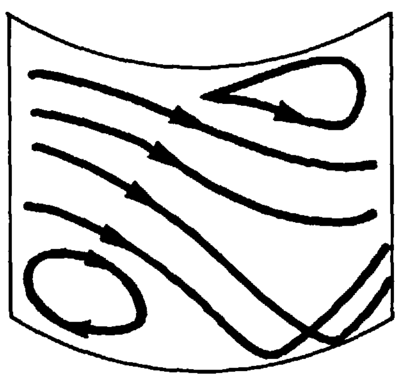

Solids: −52 +72 #

Flowrate: 80 c.c./sec.

FIGURE A.2.3: Turbulance in the Observation Zone

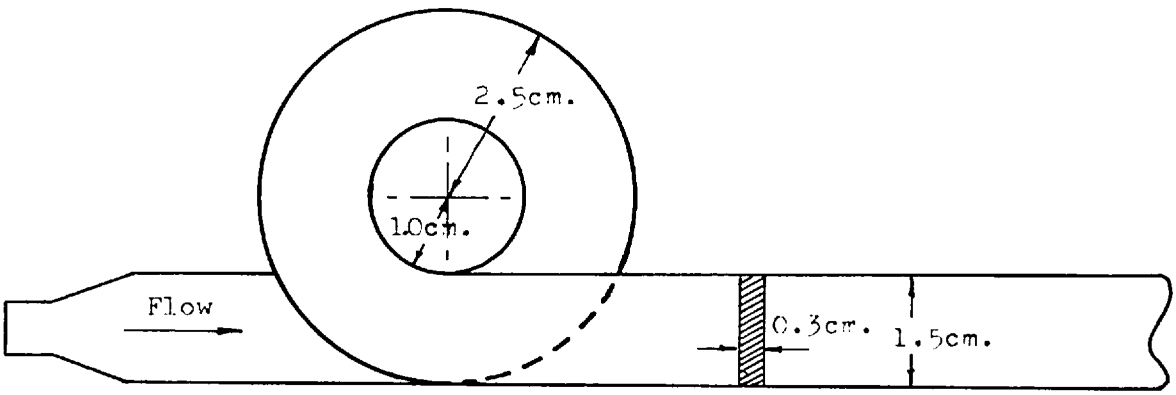

FIGURE A.2.4: Mark 2 Cell

2.3.1 Testwork Using the Mark 2 Cell

The Mark 2 cell was tested in the same circuit as that employed for the Mark 1 (Figure A.2.2) and a series of similar tests was carried out.

To make visual observation easier, the mixtures were made up from two differently coloured minerals; blue crysocolla was used for the coarser sizes and quartz for the finer sizes. The magnitude of the concentration gradient produced was estimated by observing the intensity of colouration at different positions across the helix. This work was qualitative and the effects observed were similar to those illustrated in Figure A.2.5. This is a colour photograph of the results obtained with a full size distribution of ground glass (Distribution No. 6, Table A.3.2. page 37) in which the material coarser than 72 mesh is green and the fine material yellow. The concentration gradient across the channel is clearly visible.

2.4 Summary and Conclusions

The results obtained with the Mark 1 cell showed that a flow velocity of 120cm/sec. was too small to create effective concentration profiles except with very coarse particles.

Runs conducted with the Mark 2 cell suggested that the radial motion created for particle sizes down to 100 mesh B.S. would be sufficient to supply a measurable concentration gradient. The concentration profile appeared to persist for some considerable distance downstream of the helix.

These findings were considered to be sufficiently

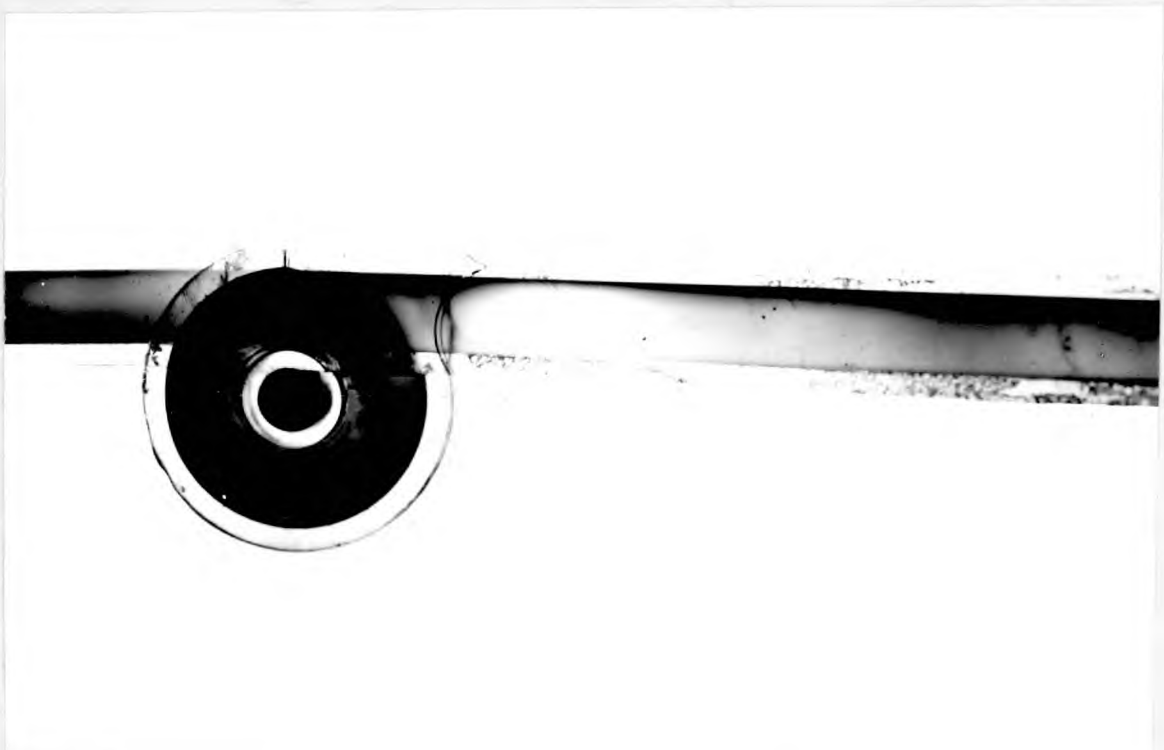

FIGURE A.2.5: Photograph of sizing effect.

encouraging to justify the construction of a test rig incorporating means for measuring the concentration of particles at different points within the flow channel.

3. DEVELOPMENT OF PROTOTYPE SIZER

3.1 Measuring System

3.1.1 Introduction

The ideal measuring system for the prototype sizer would have been capable of determining the particle concentration at a variety of points within the helix itself. This proved to be impracticable for several reasons. Of the available measuring techniques, only a beta-radiation gauge of the transmission variety possessed the necessary sensitivity to cope with the small path length and narrow range of concentrations likely to be encountered. Unfortunately, a 'spot' source of specific activity high enough to ensure good statistical accuracy in the counting equipment would have been prohibitively expensive. Also, the radiation detector (an ionisation chamber) had to be placed clear of the helix because of its size.

Fortunately, the concentration gradients produced within the helix were found to persist at considerable distances downstream of the helix. It was thus possible to use a cheap 'line' source of considerable area and low specific activity, and to site the source and detector on the leadout from the helix.

3.1.2 Measuring System

The Strontium - 90 beta-radiation source and ionisation chamber were disposed on opposite sides of the flow channel at a position just far enough downstream to ensure that the helix did not interfere with the radiation path. (Figure A.3.1)

The source, one of a standard range made by the

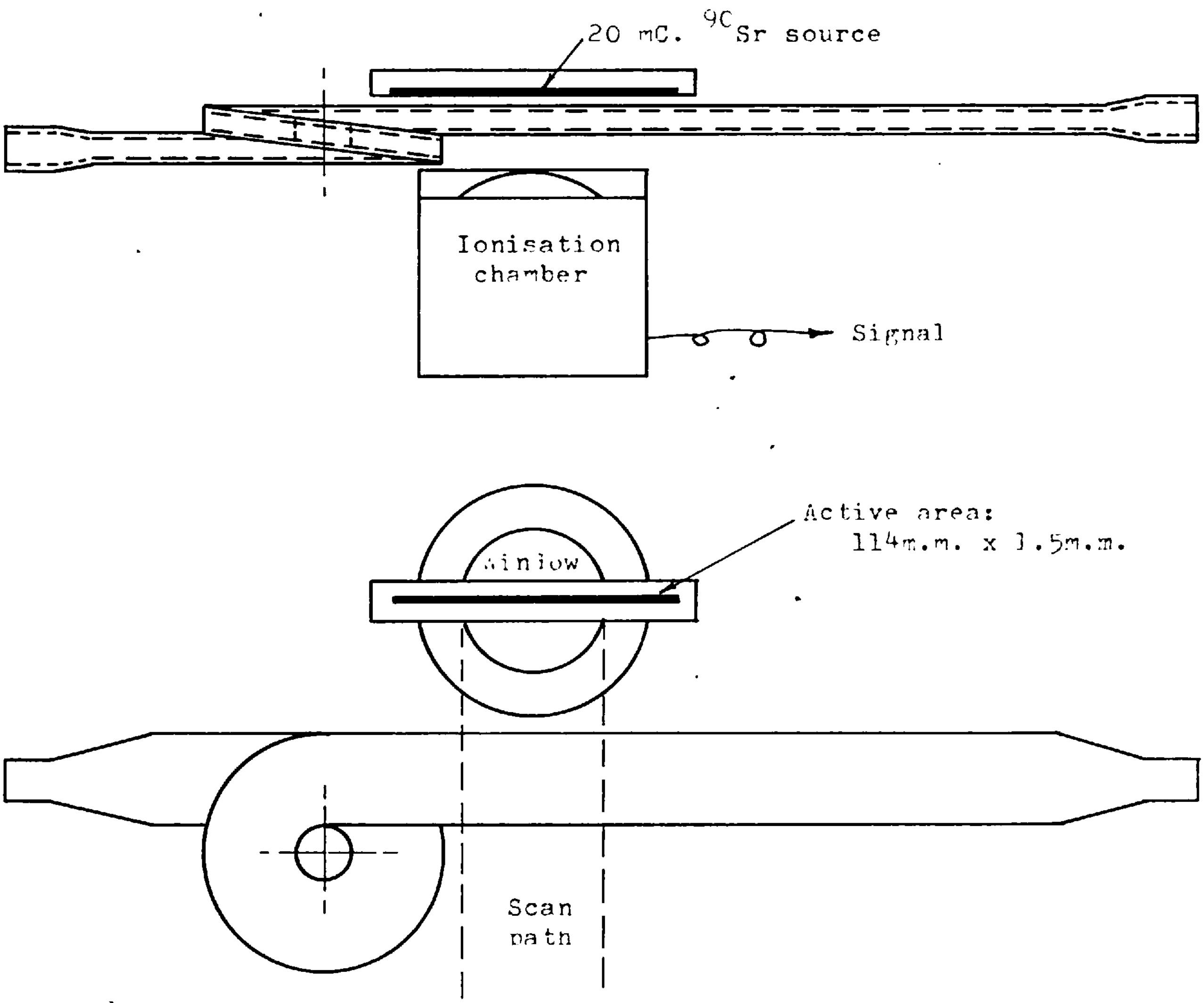

FIGURE A.3.1: Geometry of Measuring System

Radiochemical Centre at Amersham, was supplied in the form of a metal foil having an active area of 114 x 3 m.m. and a total activity of 20 millicuries. With a view to improving the resolution of the density measurements, the source width was reduced to 1.5 m.m. by altering the dimensions of the slit in the retaining plate of the source holder. Since the window of the ionisation chamber was 7.6 cm. in diameter, the effective source activity was only about 7 millicuries.

The remainder of the measuring system consisted of a standard 'Atomette' radiation gauge electronics unit (Baldwin Instrument Co.) and a potentiometric chart recorder. This system converted the current from the ionisation chamber to a voltage, which was subtracted from a preset reference voltage to provide a signal which increased as the concentration of particles in the measuring zone increased. This signal was then fed to the chart recorder. An outline circuit diagram is shown in Figure A.3.2.

Since this system of measurement was employed throughout the work, later versions of the equipment differing only in stability and sensitivity, the basic relationship between particle concentration and signal output to the chart recorder is developed and presented here.

The attenuation of beta-radiation by an absorber may be represented as follows: [3]

$$- dI = \mu PXI \quad \ldots \quad \ldots \quad \ldots \quad (3.1)$$

$$I = I_o e^{-\mu PX} \quad \ldots \quad \ldots \quad (3.2)$$

where I is the intensity of radiation reaching the detector for an incident intensity of I_o on the absorber, μ is an average mass absorption coefficient for all absorbers

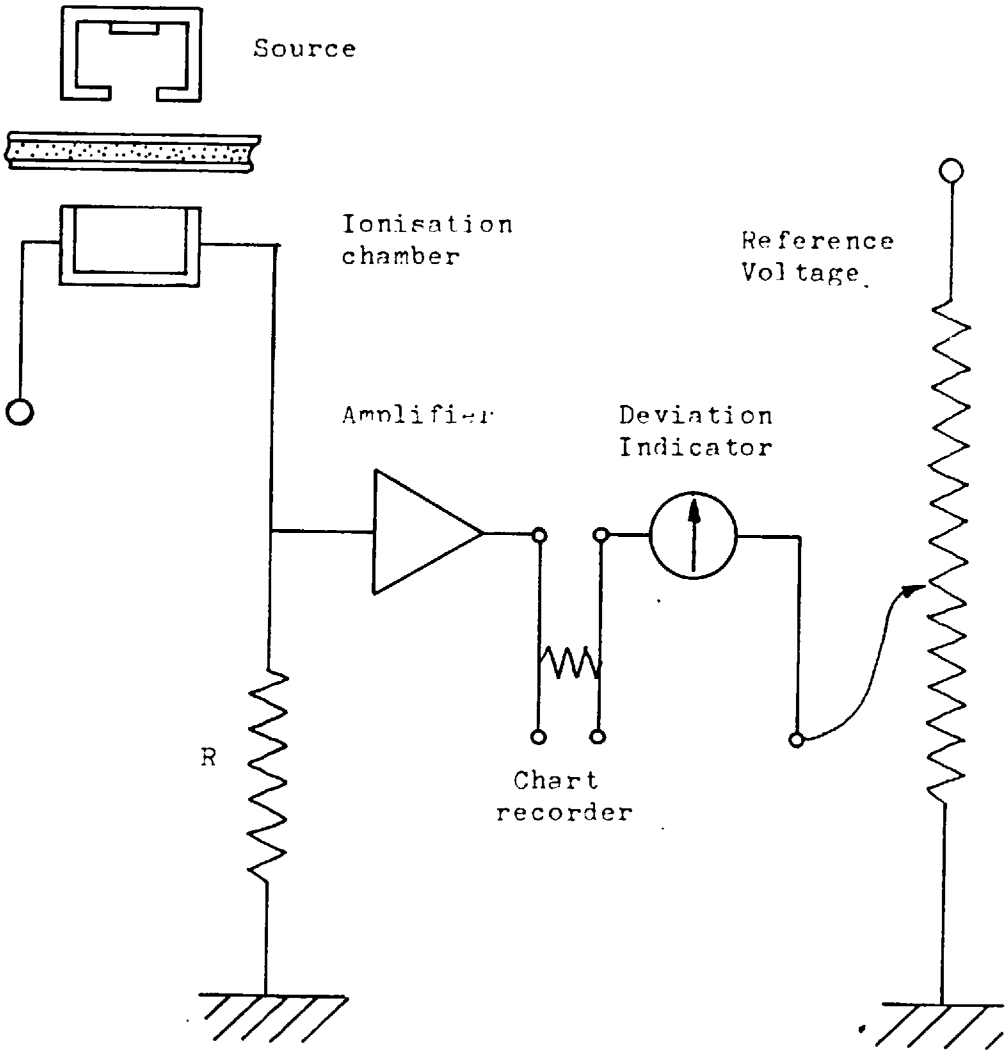

FIGURE A.3.2: Outline Circuit Diagram

(5.8cm.^{2}/gm.), P is the density (gm/cm.^{3}) and X is the thickness (cm.) of the absorber.

In the equipment just described the current from the ionisation chamber , which is proportional to I, is converted to a voltage and subtracted from a preset reference voltage. Hence the signal reaching the chart recorder may be represented by

$$S = E_o - E_1 e^{-\mu PX} \quad \ldots \quad \ldots \quad \ldots \quad (3.3)$$

The radiation reaching the detector through the measurement zone in the sizer outlet is attenuated not only by the suspension but also by the perspex walls of the channel, by the air in the gaps between the channel and the source and detector, and by the window of the detector. Equation (3.3) should therefore be replaced by an expression of the form

$$S = E_o - E_1 \exp[\, -\mu(P_1X_1 + P_2X_2 + \ldots)] \quad \ldots \quad (3.4)$$

However, since these additional attenuations are always present, and - with the exception of the air attenuation - do not vary significantly even with changes in the ambient conditions, their effect may be incorporated into the constant 'E_1' .

$$\therefore S = E_o - E_2 \exp[\, -\mu PX] \quad \ldots \quad \ldots \quad (3.5)$$

where X represents the thickness and P the density of the suspension in the measurement zone. (Variations in the attenuation of the air are compensated for in the standardisation technique.)

It is convenient to replace P in equation (3.5) by the volume concentration of solids in the suspension (C_v), leading to the result

$$S = E_o - E_3 \exp[\, -\mu X(\sigma - 1)\, C_v] \quad \ldots \quad (3.6)$$

where σ = specific gravity of the solid particles

$E_3 = E_2 \exp [-\mu X]$

3.2 First Test Rig

To enable measurements of particle concentration to be made at positions corresponding to different radii within the helix, it was necessary to mount the beta-source and detector so that they could be traversed across the channel. Safety regulations also dictated that the source-detector assembly should be totally enclosed within a structure capable of providing an adequate radiation shield.

The layout adopted is shown in Figures A.3.3, A.3.4. It consisted of a rectangular cross-section metal frame with a totally enclosed box mounted on slides within it, the box being traversed by means of a hand crank. The frame and box were constructed of $\frac{1}{2}$ inch mild steel. Additional radiation screening was provided by external lead sheet as required. The sizer passed through slits in the outer frame walls and was clamped to these walls. Corresponding lateral slits in the walls of the box permitted the sizer helix and channel to pass through it, while at the same time the box could be traversed back and forth. The beta-source was mounted on the underside of the lid of the box and the detector clamped to one of the side walls by means of a bracket. The configuration of source, sizer and detector was shown previously in Figure A.3.1.

Initially the sizer was fed from a constant head tank equipped with an agitator, situated some fifteen feet above the sizer inlet. The discharge from the sizer was pumped back up to the head tank by means of a Monopump. The flow-rate through the sizer was determined by taking timed samples

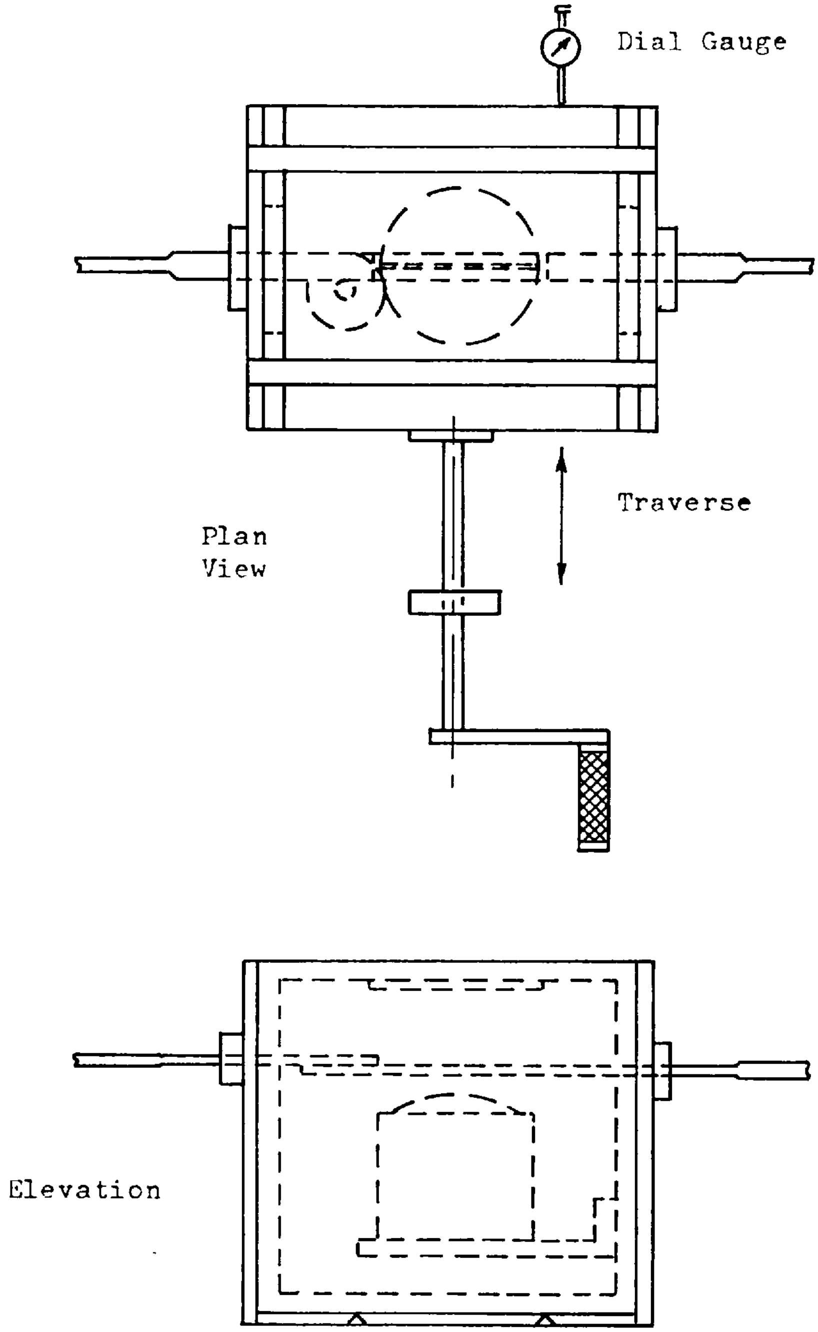

FIGURE A.3.3 First Test Rig (Head Assembly)

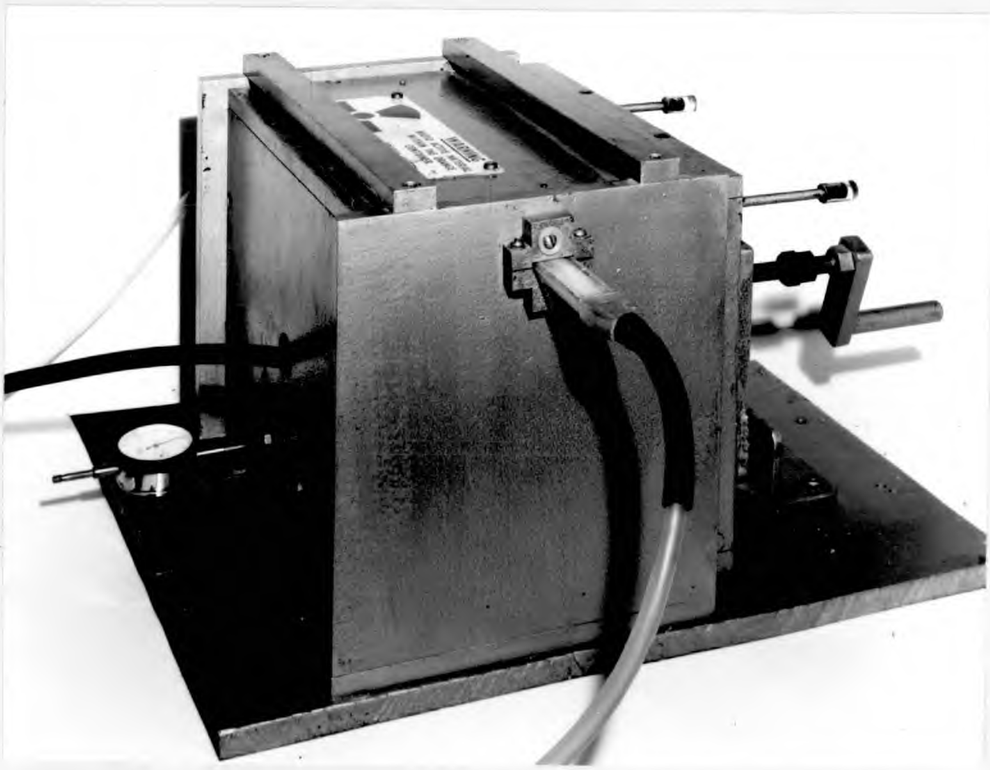

FIGURE A.3.4: Photograph of Head Assembly.

of the discharge, the flow being regulated by means of a clamp attached to the feed line. (Figure A.3.5.)

Preliminary tests run with this circuit revealed that the suspension passing through the sizer contained significantly higher proportions of solids than the prepared feed. This was clearly due to settling of the coarser solids in the head tank. Efforts were made to overcome this, but evidence of settling persisted. The constant head circuit had to be discarded.

3.3 Second Test Rig

The head assembly used in the first test rig was retained unchanged. The constant head tank was discarded, and a circuit with smaller volume was constructed in which the sizer was fed direct from a monopump equipped with a 'Bercotrol' power regulator (British Electrical Control Company) (Figure A.3.6). The size of monopump chosen was such that it had to run at about 80% of its maximum delivery rate in order to achieve the desired flow of 90 c.c./sec. This was intended to avoid low-frequency pulsations in the feed flow that might have been created by a larger pump running more slowly.

This circuit immediately gave far more satisfactory results and, in its basic form, was used for all the remaining work described in this thesis. Various additions were made to the instrumentation in the later stages and these will be described as they arise.

3.4 Mark 3 Cell

The Mark 2 cell was fabricated to permit visual observations. The perspex used in its construction was nearly 3 m.m. in thickness and it was therefore quite unsuitable for use with

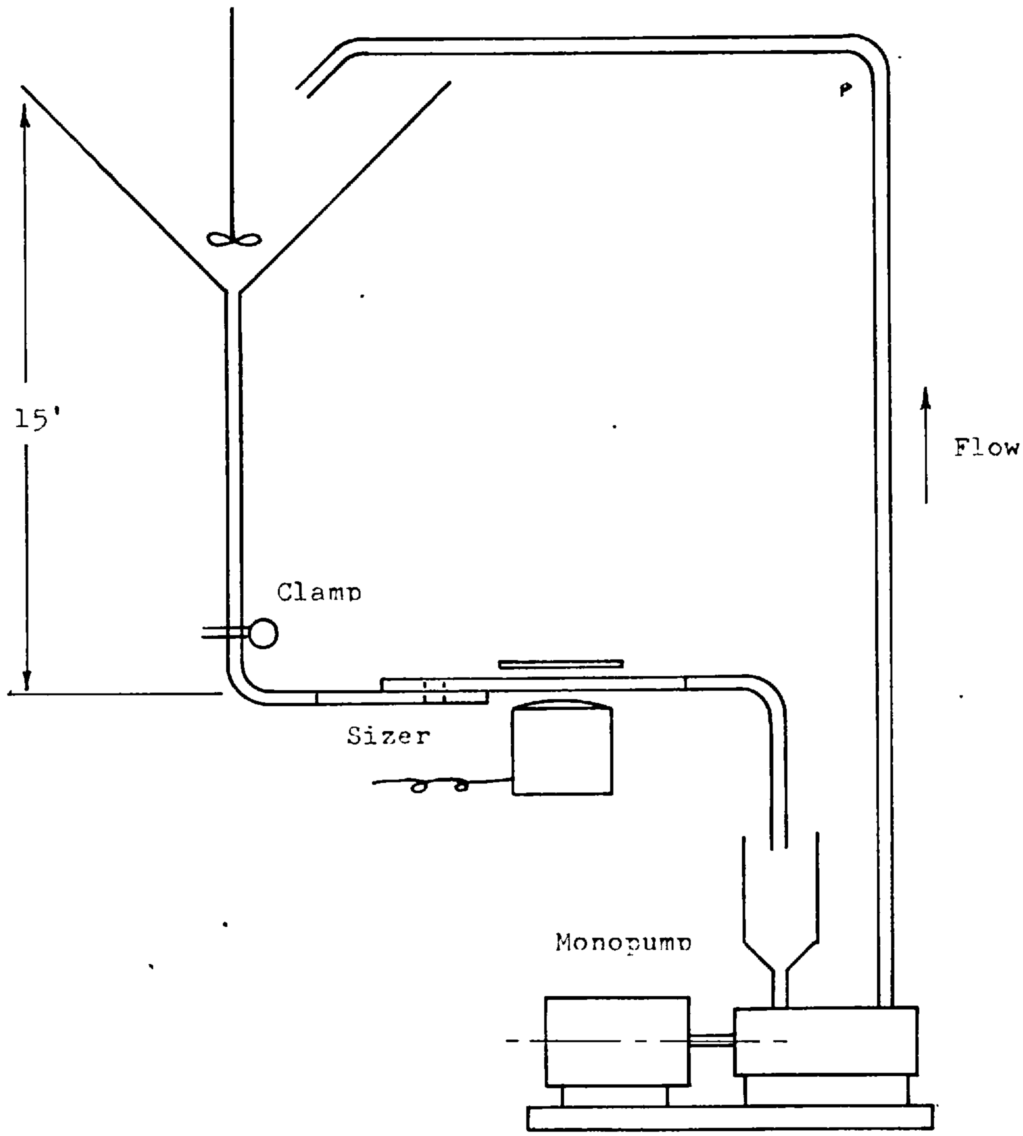

FIGURE A.3.5: First Test Rig (Suspension Flow)

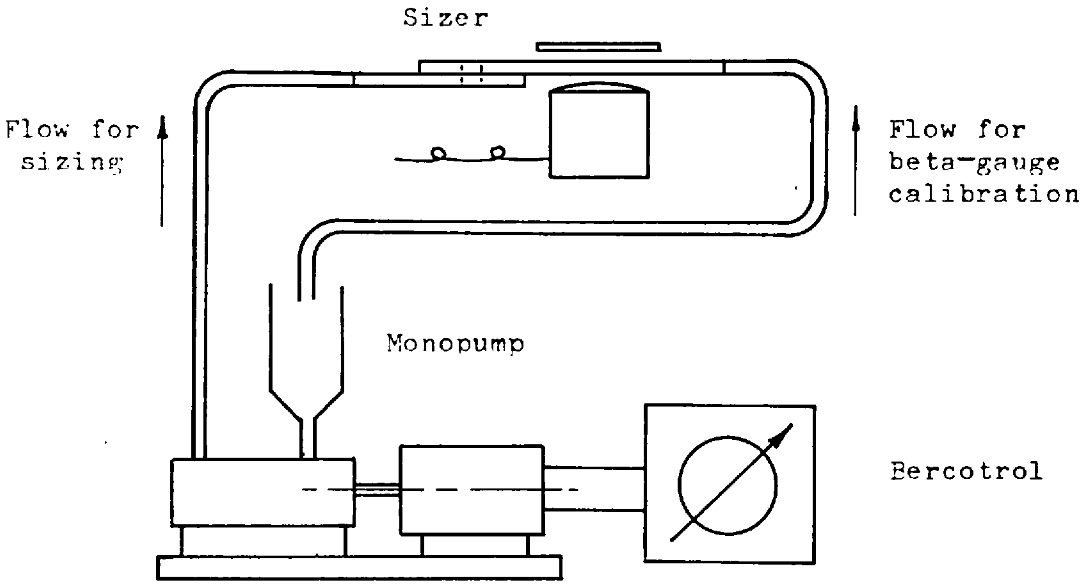

FIGURE A.3.6: Second Test Rig (Suspension Flow)

low penetration beta radiation. Another factor affecting the choice of a new cell was that it was considered desirable to determine the extent of the influence exerted by the radius of the helical turn on the radial motion of the particles.

The third version of the cell is shown in Figure A.3.7. The cross-sectional area of the flow channel remains the same, but the radius of the helix has been reduced by 0.5 cm. The material used was 1.6 m.m. perspex.

3.4.1 Testwork Using Mark 3 cell

The Mark 3 cell was assembled in the test circuit shown in Figure A.3.6 with the pulp flow in the direction indicated for calibration of the beta-gauge. The Bercotrol Unit was calibrated against flowrate by taking timed samples of the suspension. The beta-gauge was then calibrated over a range of solids concentrations, using commercially supplied quartz sand of specific gravity 2.70. (This material was used for all the work described in Section A of this thesis.) The calibration technique was as follows:

The beta gauge was first standardised according to the manufacturers recommended procedure, which eliminated spurious signals within the equipment and compensated for source decay and changes in ambient conditions. The deviation indicator was then set to give a selected reading on the chart recorder with the source and detector set at a particular reference position on the sizer, which contained water only. Periodic readings at this reference positions were taken and used as a check on the calibration of the equipment.

The total supply of quartz sand was screened on a Russell machine into individual size fractions, from which particular size distributions were made up as required. For

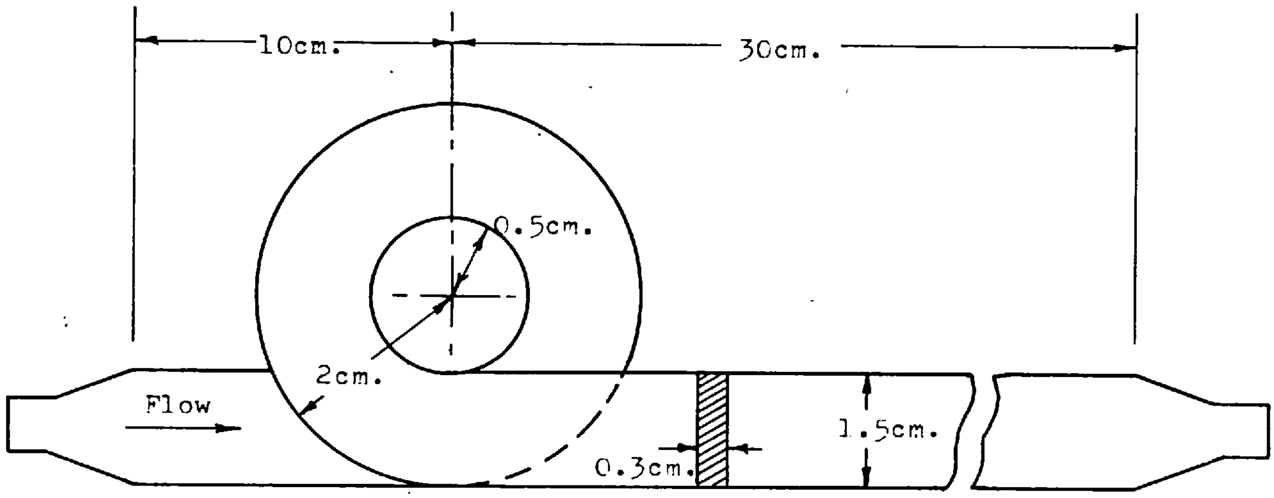

FIGURE A.3.7: Mark 3 Cell

the beta-gauge calibration and sizing runs conducted with the Mark 3 cell, one particular size distribution was used throughout. This was an 'ideal' Gaudin-Schuhmann distribution,[4] having a size modulus of 422 microns and a distribution modulus of 0.738.

The volume of the circuit was measured and the sample weights calculated to give solids concentrations in the circuit ranging from 0 to 50% by weight. (C_v = 0 to 0.27) Each sample was pumped through the circuit at about 60c.c./sec. and measurements were recorded at 0.2 cm. intervals across the sizer channel, the source and detector being positioned by means of a dial gauge attached to one side of the head box. (Figure A.3.3.) For each measuring position, the readings obtained on the chart recorder were plotted against volume concentration of solids. This completed the calibration of the beta-gauge and the flow direction in the circuit was then reversed.

The objects of the sizing runs which followed were twofold: first, to estimate visually whether decreasing the radius of the helix resulted in any marked increase in the radial motion of the particles,and second, to determine whether or not the visually observed concentration gradients could be measured using a beta-gauge.

Four test runs were made, the details of which are given in Table 3.1 overleaf. They covered two levels each of solids concentration in the feed, and flowrate.

TABLE A.3.1.

Test Runs Conducted with Mark 3 Cell

CONC$^{N.}$ OF SOLIDS IN FEED		FLOWRATE
WT.(C_w)	VOL.(C_{vf})	(c.c./sec.)
0.20	0.085	60
0.20	0.085	90
0.30	0.137	60
0.30	0.137	90

Natural quartz: G - S Dist^n, N = 0.738 k = 422μ

Visual observation of the behaviour in the helix suggested that there was little change in the radial motion of the particles. The measurements made with the beta gauge are shown in Figure A.3.8, and it can be seen that quite steep concentration gradients were found. This confirmed that the profiles previously observed visually were of sufficient magnitude for measurement by beta-ray attenuation.

The measurements made were unsatisfactory in one important respect, however. A detailed examination of the geometry of the system revealed that the apparent concentration of solids recorded at a given position was, in fact, an average figure for a zone extending perhaps as far as 0.5cm. on either side of the position.

At this point in the work the Mark 3 cell was badly

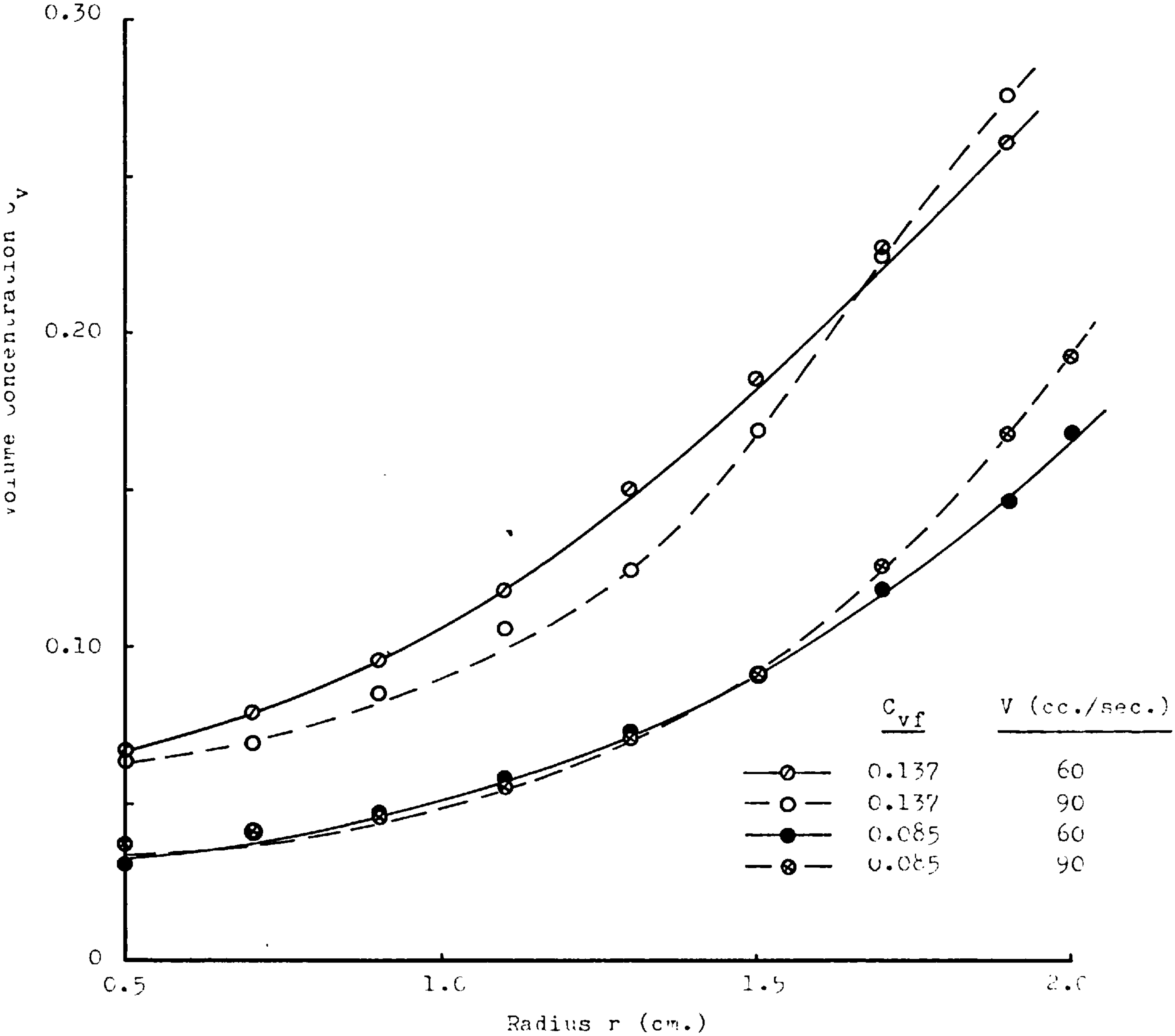

FIGURE A.3.8: Concentration Profiles Obtained with the Mark 3 Cell damaged in the course of an alignment check on the source-detector assembly. It was therefore decided that a new cell could conveniently be introduced at this stage, since certain desirable modifications to the equipment would necessitate recalibration of the cell in any event.

3.5 Mark 4 Cell

In view of the constructional difficulties encountered with the Mark 3 cell and the absence of any real gain resulting from the reduced radius of helix, it was decided to revert to the design adopted for the Mark 2 cell. The Mark 4 was therefore identical to the Mark 2 (Figure A.2.4) except that it was fabricated in 1.6m.m. perspex.

3.5.1 Modifications to Test Rig

The poor resolution of the measuring system, leading to the recording of average densities over a zone about 1 cm. in width, was considered unacceptable. It was therefore decided to collimate the radiation entering the ionisation chamber. This was achieved very simply by screwing two semi-circular brass plates to the rim of the chamber casing, the screws passing through slots in the plates. A collimation slit varying from zero up to 3 m.m. could be obtained by loosening the screws and sliding the plates. (Figure A.3.9.)

The collimation slit was set to 1.5m.m. and aligned with the source. This was a simple operation to perform since even slight misalignments could be detected by marked reductions in the intensity of radiation reaching the ionisation chamber. The Mark 4 cell was then inserted into the head assembly and aligned with source and collimation slit.

With the modified system, the solids concentration

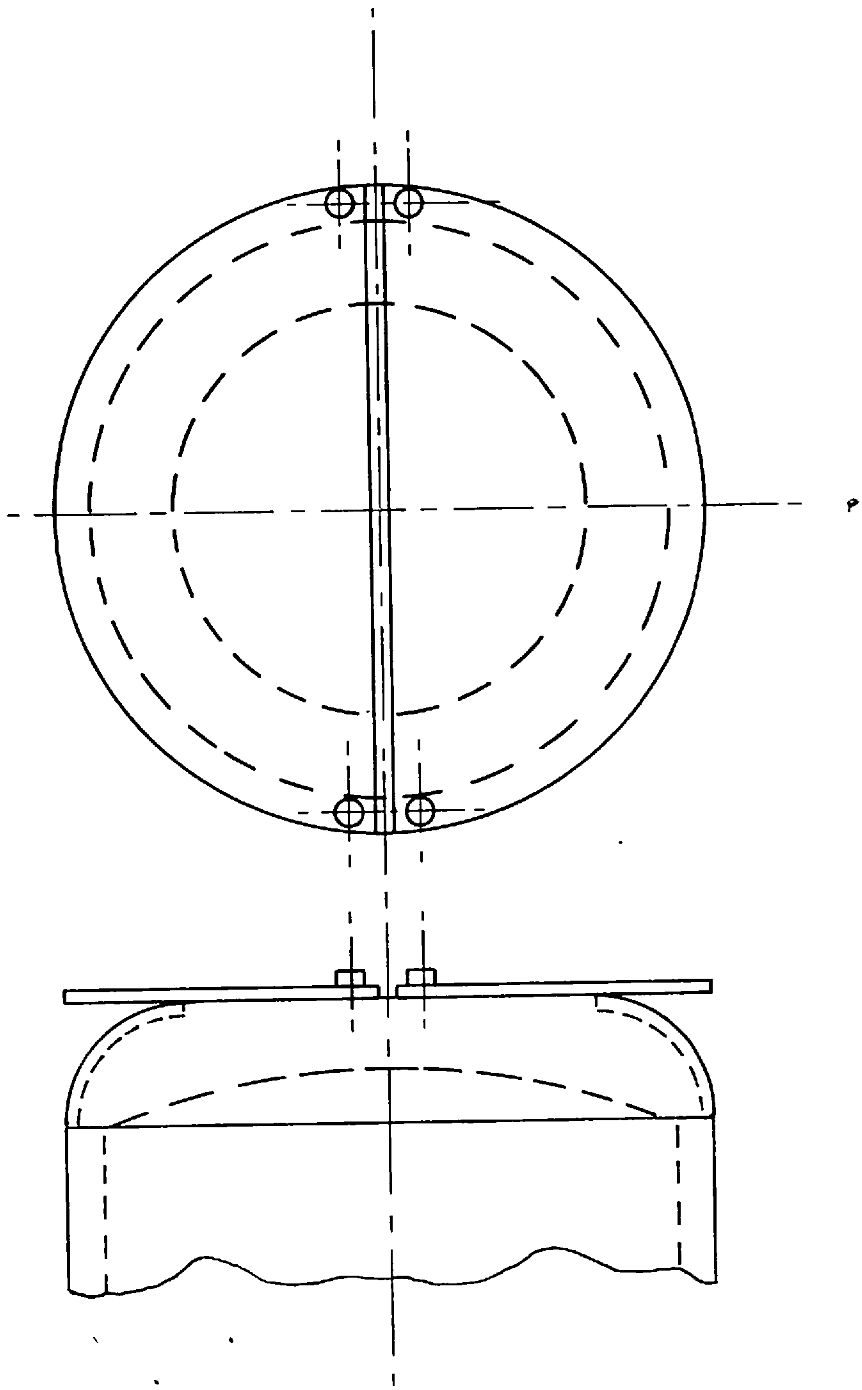

FIGURE A.3.9: Collimation Device

was measured over an area 1.5 mm. wide by 7.6cm. long. The source was actually 11.4 cm. long, but the diameter of the window in the ionisation chamber was only 7.6 cm., hence the effective collimation aperture was of this length. (See Figure A.3.1.)

3.5.2 Testwork using Mark 4 Cell.

The beta-gauge was calibrated for the Mark 4 cell in the manner described previously. (Section 3.4.1).

The testwork which followed was of considerable importance, since the main objective was to assess the ability of the proposed analysis system to distinguish between the various types of size distribution likely to be encountered in a grinding circuit. It was necessary at this stage to decide on the feed conditions to be used, since these would be kept constant throughout. The results obtained with the Mark 3 cell (Figure A.3.8) revealed that satisfactory concentration profiles could be obtained with any of the combinations of feed conditions that were tried. However, the higher feed concentrations imposed a considerably greater strain on the pump and difficulties were experienced in keeping the solids in suspension at the lower flowrate. (60cc/sec.) It was therefore decided that a feed concentration of 20% solids by weight (C_v = 0.085) and a flowrate of 90 c.c./sec. would be suitable. These conclusions were confirmed by tests similar to those shown in Table 3.1, conducted while the Mark 4 cell and test rig were being checked and calibrated.

In view of the widespread usage of the Gaudin-Schuhmann or log-log size distribution function, it was decided to use this type of distribution in all work relating to the testing or calibration of the size analyser. It will be apparent, however, that the action of the size analyser is not in any way dependent on this form of presentation. Alternative calibration systems are in fact developed for the work conducted on glass spheres. (Section B.5.4).

Twelve different size distributions were used to test the size analyser. The properties of these distributions were carefully chosen to span a wide range of conditions. Ten were 'ideal' Gaudin-Schuhmann distributions: the remaining two were unusual types, one being completely deficient in a particular size fraction and the other having an unusually high proportion of the same size fraction. Full details of the distributions are given in Table A.3.2 and Figures A.3.10-A.3.13. It can be seen that distributions 1 - 4 have the same distribution modulus but differing size moduli. On the other hand, distributions 2,5,6,7 have the same size modulus but differing distribution moduli. Distributions 8,9 form other groups with 3,4, while distribution 10 was designed to investigate the effect of having a small size modulus and an abnormally large distribution modulus. Distributions 2,8,9, 10 all contain the same proportion of minus 200 mesh material. Finally, distributions 11, 12 are the unusual types referred to previously.

<u>TABLE A.3.2.</u>

(see overleaf)

TABLE A.3.2.

Size Distributions used in Tests with Mark 4 Cell

B.S. Mesh	(μ)	WT. % IN EACH SIZE FRACTION FOR DIST^N NO:- 1	2	3	4	5	6	7	8	9	10	11	12
+36	422												
-36 +52	295	23.2											
-52 +72	211	16.9	21.9			15.7	32.8	43.4				17.0	28.2
-72 +100	152	12.8	16.8	21.5		13.0	21.7	24.2	27.5			13.0	19.8
-100 +150	104	11.5	15.0	19.2	24.4	12.6	16.5	15.4	22.5	42.1		40.0	
-150 +200	76	7.4	9.5	12.2	15.6	8.7	9.0	7.0	13.2	21.1	63.2	6.2	11.0
-200	-	28.2	36.8	47.1	60.0	50.0	20.0	10.0	36.8	36.8	36.8	23.8	41.0
TOTAL		100.0	100.0	100.0	100.0	100.0	100.0	100.0	100.0	100.0	100.0	100.0	100.0
Size Mod.(k)		422	295	211	152	295	295	295	211	152	104	-	-
Dist^n Mod.(N)		0.738	0.738	0.738	0.738	0.510	1.180	1.698	0.979	1.443	3.188	-	-

The test samples were made up from the size fractions prepared on the Russell screen, the total weight of each sample being such as to give a suspension containing 20% solids by weight (C_{v_f} =0.137)when added to the circuit. Each sample was run through the size analyser at a flowrate of approximately

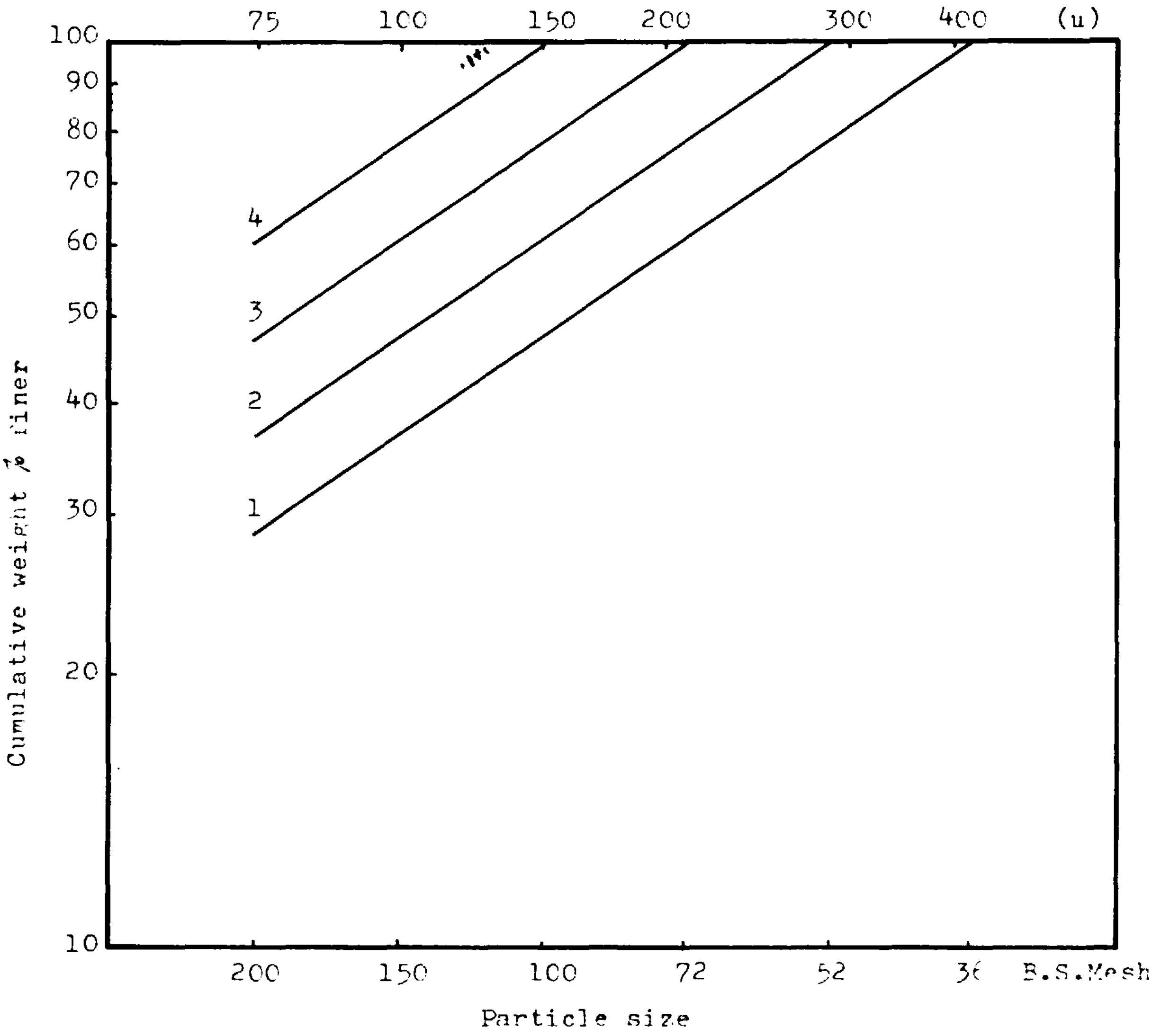

FIGURE A.3.10: Size Distributions 1,2,3,4

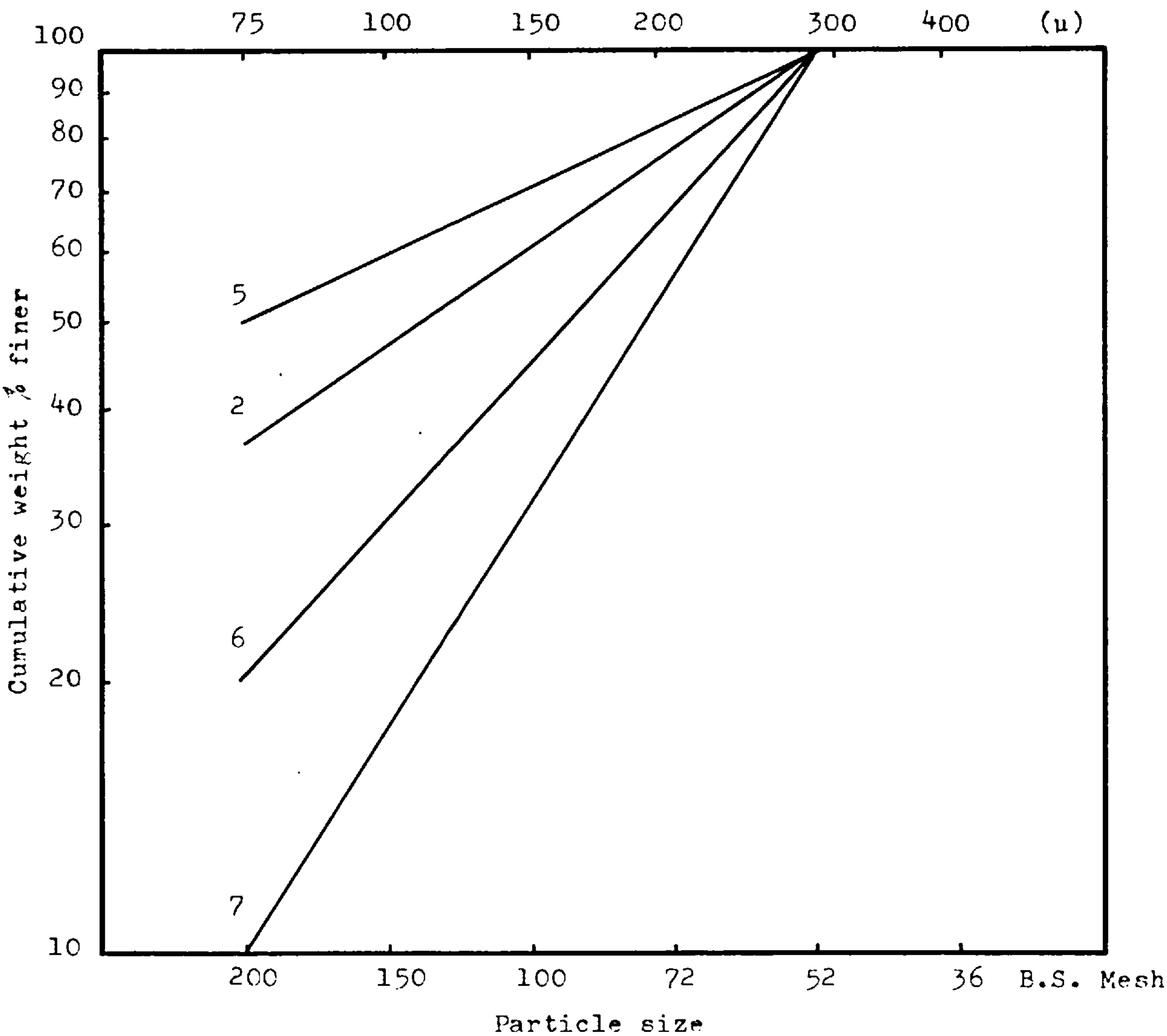

FIGURE A.3.11: Size Distributions 2,5,6,7

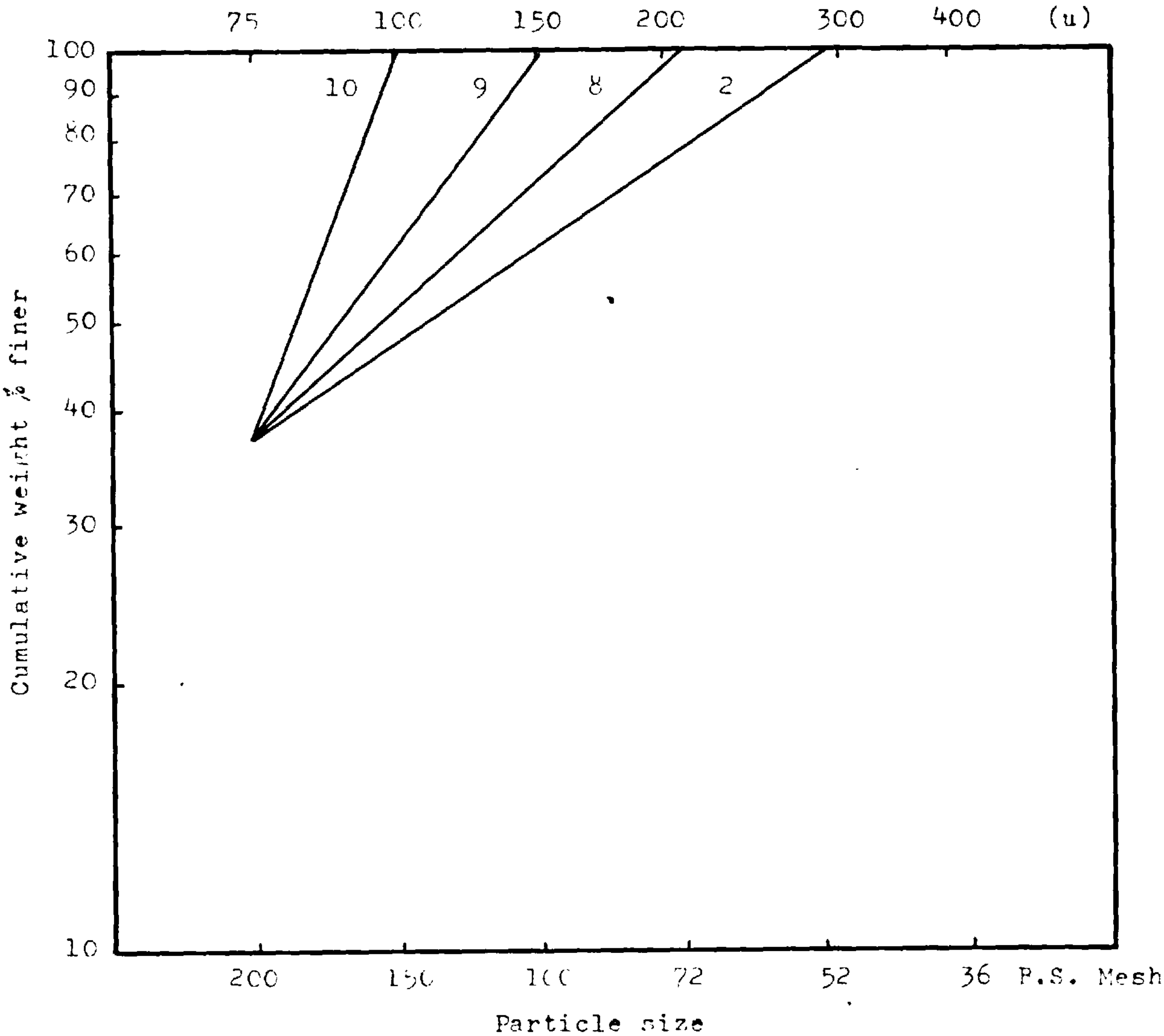

FIGURE A.3.12: Size Distributions 2,8,9,10

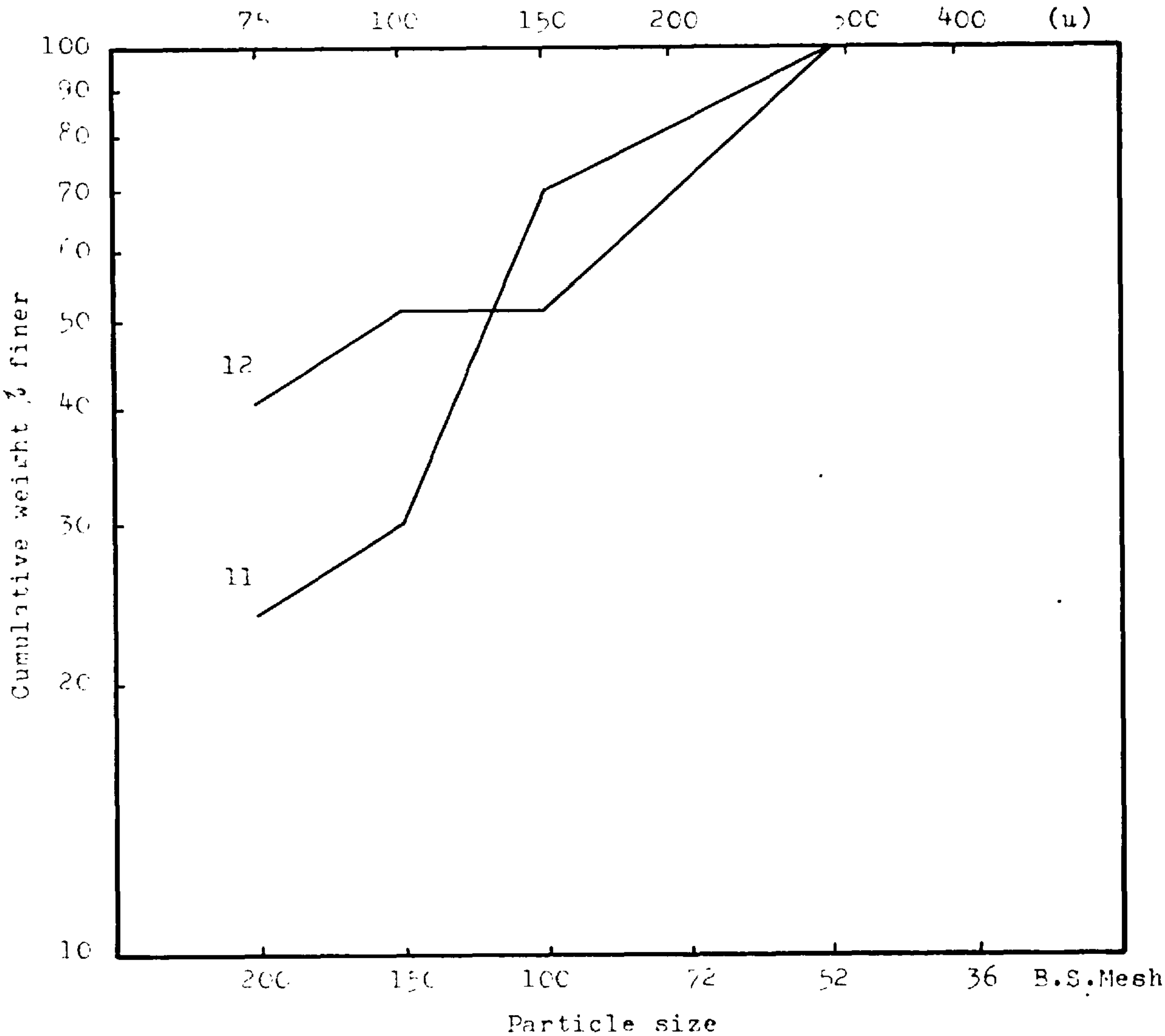

FIGURE A.3.13: Size Distributions 11,12

90c.c./sec. and the particle concentration measured at selected intervals across the sizer channel. The results of these measurements are shown in Figures A.3.14 - A.3.17.

The concentration profiles shown in each group all vary in the correct sense and the differences between the profiles are clearly detectable. However, in nearly all cases the spacing of the concentration profiles was far more irregular than would have been expected from consideration of the size distributions causing them. Two factors contributing to this effect were discovered in the course of the tests. First, the sensitivity of the beta-gauge was poor, this being mainly due to the thick walls (1.6mm.)of the Mark 4 cell. Second, the system of flowrate control, which consisted of calibrating the flowrate in the circuit against the Bercotrol setting, was found to be inadequate. Significant variations in flowrate were found for successive test runs conducted at the same Bercotrol setting. A third possible factor was discovered when check sieve analyses on some of the reclaimed samples revealed considerable deviations from the nominal or made-up distributions. The cause of these deviations was found to be in the size fractions obtained from the Russell screen, which in some instances contained as much as 20% by weight of oversize material.

3.6 Summary and Conclusions

In general the concentration profiles obtained with the Mark 4 cell varied sufficiently from one distribution to another to confirm the potential usefulness of the technique as a means of size distribution analysis. The next object therefore became the development of a suitable calibration technique.

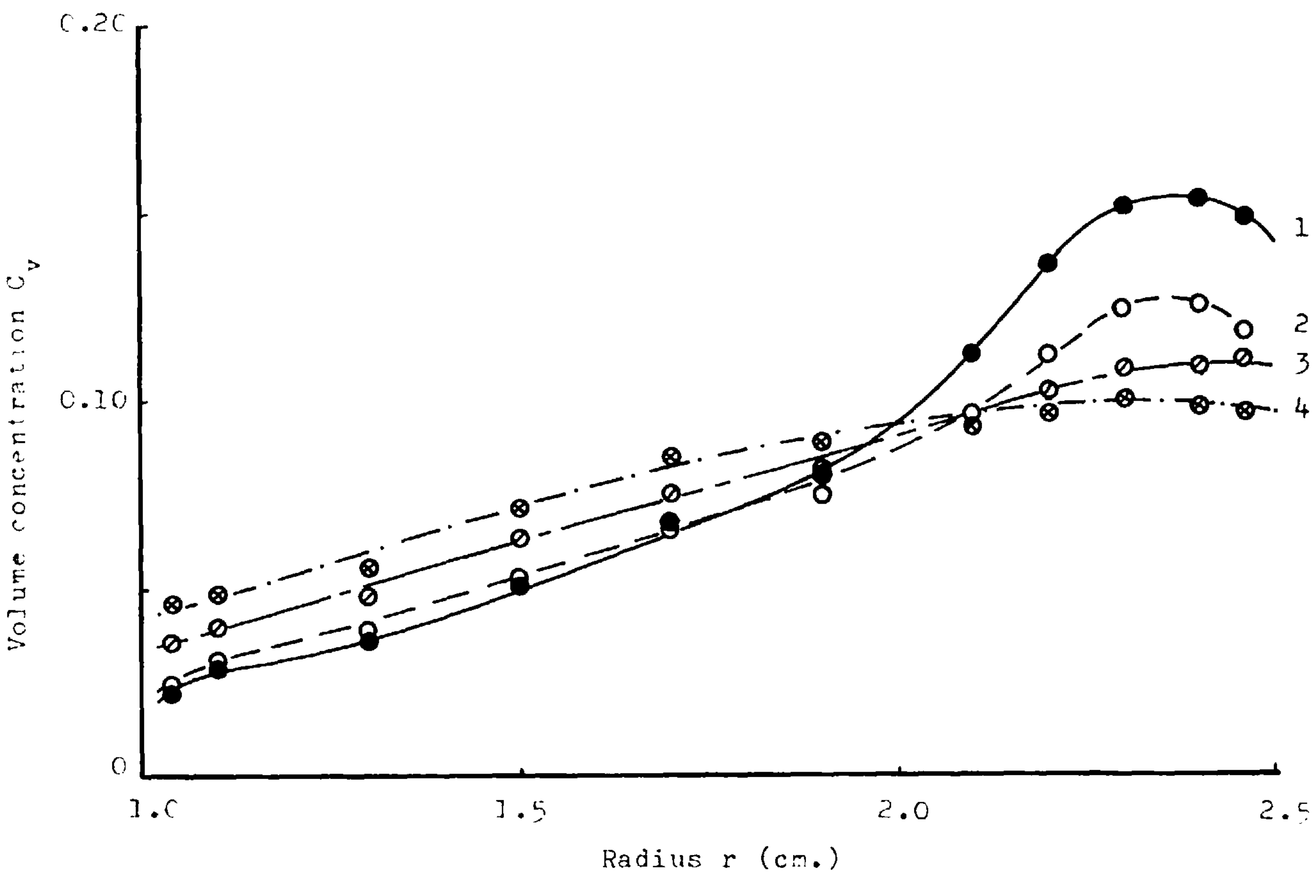

FIGURE A.3.14: Concentration Profiles Obtained with the Mark 4 Cell Size Distributions 1,2,3,4

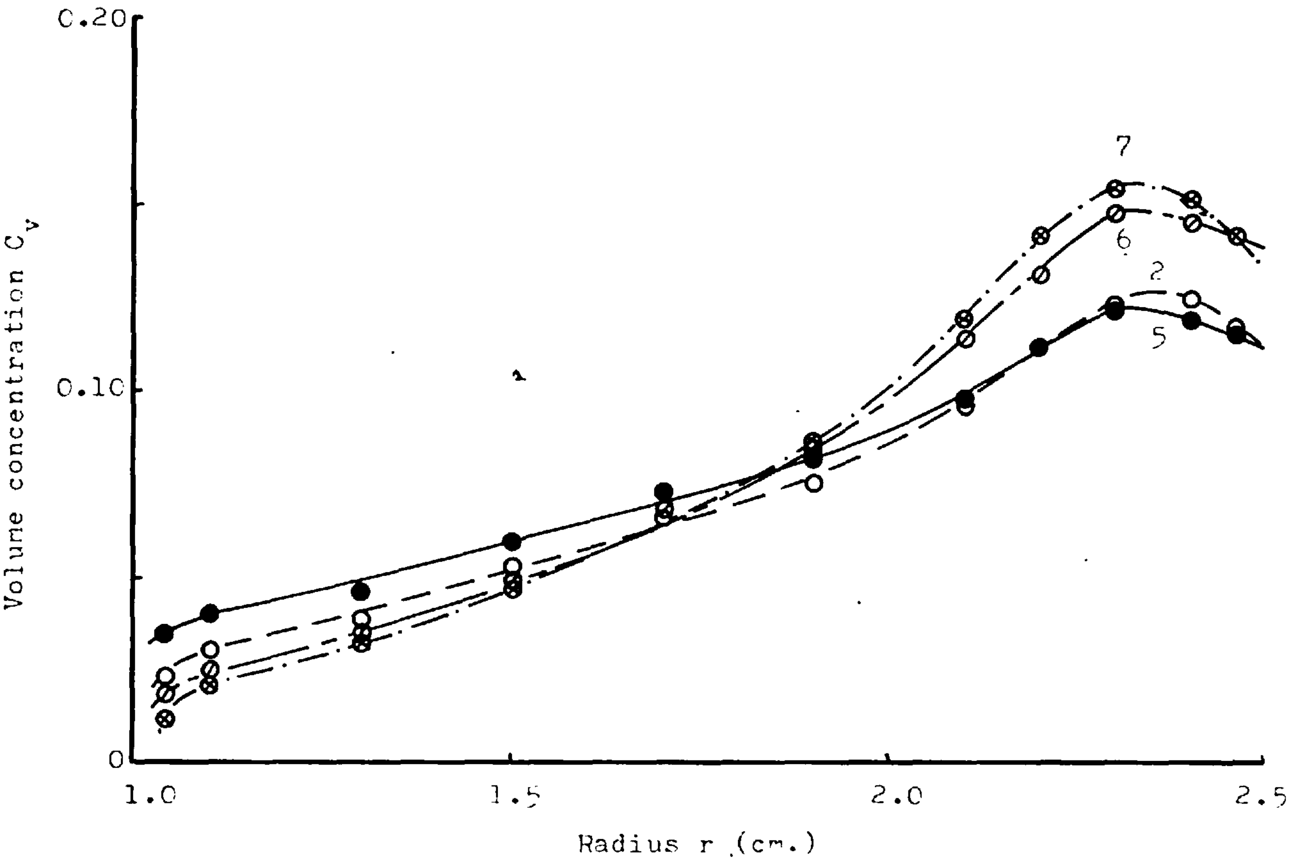

FIGURE A.3.15: Concentration Profiles Obtained with the Mark 4 Cell Size Distributions 2,5,6,7

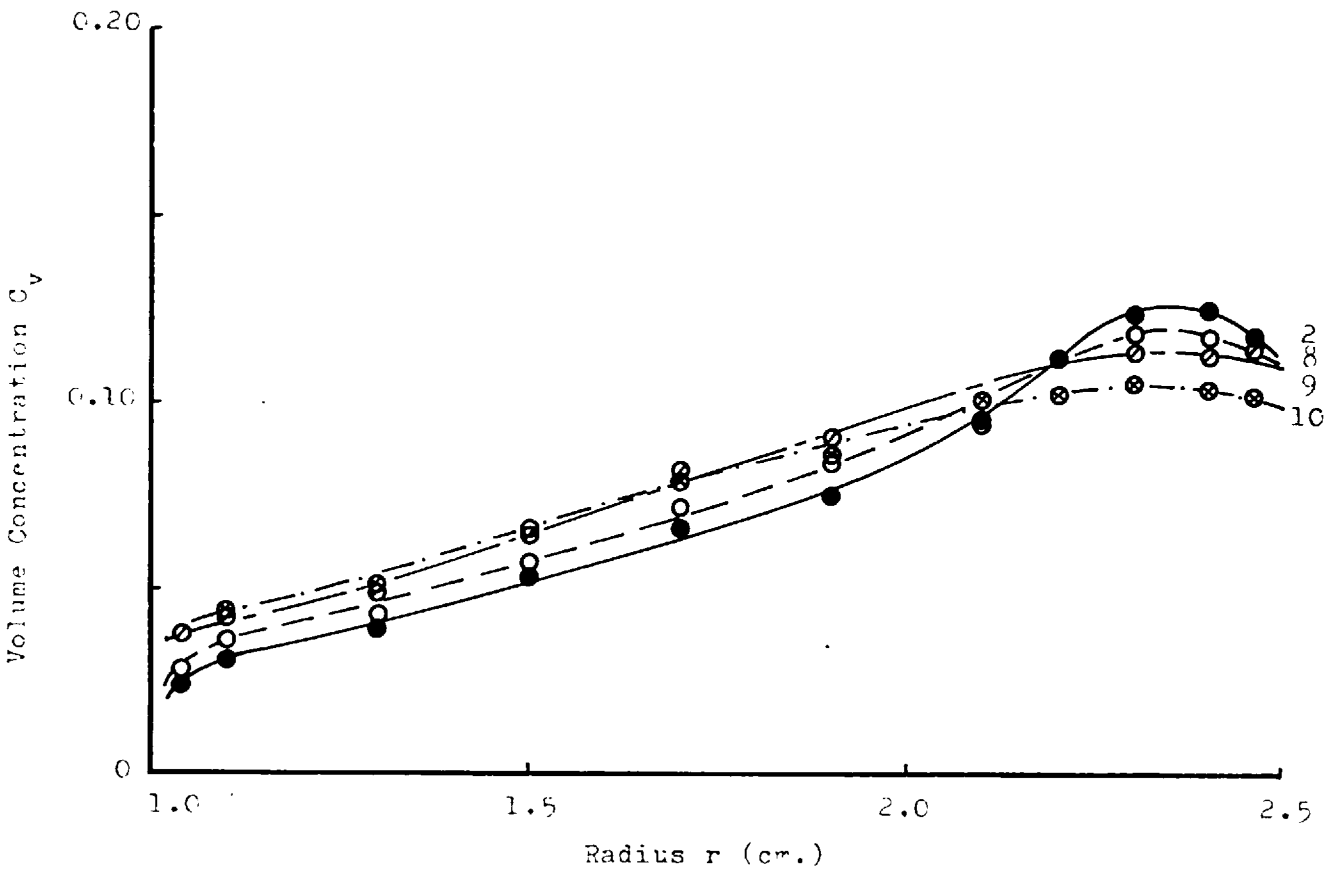

FIGURE A.3.16: Concentration Profiles Obtained with the Mark 4 Cell Size Distributions 2,8,9,10

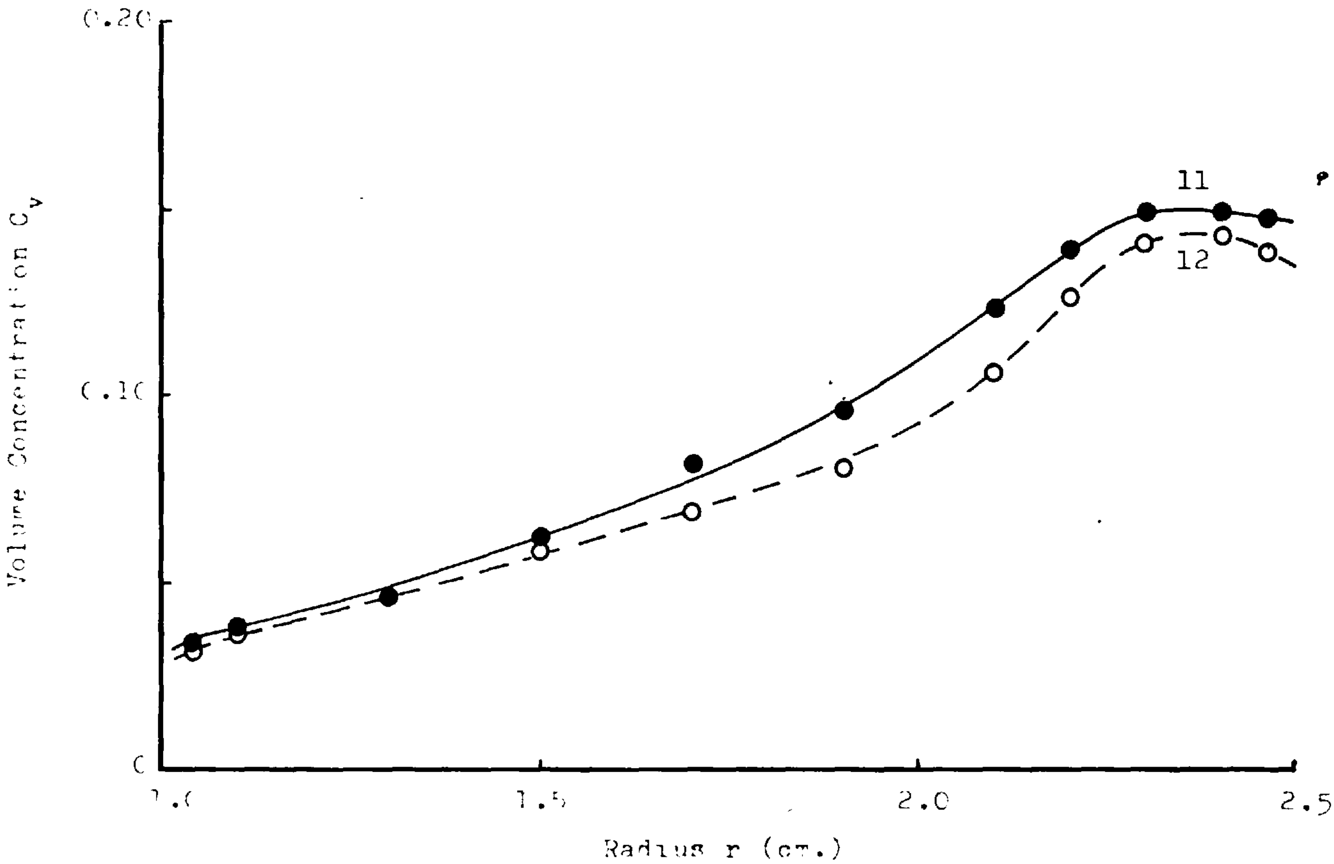

FIGURE A.3.17: Concentration Profiles Obtained with the Mark 4 Cell
Size Distributions 11,12

Certain modifications to both the equipment and the test techniques were clearly desirable. These were effected before commencing the next phase of the testwork. (See sections 4.1.2, 4.1.3).

4. CALIBRATION OF SIZER

4.1 Mark 5 Cell

4.1.1 Introduction

The work carried out with the Mark 1 - 4 cells was designed to establish whether or not the basic technique could be used to differentiate between various size distributions and was mostly qualitative in nature. The results obtained were encouraging and so the next stage of the work clearly involved finding some suitable calibration technique by means of which the qualitative differences observed earlier could be converted into measurements of one or more parameters of the size distributions concerned.

Certain weaknesses in the equipment and experimental techniques had come to light during the tests conducted with the Mark 4 cell and these were dealt with before proceeding further.

4.1.2 Mark 5 Cell

The relatively low sensitivity of the existing experimental rig was mainly caused by the thick walls of the Mark 4 cell. These were 0.15cm. in thickness, giving a total wall absorption in the radiation path of 0.3cm. of perspex. For a suspension containing 10% by volume of ground quartz (σ= 2.70) and a channel depth of 0.3cm., this meant that 89% of the absorption was contributed by the perspex and water and only 11% by the quartz particles.

The Mark 4 cell was therefore removed from the measuring head and the channel walls in the measurement zone were milled down to give a thickness of 14/1000 inches. This boosted the proportion of the total absorption mass contributed by the quartz particles from 11% to nearly 19%.

The overall improvement was somewhat less than indicated by these figures, due to the unchanged attenuation occurring in the air gaps and detector window. However, the change was important enough to require identification and so the modified Mark 4 cell was redesignated as the Mark 5.

4.1.3 Modifications to Test Rig

One of the drawbacks attached to the existing equipment was that it was impossible to be certain that the desired flowrate was being maintained. Also, while calibrating the Mark 5 cell it became apparent that the thin walls were sensitive to the pressure changes occurring in association with flowrate variations. Some means of measuring and recording the flowrate of the suspension was therefore required.

Turbine flowmeters were tried, but the finer particles got into the bearings and caused the rotors to sieze up. Rotameter flowmeters were also tried without success. Eventually an electromagnetic flowmeter was obtained, which gave consistently reliable results throughout the remaining test programme. This was a 1/4 inch diameter Kent 'Veriflux', which was installed some four feet downstream of the monopump outlet. The signal from the Veriflux was led to a Honeywell-Brown six point chart recorder, on which density readings were also recorded. This density record was a duplicate of that made on the original Kent chart recorder. The modified test rig is shown in Figure A.4.1.

4.1.4 Testwork Using Mark 5 Cell

The flowmeter and beta-gauge were checked and calibrated. It was decided to use samples having the same size distributions as were used with the Mark 4 cell, since these gave good coverage of the desired range of sizes. Also, this

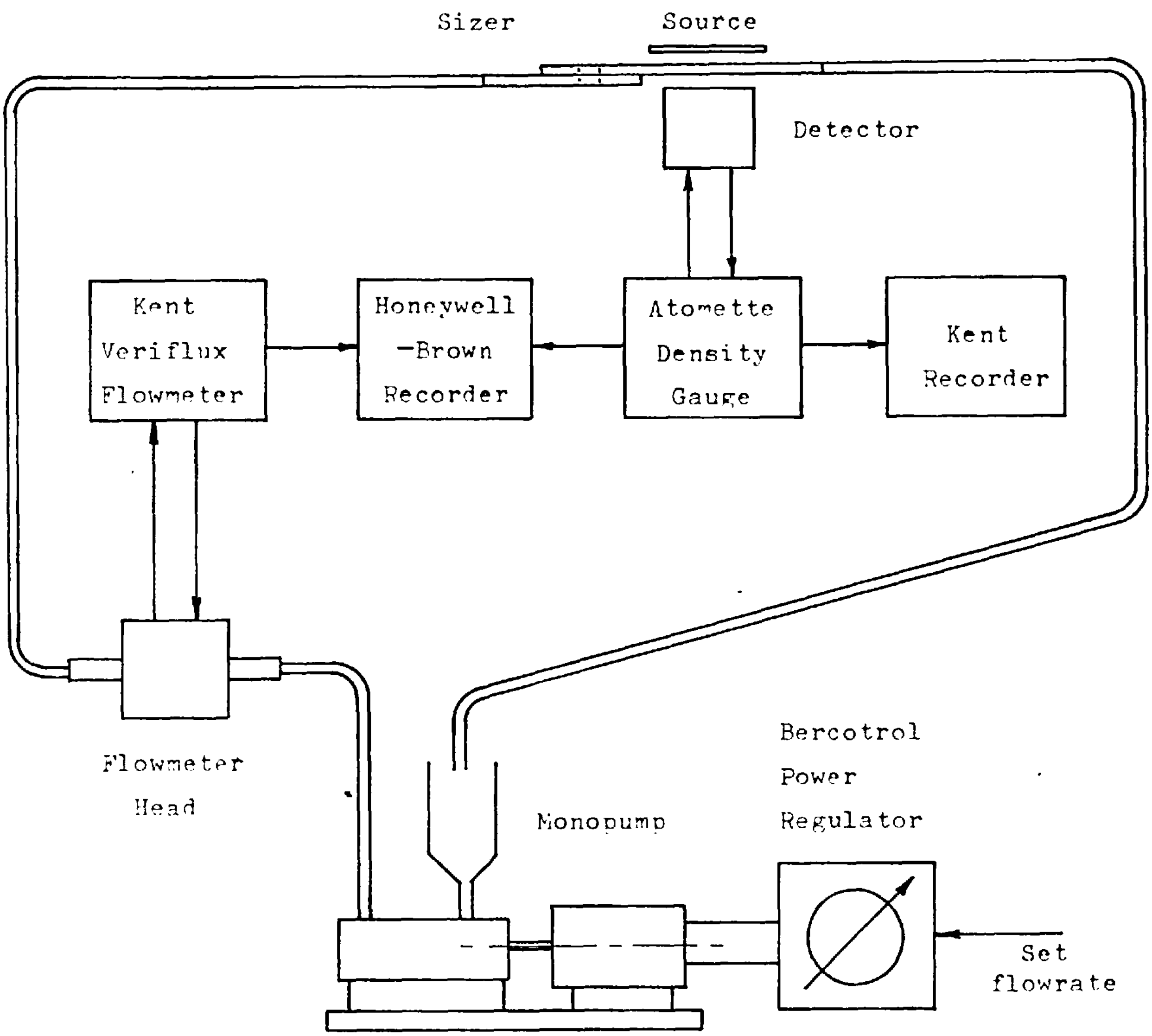

FIGURE A.4.1: Modified Second Test Rig

made it possible to check the results obtained with different cells against each other. However, the size distributions used in the Mark 4 cell tests were unsatisfactory in one important respect, for size analyses of the reclaimed samples revealed that the Russell screen fractions used in making up the samples deviated considerably from their nominal composition.

A new set of 8 inch British Standard Sieves was therefore obtained and all materials used subsequently were prepared and analysed using these sieves. (Check analyses of reclaimed samples revealed no significant errors in later tests.)

The twelve size distributions were run through the sizer under the feed conditions previously selected. i.e. a suspension flowrate of 90c.c./sec. and a concentration of solids equal to 20% by weight (C_{vf}=0.137). Some difficulty was encountered with all samples due to flexure of the channel walls, and to ensure that the readings obtained could be accurately compensated for this effect, two full scans were carried out on each sample. Quite marked temperature rises were recorded over the total duration of the scans, changes of the order of 15°C being not uncommon. The differences between the corrected observations were small in all cases and it was therefore concluded that temperature was not a significant variable. The mean of the two sets of readings was taken as the final result in each case. The results are presented and discussed in the next section.

4.1.5 Analysis of Data

The object of this stage of the work was to relate the measurements obtained with the Mark 5 cell to the size distributions producing them. It was desirable to keep the calibration technique as simple as possible and for this reason it was decided to use the density gauge output directly, instead of converting it into the corresponding particle concentration. The signal obtained from the density gauge (S) as it was scanned across the sizer outlet has been plotted in Figures A.4.2 - A.4.5 for the four groups of size distributions shown earlier in Figures A.3.10 - A.3.13.

Two techniques were employed in the attempt to devise a suitable calibration method. The first consisted of plotting the readings obtained at a particular position against the weight fractions of material (M_F) finer than various sizes in the feed and looking for the best correlation between the two. This system was not very successful: the failure is evident in the results already shown in Figure A.4.4. Distributions 2,8,9,10 all contained 36.8% -200 mesh material and if a satisfactory correlation existed, the minimum readings near r = 1.0 should have been the same for all distributions. In fact, the curves for distributions 9 and 10 are virtually coincident in this region, but 2 and 8 fall a considerable distance away.

The second technique was based on one of the most striking features of the density gauge profiles, namely the change in the difference between the maximum and minimum readings from one size distribution to another. This quantity, designated ΔS, is illustrated in Figure A.4.2 and the values of ΔS for the size distributions are given in Table A.4.1.

TABLE A.4.1

(see overleaf)

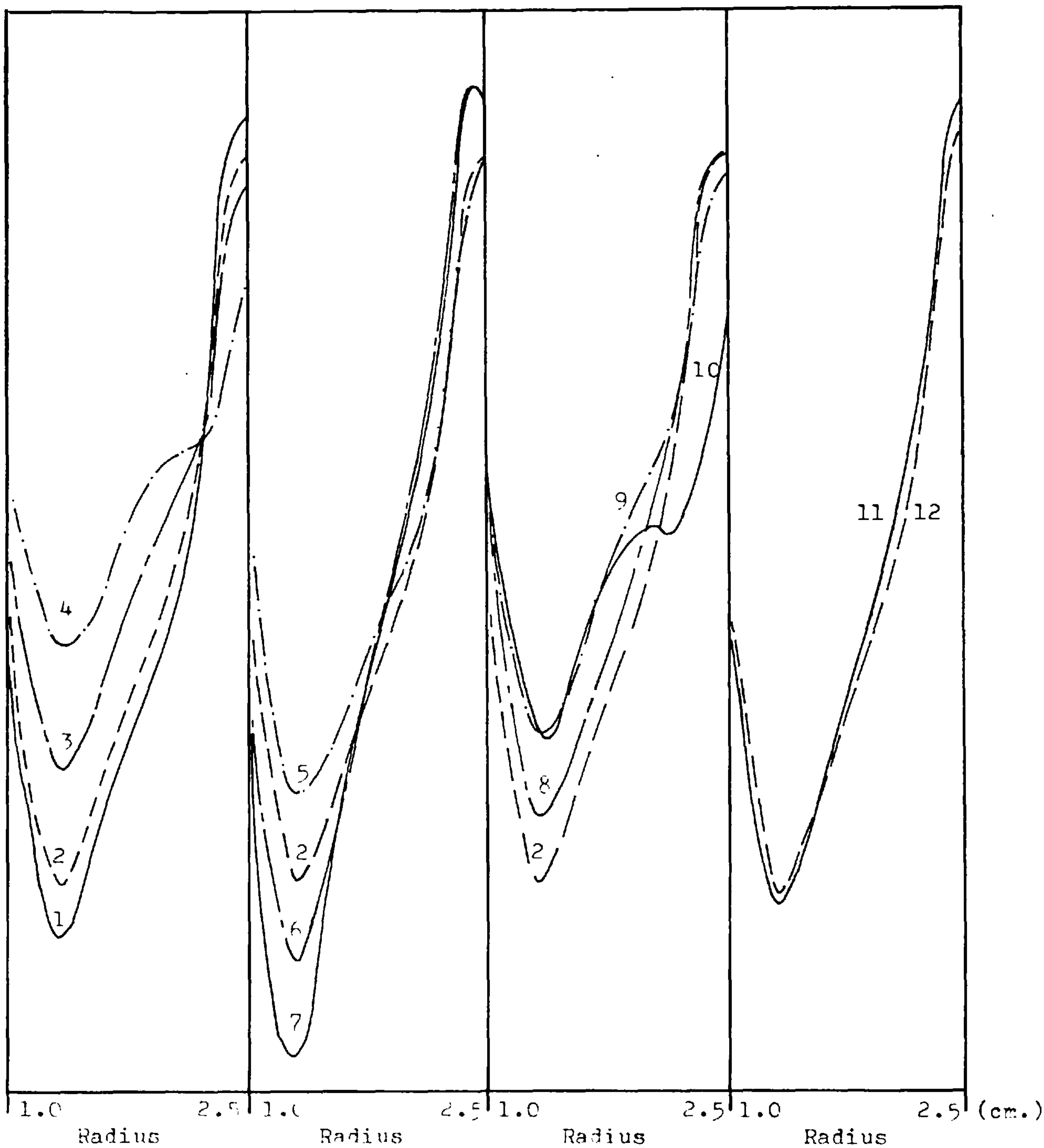

FIGURE A.4.2 FIGURE A.4.3 FIGURE A.4.4 FIGURE A.4.5

Density Gauge Profiles Obtained with the Mark 5 Cell

TABLE A.4.1

Values of ΔS for Quartz Size Distributions

SIZE DISTRIBUTION NO.	SIZE MODULUS 'k'	DISTRIBUTION MODULUS 'N'	ΔS
1	422	0.738	53.5
2	295	0.738	47.4
3	211	0.738	38.4
4	152	0.738	24.2
5	295	0.510	40.9
6	295	1.180	56.6
7	295	1.698	62.8
8	211	0.979	44.8
9	152	1.443	36.5
10	104	3.188	26.2
11	(175)	(2.313)	52.1
12	(295)	(0.772)	49.4

The Gaudin-Schuhmann distributions (1 - 10) can be completely specified by means of two parameters, the size and distribution moduli, and these provided an obvious starting point for the calibration attempt. ΔS was plotted against k for distributions 1 - 4 and against N for distributions 2,5,6,7 (Figures A 4.6, A.4.7).

The shape of the N vs. ΔS curve (Figure A.4.7) suggested a relationship of the type $\Delta S \propto \log N$ and so a plot of ΔS vs. log N was constructed. (Figure A.4.8).

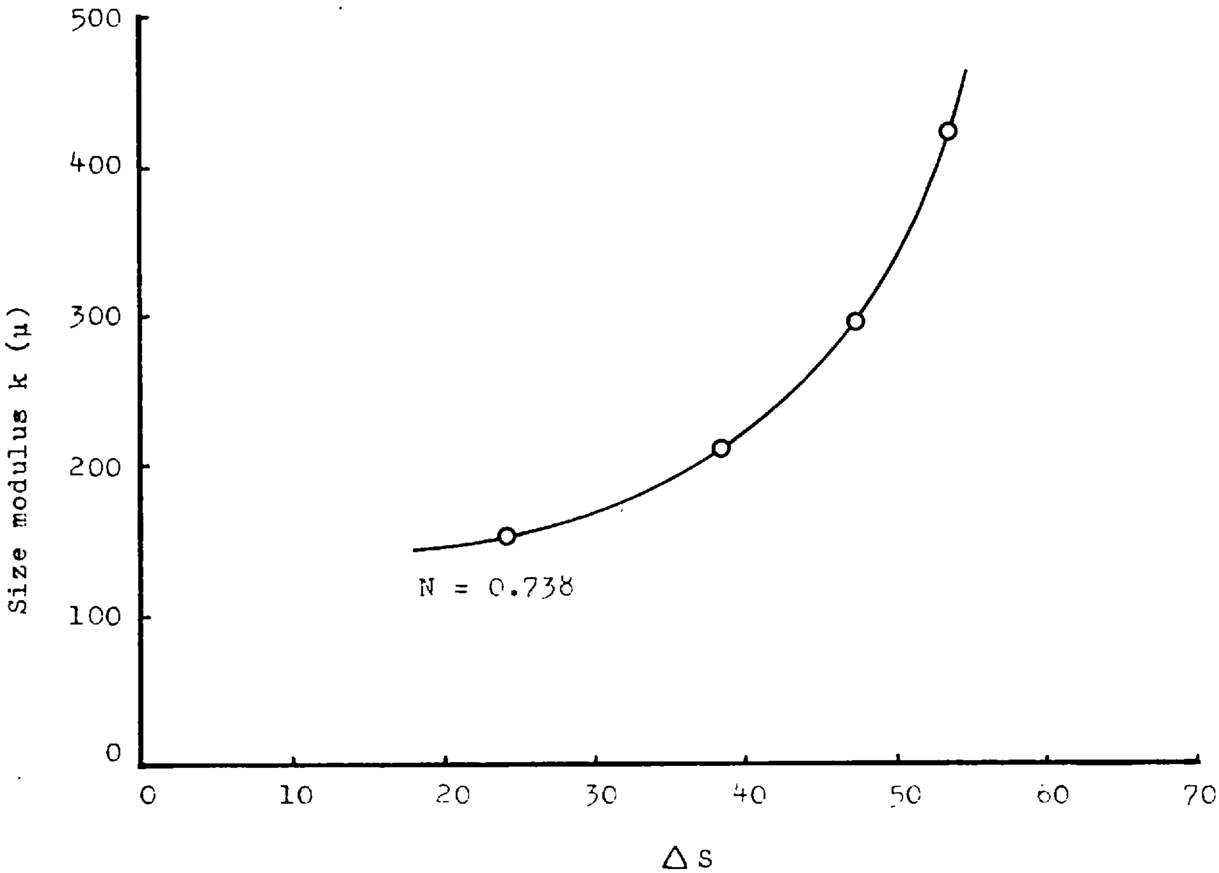

FIGURE A.4.6: ΔS vs. k for Mark 5 Cell

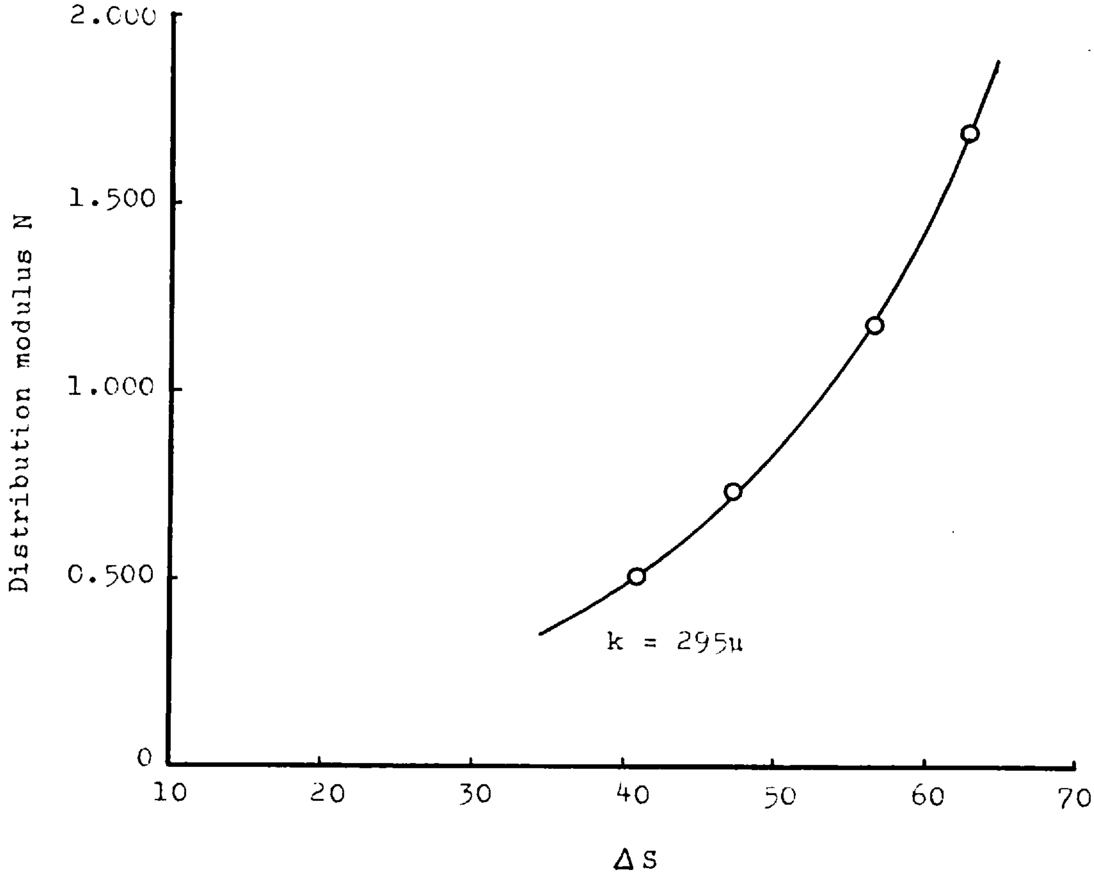

FIGURE A.4.7: ΔS vs. N for Mark 5 Cell

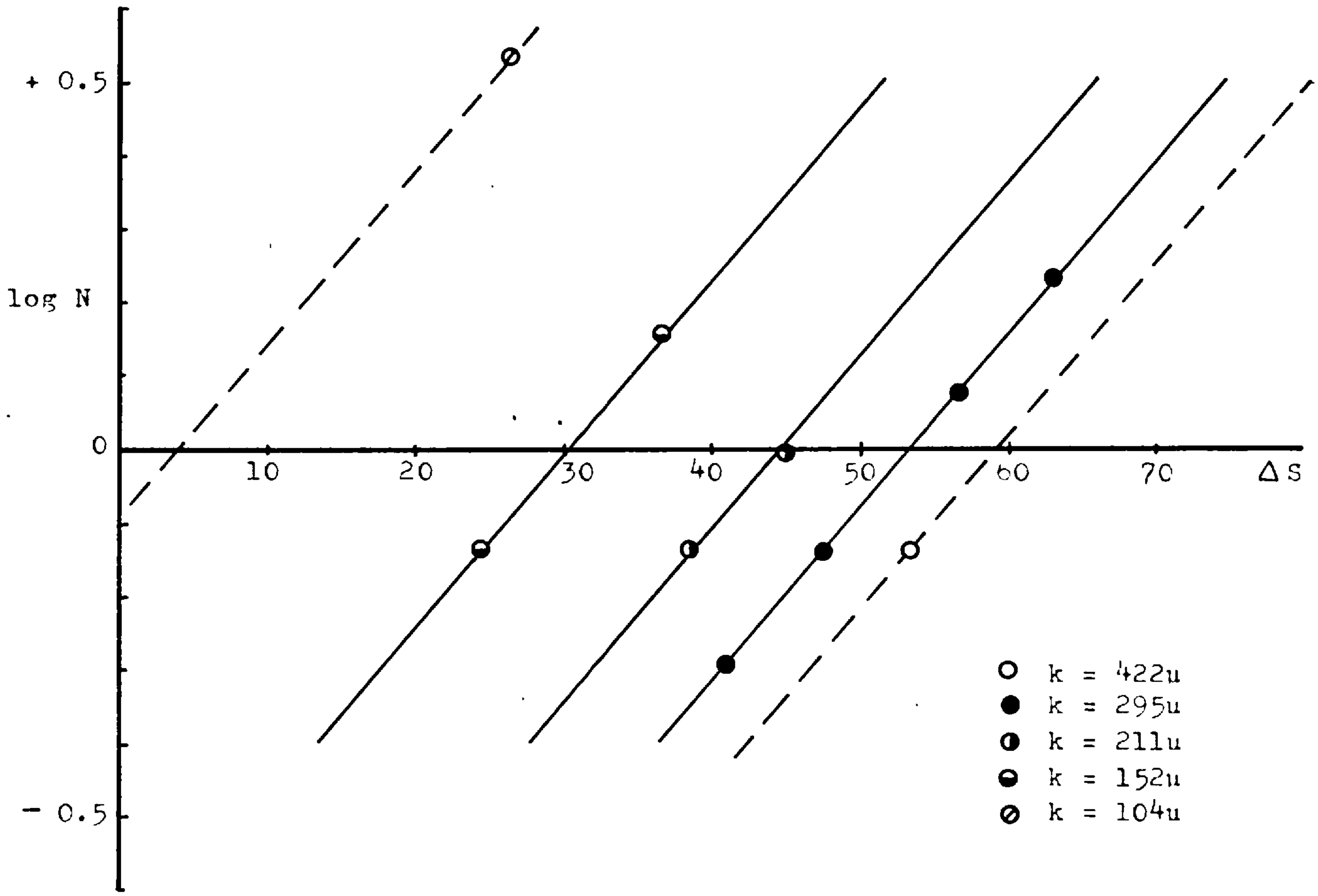

FIGURE A.4.8: ΔS vs. Log N for Mark 5 Cell

The results immediately suggested the family of straight lines shown, which all have the same slope but intercepts that vary with the size modulus in some manner. Therefore:

$$S = A + A_1 \log N \quad \ldots \quad \ldots \quad \ldots \quad (4.1)$$

where A_1 is the slope $\left[\frac{d\Delta S}{d \log N}\right]$ and A the intercept on the ΔS axis.

A further plot of A versus k (Figure A.4.9) suggested the relationship

$$A = B + B_1 \log (k - 90) \quad \ldots \quad \ldots \quad (4.2)$$

where B_1 is the slope and B the intercept on the A axis.

This was confirmed on the same plot. Calculated values of the slopes A_1, B_1 and the constant B were obtained.

$A_1 = B_1 = 41.7 \qquad B = -43.4$

4.1.6 Final Calibration Technique

Combining equations 4.1, 4.2 leads to the result

$$\Delta S = 41.7 \log N (k-90) - 43.4 \quad \ldots \quad \ldots \quad (4.3)$$

Values of N(k - 90) have been calculated for the 10 ideal Gaudin-Schuhmann distributions and plotted on a logarithmic scale against ΔS. (Figure A.4.10). Equation 4.3 has also been plotted on the same graph: it can be seen that it represents a satisfactory approximatioh to the results. The results for the two non-ideal distributions have also been included, plotted against estimated average values of N(k - 90).

In order to confirm the applicability of equation 4.3 two new size distributions (13, 14) were made up and run through the equipment. These were both ideal Gaudin-Schuhmann distributions and had values of N(k - 90) chosen to fill gaps in the coverage provided by distributions 1 - 10.

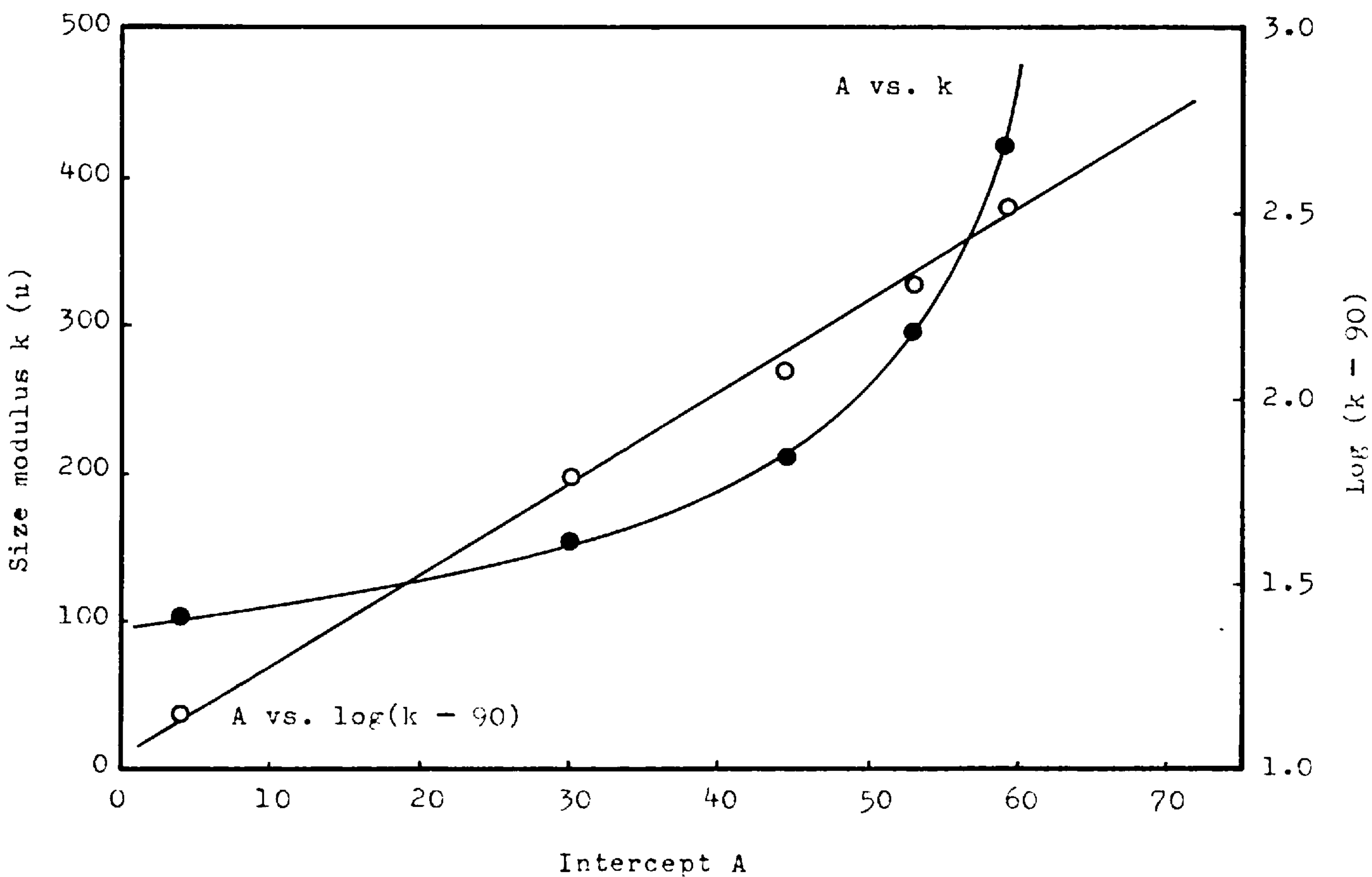

FIGURE A.-.9: Intercept (A) vs. k for Mark 5 Cell

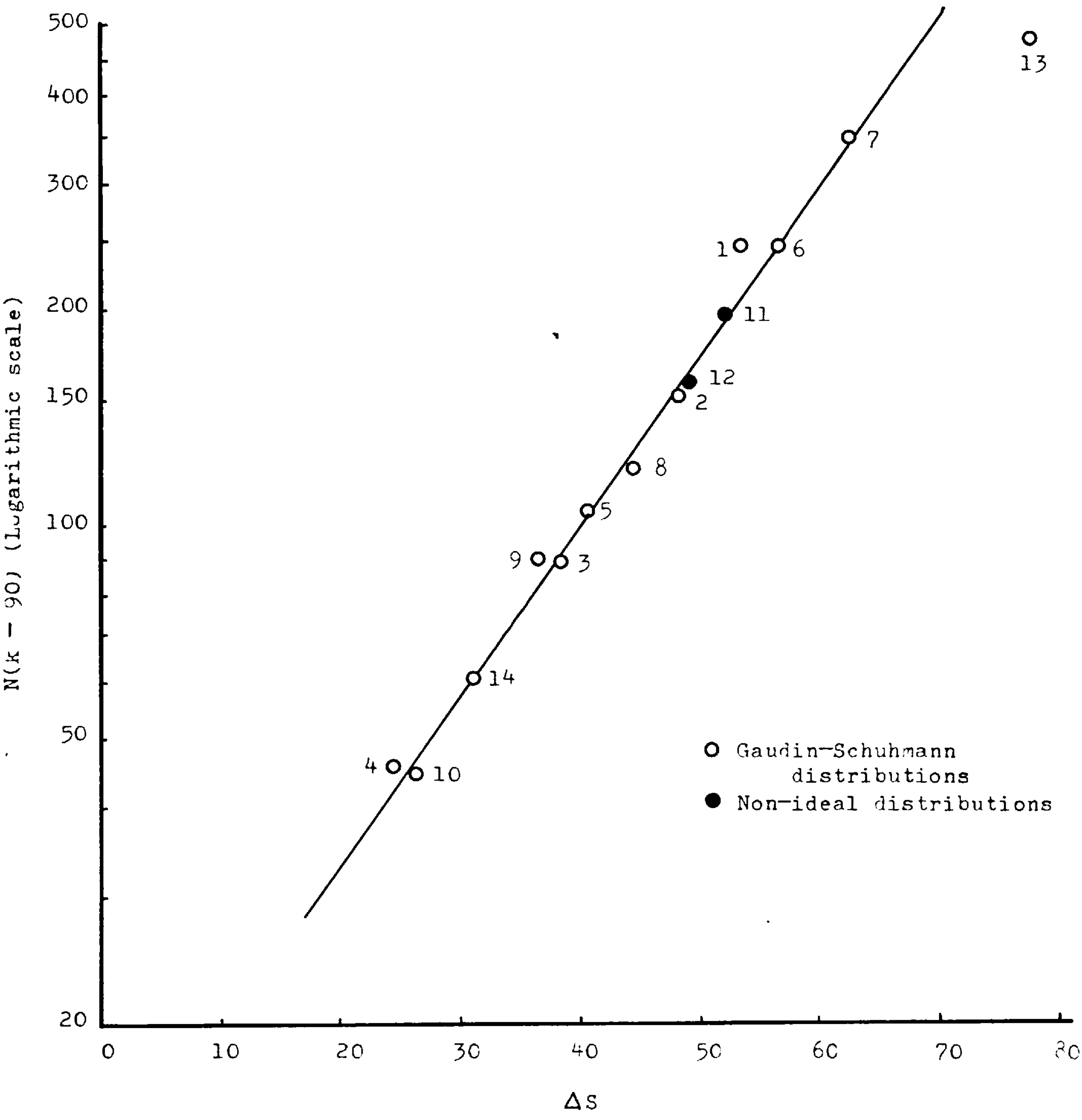

FIGURE A.4.10: Size Distribution Calibration for Mark 5 Cell

Details are given in Table A.4.2.

TABLE A.4.2.

Extra Size Distributions used in Tests with Mark 5 Cell

SIZE FRACTION		WT.% IN EACH SIZE FRACTION FOR DISTRIBUTION NO.	
B.S.Mesh	(μ)	13	14
+36	422	-	-
-36 +52	295	42.1	-
-52 +72	211	21.1	-
-72 +100	152	14.7	-
-100 +150	104	9.1	31.5
-150 +200	76	4.9	17.8
-200	-	8.1	50.7
TOTAL		100.0	100.0
Size Modulus (k)		422	152
Dist^{n}. Modulus (N)		1.443	0.979

The values of ΔS measured for distributions 13 and 14 were 78.0 and 31.2 respectively. These results have also been plotted on Figure A.4.10 and it can be seen that distribution 14 conforms exactly with the calculated equation, but that distribution 13 falls a considerable distance away from it. The empirical equation (4.3) developed above therefore appears to break down at values of N(k - 90) much in excess of 400, corresponding say to distributions containing 30 - 40% or more of +52 mesh particles.

It is now possible to define the quantity N(k - 90) for an unknown distribution by measuring ΔS under standard conditions. In practice, the size distributions resulting from a particular combination of feed material and size reduction machine tend to have a constant value of N, so wherever this condition occurs the size distribution of the product is adequately defined by a single measurement of ΔS.

In cases where nothing is known regarding the size distribution characteristics of the material or where N is known to vary, the value of N(k - 90) found for the material may be used to discover a single point on the size distribution plot.

4.1.7 Calibration for Unknown Size Distributions.

Any size distribution that can be approximately represented by a Gaudin-Schuhmann distribution function[4] will exhibit a straight line over the greater part of its length if plotted in the form of log wt.% finer versus log size. In terms of the symbols used in this presentation, the Gaudin-Schuhmann function may be represented as follows:

$$M_F = \left[\frac{D}{k} \right]^N \qquad \ldots \quad \ldots \quad \ldots \quad (4.4)$$

$$\text{or } \log M_F = N(\log D - \log k) \qquad \ldots \quad (4.5)$$

A given value of N(k - 90) can arise from various combinations of N and k. Each of these possible combinations of values of N and k represents a different size distribution. However, by defining a pair of limiting slopes N_1, N_2, within which the slope of the unknown distribution should nearly always lie, one point on the actual distribution can be estimated closely from the intersection of the two limiting distributions. The procedure for this is as follows: the measured value of ΔS and the slopes N_1, N_2 are substituted in equation 4.3 and the corresponding size moduli k_1, k_2 are determined. The intersection of the two distributions at (M_{Fi}, D_i) can then be found from

$$Di = \left[\frac{\dfrac{N_1}{k_1}}{\dfrac{N_2}{k_2}} \right]^{\frac{1}{N_1 - N_2}} \quad \ldots \quad \ldots \quad \ldots \quad (4.6)$$

$$M_{Fi} = \left[\frac{Di}{k_1} \right]^{N_1} = \left[\frac{Di}{k_2} \right]^{N_2} \quad \ldots \quad \ldots \quad (4.7)$$

Over the range of size distributions normally encountered, the point of intersection (M_{Fi}, D_i) of the limiting lines is relatively insensitive to whatever values of the slopes N_1, N_2 are chosen. This is illustrated in Table A.4.3, where the intersection point is calculated over the useful range of ΔS for two different sets of limiting slopes.

TABLE A.4.3

(see overleaf)

TABLE A.4.3

Intersection Calibration for Unknown Size Distributions

ΔS	PARTICLE SIZE $D_i (\mu)$		CUM. WT. FRACTION FINER (M_{Fi})	
	$N_1 = 1.500$ $N_2 = 0.500$	$N_1 = 1.200$ $N_2 = 0.600$	$N_1 = 1.500$ $N_2 = 0.500$	$N_1 = 1.200$ $N_2 = 0.600$
20	95.0	95.3	0.779	0.776
30	101.6	102.4	0.703	0.699
40	115.3	117.2	0.630	0.624
50	141.4	145.5	0.568	0.563
60	189.1	197.1	0.521	0.515
70	273.9	288.9	0.490	0.484

The intersection calibration graph has been plotted in Figure A.4.11 for limiting slopes of 1.500, 0.500. To illustrate the technique, the ΔS reading obtained for the ten distributions that have slopes falling between 0.500 and 1.500 has been used to read off an intersection point for each. In Table A.4.4 these results are compared with the known composition of the distributions.

TABLE A.4.4

(see overleaf)

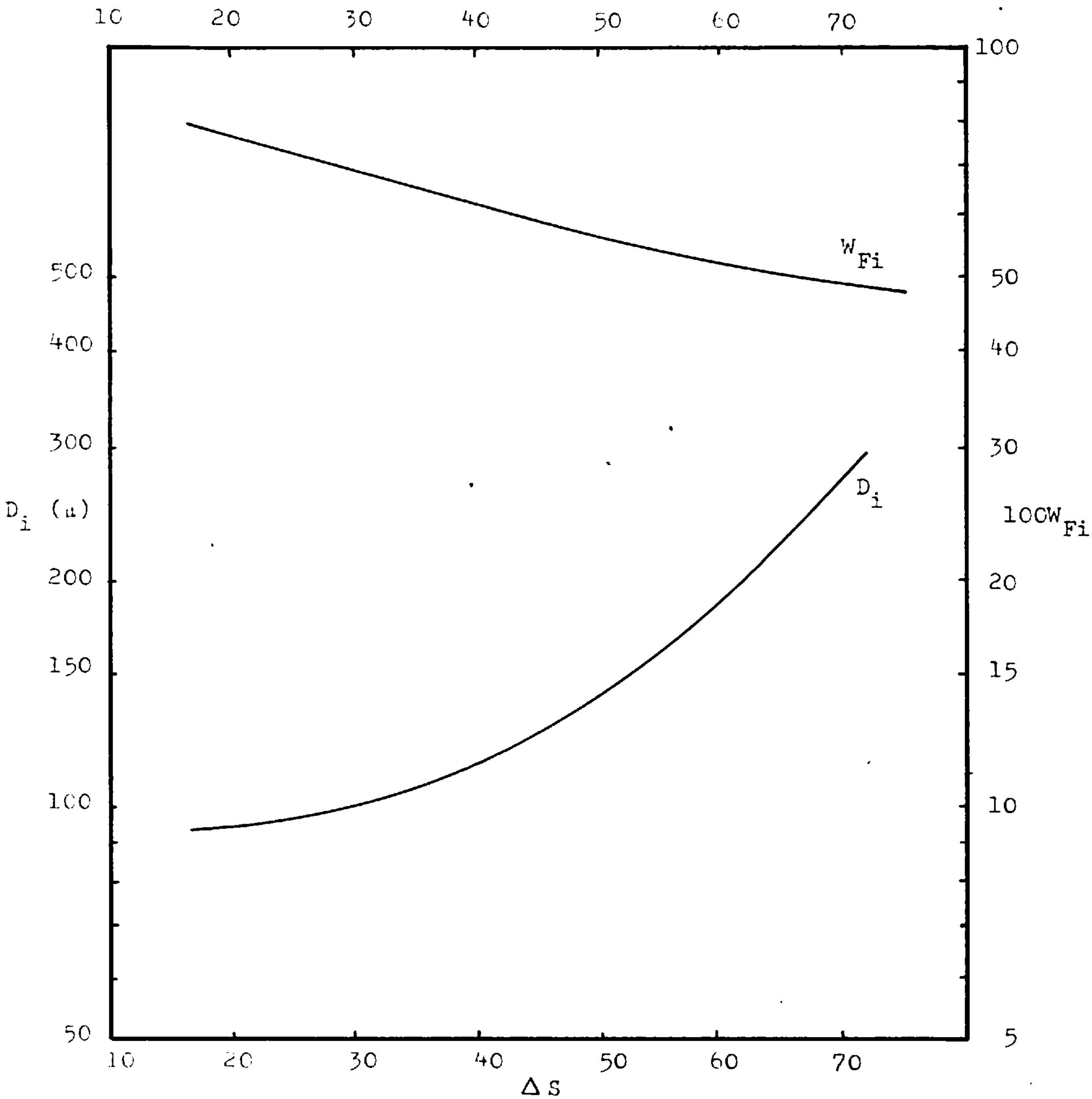

FIGURE A.4.11: Intersection calibration for unknown size distributions.

TABLE A.4.4

Intersection Calibration applied to Distributions

SIZE DISTN. NO.	ΔS	D_i (μ)	M_{Fi} Known	M_{Fi} Meas.	SIZE DISTN. NO.	ΔS	D_i (μ)	M_{Fi} Known	M_{Fi} Meas.
1	53.5	155	0.477	0.550	7	62.8	208	0.553	0.511
2	47.4	133	0.556	0.582	8	44.8	126	0.604	0.598
3	38.4	112	0.627	0.641	9	36.5	109	0.619	0.655
4	24.2	97	0.718	0.748	14	31.0	103	0.683	0.694
5	40.9	117	0.624	0.624	Grind 1	28.2	100	0.720	0.717
6	56.6	170	0.522	0.535	Grind 2	36.2	109	0.700	0.657

Also included in Table A.4.4 above are the results obtained for two samples of quartz having unknown size distributions, which were ground for different lengths of time and then size analysed both by measuring ΔS and by dry sieving.

It can be seen that the values of M_{Fi} estimated from the sizer measurements agree with the known or made-up values to within 2 or 3 percent for the most part. Since the accuracy of size analyses conducted by dry sieving is probably not much better than this, the suggested method of calibration would appear to be satisfactory.

4.2 Summary and Conclusions

The Mark 5 cell provided a substantial improvement in sensitivity for the measurement of particle concentration, but this improvement was achieved at the cost of considerable flexure of the thin channel walls. This was a most undesirable effect, which necessitated careful and time consuming compensations for the errors introduced in all measurements made with this cell. Later versions of the cell were carefully checked to ensure that wall flexure was kept within acceptable limits. (Section B.5.1.2).

An empirical calibration technique was developed for particle size distributions of the Gaudin-Schuhmann type which related the difference between the maximum and minimum density gauge outputs to the Size and Distribution moduli of the size distributions. The upper limit of validity for the calibration appeared to correspond to size distributions containing more than about 30% of +52 mesh particles. The lower limit for the calibration, in theory, can be calculated from equation 4.3 by putting $\Delta S = 0$, giving $N(k - 90) = 11$. This corresponds to a size distribution containing about 80% -200 mesh.

A further calibration was suggested for size distributions about which nothing was known before hand. This provided a single point on the size distribution plot. When this system was applied to the results already obtained, the agreement was generally satisfactory. Two 'unknown' samples of ground quartz, which were analysed both by dry sieving and using the size analyser, also gave reasonable agreement.

The empirical calibrations available at the conclusion of this phase of the work justified describing the device for the first time as an 'On-Stream Particle Size Distribution Analyser'. However, there were two important restrictions on its performance that seriously limited it's usefulness. First, while in principle the device depended on the application of a centrifugal force to create radial motion of the particles in suspension, the exact form of the force field and the type of particle motion was unknown and hence any deviations from the calibration could not be explained or compensated. Second, the particles used so far were all of the same composition and specific gravity. While it was considered likely that some kind of calibration could be obtained for a heterogenous material of unvarying composition that consisted for the most part of material of one specific gravity, this calibration would be less accurate than one obtained on a homogenous material. Materials containing appreciable proportions of constituents having different specific gravities or materials whose composition varied, clearly could not be dealt with under any empirical system of calibration.

The second major stage in the research programme was planned, therefore, in the hope that it would go some way towards lifting the first of the restrictions discussed above by providing a basic theory of operation of the device. (See Part B.). Any extension of the system to cover heterogenous materials seemed unlikely to be successful until a workable theory for homogenous ones had been developed, so this aspect of the problem was not considered during the remainder of the work described in this thesis.

PART B
INTRODUCTION

The second part of this thesis which now follows describes work that was designed to supply a basic theory of operation for the device, justified where necessary by further testwork, and capable of simulating the results obtained during the first stage of the work. This objective was of paramount importance in determining both the style of analysis and the degree of refinement required. Simplifying assumptions were introduced wherever possible: indeed, at many stages the analysis could not have proceeded without them. For example, all the theoretical analysis and experimental work that is subsequently included is devoted to spherical particles, since irregular particles make the analysis too difficult and they can in any case be related to an equivalent sphere in terms of any particular aspect of their behaviour.

The behaviour of particulate suspensions in passing through enclosed helical channels at high flowrates is extremely complex, not the least of the difficulties being that the behaviour of pure fluids under these conditions has still not been adequately established. The factors that can play a significant part in determining the suspension behaviour may be divided into three groups:

(a) Fluid properties: density, viscosity, axial and radial flow velocity distributions, vorticity.

(b) Particle properties: density, shape, size and size distribution, surface charge, solubility.

(c) Suspension properties: volume flowrate, solid/fluid ratio, temperature, gravity.

It was established previously (Section A.4.1.4) that temperature changes did not exert a significant effect on the performance of the sizer. The effect of gravity has not been examined quantitatively, since the treatment adopted considers only the overall or average effect over the full depth of the channel. The analysis which follows takes the remaining factors into account as they arise. It deals with the problem in three stages: first, the likely behaviour of a pure fluid within a helical channel, second, the behaviour of spherical particles in ideal or unbounded radial force fields and, finally, what happens when a suspension of particles moves through an enclosed helical channel.

The simplified theory developed in the last part of the analysis is then applied to the results of further testwork, conducted on an improved version of the equipment using glass spheres.

2.0 FLUID BEHAVIOUR

The behaviour of the fluid component of the suspension is important in the present application only insofar as it affects the behaviour of the solid particles. Therefore the analysis which follows is restricted to certain topics.

2.1 Fluid Flow Model

The flow behaviour in curved channels is characterised by a non-dimensional parameter[5] (ϕ) which is related to the Reynolds Number. In terms of the symbols used in this analysis

$$\phi = \left[\frac{4LV\rho}{n}\right] \left[\frac{r_m - r_i}{r_m + r_i}\right]^{\frac{1}{2}}$$

$$\therefore \phi = R_F \left[\frac{r_m - r_i}{r_m + r_i}\right]^{\frac{1}{2}} \quad \ldots \quad \ldots \quad \ldots \quad (2.1)$$

The fluid flow is laminar at low values of ϕ, and considerable theoretical and practical work has been carried out on fluid behaviour under these conditions. At values of ϕ in excess of 2000 the flow is turbulent and the theory becomes so difficult that little effective progress has been made.

Under the conditions employed in the on-stream sizer, the value of ϕ for the fluid (water) is a little over 15,000, placing the conditions well in the region of turbulent motion. A short description of the likely behaviour is therefore essential. The information available is limited, most of what follows being based on papers by

Hawthorne[5] and Barua[6].

On passing from a straight pipe into a bend, a mass of fluid flowing under turbulent conditions has a secondary flow induced within it which acts at right angles to the main or 'axial' flow. It seems probable that this secondary flow is initially oscillatory in nature, but as the fluid moves through the bend the oscillations are progressively damped. If the bend is long enough, the oscillations are completely damped out and a state of 'fully developed curved flow' is reached in which a steady axial velocity distribution exists.

The state of 'fully developed curved flow' has been represented[6] at high values of ϕ by an approximate flow model of the type shown in Figure (B.2.1.). It consists of a central core of fluid, in which the secondary flow is considered to act entirely in the plane of the bend, surrounded by a boundary layer in which the secondary flow from the core is returned around the walls of the pipe. Viscous effects are considered to be effective in the boundary layer only. The type of axial velocity distribution corresponding to this secondary flow is shown in the lower section of Figure (B.2.1).

Finally, on leaving the bend the axial velocity distribution again changes in an 'outlet transition region', which may extend downstream for a distance equivalent to 50 pipe diameters or more.

There are two aspects of the fluid behaviour outlined above which are of great importance in determining the motion of any suspended particles. These are the axial velocity distribution of the fluid (or suspension) and the magnitude of the secondary fluid flow.

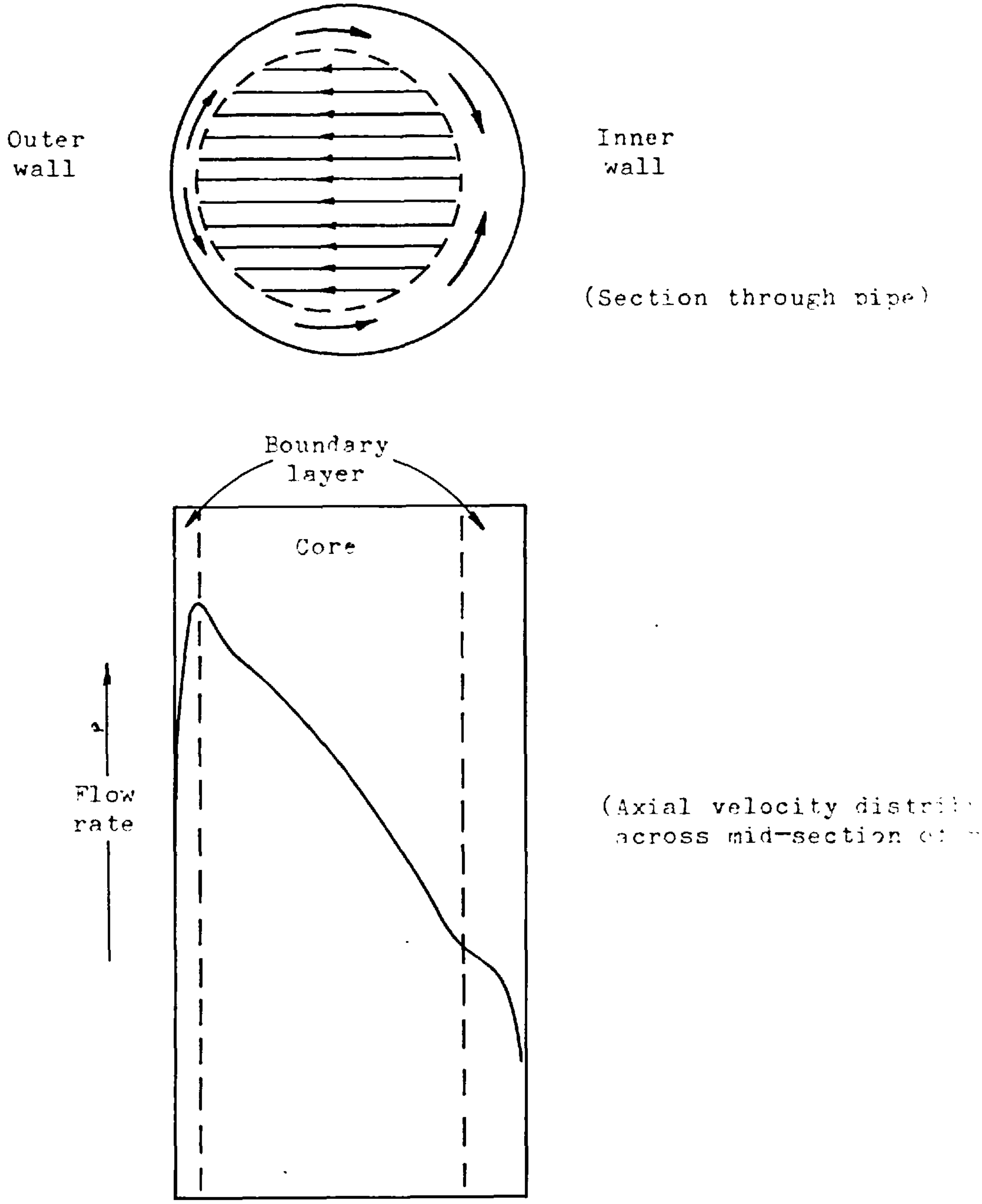

FIGURE B.2.1: Model of fully developed curved flow for high values of 'ϕ' in a circular pipe.

2.2 Axial Velocity Distribution

The type of axial velocity distribution occurring across the midsection of a straight pipe of circular cross-section for a pure fluid at high Reynolds Numbers is illustrated in Figure (B.2.2). ~~Unfortunately, this type of distribution does not lend itself to any simple form of mathematical description.~~ Where it has been necessary to ~~simulate~~ simplify such a distribution for purposes of calculation, past workers[7,8] have used either a series of straight line sections of varying slope or a suitable polynominal equation. A straight line approximation has been used in the present analysis where required. (Section B.5.3.1).

The axial velocity distribution occurring at the inlet to a bent pipe undergoes a progressive change until a new steady distribution is achieved under conditions of fully developed curved flow. (Figure B.2.3, curves 2,3,4). This change in the axial velocity profile is caused by the generation of a secondary fluid flow, which will now be discussed in more detail.

2.3 Secondary Fluid Flow

There are two types of secondary fluid flow which must be taken into account. The first kind is recirculatory in nature, arising from pressures and forces that are caused entirely by fluid behaviour. The second kind of flow involves a net transference of fluid from one zone of the channel to another and is caused by displacement as solid particles move through the fluid. This displacement flow is considered later in section 3.1.2 (c).

The recirculatory secondary flow results from frictional effects at the walls of the channel, which cause a reduction

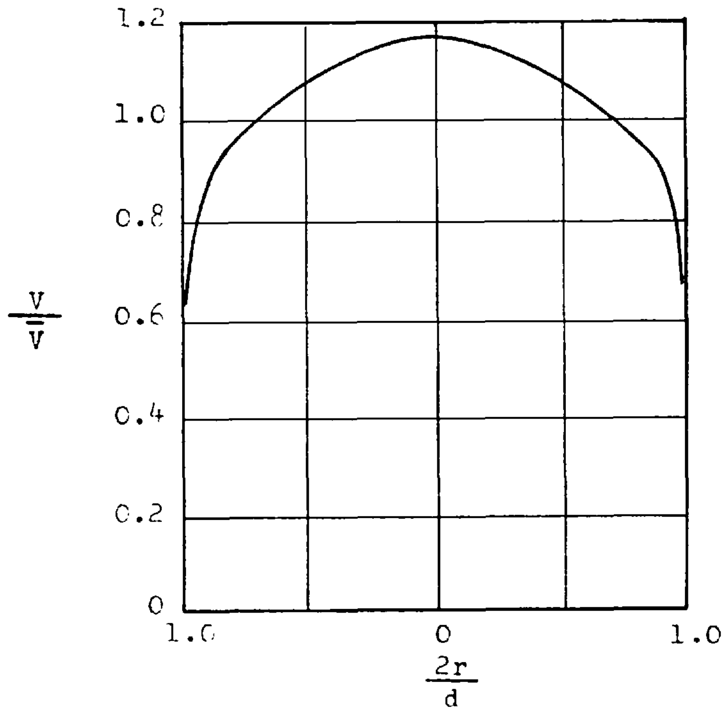

FIGURE B.2.2: Axial velocity distribution at mid-section of a straight pipe (Turbulent flow)

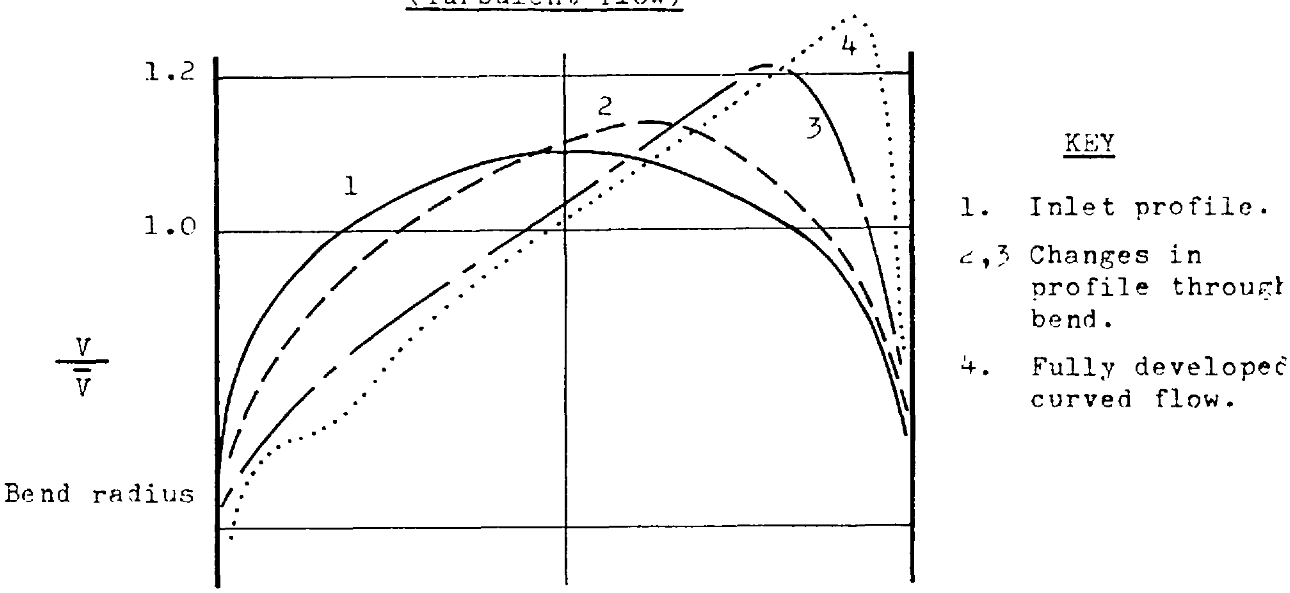

FIGURE B.2.3: Displacement of the axial velocity profile in a bent pipe. (Turbulent [illegible] in the fluid velocity and set up pressure gradients within the fluid. This results in a movement of the high velocity core of the fluid towards the outer wall of the bend, while the low velocity fluid near the walls moves towards the inner wall of the bend.

For a given fluid and channel shape, the magnitude of the secondary flow is governed by four main factors; two of which relate to the fluid conditions and two to the geometry of the system. These are as follows:-

(a) The Reynolds Numbers of the fluid $= R_F$

(b) The axial velocity distribution at the inlet to the bend;

(c) The Curvature Ratio $= \dfrac{\text{Mean radius of pipe curvature}}{\text{Width (diameter) of pipe}}$

$$= \frac{\frac{1}{2}(r_m + r_i)}{\frac{1}{2}(r_m - r_i)} = \frac{r_m + r_i}{r_m - r_i}$$

(d) The Aspect ratio for the given shape of pipe

$$= \frac{\text{Pipe dimension perpendicular to plane of bend}}{\text{Pipe dimension in plane of bend}}$$

The Reynolds Number for the fluid is incorporated in the parameter $\emptyset$ (equation 2.1) which determines whether the fluid flow is laminar or turbulent.

The influence of the inlet axial velocity profile on the secondary flow is likely to be complex, but under the constant conditions employed within the on-stream sizer it should not vary significantly. In any case it seems reasonable to suppose that with large bend deflections the fully developed curved flow which ultimately results will be substantially independent of any moderate changes in the inlet velocity distribution.

Reducing the curvature ratio tends to increase the secondary flow, since the pressure gradients become larger. However, if the axial flow velocity is high enough, separation of the boundary layer probably occurs at the inner wall of the bend and a diminished or even reversed secondary flow may result. This effect has only been observed at large aspect ratios[9], however, and since the aspect ratio of the present device is very small it is difficult to say whether or not separation of the boundary layer is likely to occur.

The effect of aspect ratio has only been considered under laminar conditions[10], where it appears that very large or very small aspect ratios cause a substantial reduction in the secondary flow.

2.4 Behaviour Within the Sizer Helix

In the case of the present device, the Reynolds Number is high, the axial velocity distribution is unknown and both the curvature ratio and the aspect ratio are very small. The magnitude of the secondary flow occurring under these conditions is difficult to assess. On the whole, it seems likely to be small and may be oscillatory over the greater part of the bend. The possibility of boundary layer separation at the inner wall cannot be excluded.

In view of the complex nature of the flow behaviour and the theoretical difficulties that arise when considering the behaviour of a pure fluid, it is obvious that, when the additional complication of quite high concentrations of suspended particles is introduced, the problems become formidable.

2.5 Summary and Conclusions

No attempt has been made in the present work to resolve these difficulties. There were two reasons for this. First, it would have involved a separate research programme much of which would have been devoted to pure hydrodynamics. Second, as described in Part A of this thesis, the experimental measurements available were restricted for practical reasons to the outlet from the helix, and changes occurring at different positions through the helix could at best only be observed visually.

The exact nature of the axial velocity profile of the suspension at the inlet to the helix and the progressive changes in this profile caused by secondary flow were unknown. The behaviour of the suspension was therefore analysed in terms of its average motion over the full depth of the channel. Mean velocity profiles were assumed by analogy with the expected behaviour of pure fluids under similar conditions.

In the next section, which deals with the behaviour of suspensions in unbounded radial force fields, a number of simple axial velocity distributions are assumed merely for illustrative purposes.

3. BEHAVIOUR OF SUSPENSIONS IN UNBOUNDED RADIAL FORCE FIELDS.

3.1 Forces operating on a Single Particle.

3.1.1. Accelerative Force

Consider a spherical particle of diameter D, situated at a radius r within a body of fluid that is moving in a circular path with a steady velocity V. (Figure B.3.1.a) The centrifugal force acting on the particle creates a relative velocity U between the particle and the fluid, and if there are no shearing effects within the fluid the relative velocity will be in a radial direction. In most cases there will be a velocity gradient within the fluid, however, and this gradient acts on the particle causing it to rotate about an axis perpendicular to the direction of the velocity gradient. As the particle moves relative to the fluid in the radial direction, the superimposed rotation creates a lift force known as the Magnus Effect[20] which acts perpendicular to the plane in which the direction of motion and the rotational axis lie. The effect is illustrated (Figure B.3.1.b) for a fluid velocity gradient in the radial direction.

The particle velocity relative to the fluid is therefore in a direction making an angle Θ with the radius of motion, and the tangential (u_T) and radial (U) velocity components are

$$u_T = u \sin\Theta \qquad \ldots \qquad \ldots \qquad \ldots \qquad (3.1)a$$

$$U = u \cos\Theta \qquad \ldots \qquad \ldots \qquad \ldots \qquad (3.1)b$$

The magnitude of Θ will depend on the fluid velocity gradient $\left[\frac{dV}{dr} \right]$.

The accelerative force acting on the particle to

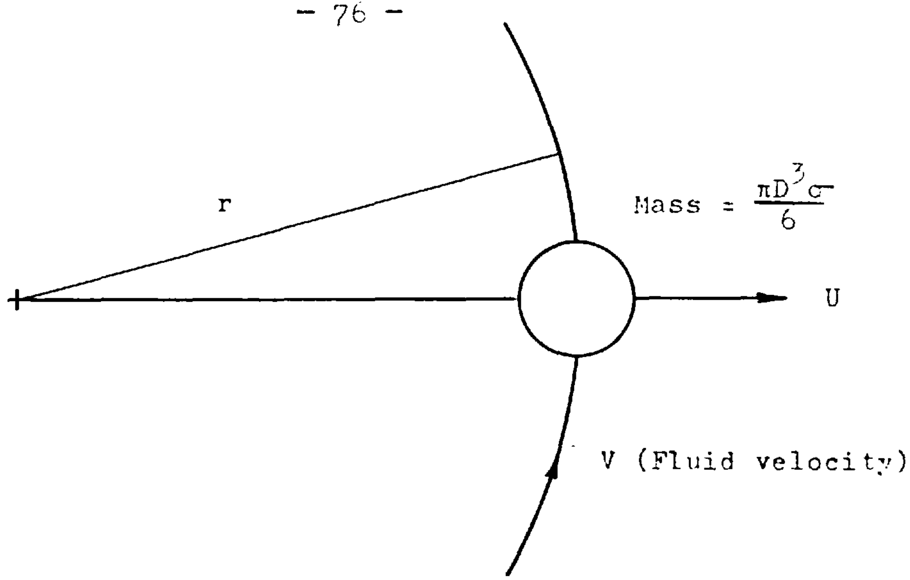

FIGURE B.4.1(a): Forces Acting on a Spherical Particle Tangential Fluid Velocity the same at all Points

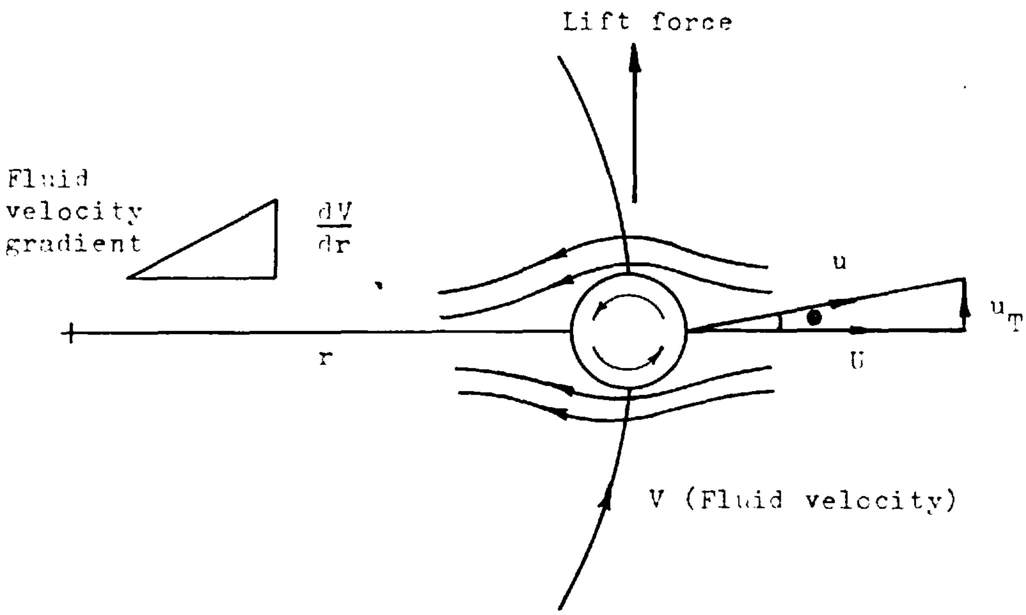

FIGURE B.4.1(b): Forces Acting on a Spherical Particle Tangential Fluid Velocity Increasing in the Radial Direction produce the velocity u relative to the fluid is therefore

$$F_A = \frac{\pi D^3 \sigma}{6} \cdot \frac{(V-u_T)^2}{r} \quad \ldots \quad \ldots \quad (3.2)$$

or if u_T is substituted for, from equation (3.1)a

$$F_A \doteq \frac{\pi D^3 \sigma}{6} \cdot \frac{(V-u\operatorname{Sin}\theta)^2}{r} \quad \ldots \quad (3.3)$$

3.1.2 Retarding Forces

There are three factors to be considered here: a pressure gradient force analagous to the displacement force encountered by particles falling under gravity in a fluid, a drag force which depends on a number of factors, and certain interference effects caused by neighbouring particles.

(a) Pressure Gradient Force (F_p)

It is first necessary to derive an expression for the pressure gradient within the fluid. Consider a cylinder of fluid disposed between radii of motion r and r+ δr, the fluid velocities at these radii being V and V+ δV respectively (Figure B.3.2.) If the area of the ends of the cylinder is a and the pressures corresponding to radii r, r+ δr are p and p+ δp, then the mean centrifugal acceleration is

$$\frac{(V + \frac{1}{2}\delta V)^2}{r + \frac{1}{2}\delta r}$$

Mean centrifugal force on cylinder = $\dfrac{\rho a \delta r (V+\frac{1}{2}\delta V)^2}{r+\frac{1}{2}\delta r}$

Pressure force acting on cylinder = $a\delta p$

For equilibrium $\quad a\delta p = \dfrac{\rho a \delta r\, (V+\frac{1}{2}\delta V)^2}{r+\frac{1}{2}\delta r}$

Rearranging and taking the limits as $\delta r \longrightarrow 0$ gives

$$\frac{dp}{dr} = \frac{\rho V^2}{r} \quad \ldots \quad \ldots \quad \ldots \quad (3.4)$$

The tangential velocity of the particle and fluid (V) will vary with the radius r in a manner presently indeterminate. It may be shown, however, that the final expression for the displacement force, to a close approximation, is independent of the type of tangential velocity distribution.

By way of illustration, two types of tangential velocity distribution will be considered: an ideal 'free vortex' distribution ($V = \frac{A}{r}$) and a constant tangential velocity. Consider a spherical particle of diameter D, travelling at a radius of motion r within the fluid. Let the local rectangular axes be y, z with origin at the centre of the sphere. Now consider a small element on the surface of the sphere (Figure B.3.3.)

In terms of the given set of co-ordinates, we have

$$y^2 + z^2 = \left(\frac{D}{2}\right)^2$$

$$\text{or} \quad z^2 = \left(\frac{D}{2}\right)^2 - y^2$$

$$\therefore -dz = \frac{y}{z}\, dy$$

We have $dA = -2\pi z dz = 2\pi y.dy$

The component of pressure force in the y direction, acting on the elemental surface area, is given by the product of the pressure at radius (r+y) and the projected area of the element in the y direction (dA).

The net component pressure force relative to the central plane of the sphere is given by the product of the pressure difference Δp between r and (r+y) and the

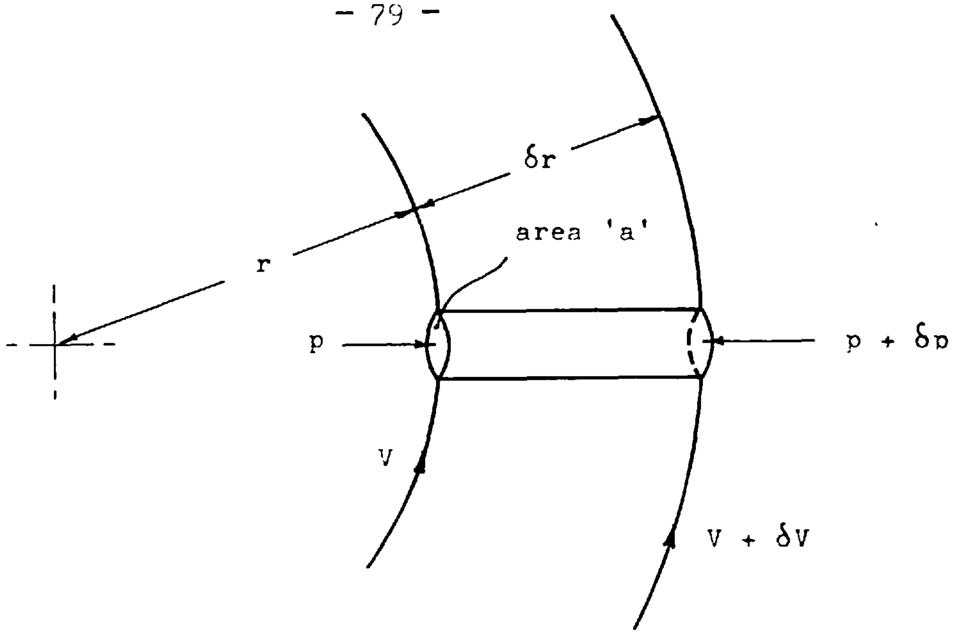

FIGURE B.3.2: Pressure gradient force

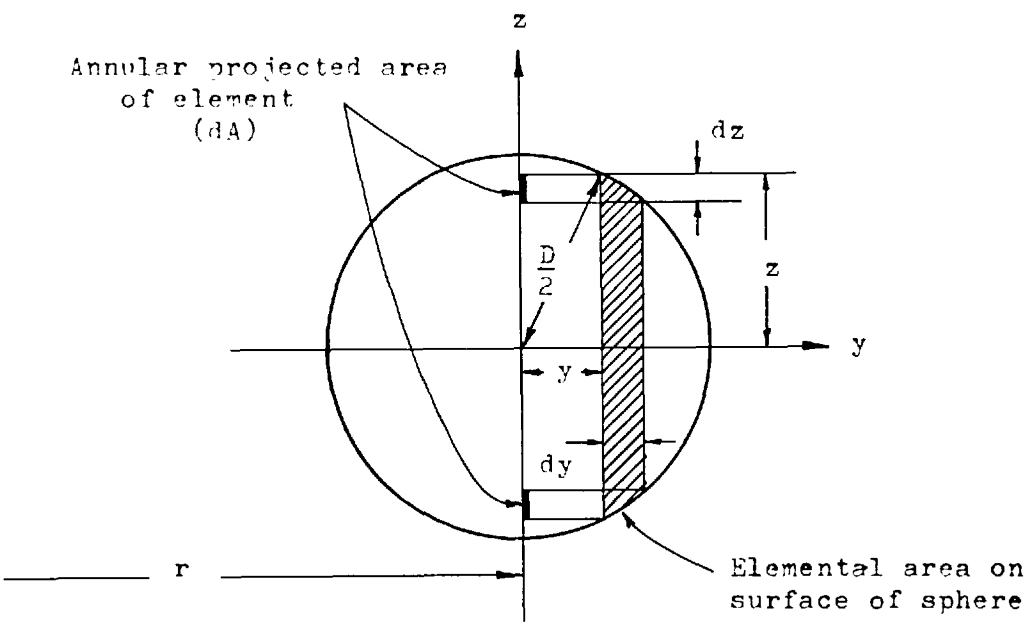

FIGURE B.3.3: Force on a sphere

projected area dA.

$$\text{i.e.} \quad dF_p = \Delta p . dA$$

Δp may be calculated for a free vortex tangential velocity distribution using equation (3.2)

$$\Delta p = \rho A^2 \int_r^{r+y} \frac{dr}{r^3}$$

Integrating:

$$\therefore \Delta p = \frac{\rho A^2}{2} \cdot \frac{y(2r+y)}{r^2(r+y)^2} \quad \ldots \quad \ldots \quad (3.5)$$

The net component pressure force $dF_p = \Delta p . dA$

$$\therefore \quad dF_p = 2\pi y . \frac{\rho A^2}{2} . \frac{y(2r+y)}{r^2(r+y)^2} \, dy = \frac{\pi\rho A^2}{r^2} \cdot \frac{y^2(2r+y)}{(r+y)^2} \, dy \quad \ldots \quad (3.6)$$

Hence the total force on the sphere due to the pressure gradient

$$F_p = \frac{\pi\rho A^2}{r^2} \int_{-\frac{D}{2}}^{+\frac{D}{2}} \frac{y^2(2r+y)}{(r+y)^2} \, dy$$

$$\therefore \quad F_p = \pi\rho A^2 \left[\frac{4rD}{4r^2 - D^2} - \ln\left(\frac{2r+D}{2r-D} \right) \right] \quad \ldots \quad \ldots \quad \ldots \quad (3.7)$$

Let the ratio of particle diameter to radius of motion $\left(\frac{D}{r}\right) = q$

$$\therefore \quad F_p = \pi\rho A^2 \left[\frac{4q}{4-q^2} - \ln\left(\frac{1+\frac{1}{2}q}{1-\frac{1}{2}q} \right) \right] \quad \ldots \quad \ldots \quad \ldots \quad (3.8)$$

The expressions in (3.8) containing q may be expanded as a series:

$$\therefore F_p = \pi\rho A^2 . \frac{q^3}{6} \left[1 + \frac{3q^2}{10} + \frac{9q^4}{112} + \ldots\ldots + \frac{3}{2^{r+1}} \left(\frac{r+2}{r+3}\right) q^r + \ldots \right] \quad \ldots\ldots \quad (3.9)$$

Since $\frac{3q^2}{10} < 10^{-3}$ for all cases of interest in the present analysis, the force F_p is given with sufficient accuracy by

$$F_p = \pi\rho A^2 . \frac{q^3}{6} = \frac{\pi D^3}{6} \cdot \frac{\rho A^2}{r^3} \quad \dots \quad \dots \quad (3.10)$$

Since $\frac{A}{r} = V$, then

$$F_p = \frac{\pi D^3 \rho}{6} \cdot \frac{V^2}{r} \quad \dots \quad \dots \quad \dots \quad \dots \quad \dots \quad (3.11)$$

A similar analysis for V = constant = $\overline{V}$ gives

$$F_p = \frac{\pi\rho\overline{V}^2 r^2 (4-q^2)}{4} \left[\frac{4q}{4-q^2} - \ln\left(\frac{1+\frac{1}{2}q}{1-\frac{1}{2}q}\right)\right] \dots \quad (3.12)$$

Hence

$$F_p = \pi\rho\overline{V}^2 r^2 \frac{q^3}{6}\left[1+\frac{q^2}{20} + \frac{6q^4}{1120} + \dots\right] \dots \quad \dots \quad (3.13)$$

which, for the present conditions, may again be taken as

$$F_p = \frac{\pi D^3 \rho}{6} \cdot \frac{\overline{V}^2}{r} \quad \dots \quad \dots \quad \dots \quad \dots \quad \dots \quad (3.14)$$

As a rough guide to the magnitude of the error involved, for a particle of 1 mm. diameter moving at a radius of 1cm. the pressure gradient force is about 0.3% larger than the 'displacement' calculation indicates.

For present purposes, the pressure gradient force can therefore be represented with sufficient accuracy by a force equal in magnitude but opposite in sense to the centrifugal force generated by the tangential velocity acting at the centre of the mass of fluid displaced by the particle.

(b) Drag Force

It is assumed in this section of the analysis that the flow behaviour of the pure fluid (which is travelling along a circular path with velocity V) does not interfere with the motion of the particles relative to the fluid, i.e. the particles may be considered to encounter ideal forms of fluid drag. This assumption is questionable and it is considered at greater length in the later sections dealing with the behaviour in enclosed channels.

The fluid drag force opposing relative motion between the particle and fluid is a function of the velocity . It has only been explicitly defined under physical conditions corresponding to low (< 3) and high (> 160) Reynolds Numbers (R_p), the so called 'laminar' and 'turbulent' regimes. At Reynolds numbers between 3 and 160, the 'transitional' regime, the magnitude of the drag force cannot be given explicitly. A number of techniques have been developed for calculating the drag force in this region [11, 12,21] mostly based on dimensional analysis. However, these are only capable of providing the terminal velocity of the particle.

The basic expression for the drag force (G) is

$$G = C.\tfrac{1}{2}\rho u^2 . \frac{\pi D^2}{4} = \frac{\pi D^2 \rho}{8} . C . u^2 \quad \ldots \quad \ldots \quad (3.15)$$

in which the drag coefficient takes values which vary with the Reynolds number.

Equation (3.15) is strictly valid only when the relative velocity between particle and fluid (u) is constant. Where it is varying with time, the drag force should be described[18] by an equation of the form

$$G = \frac{\pi D^3 \rho}{12} . \frac{du}{dt} + \frac{\pi D^2 \rho . Cu^2}{8} + \frac{3}{16} (\pi n)^{\frac{1}{2}} D^3 \int_0^t \frac{du}{dY} . \frac{dY}{(t-Y)^{\frac{1}{2}}} \quad \ldots \quad (3.15a)$$

in which the first term represents the 'added mass' effect, the second term gives the 'steady state' drag, and the third term is a function of the previous history of the particle.

The full equation for the drag force has not been used in the subsequent analysis. There are two reasons for this: first, its introduction leads to equations that are not amenable to analytic treatment, and second the precision of the remainder of the analysis is not high enough to warrent such detailed treatment of one particular aspect. For illustrative purposes, therefore, the equilibrium drag force given in equation (3.15) has been assumed to hold under conditions of changing velocity.

Laminar regime: $R_p = \frac{uDp}{n} < 3.$ $C = \frac{24}{R_p}$

Substituting this value in (3.15) gives the laminar drag force as

$$3\pi Dnu = 3\pi DnU\,\mathrm{Sec}\,\theta$$

and to obtain the radial component of the drag force this must be multiplied by Cos θ, giving

$$G_L = 3\pi DnU \quad \ldots \quad \ldots \quad \ldots \quad \ldots \quad \ldots \quad (3.16)$$

Turbulent regime: $R_p > 160,$ $C = 0.4$

Substituting this value in (3.15) gives for the turbulent drag force:

$$\frac{\pi D^2 \rho u^2}{20} = \frac{\pi D^2 \rho U^2 \mathrm{Sec}^2\theta}{20}$$

and for the radial component

$$G = \frac{\pi D^2 \rho U^2 \mathrm{Sec}\theta}{20} \quad \ldots \quad \ldots \quad \ldots \quad (3.17)$$

The value of Sec θ depends on the relative magnitudes of u_T and U and hence oh the fluid velocity gradient $\frac{dV}{dr}$.
It will only equal unity when V is the same at all radii of motion.

(c) Interference Effects from Neighbouring particles.

The presence of other particles in the suspension affects the motion of an individual particle in two ways. First, since all the particles are suspended in the fluid, the inertial effect at any point within the suspension must increase in proportion to the increased mass of material present per unit volume. Second, neighbouring particles will influence and alter the fluid flow behaviour, so that a particle moving in the presence of other particles will exhibit different behaviour from one in isolation.

The inertial effect is readily compensated by replacing the fluid density (ρ) in equations (3.11) and (3.14) by the suspension density (P). The effect of neighbouring particles on the fluid flow behaviour has been investigated by a number of workers[13,14,15,19], the results being quoted in convenient summary form by Orr[16]. The actual velocity (u) of a particle relative to the fluid in which it and neighbouring particles are suspended can be related to the velocity (u_T) which that particle would attain in the absence of any other particles by the equation

$$u = u_T(1-C_V)^Q = u_T \left[\frac{\sigma - P}{\sigma - 1}\right]^Q \quad \ldots \quad (3.18)$$

where C_V is the volume concentration of particles in the suspension and Q an exponent which varies with the Reynolds number for the particle.

TABLE B.3.1

(see over page)

TABLE B.3.1	
Variation of Q with Reynolds Number (R_p)	
R_p	Q
10^{-2}	4.6
10^{-1}	4.5
1	4.2
10	3.6
10^2	3.1
10^3	2.5
10^4	2.3
10^5	2.3

This correction factor has been rounded off in the illustrations of laminar and turbulent motion which follow, the value of Q being taken as 5 for laminar conditions and 2 for turbulent conditions. At volume concentrations of 0.15 or less the errors introduced are not appreciable.

When using equation 3.18 to correct particle velocites falling in the transitional regime, however, the Reynolds Number (R_p) must be calculated and the appropriate value of Q employed.

3.2 Radial Motion of a Single Particle.

The motion of an individual particle may now be determined by equating the net force to the product of the particle mass and the resultant acceleration

$$\text{Net force} = F_A - F_P - G$$

$$\text{Mass x acceleration} = \frac{\pi D^3 \sigma}{6} \times \frac{d^2r}{dt^2}$$

Equating these and rearranging gives

$$\frac{d^2r}{dt^2} + \frac{6G}{\pi D^3 \sigma} = \left(\frac{\sigma - P}{\sigma}\right) \frac{(V - u\sin\theta)^2}{r} \quad \ldots \quad \ldots \quad (3.19)$$

Equation (3.19) is unsatisfactory in its present form, since the drag force G is unspecified. This is because there is, as yet, no means of determining the type of drag force that is operative for a given set of conditions.

The limits within which the drag forces given in equations (3.16) and (3.17) are operative may be estimated for the actual sizing conditions described in Part A by calculating the sizes of particles that just fall within the limiting Reynolds Numbers at terminal velocity. It is necessary to assume a special type of fluid velocity distribution for this purpose.

3.2.1 Laminar Conditions

Ignoring for the moment interference effects produced by other particles, combining equations (3.16) and (3.18) yields

$$\frac{d^2r}{dt^2} + \frac{18n}{D^2\sigma} \cdot \frac{dr}{dt} = \frac{(\sigma - P)}{\sigma} \frac{(V - u\sin\theta)^2}{r}.$$

Writing U for $\frac{dr}{dt}$, this becomes

$$\frac{dU}{dt} + \frac{18n}{D^2\sigma} \cdot U = \left(\frac{\sigma - P}{\sigma}\right) \frac{(V - u\sin\theta)^2}{r} \quad \ldots \quad \ldots \quad \ldots \quad (3.20)$$

In order to obtain an estimate of the limiting particle size for which laminar motion can occur, two simplifyihg assumptions are made. First, θ is put equal to zero, (implying that there is no relative tangential motion between particle and fluid) so that u SinΘ disappears. This is necessary because u Sin Θ ($=u_T$) is a complicated function of the fluid velocity gradient $\frac{dV}{dr}$, the particle size and a number of other factors. Second, it is assumed that a terminal velocity (U_{TER}) is reached at which $\frac{dU}{dt} = 0$. This assumption places a constriction on V, since

$$\frac{dV}{dt} = 0, \quad \therefore \quad U = \text{constant}$$

$$\therefore \quad \frac{(V - u\sin\Theta)^2}{r} = \frac{V^2}{r} = \text{constant (B, say)}$$

$$\therefore \quad V = Br^{\frac{1}{2}} \quad \dots \quad \dots \quad \dots \quad \dots \quad (3.21)$$

But the first assumption of $\Theta = 0$ implied $\frac{dV}{dr} = 0$, or V = constant, so the two assumptions are mutually contradictory and it would appear that there is no set of conditions under which a true terminal velocity can be attained by a particle.

However, the apparent terminal velocity obtained by putting $\frac{dU}{dt} = 0$, $\Theta = 0$ and V = constant may be used to estimate the limiting particle size:

$$U_{TER} = \frac{(\sigma - P)D^2V^2}{18nr} \quad \dots \quad \dots \quad \dots \quad \dots \quad (3.22)$$

The condition defining the limiting particle size for laminar motion (D_{LIM}) is

$$\frac{U_{TER}\,D_{LIM}\,P}{n} = 3$$

and combining this with (3.22) and rearranging

$$D_{LIM} = \left[\frac{54n^2r}{P(\sigma - P)V^2}\right]^{1/3} \dots \quad \dots \quad \dots \quad \dots \quad (3.23)$$

For glass spheres of density 2.44, suspended in water ($n = 10^{-2}$ poise) at a volume concentration of 0.10, and travelling at a tangential velocity of 200cm/sec at a radius of 1.0cm:

$$D_{LIM} = 45\mu$$

If the other conditions are kept constant and the radius of motion is increased to 2.5cm., the limiting size becomes 61μ.

Equation (3.22) gives the apparent terminal velocity of the particle but provides no indication of how rapidly this velocity is reached. This must be found by solving equations (3.19) or (3.20). Unfortunately, the form of these equations is such that an explicit solution is unobtainable. Also, V is some unknown function of **r.** An indication of the type of behaviour to be expected may be obtained by assuming (from equation 3.21) that $V = Br^{\frac{1}{2}}$ and that $\theta = 0$.

When these values are substituted in (3.20), the accelerative force at all radii of motion becomes the same and hence

$$\frac{dU}{dt} + \frac{18}{D^2\sigma} U = \left(\frac{\sigma - P}{\sigma}\right)B^2 \quad \ldots \quad \ldots \quad \ldots \quad (3.24)$$

Equation (3.24) may be solved explicitly to give

$$U = \frac{(\sigma - P)D^2B^2}{18n}\left(1 - e^{-\frac{18n \cdot t}{D^2\sigma}}\right) \quad \ldots \quad \ldots \quad (3.25)$$

Integrating again to find the distance travelled:

$$r = r_o + \frac{(\sigma - P)D^2B^2}{18n}\left[t - \frac{D^2\sigma}{18n}\left(1 - e^{-\frac{18n \cdot t}{D^2\sigma}}\right)\right] \quad \ldots \quad (3.26)$$

The velocities and distances given by equations (3.25) and (3.26) have been calculated for a 45μ glass sphere under the same conditions used for the earlier limiting size example. The approach to the apparent terminal velocity is exceedingly rapid, as 99% of terminal velocity is reached within a distance of about one particle diameter when accelerating from rest. (Figures B.3.4, B.3.5).

In view of this, it is not unreasonable to assume that the radial motion of particles under laminar conditions is adequately described by their terminal velocities, which are considered to be achieved instantaneously from rest.

An indication of the error introduced by this assumption has been given by plotting on Figure B.3.5 both the actual distances moved and the distances moved assuming instantaneous terminal velocity. The latter results are greater than the true distances by about 12 microns. This result may also be calculated from equations (3.25) and (3.26). If E(r) is the difference between the distances calculated by the two methods, then

$$E(r) = \frac{(\sigma - P)D^2B^2}{18n} \left[\left(t + \frac{D^2\sigma}{18n}\right) \left(1 - e^{-\frac{18n}{D^2\sigma} \cdot t} \right) - t \right] \qquad \ldots \quad \ldots \quad (3.27)$$

This reduces when t is large to the simple result

$$E(r) = \frac{\sigma(\sigma - P)D^4B^2}{324\, n^2} \qquad \ldots \quad \ldots \quad \ldots \quad (3.28)$$

The calculated value corresponding to the conditions used is therefore E(r) = 12.05μ.

With the type of tangential velocity distribution assumed in equation (3.23) the accelerative force is the same at all radii of motion. The particle motion has been calculated for a slightly more realistic case where V is constant and the accelerative force therefore varies with the radius of motion. The resulting variation in apparent

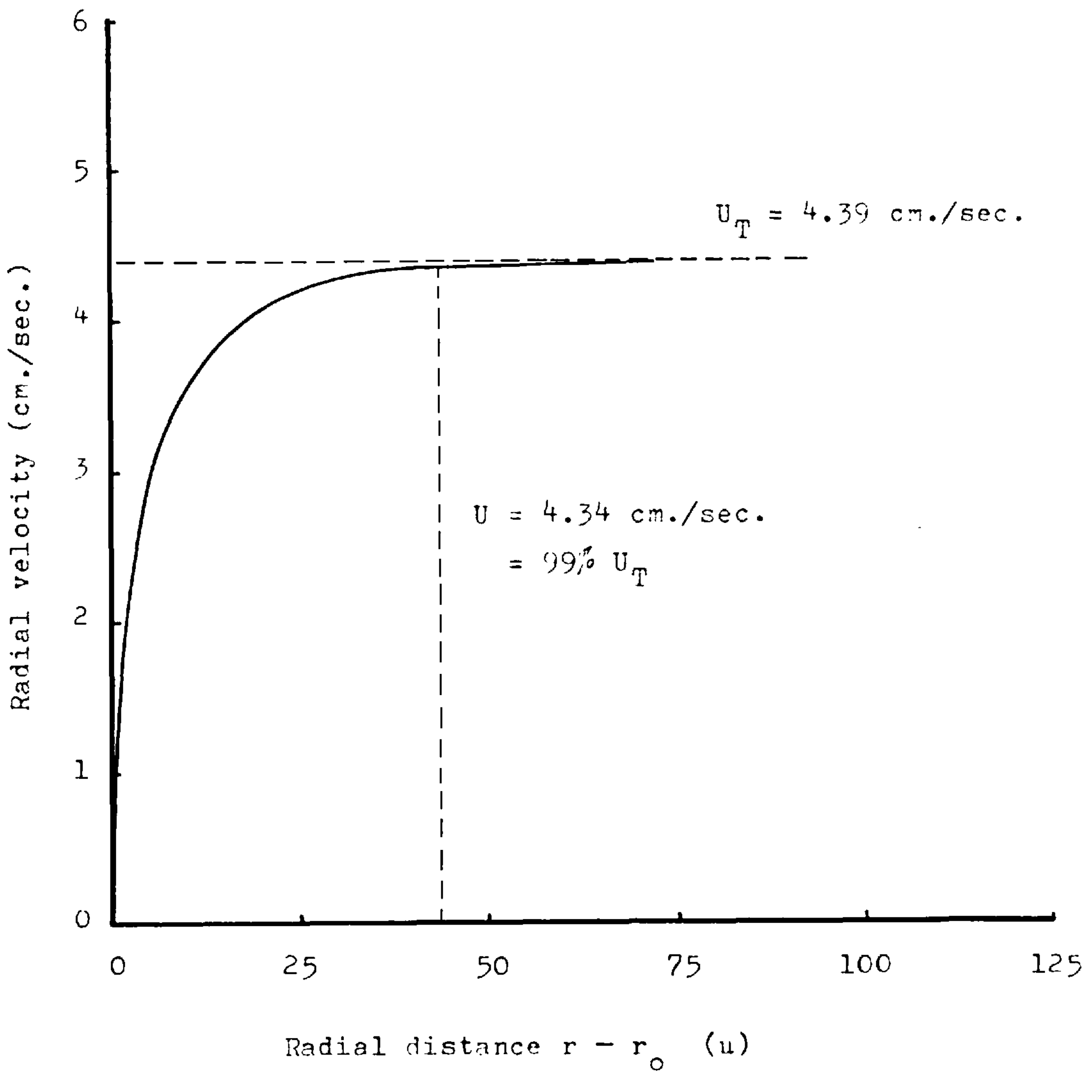

FIGURE B.3.4: Laminar motion of a 45µ glass sphere

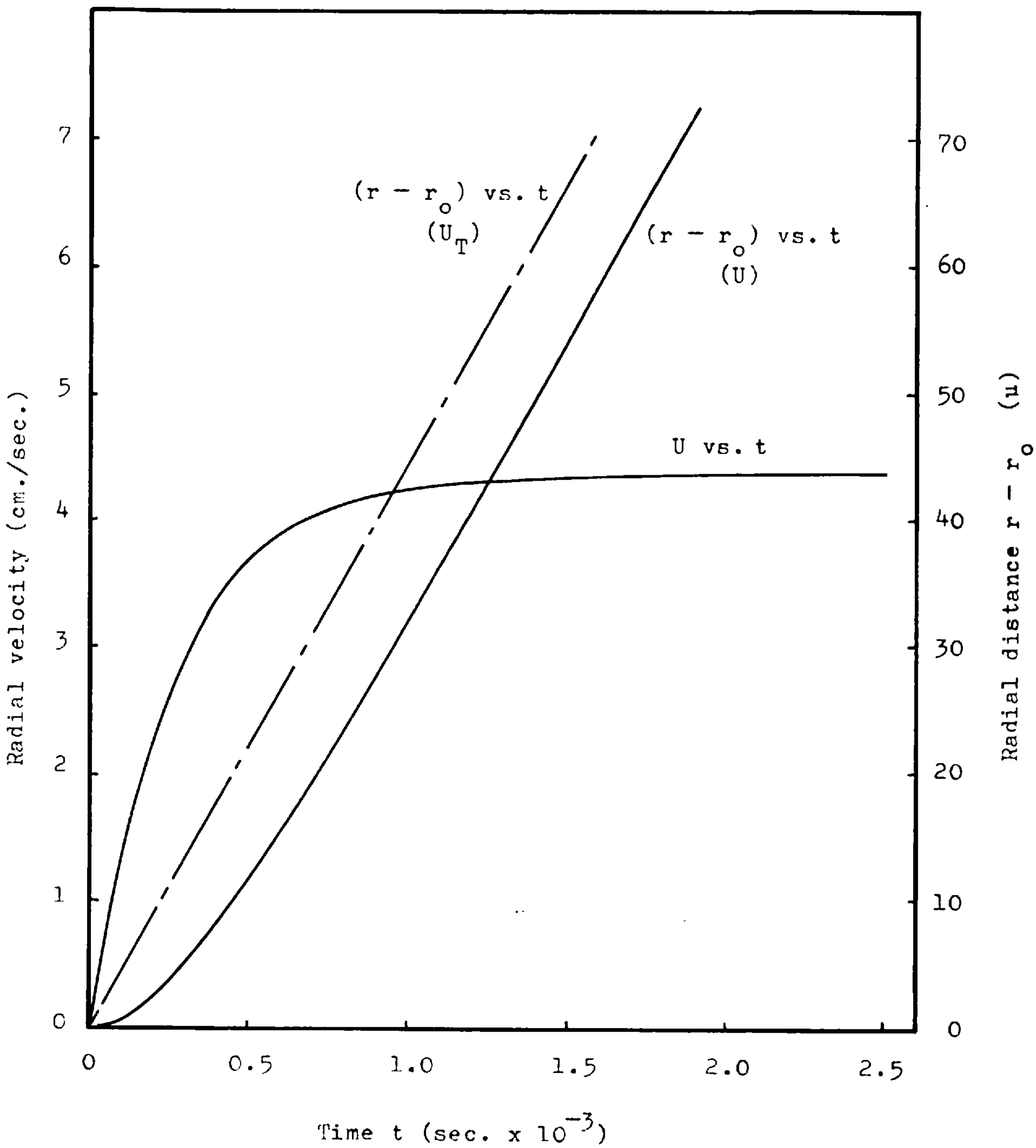

FIGURE B.3.5: Laminar motion of a 45u glass sphere terminal velocity with radius of motion is shown in Figure B.3.6.

If the apparent terminal velocity is used it is possible to apply a correction for the interference effects caused by the presence of other particles. This merely involves multiplying the terminal velocity by the factor $(1-C_V)^Q$. Equation (3.22) may then be corrected as follows, taking Q as approximately equal to 5:

$$C_V = \frac{P-1}{\sigma-1} \qquad \therefore\ (1-C_V)^5 = \left(\frac{\sigma-P}{\sigma-1}\right)^5$$

$$U_{TER} = \frac{(\sigma-P)^6 D^2 B^2}{(\sigma-1)^5\ 18n} \quad \ldots \quad \ldots \quad \ldots \qquad (3.22)a$$

The amended value of U_{TER} calculated from equation (3.22)a has also been shown on Figure (B.3.6).

3.2.2 Turbulent Conditions

Combining equations (3.17) and(3.18) gives

$$\frac{d^2r}{dt^2} + \frac{3PSec\theta}{10D\sigma} \cdot \left(\frac{dr}{dt}\right)^2 = \left(\frac{\sigma-P}{\sigma}\right) \frac{(V-\mu Sin\theta)^2}{r} \quad \ldots \qquad (3.29)$$

Writing U for $\frac{dr}{dt}$, and assuming $\theta = 0$

$$\frac{dU}{dt} + \frac{3P}{10D\sigma}U^2 = \left(\frac{\sigma-P}{\sigma}\right)\frac{V^2}{r} \quad \ldots \quad \ldots \quad \ldots \qquad (3.30)$$

The apparent terminal velocity ($\frac{dU}{dt} = 0$) is given by

$$U_{TER} = \left[\ \frac{10}{3}\left(\frac{\sigma-P}{\sigma}\right) D\ \frac{V^2}{r}\ \right]^{\frac{1}{2}} \quad \ldots \quad \ldots \quad \ldots \qquad (3.31)$$

To estimate the smallest particle size for which turbulent motion can take place, the condition $R_P = 160$ can be combined with equation (3.31), yielding

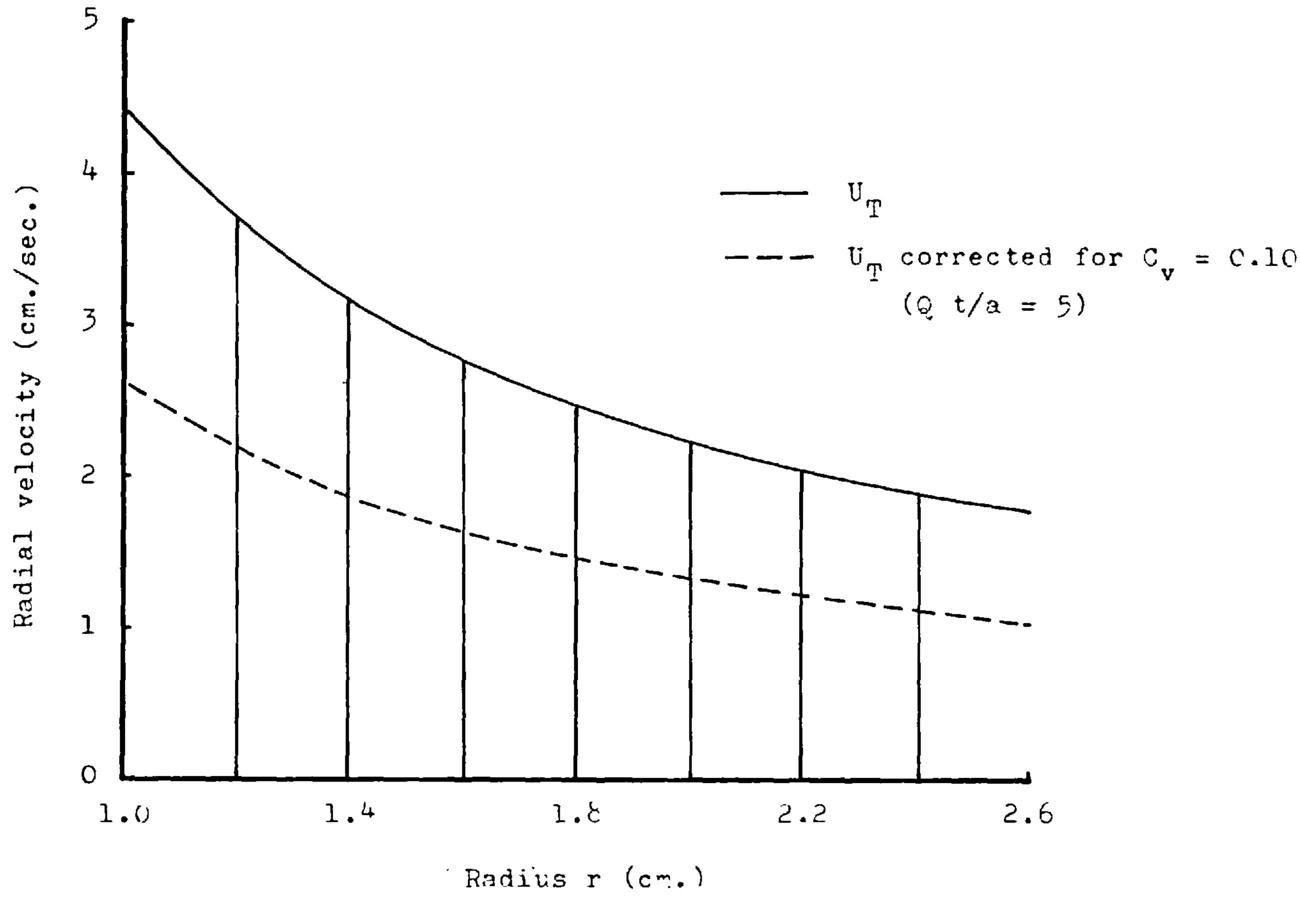

FIGURE B.3.6: Laminar motion of a 45u glass sphere

$$D_{LIM} = \left[\frac{7680\ n^2 r}{P(\sigma - P)\ V^2}\right]^{1/3} \quad \ldots \quad \ldots \quad \ldots \quad (3.32)$$

For glass spheres of density 2.44 suspended in water at a volume concentration of 0.10 and travelling at a tangential velocity of 200 cm/sec. at a radius of 1cm.

$$D_{LIM} = 235\mu$$

If the other conditions are kept constant and the radius of motion is increased to 2.5cm., the limiting size increases to 319μ.

Equation 3.31 can be adapted to give the apparent terminal velocity of a particle under turbulent conditions for an accelerative force that is constant at all radii of motion. The rapidity with which this apparent terminal velocity is achieved may be calculated by solving equation 3.30 for the same conditions ($\Theta = 0$, $V = Br^{\frac{1}{2}}$)

$$\frac{dU}{dt} + \frac{3P}{10D\sigma} . U^2 = \left(\frac{\sigma - P}{\sigma}\right) B^2$$

But $\frac{dU}{dt} = \frac{dU}{dr} . \frac{dr}{dt} = U\frac{dU}{dr}$

Substituting this value and multiplying by 2 gives

$$2U.\frac{dU}{dr} + \frac{6P}{10D\sigma} . U^2 = 2\left(\frac{\sigma - P}{\sigma}\right) B^2$$

This equation may be converted to a form capable of direct solution by a change of variable:

Let $U^2 = T$

$$\therefore \frac{dT}{dr} + \frac{6P}{10D\sigma} . T = 2B^2 \left(\frac{\sigma - P}{\sigma}\right) \quad \ldots \quad \ldots \quad \ldots \quad (3.33)$$

Solving 3.33 and applying the condition $U = 0$ at $r = r_0$

$$U = \left[\frac{10}{3} \left(\frac{\sigma - P}{P}\right) DB^2 \left(1 - e^{-\frac{6P(r - r_o)}{10D\sigma}}\right)\right]^{1/2} \quad \ldots \quad (3.34)$$

To find the distance travelled before reaching 99% of terminal velocity;

$$\left[1 - e^{-\frac{6P}{10D\sigma}(r-r_0)}\right]^{1/2} = 0.99 \qquad \dots \qquad \dots \qquad (3.35)$$

For glass spheres of density 2.44 suspended in water at a volume concentration of 0.10, this can be rearranged to give

$$\left(\frac{r - r_0}{D}\right) = 13.9 \qquad \dots \qquad \dots \qquad (3.36)$$

so that a particle must travel a distance equivalent to 14 diameters before reaching 99% of the terminal velocity. The errors introduced by assuming that a particle achieves an instantaneous terminal velocity from rest are therefore much larger than those incurred in the case of laminar motion.

The results obtained above for a special type of axial velocity distribution have been checked for a slightly more realistic case where V is constant and the accelerative form therefore varies from one radius of motion to another. In this case θ is genuinely equal to zero. i.e.

$$\frac{dU}{dt} + \frac{3P}{10D\sigma}.\ U^2 = \left(\frac{\sigma - P}{\sigma}\right)\frac{V^2}{r}$$

Putting $U^2 = T$ as before, this reduces to

$$\frac{dT}{dr} + \frac{6P}{10D\sigma}.\ T = \frac{2V^2}{r}\left(\frac{\sigma - P}{\sigma}\right) \qquad \dots \qquad \dots \qquad \dots \qquad (3.37)$$

Equation (3.37) cannot be solved explicibly, but certain numerical solutions have been obtained by a method involving finite differences (Appendix 1.)

The velocity as a function of radial distance and the velocity and radial distance as a function of time were determined for the limiting particle size conditions ($D=235\mu$, $\sigma=2.44$, $C_V=0.10$, $V=200cm/sec$, $r_0=1.0cm$). The results are shown in Figures B.3.7, B.3.8.

The absence of a true terminal velocity is readily apparent, since the actual velocity is continuously changing. The apparent terminal velocity obtained by putting $\frac{dU}{dt} = 0$ in equation 3.30 has been included for purposes of comparison and it can be seen that it represents a close approximation to the actual velocity once the initial period of acceleration over.

If the apparent terminal velocity is taken as the basis for predicting particle behaviour and is assumed to be achieved instantaneously from rest, the minimal positional error incurred during the time the particle actually took to reach this velocity would be nearly one millimetre for a 235μ particle. For particles larger than this the error would be correspondingly larger.

The behaviour of particles starting at other radii is shown in Figure (B.3.9) for the tangential velocity V = constant = 200cm/sec.

It is apparent that particles starting from different radii all accelerate at about the same rate, and all ultimately exhibit the same variation in velocity with radial distance.

The velocities shown in Figures B.3.7 - B.3.9 may be corrected for the presence of other particles by multiplying by the factor $(1 - C_v)^2$, which in this instance is equal to 0.81.

3.3 Tangential Motion of A Single Particle

If it is assumed that there is no relative motion

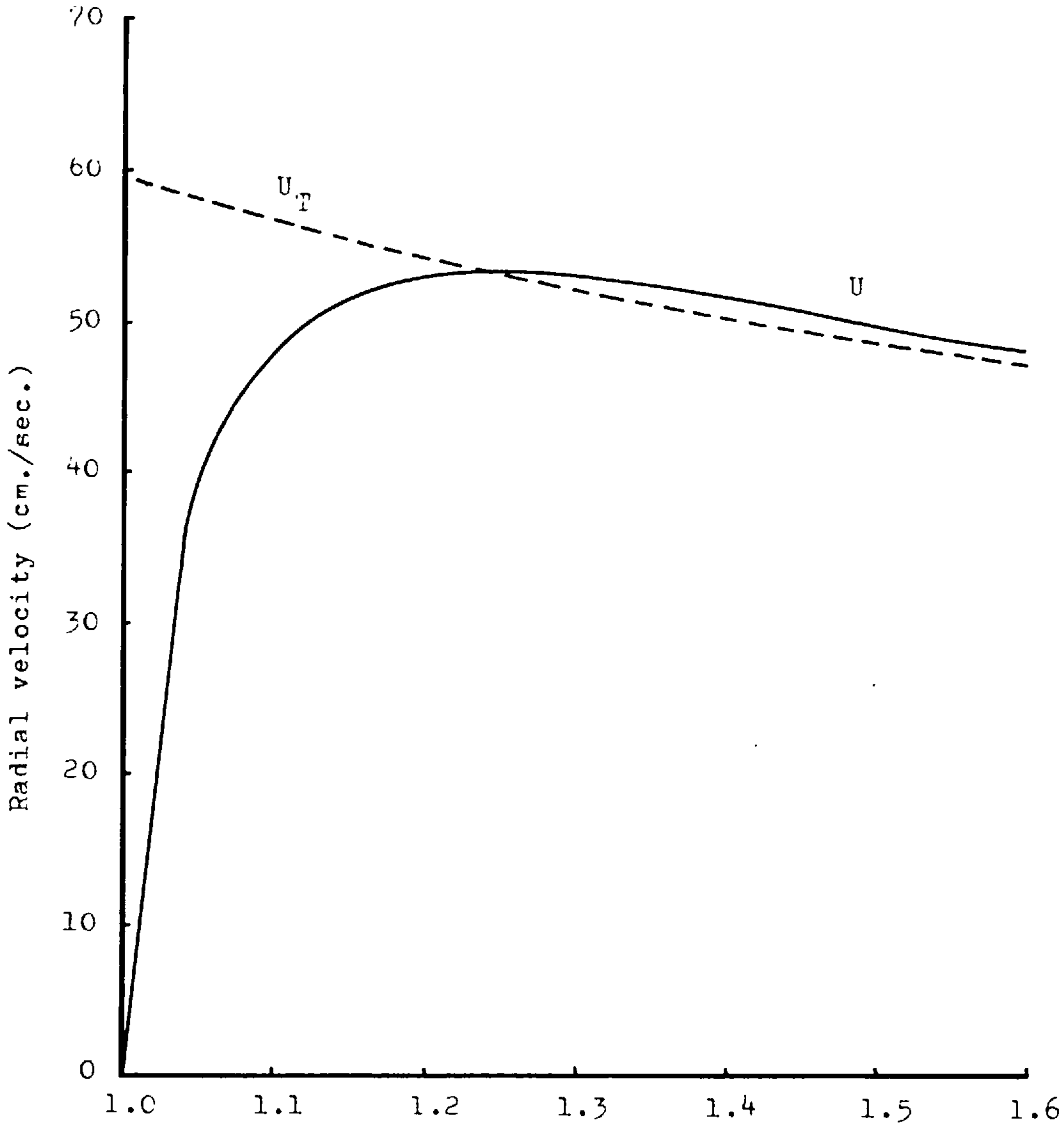

FIGURE B.3.7: Turbulent motion of a 235μ glass sphere

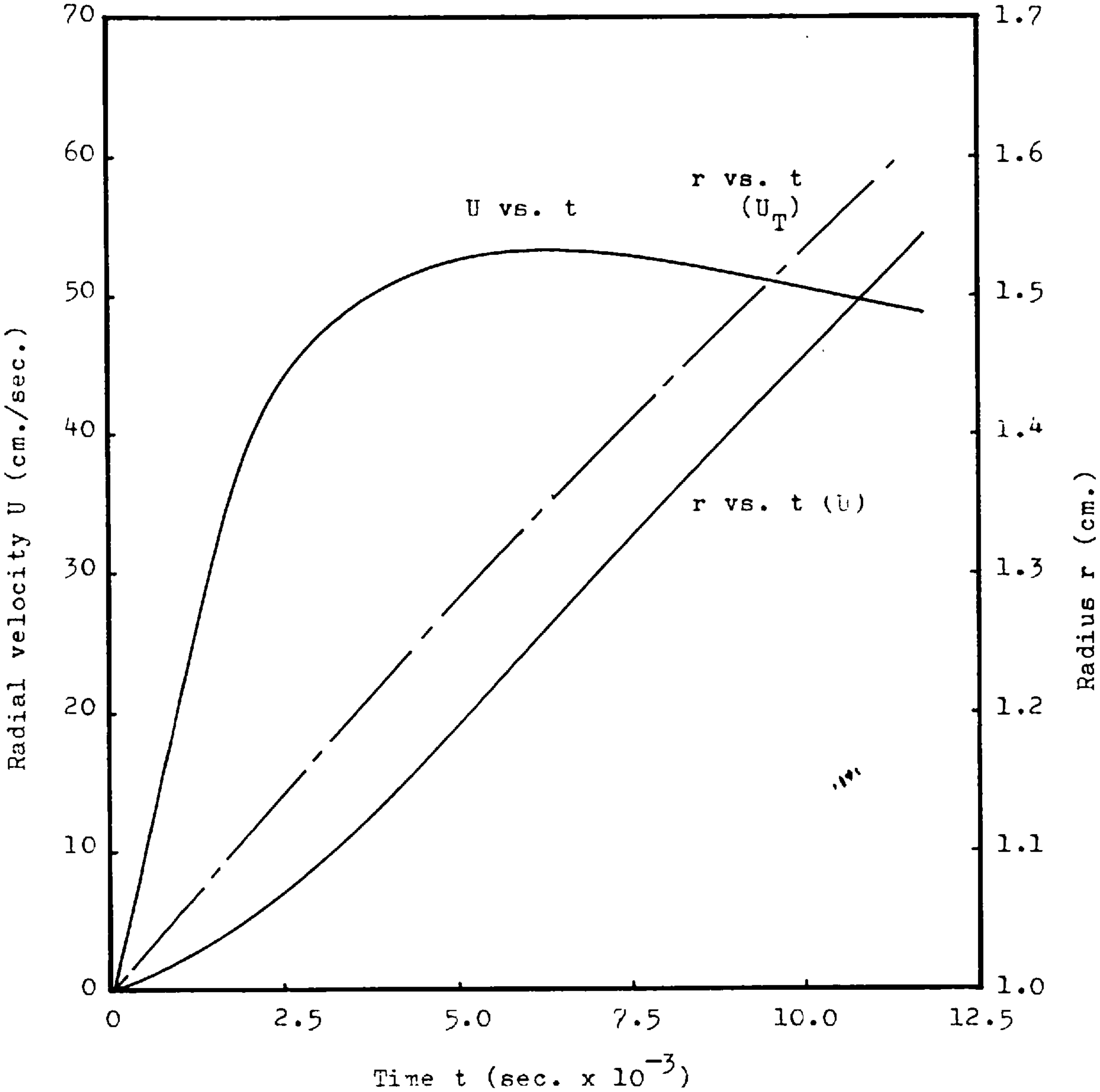

FIGURE B.3.8: Turbulent motion of a 235μ glass sphere

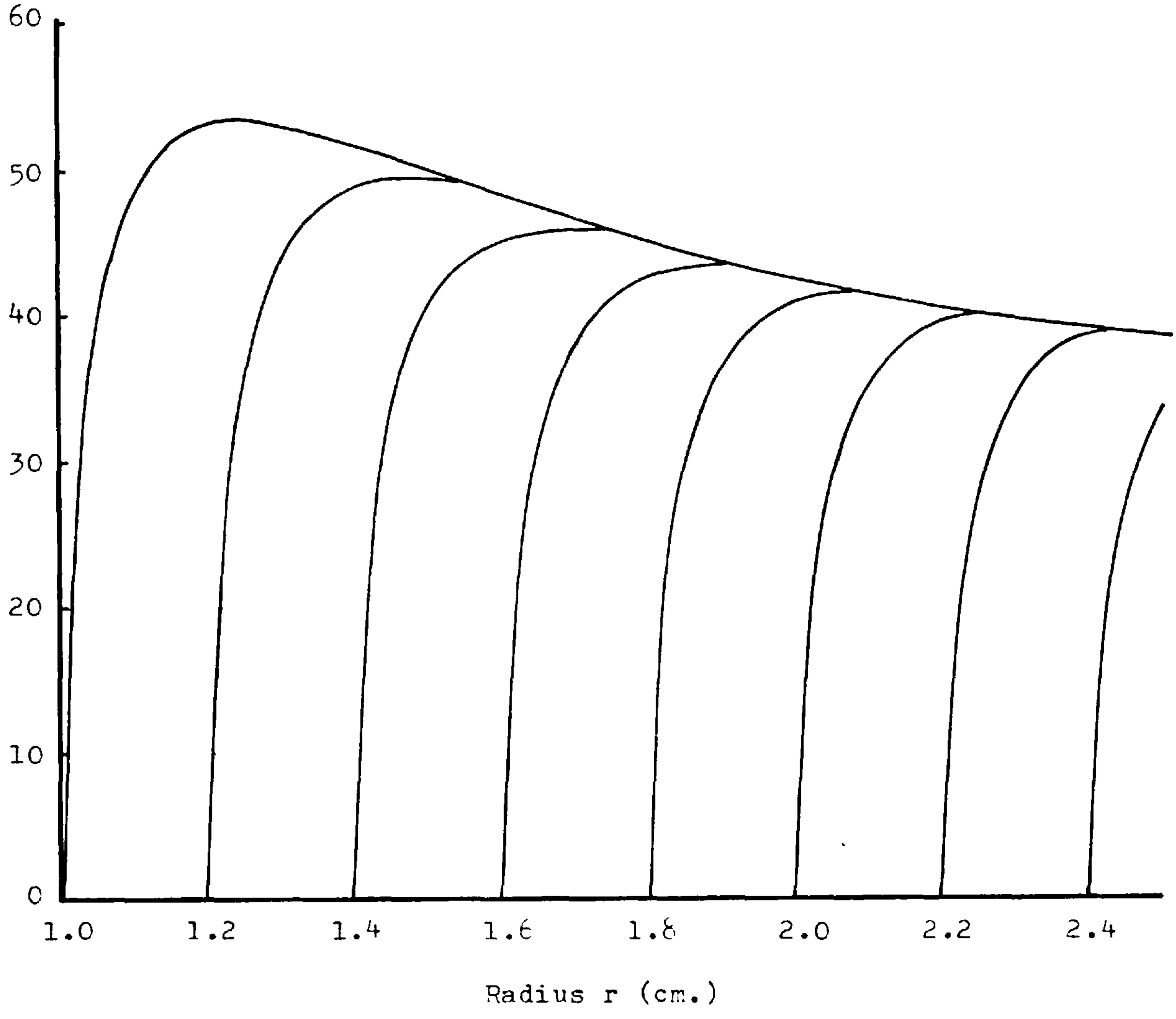

FIGURE B.3.9: Turbulent motion of 235u glass spheres starting from different positions.

between the particle and fluid in the tangential direction, the tangential velocity of the particle is equal to the fluid tangential velocity (V). This is most conveniently expressed in terms of the angular velocity

$$\frac{d\alpha}{dt} = \frac{V}{r} \quad \ldots \quad \ldots \quad \ldots \quad \ldots \quad (3.35)$$

But $\dfrac{d\alpha}{dt} = \dfrac{dr}{dt} \cdot \dfrac{d\alpha}{dr} = U . \dfrac{d\alpha}{dr}$

$$\frac{d\alpha}{dr} = \frac{V}{U}\left(\frac{1}{r}\right) \quad \ldots \quad \ldots \quad \ldots \quad (3.36)$$

Since both V and U are functions of the radius of motion (r), if the form of these functions is known, equation (3.36) may be integrated to find α.

For example, if V is assummed constant at all radii of motion and U is taken as the apparent terminal velocity:

3.3.1 Laminar Flow Conditions

$$U = \frac{K_L V^2}{r}, \quad K_L = \frac{(\sigma - P)^6 D^2}{18\, n\, (\sigma - 1)^5} ; \quad \frac{d\alpha}{dt} = \frac{1}{K_L V}$$

$$\alpha = \frac{1}{K_L V}(r - r_0) \quad \ldots \quad \ldots \quad \ldots \quad (3.37)$$

3.3.2 Turbulent Flow Conditions

$$U = \frac{K_T V}{r^{\frac{1}{2}}}, \quad K_T = \left[\frac{10}{3}\left(\frac{\sigma - P}{\sigma}\right) D\right]^{\frac{1}{2}}, \quad \frac{d\alpha}{dt} = \frac{1}{K_T r^{\frac{1}{2}}}$$

$$\alpha = \frac{2}{K_t}\left(r^{\frac{1}{2}} - r_0^{\frac{1}{2}}\right) \quad \ldots \quad \ldots \quad \ldots \quad (3.38)$$

3.4 Particle Tracks through Radial Force Fields

The tracks of single particles through unbounded radial force fields may now be calculated for conditions where the drag forces are determinate. This is most conveniently done in terms of the polar co-ordinates (r,α).

3.4.1 Laminar Flow Conditions

The tracks have been calculated for 45μ glass spheres starting at different initial radii. The conditions assumed are as for the calculation of the limiting size itself: i.e. $\sigma = 2.44$, $C_v = 0.10$, V = constant = 200cm/sec, $n = 10^{-2}$ poise.

Since $\frac{dr}{dt} = K_L . \frac{V^2}{r}$ where $K_L = \frac{(\sigma - P)^6 D^2}{18\, n\, (\sigma - 1)^5}$

$$r = [r_0^2 + 2K_L V^2 t]^{\frac{1}{2}} \quad \ldots \quad \ldots \quad (3.39)$$

and $\frac{d\alpha}{dr} = \frac{1}{K_L V}$

$$\therefore \quad \alpha = \frac{(r - r_0)}{K_L V} \quad \ldots \quad \ldots \quad \ldots \quad \ldots \quad (3.40)$$

The various values of (r,α) obtained from equation (3.40) have been plotted in Figure (B.3.10) Also marked are the relative positions of particles at a given time t. The equation governing these positions is:

$$\alpha = \frac{r_0}{VK_L} \left[\left(1 + \frac{2V^2 K_L t}{r_0^2} \right)^{\frac{1}{2}} - 1 \right] \ldots \quad \ldots \quad \ldots \quad (3.41)$$

3.4.2 Turbulent Flow Conditions

The tracks have been calculated for the limiting size (235μ) starting from various initial radii. The conditions assumed are again the same as those used for the calculation of the limiting size i.e. $\sigma = 2.440$, $P = 1.144$, V = constant = 200cm/sec, $n = 10^{-2}$ poise.

We have $\frac{dr}{dt} = K_T \frac{V}{r^{\frac{1}{2}}}$ where $K_T = \left[\frac{10}{3} \left(\frac{\sigma - P}{P}\right) D \right]^{\frac{1}{2}}$

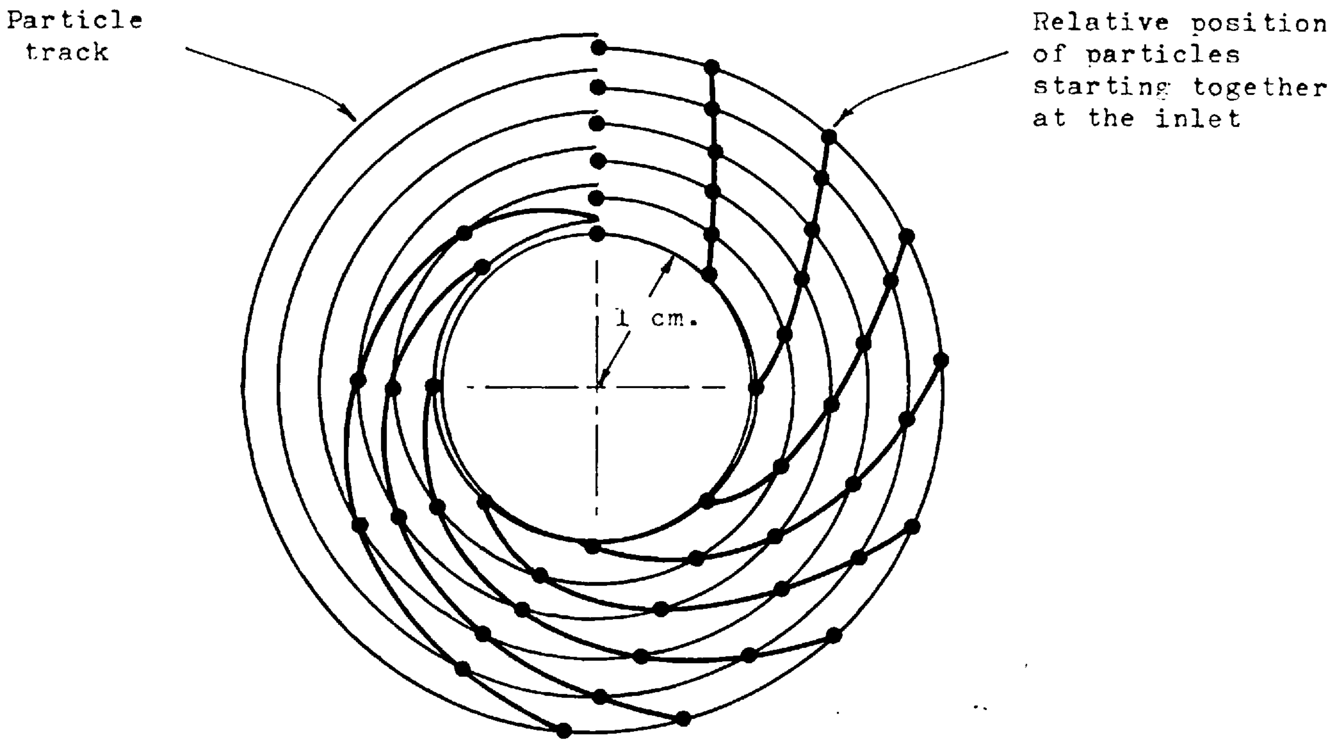

FIGURE B.3.10: Particle tracks under laminar conditions

$$r = [\ r_0^{3/2} + \frac{3}{2} K_T V . t]^{2/3} \quad \ldots \quad \ldots \quad \ldots \quad (3.42)$$

And $\frac{d\alpha}{dr} = \frac{1}{K_T r^{\frac{1}{2}}}$

$$\therefore \quad \alpha = \frac{2(r^{\frac{1}{2}} - r_0^{\frac{1}{2}})}{K_T} \quad \ldots \quad \ldots \quad \ldots \quad (3.43)$$

The various values of (r,α) obtained from equation (3.43) have been plotted in Figure (B.3.11). Also marked are the relative positions of particles at time t, obtained from the following equation:

$$\alpha = \frac{2r_0^{\frac{1}{2}}}{K_T} \left[\left(1 + \frac{3}{2} \frac{K_T V t}{r_0^{3/2}} \right)^{1/3} - 1 \right] \ldots \quad (3.44)$$

The errors present in the data presented in Figures B.3.10, B.3.11 are confined to one source, namely the replacement of the true velocity by the apparent terminal velocity. No error is involved in taking $\theta = 0$ since the necessary condition for this is fulfilled (i.e. V = constant)

3.5 Concentration Variation resulting from Particle Motion

The changes in suspension concentration caused by the radial motion of the particles shown in Figures (B.3.7, B.3.8) may be calculated from a knowledge of the relative positions of particles obtained from equations (3.40) and (3.43).

3.5.1 Concentration Variation for Laminar Particle Motion

Assuming a continuing supply of particles fed at the intervals shown in Figure 3.7, and applying equation (3.36),

$$\frac{d\alpha}{dr} = \frac{1}{K_L V} \quad \ldots \quad \ldots \quad \ldots \quad \ldots \quad (3.45)$$

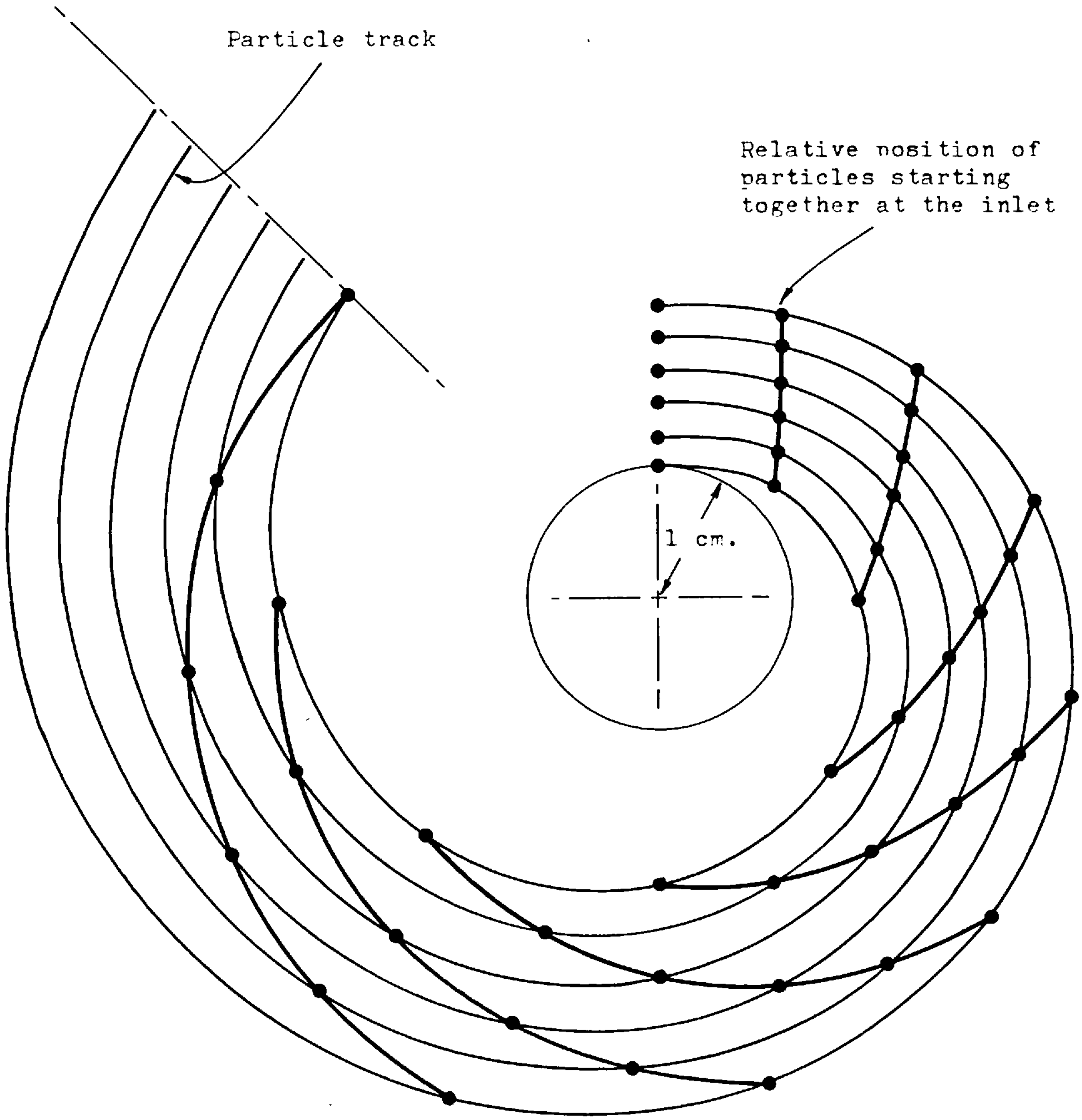

FIGURE B.3.11: Particle tracks under turbulent conditions

Equation (3.45) indicates that if V is constant, the angular progress of a particle for a given increment in radius is independent of the radius of motion of the particle. A band of particles starting together at the inlet to the helix (Figure B.3.10) will therefore all move radially at the same rate, and the concentration measured along any radius at an angle α to the inlet will be unchanged within the band of particles, although the band will have moved some distance radially. This effect is illustrated in Figure (B.3.12) for $\alpha = 315^{\circ}$.

3.5.2 Concentration Variation for Turbulent Particle Motion

Applying equation (3.36) to turbulent flow conditions:-

$$\frac{d\alpha}{dr} = \frac{1}{\bar{K}_T r^{\frac{1}{2}}} \quad \ldots \quad \ldots \quad \ldots \quad \ldots \qquad (3.46)$$

Equation (3.46) indicates that the particles starting at larger radii of motion will make less angular progress for a given increment in radius than those starting at small radii of motion. Hence to traverse a given angle α, particles starting at successively larger radii will have to move through successively larger radial distances. Consequently, the concentration measured along the radius at an angle α to the inlet will increase progressively as the measuring point is moved outwards within the band of particles. The effect is illustrated in Figure (B.3.13) for $\alpha = 315^{\circ}$.

Since V does not appear in equation 3.46, the behaviour discussed above should be independent of the tangential velocity distribution.

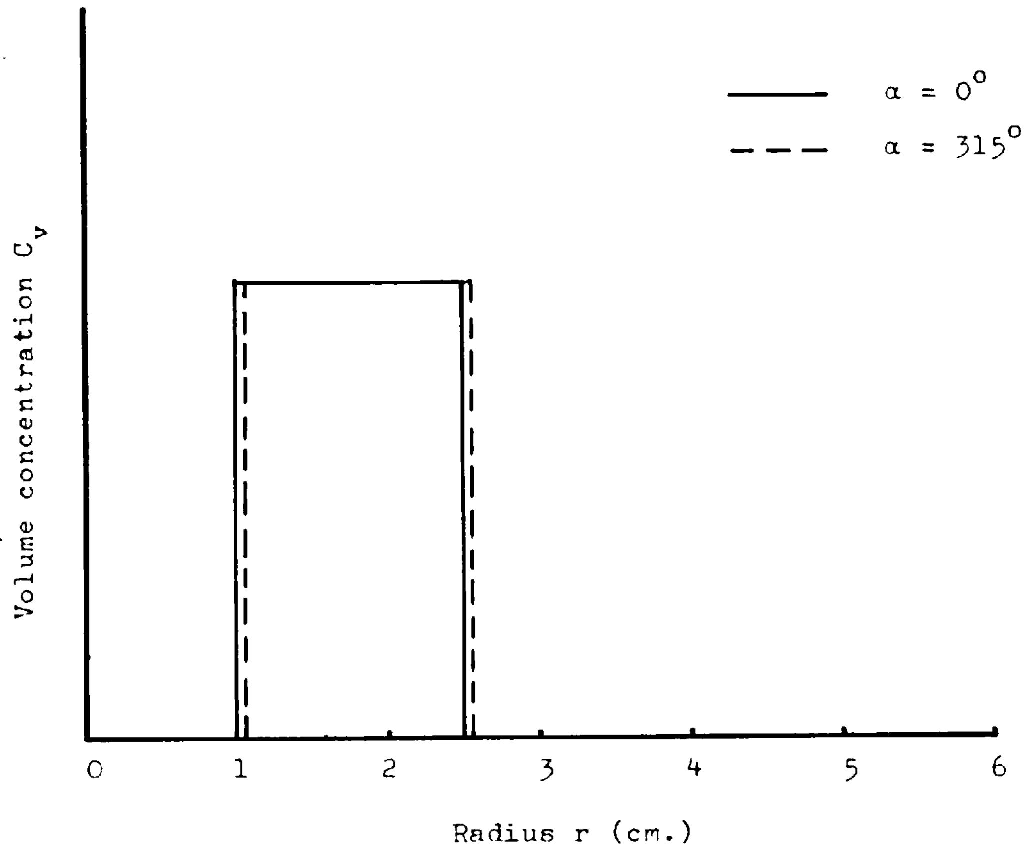

FIGURE B.3.12: Concentration variation for laminar motion

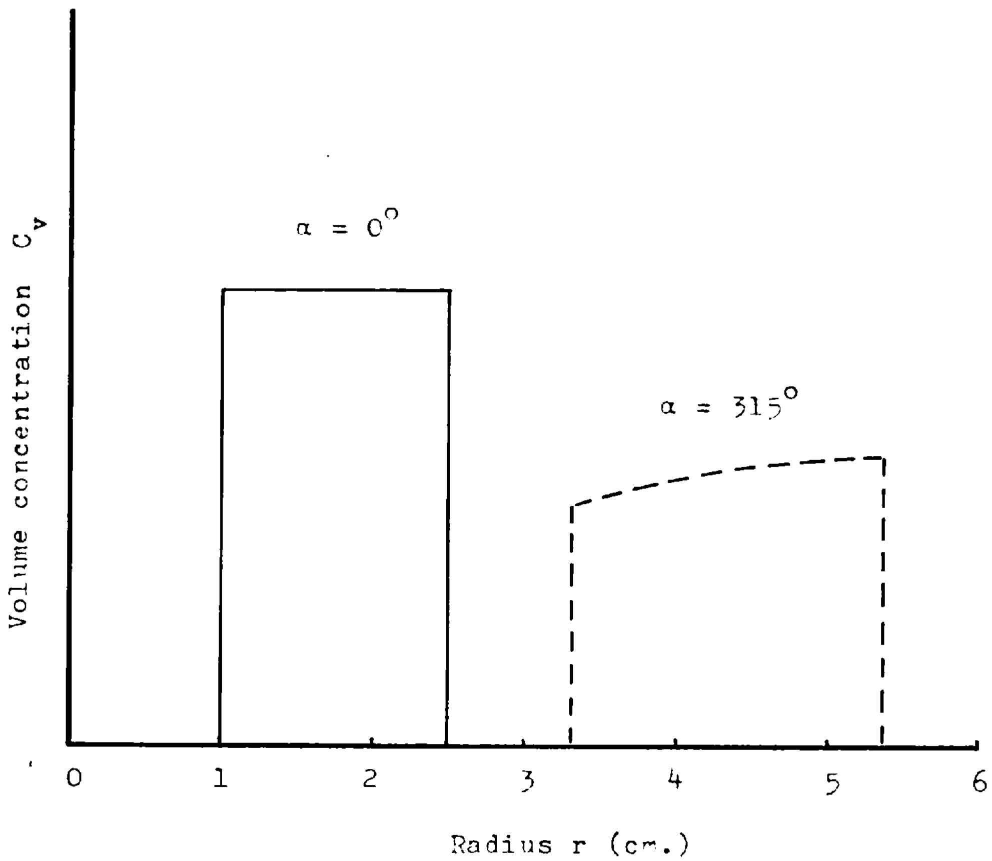

FIGURE B.3.13: Concentration variation for turbulent motion

3.6 Summary and Conclusions

Particles in suspensions that are subjected to unbounded radial force fields are acted upon by a number of forces which cause the particles to move relative to the fluid. Some of the forces can be calculated with reasonable accuracy for all conditions: examples of this type are the acceleration, pressure gradient and interference effects. Others, such as the fluid drag and the Magnus forces, can only be calculated over a limited range of conditions.

Complete solutions to the equation of motion for single particles cannot be obtained explicitly, and would be difficult to obtain using numerical techniques even supposing that all the required data were available. Even when the Magnus forces are neglected, the equation of motion can only be solved explicitly for one special axial velocity profile that gives a constant accelerative force and hence true terminal velocities for the particles. Moreover, the terminal drag forces can only be specified at low and high Reynold's numbers, corresponding to the laminar and turbulent regimes of motion. Under the conditions of interest to the present investigation, laminar drag forces appear to be operative at particle sizes smaller than 45μ, while full turbulent drag does not occur until a particle size of 235μ is reached. These estimates are probably not accurate but serve to illustrate the situation.

In the later sections of this analysis it is frequently necessary to express the particle radial velocity in terms of a simple explicit function. This has been achieved by using the apparent terminal velocity, which is obtained by putting $\frac{d^2r}{dt^2} = 0$ in the equation of motion (equation 3.19) and ignoring any relative tangential motion between particle and fluid (i.e. neglecting the Magnus effect). It must be born in mind that this introduces errors into calculations of both the velocity and the position of particles, the errors apparently being smaller for laminar motion than for turbulent motion.

It is worth noting that V has so far been assumed a function of r only, so that velocity gradients in the radial direction have been denoted by $\frac{dV}{dr}$. In the next section, changes in V with α (or t) must be taken into account as well. The notation for velocity gradients therefore becomes $\frac{\partial V}{\partial r}$, $\frac{\partial V}{\partial \alpha}$ etc.

4. BEHAVIOUR OF SUSPENSIONS IN ENCLOSED HELICAL CHANNELS

4.1 Forces operating on a Single Particle.

The introduction of boundaries to the simple radial force field considered in section 3 results in a number of important changes in the behaviour of both the fluid and the suspension as a whole.

Frictional and boundary layer effects arising at the channel walls result in a complex and changing axial velocity distribution and set up a secondary fluid flow as described earlier. Also, the outer wall constitutes a barrier to any further radial motion of the suspended particles, resulting in an accumulation of particles near the wall. Finally, containing the suspension within a channel of finite dimensions means that the radial motion of the particles must displace an equivalent volume of fluid, giving rise to a further secondary fluid flow.

The particle accumulation near the outer wall results in certain forces not previously considered, which must be examined since they can exert an appreciable influence on the particle motion.

4.1.1. Accelerative Force

Due to the complexity and changing nature of the axial velocity distribution, it is impossible to determine the forces acting on a particle at a given instant. (Sections B.2.2-4) Also, the equations governing the radial motion of particles (3.20, 3.30) cannot be solved explicitly in the great majority of cases, even when simple and invarient axial velocity distributions are assumed.

Consequently, in much of the subsequent analysis it has been necessary to make certain simplifying assumptions concerning the fluid and particle velocities. In particular, the velocity calculated for either fluid or particles at any given position (r,α) is in all cases an average velocity taken over the full depth of the channel. Other assumptions or limitations are discussed as they arise.

The Magnus effect discussed in Section 3.1.1 was not taken into account in the earlier parts of this analysis, since its introduction would have resulted in considerably more complicated equations and the labour involved in solving these for purely illustrative purposes seemed unjustified. In the present instance it cannot be included, partly due to lack of information concerning fluid behaviour, but also because of the formidable difficulties involved in attempting to set up any kind of model capable of predicting the interactions between appreciable concentrations of particles that are moving radially as well as tangentially and a fluid whose axial velocity distribution is changing and which may also be exhibiting two different types of radial flow. Not the least of the difficulties is the fact that neither the fluid behaviour[5] nor the Magnus effect[20] have been adequately defined under these conditions.

The effect of the Magnus or lift force is to decrease the retention time of particles in regions where the fluid axial velocity increases with the radius of motion and to increase the retention time in regions where the axial velocity decreases with the radius of motion. The apparent radial velocities of the particles in these regions will correspondingly be increased and decreased respectively.

The accelerative force exerted at any position

(r,α) within the helix may be expressed as follows

$$F_A = \frac{\pi D^3 \sigma}{6} \cdot \frac{V^2}{r} \quad \ldots \quad \ldots \quad \ldots \quad \ldots \quad (4.1)$$

In order to make use of equation (4.1) the variation in V with both r and α must be known or assumed.

4.1.2 Retarding Forces

(a) Pressure Gradient Force

The pressure gradient force may be expressed as follows:

$$F \quad = \frac{\pi D^3 P}{6} \cdot \frac{V^2}{r} \quad \ldots \quad \ldots \quad \ldots \quad \ldots \quad (4.2)$$

There may also be a contribution to the pressure gradient from the particle shearing pressure (see Section 4.1.2.d) though only if the velocity gradient $(\frac{\partial V}{\partial r})$ is small. If the pressure gradient force is to be calculated the dependence of V on r and α must again be known.

(b) Drag Force.

In the case of an unbounded radial force field, it was assumed that particles moving radially could undergo ideal forms of fluid drag, irrespective of the type of behaviour exhibited by the fluid in its tangential flow. This assumption was probably at least partially incorrect, since while it is conceivable that a particle could move radially under the influence of ideal forms of drag if located within a mass of fluid undergoing laminar tangential flow, it is difficult to imagine how the particle could experience viscous drag if the surrounding fluid is turbulent and exhibiting vorticity.

Also, from the approximate calculations of the limiting particle sizes for which ideal laminar and turbulent drag should occur (made in Section B.3) it can be seen that the bulk of the particles of interest from a sizing point of view fall in the transitional regime of particle-fluid motion, where the drag forces cannot be precisely defined in any case.

It can be seen from the foregoing that none of the forces responsible for the particle motion that have been considered so far can be defined accurately. The consequences of this lack of information are discussed in Section 4.2.

(c) Secondary Fluid Flow

In addition to the 'displacement' secondary fluid flow (Section B.3.1.2.c), there may be a recirculatory type of secondary flow created by the pressure gradients within the channel (Section B.2.3). In the case of a pure fluid, this flow is probably small and oscillatory in nature, and is progressively damped out in passage through the helix. (Section B.2.4) It is possible that the presence of solid particles would modify this behaviour, however. If the particles are uniformly distributed throughout the full depth of the channel, a recirculatory flow of this type should tend to cancel out any effect it may have on the motion or concentration of the particles, since while one half of the flow augments the radial motion of the particles, the other half reduces it by the same order of magnitude. Where the particle radial velocity is large in comparison with the secondary fluid flow, the average particle concentration over the full depth of the channel should therefore be little affected. In cases where these velocities are of the same order of magnitude, the secondary flow could give rise to some unusual behaviour. Where the fluid velocity is much in excess of the particle velocity, effective radial motion of the particles will only become possible when the oscillations have been damped out. Results quoted by Hawthorne[5] suggest that it is unlikely that this condition would be reached for a pure fluid travelling through the helix under the chosen conditions.

(d) Particle Shearing Forces

The accumulation of particles near the outer wall introduces new forces in addition to those already discussed (Section B.3.1.). The mechanism creating these new forces depends on the magnitude of the fluid velocity gradient ($\frac{dV}{dr}$), ~~that is to say~~ and upon whether particle inertia or fluid viscosity effects predominate. Throughout this section, the variation in V with α that is known to occur in pure fluids (Section B.2.2) is not taken into account, on the grounds that the shearing forces under discussion will oppose and minimise the effect. V is therefore considered to be a function of r only, and the notation has been modified accordingly. While this assumption simplifies the analysis, it also introduces a corresponding error into the results, which must be regarded only as approximations to the correct solution. The problem was first considered by Bagnold[17], but the present treatment, although based on and identical to his in form, leads to slightly different relationships.

Consider two adjacent layers of particles, of diameter D, moving at a velocity of V relative to each other. (Figure B.4.1.) Let the distance between the centres of neighbouring particles be L , and between adjacent layers βL.

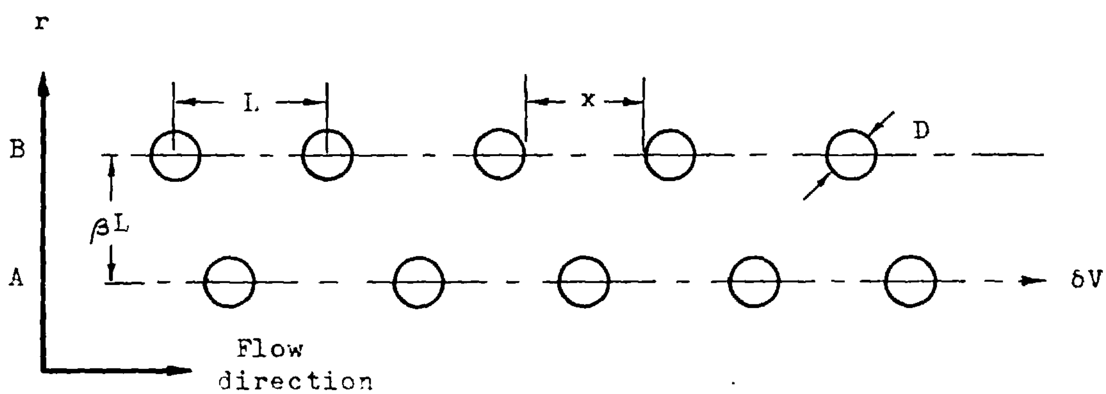

FIGURE B.4.1: Particle shearing forces.

Let the 'linear particle concentration' (λ) be defined as follows:-

$$\lambda = \frac{D}{x} = \frac{D}{L-D} \quad \ldots \quad \ldots \quad \ldots \quad \ldots \qquad (4.3)$$

The two possible mechanisms whereby particle shearing forces may be created will now be considered separately:

(i) Fluid viscosity dominant ($\frac{dV}{dr}$ small)

The passage of each A particle over a B particle is considered to invlove a temporary reduction in the shear velocity from its mean value $\delta\overline{V}$ during approach, followed by an increase during recession.

Suppose that the amplitude of the shear velocity fluctuation (ζ) bears some ratio $f(\lambda)$ to the mean shear velocity $\delta\overline{V}$.

Then $\zeta = f(\lambda).\ \delta V \quad \ldots \quad \ldots \quad \ldots \qquad (4.4)$

Supposing further that the fluctuation is approximately harmonic, then if ξ is the instantaneous shear velocity and t represents time:

$$\xi = \delta V + \zeta \operatorname{Sin} t = \delta V(1+f(\lambda) \operatorname{Sin} t) \quad \ldots \qquad (4.5)$$

Hence the instantaneous shear stress (τ) is given by

$$\tau = n . \frac{\xi}{\beta L} = \frac{n}{\beta L}.\ \delta V(1+f(\lambda) \operatorname{Sin} t) \quad \ldots \quad \ldots \qquad (4.6)$$

The work done per unit area of shear plane (W) in one complete velocity fluctuation is

$$W = \int_0^{2\pi} \tau\, \xi\, dt$$

$$W = \frac{n\ \delta V^2}{\beta L} \int_0^{2\pi} (1+f(\lambda) \operatorname{Sin} t)^2 dt \quad \ldots \quad \ldots \qquad (4.7)$$

The distance moved in one complete velocity fluctuation (δx) is given by

$$\delta x = \delta V \int_0^{2\pi} (1+f(\lambda)\,\text{Sin } t)dt \quad \ldots \quad \ldots \qquad (4.8)$$

$$\therefore \delta x = 2\pi.\delta V$$

Hence the mean shear stress ($\bar{\tau}$) within the suspension is

$$\bar{\tau} = \frac{W}{\delta x} = \frac{n.\delta V}{2\pi\beta L} \int_0^{2\pi} (1+f\ (\lambda)\text{Sin } t)^2 dt \quad \ldots \qquad (4.9)$$

On integrating,

$$\bar{\tau} = n.\ \frac{\delta V}{\beta L}\left[\ 1+\frac{f(\lambda)^2}{2}\ \right] \quad \ldots \quad \ldots \quad \ldots \qquad (4.10)$$

But $\delta V = \beta L.\ \frac{dV}{dr}$

$$\therefore \bar{\tau} = n\left[\ 1+\frac{f(\lambda)^2}{2}\ \right]\frac{dV}{dr} \quad \ldots \quad \ldots \quad \ldots \qquad (4.11)$$

When λ, and hence $f(\lambda)$ is equal to zero, equation (4.11) reduces to the correct pure fluid relationship. The result quoted by Bagnold omits the squared power of $f(\lambda)$. The reason for this is not clear.

To obtain the transverse pressure corresponding to the mean shear stress, use may be made of the relationship between these forces and the angle of the resultant:

$$\text{i.e. } \frac{\bar{\tau}}{p_b} = \tan \gamma \quad \ldots \quad \ldots \quad \ldots \quad \ldots \qquad (4.12)$$

Hence

$$p_b = n\left[1+\frac{f(\lambda)^2}{2}\right]\frac{dV}{dr}.\ \text{Cot}\,\gamma \quad \ldots \quad \ldots \qquad (4.13)$$

Bagnold found for his experiments with spherical particles of the same density as the fluid that

$$\bar{\tau} = (1+\lambda)(1+\tfrac{1}{2}\lambda)n\frac{dV}{dr} \quad \ldots \quad \ldots \quad \ldots \quad \ldots \qquad (4.14)$$

and ~~With~~ Tan γ = 0.75.

$$\therefore p_b = 1.33(1+\lambda)(1+\tfrac{1}{2}\lambda)\ n\ \frac{dV}{dr} \quad \ldots \quad \ldots \qquad (4.15)$$

Thus the presence of particles modifies the viscous forces in such a way that a transverse pressure is set up, in addition to that already present in the suspension.

This pressure acts on fluid and particles alike, and can therefore be regarded as an addition to the pressure gradient considered in Section 4.1.2.

To determine whether or not the shearing pressure makes a significant contribution to the pressure gradient, a likely order of magnitude may be calculated for it in the regions where the velocity gradient will be greatest, i.e. near the walls of the channel.

From Figure B.2.2 it is apparent that the velocity gradient in these regions could be very large, reaching perhaps 500 sec^{-1} in close proximity to the walls. The densities recorded in these zones for the particle sizes of interest in the present analysis ranged from 1.10 up to about 1.4, depending on the feed concentration. (See Section B.5.2)

The shearing pressure (p_b) has been calculated for particle sizes of 45μ and 235μ at several concentrations for each wall position. The corresponding fluid pressure gradient force on the particle (F_p) has been calculated and converted to a pressure (p) per unit projected area of the particle to provide a basis for comparison. The ratio (p_b/p) is presented below in Table B.4.1 for the following assumed conditions

$\sigma = 2.44$

$V = 200 cm/sec.$ $\qquad$ $D = 4.5 \times 10^{-3}, 23.5 \times 10^{-3} cm.$

$\frac{dV}{dr} = 500\ sec^{-1}$ $\qquad$ $P = 1.10 - 1.40$

$n = 10^{-2}$ poise

From eqn. 4.15: $p_b = 1.33(1+\lambda)(1+\frac{1}{2}\lambda)\,n\frac{dV}{dr}$

Also $p = F_p \div \frac{\pi D^2}{4} = \frac{\pi D^3}{6}.\,P.\,\frac{V^2}{r} \div \frac{\pi D^2}{4} = \frac{2}{3}DP\frac{V^2}{r}$

TABLE B.4.1

RATIO OF VISCOUS PARTICLE SHEARING PRESSURE TO FLUID PRESSURE IN WALL REGIONS OF CHANNEL

PULP DENSITY P	VOLUME CONC^N OF SOLIDS C_V	LINEAR PARTICLE CONC^N λ	$(\frac{p_b}{p})$ AT WALL POSITIONS			
			D = 45μ		D = 235μ	
			r=1.0cm	r=3.5cm	r=1.0cm	r=2.5cm
1.10	0.069	1.040	0.156	0.391	0.030	0.075
1.20	0.139	1.797	0.245	0.613	0.047	0.117
1.30	0.208	2.781	0.385	0.960	0.074	0.184
1.40	0.278	4.249	0.650	1.620	0.124	0.311

Depending on the particle size, the shearing pressure developed ranges from 3 to 16% of the fluid pressure for low concentrations at the inner wall up to > 100% for high concentrations at the outer wall. These represent the maxima for the inner and outer zones respectively, since the shearing effect will progressively diminish as the point under consideration moves into the main body of the channel.

However, in view of the large velocity gradient that must occur within the sizer, and which has been used in the above calculations ($\frac{dV}{dr}$ = 500 sec^{-1}), it is most unlikely that the fluid viscosity determines the shearing behaviour. The mechanism outlined in the next section is therefore considered to be the only one of interest as far as the performance of the sizer is concerned.

(ii) Particle Inertia dominant ($\frac{dV}{dr}$ large)

Any forces set in operation between adjacent layers of particles are considered to be due to interparticle collisions. The particles are assumed to be oscillating in all three dimensions, the oscillations being the result of collisions between particles.

Referring to Figure B.4.1, each particle in layer A will suffer a number of glancing collisions, the average angle of impact (α) being determined by the collision conditions. At each collision, the particle experiences a change of momentum in the 'r' direction equal to

$$\frac{2\pi D^3 \sigma}{6} \cdot \delta V \cdot \cos \alpha \quad \ldots \quad \ldots \quad \ldots \qquad (4.16)$$

Due to the random motion of the particles in both layers and the existance of more than one possible packing configuration, each A particle will only encounter a proportion of the B particles. This proportion will be a function of the linear particle concentration.

Denoting the proportion of effective collisions by $f_1(\lambda)$, the frequency of collisions (δN) is given by

$$\delta N = \frac{f_1(\lambda)\,\delta V}{L} \quad \ldots \quad \ldots \quad \ldots \quad \ldots \qquad (4.17)$$

Bagnold assumes in his treatment that the frequency of collisions is inversely proportional to the distance (x) between the nearest points of adjacent spheres. His reason for this is not clear, and since the collisions are considered to be caused by the passage of particles in adjacent layers over each other, it would seem that the frequency of collisions must rather depend on the distance (L) between the centres of adjacent particles.

The force exerted on each A particle (F_B) is equivalent to the total rate of change of momentum:

$$F_B = \frac{\pi D^3 \sigma}{3L} . \delta V^2 f_1(\lambda) \text{Cos } \alpha \quad \dots \quad \dots \quad \dots \qquad (4.18)$$

If $\frac{dV}{dr}$ is the velocity gradient normal to the line of motion, then

$$\delta V = L . \frac{dV}{dr} \quad \dots \quad \dots \quad \dots \quad \dots \quad \dots \qquad (4.19)$$

$$\therefore \quad F_B = \frac{\pi \beta^2 \text{Cos } \alpha . \sigma D^3 f_1(\lambda) . L}{3} \left(\frac{dV}{dr}\right)^2 \quad \dots \quad \dots \qquad (4.20)$$

Substituting for L from equation (4.7):

$$F_b = \frac{\pi \beta^2 \text{Cos } \alpha . \sigma D^4 f_1(\lambda) . (1 + \lambda)}{3\lambda} \left(\frac{dV}{dr}\right)^2 \quad \dots \qquad (4.21)$$

To make use of the results quoted by Bagnold, equation (4.21) must be converted to give the pressure (p) created between layers A and B. This may be obtained by multiplying the force on a single particle by the number of particles present in a unit area of a layer:

$$p = F_B\left(\frac{1}{L^2}\right) = F_B . \frac{\lambda^2}{D^2(1 + \lambda^2)}$$

$$p = \frac{\pi \beta^2 \text{Cos } \alpha . \sigma D^2 f_1(\lambda)}{3(1 + \lambda)} \left(\frac{dV}{dr}\right)^2 \quad \dots \quad \dots \qquad (4.22)$$

For high shear rates and conditions such that particle inertia effects were predominant, Bagnold's results indicated the following relationship with spheres of density 1.0 suspended in water ($\lambda < 12$)

$$p = 0.042 \text{Cos } \alpha . D^2 \lambda^2 \left(\frac{dV}{dr}\right)^2 \quad \dots \quad \dots \quad \dots \qquad (4.23)$$

with $\tan \alpha = 0.32$ (average). $\therefore$ $\text{Cos } \alpha = 0.95$

Comparing equations (4.22) and (4.23) it is found that

$$f_1(\lambda) = \frac{0.126(1 + \lambda)\lambda}{\pi \beta^2} \quad \dots \quad \dots \quad \dots \qquad (4.24)$$

Substituting this result in equation (4.12)

$$F_B = 0.042\sigma D^4 \ (1+\lambda)^2 \cos a \ (\frac{dV}{dr})^2 \quad \ldots \quad \ldots \quad (4.25)$$

Taking Cos a (average) = 0.95

$$F_B = 0.040\,\sigma D^4 \ (1+\lambda)^2 \ (\frac{dV}{dr})^2 \quad \ldots \quad \ldots \quad (4.26)$$

To determine whether or not this force is of significance in relation to the accelerative and drag forces, it is necessary to calculate a likely order of magnitude for F_B.

The velocity and velocity gradient are assumed to have the same values as those employed for the 'viscosity dominant' example previously considered. The densities recorded in the wall regions for particles of interest in the present analysis ranged from 1.0 up to about 1.4, depending on the feed concentration.

Force (F_B) has been calculated for particle sizes of 45μ and 235μ at several concentrations for each wall position. The net accelerative force (F_N) has been calculated, and the ratio (F_B/F_N) is presented overleaf in Table B.4.2 from the following assumed conditions:-

σ = 2.44		D = 45μ, 235μ
V = 200cm/sec		P = 1.0 - 1.4
$\frac{dV}{dr}$ = 500sec^{-1}		

$$F_N = F_A - F_P = \frac{\pi D^3}{6} (\sigma - P) \frac{V^2}{r}$$

$$F_B = 0.040\sigma D^4 (1+\lambda)^2 (\frac{dV}{dr})^2$$

For the conditions quoted, the ratio F_B/F_A reduces to

$$\frac{F_B}{F_N} = 0.81rD \left[\frac{(1+\lambda)^5}{(1+\lambda)^3 - 0.524\lambda^3} \right] \ldots \quad \ldots \quad \ldots \quad (4.27)$$

TABLE B.4.1						
RATIO OF INERTIAL PARTICLE SHEARING FORCE TO ACCELERATIVE FORCE IN WALL REGIONS OF CHANNEL						
PULP DENSITY	VOLUME CONC^N OF SOLIDS	LINEAR PARTICLE CONC^N	$\frac{F_B}{F_N}$ AT WALL POSITIONS			
			D = 45μ		D = 235μ	
P	C_V	λ	r=1.0cm	r=2.5cm	r=1.0cm	r=2.5cm
1.05	0.035	0.680	0.011	0.027	0.056	0.139
1.10	0.069	1.040	0.016	0.041	0.085	0.213
1.15	0.104	1.402	0.023	0.059	0.122	0.306
1.20	0.139	1.797	0.033	0.083	0.173	0.432
1.25	0.174	2.248	0.047	0.116	0.243	0.606
1.30	0.208	2.781	0.066	0.164	0.343	0.858
1.35	0.243	3.429	0.094	0.236	0.492	1.231
1.40	0.278	4.249	0.139	0.347	0.725	1.813

Depending on particle size the shearing force ranges from about 6% of the net accelerative force for low densities at the inner wall of the channel up to an apparent 180% for high densities at the outer wall. It will therefore have little effect on the particle motion in the inner and central zones, since in there zones either the density or the velocity gradient is low.

In the region near the outer wall, however, the shearing force may have a considerable effect on the particle motion, especially for the larger sizes. Where the ratio F_B/F_N is less than unity the outward radial motion of the particles will be reduced, and where the ratio exceeds unity the particle motion must be reversed. The layers of particles will then dilate inwards until the forces are in equilibrium:-

$$0.040D^4 \sigma(1+\lambda)^2\left(\frac{dV}{dr}\right)^2 = \frac{\pi D^3}{6}(\sigma - P)\frac{V^2}{r} \quad \ldots \qquad (4.28)$$

Under the conditions assumed in calculating Table 4.2, this equality is reached at $\lambda = 3.05$ for 235μ glass spheres. For particles of this size which are moving at an axial velocity of 200 cm/sec and in a velocity gradient of 500sec^{-1}, the maximum permissible volume concentration of particles at a radius of 2.5cm is 0.224. If the specific gravity of the particles is 2.44, this corresponds to a limiting pulp density of 1.32 gm/c.c. As the ratio F_B/F_E is directly proportional to both particle size and radius of motion (equation 4.27), the equality shown in equation 4.28 will not normally be reached with particles smaller than 235μ.

To summarise, the 'viscosity dominant' shearing force acts so as to increase the fluid pressure gradient, but it seems unlikely that this type of force can arise with the high velocity gradients expected in the sizer. The 'inertial' shearing force may be expected to exert an appreciable influence on the motion of all sizes of particle in the region near the outer wall of the channel, and for the larger particles it can be large enough to arrest and reverse the motion if the volume concentration of particles is high.

In the region near the inner wall of the channel the velocity gradient may be quite large but the shearing force should be small for all sizes of particle, since the force is small at all densities for fine particles and for coarse particles, the density in this region is low.

4.2 Motion of Single Particles

The various forces acting on single particles were discussed in detail in Sections 4.1.1, 4.1.2. The accelerative force could not be described accurately as a function of time and position, due to the lack of information about the axial velocity profile. For the same reason, the Magnus forces and secondary fluid flow effects acting on the particles could not be specified. The fluid drag forces resulting from the motion of the particles could only be described accurately when the motion was steady and the conditions fell in either the laminer or the turbulent flow regions. If the motion was unsteady, the equations became too complicated for analytic treatment, and if the behaviour fell in the transitional region between laminar and turbulent behaviour the drag forces could not be specified. In view of this lack of information, the analytic treatment adopted in Section 3 cannot be used in the present instance, and instead of predicting the concentration variation likely to result from the motion of individual particles it is now necessary to devise methods for inferring the motion of a population of particles from measurements of the resulting particle concentrations.

4.3 Motion of Particle Populations

4.3.1 Introduction

Before commencing the final and perhaps the most important portion of the analysis, it is desirable to review the main variables and to discuss the manner in which they affect each other.

The axial or tangential velocity of a particle (V) determines the accelerative and pressure gradient forces acting on it, while the velocity gradient within the fluid surrounding the particle governs the shearing force and Magnus force which may also act on the particle. Separately or in combination, these forces determine the net accelerative force tending to produce motion of the particle relative to the fluid. The magnitude of the Reynolds Number for this motion determines the type of fluid drag force tending to oppose the motion. If the shearing and Magnus forces are neglected, the axial velocity of the particle can be put equal to that of the fluid and the particle motion relative to the fluid can then be considered to take place in a radial direction. The axial velocity profile of the fluid changes during its passage through the helix, resulting in a secondary flow of fluid in a radial direction. This secondary flow is recirculatory in nature and its effect on the motion of the particles should therefore be small when averaged out over the full depth of the channel.

The radial velocity (U) attained by a given size of particle is affected by the volume concentration of surrounding particles in addition to the forces already mentioned. Since the axial velocity profile and the concentration of particles change progressively through the helix, the radial velocity of the particles must in general also be changing continuously. Under certain conditions this change can be small, however, and the particle motion may then be approximately described by deriving an apparent terminal velocity which neglects the acceleration terms in the equations of motion.

The volume concentration of particles (C_V) controls the magnitude of the shearing forces developed in regions where the fluid velocity gradient is high. It also affects the radial velocity of the particles directly by increasing the inertia of the suspension medium and by influencing the fluid flow round the moving particles. However, within any given region, the motion of the particles changes their volume concentration, so U and C_V must normally be regarded as mutually dependent quantities.

At present a good deal of the information required for the construction of a complete model of the behaviour of the suspension at various depths and cross-sections within the helix is lacking. Hence, wherever the values of U, V, and C_V at any position (r,α) are under consideration in the analysis which follows, these quantities represent averages taken over the full depth of the channel at that position.

4.3.2 Analysis of Concentration Variation

Consider a small annular segment of suspension situated within the helix at position (r,α) and of the dimensions shown in Figure B.4.2. The segment is considered to be stationary and particles are therefore travelling through it with a tangential velocity V and a radial velocity U.

If the feed to the helix is constant, there will be steady state conditions within the helix and the quantities U, V, and C_V will remain constant at any point (r,α). Consequently, the net influx of particles to the segment under consideration must be zero. If the particle flux ($\mathcal{E}$) is defined as the product of the volume concentration and the velocity of the particles, then the radial ($\mathcal{E}_r$) and tangential ($\mathcal{E}_\alpha$) particle fluxes are given by

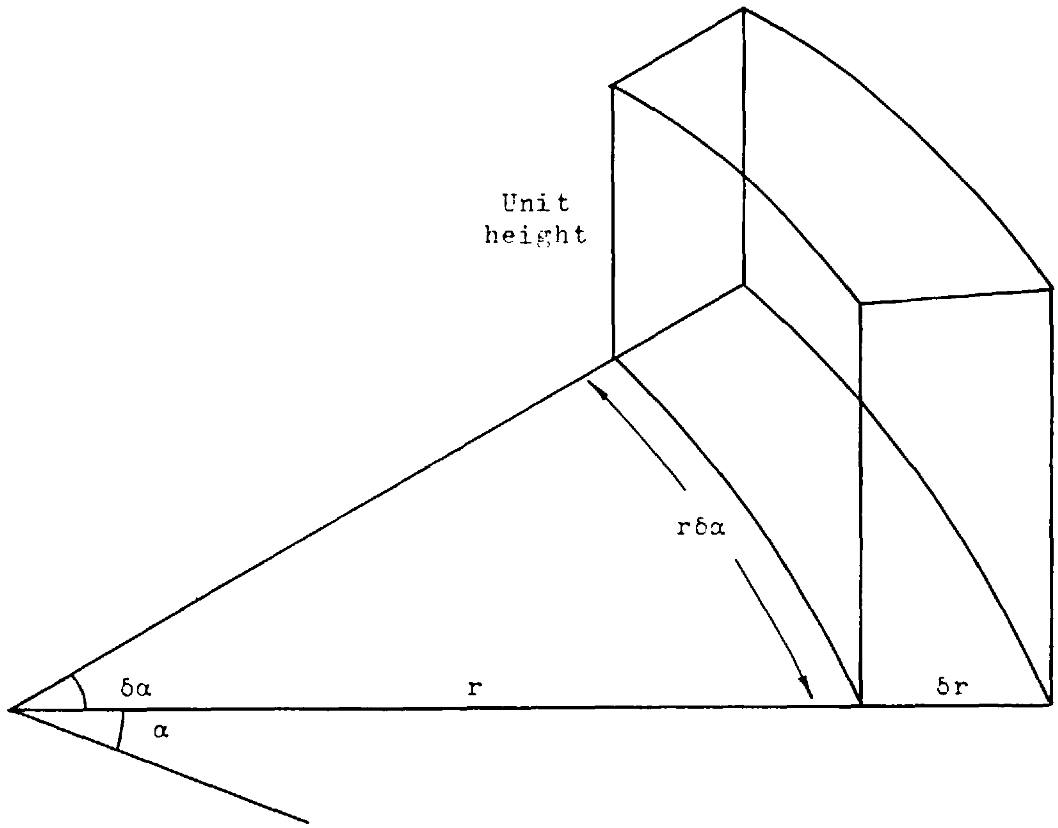

FIGURE B.4.2: Elemental volume.

$$\varepsilon_r = UC_V \quad \ldots \quad \ldots \quad \ldots \quad \ldots \quad \ldots \qquad (4.29a)$$

$$\varepsilon_\alpha = VC_V \quad \ldots \quad \ldots \quad \ldots \quad \ldots \quad \ldots \qquad (4.29b)$$

Equating the fluxes of particles entering and leaving the segment and taking the limits as $\delta r, \delta\alpha, \rightarrow 0$ gives the continuity equation for the point (r,α)

$$\frac{\partial}{\partial r}(r\varepsilon_r) + \frac{\partial \varepsilon_\alpha}{\partial \alpha} = 0 \quad \ldots \quad \ldots \qquad (4.30)$$

On substituting for ε_r, ε_α from equations 4.29

$$\frac{\partial}{\partial r}(rUC_V) + \frac{\partial}{\partial \alpha}(VC_V) = 0 \quad \ldots \qquad (4.31)$$

There are three conditions that must be satisfied by any full solution to equation 4.31: the volume concentration must be constant across the inlet to the helix, the radial flux must be zero at the walls of the helix ($r = 1.0$cm, $r = 2.5$cm) for all values of α, and the total tangential flux of particles must be constant at all cross-sections within the helix. i.e.

$$\alpha = 0 \qquad C_V = C_{Vf} \text{ (constant)} \quad \ldots \qquad (4.32)$$

$$r = 1.1,\ 2.5: \qquad UC_V = 0 \quad \ldots \qquad (4.33)$$

$$\frac{\partial}{\partial \alpha}\left[\int_{r=1}^{r=2.5} VC_V \, dr \right] = 0 \quad \ldots \qquad (4.34)$$

The full solution to equation 4.31, whereby C_V may be expressed as a function of r and α, can only be obtained when U and V are known functions of r and α. At present, this information is for the most part not available. Solutions to simplified versions of equation 4.31 may be found for the regions of interest in the present investigation by making certain assumptions concerning the behaviour of the suspension, basing the assumptions either on the experimental evidence or the results of the theoretical study presented in Section 3.

The calibration technique described in Section 4 of Part A was based on observations made in the vicinity of the channel walls and it is therefore desirable to find solutions for these regions. This work is described in Sections 5.3.1, 5.3.2.

4.4 Summary and Conclusions

The particles in a suspension flowing through an enclosed helical channel are supported and acted on by a fluid that is moving in an unsteady manner in both the tangential and radial directions. The complex and varying axial velocity profile of the fluid is caused by frictional and boundary layer effects arising at the walls of the channel.

The fluid behaviour and the channel walls are responsible for the introduction of two additional factors affecting the motion of the particles: a secondary flow of fluid in a radial direction, and a shearing force arising near the outer wall of the channel when high particle concentrations and high fluid velocity gradients occur simultaneously. The secondary fluid flow probably consists of two components: a displacement flow caused by the transference of particles towards the outer wall and a possibly oscillating flow caused by the pressure gradients set up within the fluid. The shearing force (Bagnold effect) varies in both nature and magnitude according to whether particle inertia or fluid viscosity effects are dominant.

Lack of information concerning the flow behaviour of the suspension during its passage through the helix made it impossible to calculate the absolute magnitudes of any of the forces acting on the particles. The likely magnitude of the two types of shearing force were compared with the accelerative force on a relative basis, making use of assumed values of the axial velocity and velocity gradient.

It was not possible to predict the changes in particle concentration which would result from the motion of individual particles because of the inadequacy of the existing theory and the almost total lack of data relating to many aspects of fluid and suspension behaviour. Instead, a continuity equation was derived for the particles in terms of their concentration at any point and the radial and tangential velocities at that position. If suitable solutions of the continuity equation can be found, it should be possible to infer the velocities of particles from a knowledge of the initial and final concentrations occurring within the helix.

5. TESTS CONDUCTED WITH GLASS SPHERES

5.1 Mark 6 and Mark 7 Cells

5.1.1 Introduction

The main objective of the work carried out using glass spheres was to provide reliable data for the development and verification of a theoretical model of the sizer performance. The experimental work was carried out during the same period as the detailed theoretical examination of particle behaviour set out in the preceeding four sections. In the absence of this information, the experimental programme was designed to cover a wider range of conditions than proved necessary. On the other hand, this broad test programme resulted in the acquisition of considerable information that could usefully have been applied to the theoretical study had it been available.

A new and improved experimental rig was constructed before commencing the actual test work. This incorporated a new cell, a redesigned measuring head assembly and a new set of density gauging equipment. The modifications will now be described in more detail.

5.1.2 Mark 6 and Mark 7 Cells

During the course of the test runs made with the Mark 5 cell, it was discovered that the channel walls were flexing to an extent that made it necessary to compensate all the readings obtained. A new cell (the Mark 6 cell) was therefore constructed, identical in dimensions with the cells Mark 2, 4, 5 (Figure A.2.4) but with the channel walls in the measuring zone milled down to 30/1000 inches. When the Mark 6 cell was installed and calibrated however, it was discovered that appreciable flexure of the walls was still occurring. Careful examination of the cell revealed that, while most of the channel walls had been reduced to the correct thickness of 30/1000inches, the regions adjacent to the side members of the channel were as thin as 10/1000 inches in places.

The Mark 6 cell was therefore discarded, and a new cell of the same dimensions was made. (Mark 7). In this case the channel walls were hand filed and polished to give a thickness of 40/1000 inches. This greater wall thickness reduced the sensitivity of the density gauge, but no further problems connected with wall flexure were encountered.

5.1.3. Modifications to Test Rig

A new measuring head assembly was designed and constructed. (Figures B.5.1, B.5.2). The sizer cell passed through and was clamped to a rectangular brass frame, which acted as the support and guides for the traversing head mechanism. The original strontium-90 source was one of a standard range (Section A.3.2) and the dimensions were not well suited to the existing measurement requirements. A special source was therefore ordered for the new measuring head. This was again a strontium-90 source of 20 millicuries total activity, but the active area was 40 x 3mm. compared with 114 x 3mm. for the earlier source. Although the new source and ionisation chamber were collimated as before to 1.5mm. to improve the resolution, the fact that the whole length of the new source was used in the measurements resulted in an effective source activity of 10 millicuries compared with 7 millicuries for the old rig. The measurement positions relative to the helix were the same as those employed with the earlier version of the equipment. (Figure A.3.1) The source was mounted in an aluminium head plate above the sizer cell

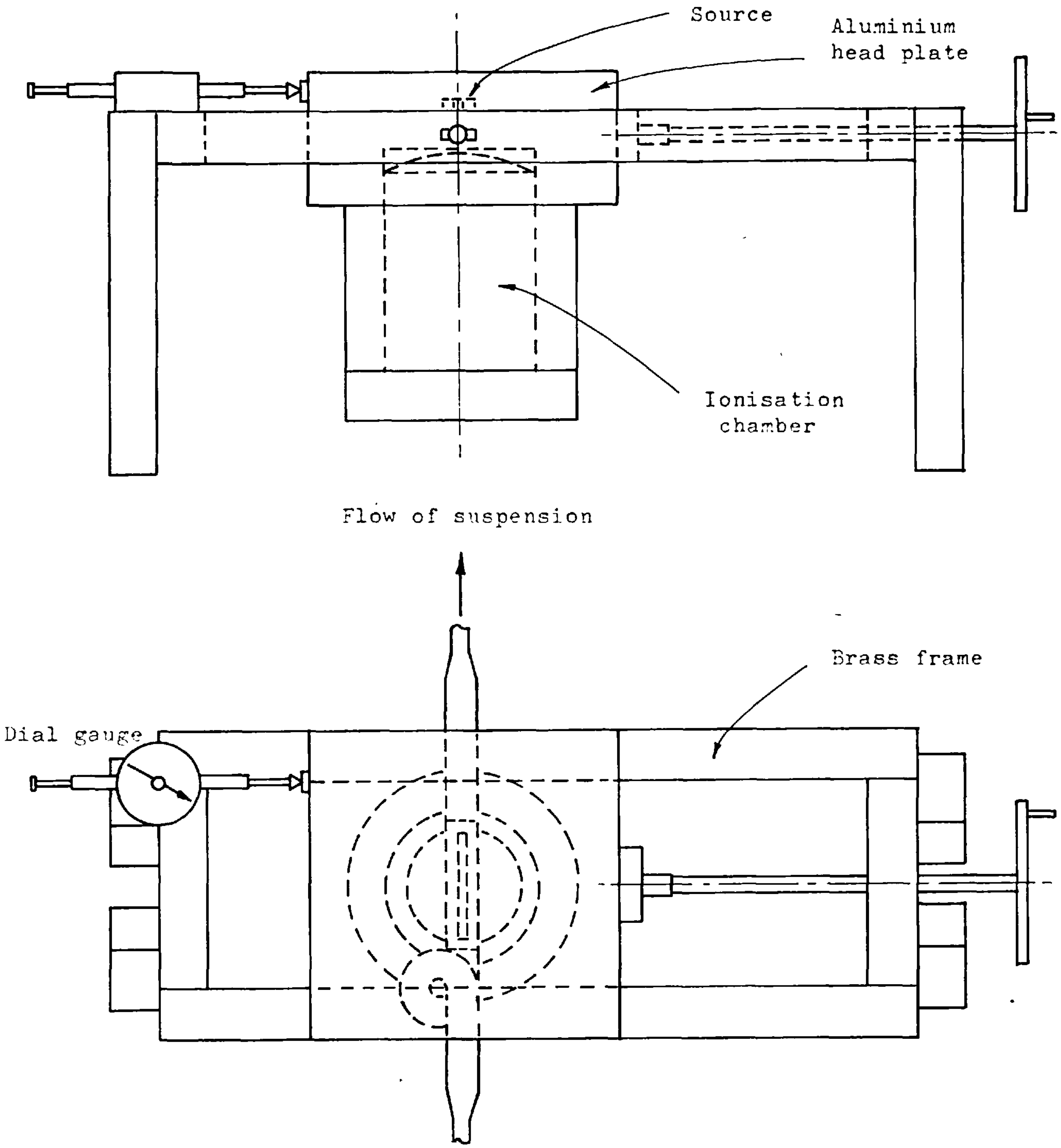

FIGURE B.5.1: Second test rig: Measuring Head.

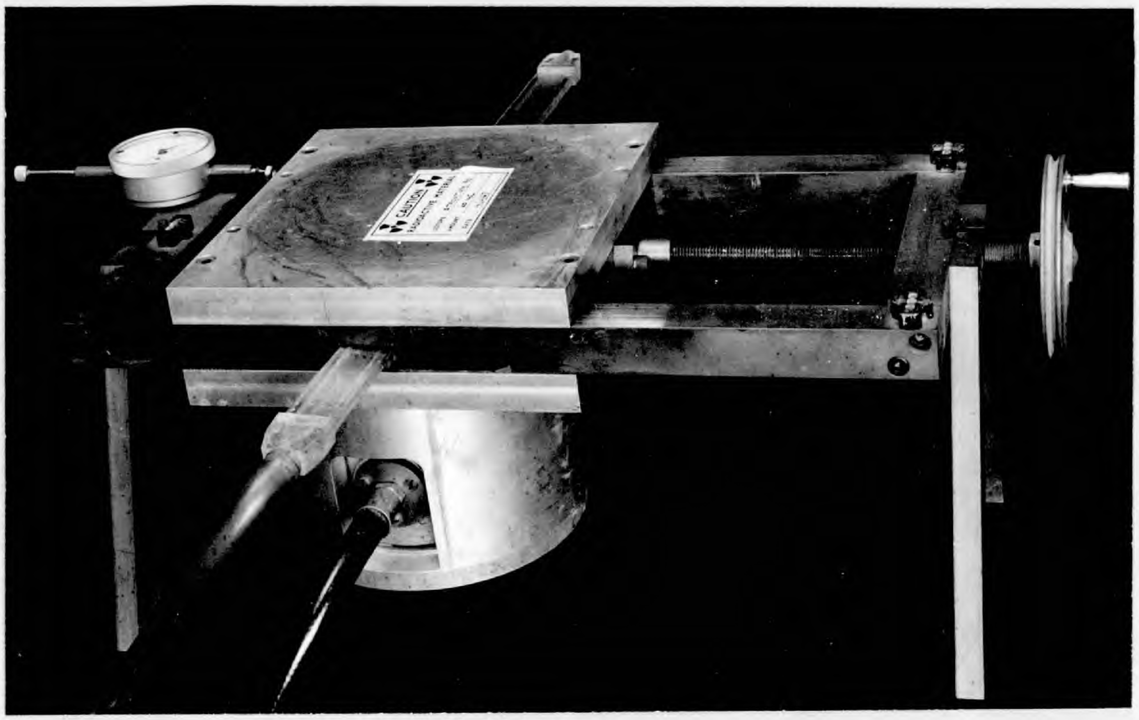

FIGURE B.5.2: Photograph of Head Assembly.

and the ionisation chamber in a cylindrical aluminium container attached to a plate below the cell. The whole head assembly could be traversed by a hand screw, the traverse position being indicated by a dial gauge as on the earlier rig. A narrow brass plate was attached to the brass frame, next to and running parallel with the sizer cell, so that the source could be blanked off from the ionisation chamber for standardisation purposes.

The 'Atomette' radiation gauge electronic unit used on the earlier rig was replaced by an 'Atomat' Series B Type U, which was very kindly supplied on loan by the Baldwin Instrument Company for a period of twelve months. The 'Atomat' unit,though identical to the'Atomette' in principle, was temperature stabilized and possessed greater flexibility in operation.

Two additions were made to the instrumentation employed in the flow circuit. The temperature of the suspension in the circuit was monitored by means of a thermistor inserted into the feed hopper of the monopump, the signal from the thermistor circuit being displayed on the six-point chart recorder. A mercury manometer was tapped into the suspension flow at the discharge from the sizer measuring channel, so that the pressure exerted on the channel walls could be monitored and kept constant with a view to eliminating uncontrolled flexure of the walls. The final test rig was otherwise as shown earlier in Figure A.4.1.

The density gauge was calibrated with the new test materials in the same manner as before. (Section A.3.6).

5.1.4 Testwork Using Mark 7 Cell

A supply of glass balls was obtained which ranged in size from 35 to 325 mesh (Tyler). This material was screened on the set of 8 inch reference screens which was used in the earlier work (Section A.4.4) to provide individual size fractions. The test method was restricted by the fact that only 2 Kg. of glass balls were available and the programme was planned in three stages:

(1) Test runs conducted on single size fractions at a number of different feed concentrations. These were intended to establish how the radial motion of a particle varied with size and with the concentration of similar particles nearby. The size fractions and feed concentrations were as follows:

Size Fractions (B.S.Mesh)	Feed Concentrations (C_{Vf})
-52 +72	0.011
-72 +100	0.022
-100 +150	0.047
-150 +200	0.066
-200 +325	0.100

Each size fraction was run at the five different feed concentrations, giving a total of 25 tests in the first stage of the work.

(2) Test runs conducted on pairs of size fractions, mixed together in varying proportions, at the constant feed concentration selected earlier for the sizing calibration. (C_{Vf} = 0.100). These were intended to establish how the presence of different concentrations of particles of other sizes affected the behaviour of a given size. Each pair of size fractions was combined in three different

ratios, 25:75, 50:50, 75:25, giving a total of 30 tests for the 5 size fractions available.

(3) Tests conducted using full size distributions, which were intended to verify any conclusions drawn from the results of stages (a) and (b). The 12 ideal Gaudin-Schuhmann distributions used throughout the earlier work with quartz were again used (See Sections A.3.9 Table A.3.2, A.4.6 Table A.4.2.)

The full programme called for a total of 67 samples, and since the supply of glass balls was only sufficient to prepare about 8 samples, all test materials had to be r reclaimed, dried and re-sized before a further series of tests could be started.

The procedure adopted for each test run was as follows: the required amount of water was measured into the circuit and the flowrate set to 90c.c./sec. The sample was then added to the monopump feed hopper and the return flow pipe positioned so as to provide sufficient agitation in the hopper to keep the solids in suspension. The back pressure exerted on the sizer 'windows' was then adjusted to 6cm. of mercury by means of a clamp on the discharge flowline. The thermistor was placed in the hopper, the chart recorders were started and the particle concentration measurements made. The flowrate and back pressure were readjusted as required during operation. At the conclusion of each run, the circuit was repeatedly flushed with fresh water until no more solids could be reclaimed. Although the overall sample recovery from the circuit was excellent for all test runs, the material lost from each sample due to temporary settling out in various dead zones within the circuit was appreciable, and the actual density in the circuit was nearly always a good deal lower than the apparent or 'made-up' value. All feed densities quoted below have therefore been calculated from the measured concentration profile.

5.2 Analysis of Results

The concentration profiles obtained for single size fractions are shown in Figures B.5.3. - B.5.7, for pairs of size fractions in Figures B.5.8 - B.5.17 and for size distributions in Figures B.5.18 - B.5.21. The most important limitation in interpreting these profiles is the fact that the measurements were conducted downstream of the helix rather than within it. The leading edge of the collimated source and detection assembly was some 5 cm. downstream of the exit from the helix, a distance equivalent to a little over four channel diameters for a circular channel having the same wetted perimeter. The influence of bends on the flow behaviour of pure fluids may extend as far as 50 pipe diameters downstream of the bend (Section 2.1), so if a similar effect occurs in the case of a suspension, the remixing caused by the persistance of a recirculatory fluid flow could result in the loss of a significant proportion of the concentration gradient before the suspension reaches the measurement zone.

5.2.1 Single Size Fractions

The shapes of the concentration profiles obtained with single size fractions of glass balls are in general similar to those recorded for ground quartz particles (Figures A.3.14 - A.3.17) although some of the features are accentuated. Considering the curves for various feed concentrations of -52 +72 glass balls, it can be seen that the region near the inner wall contains small concentrations of solids and a comparatively shallow concentration gradient,

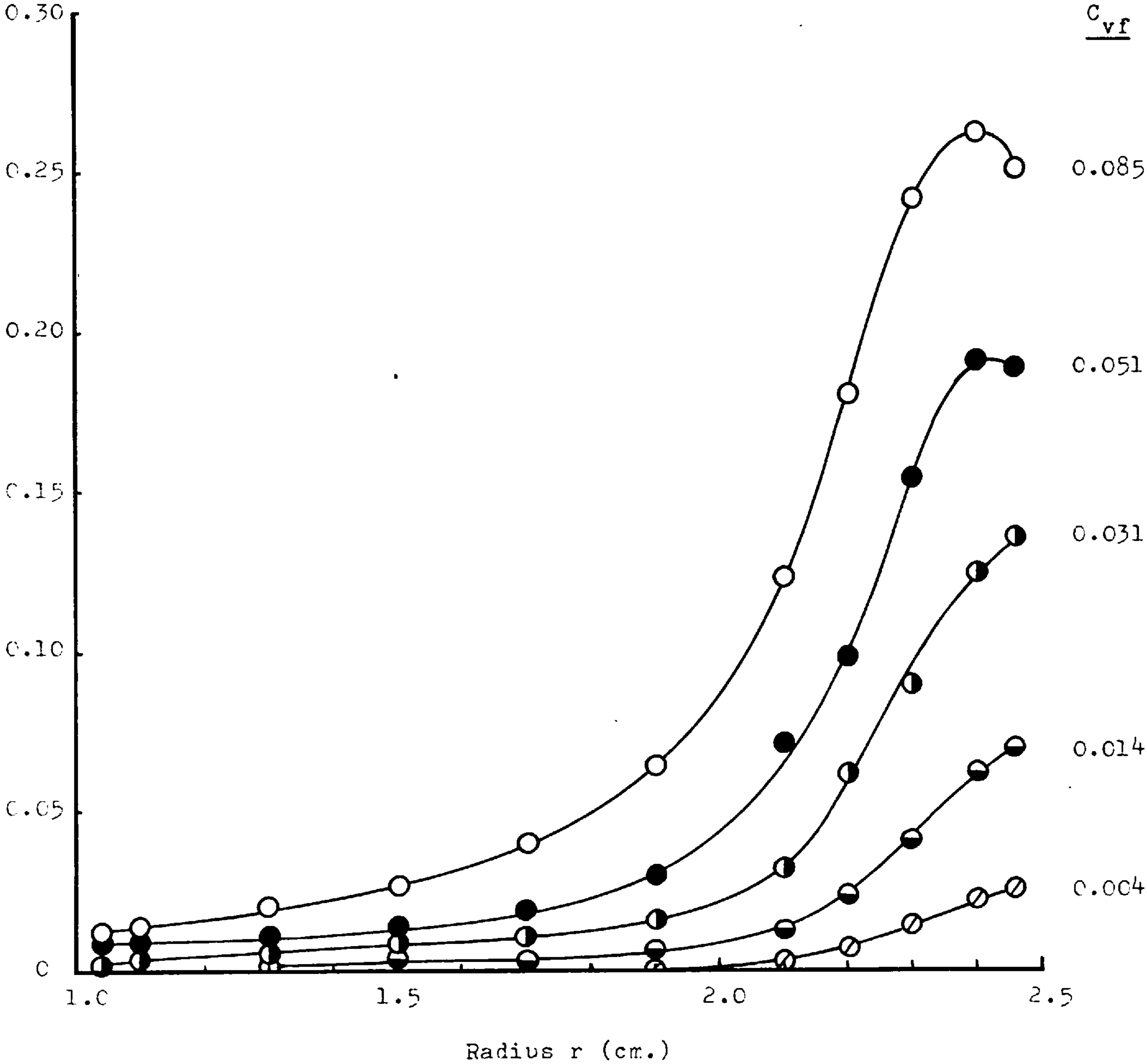

FIGURE B.5.3: Concentration profiles obtained with the Mark 7 cell using glass spheres: size fraction -52 +72 B.S.

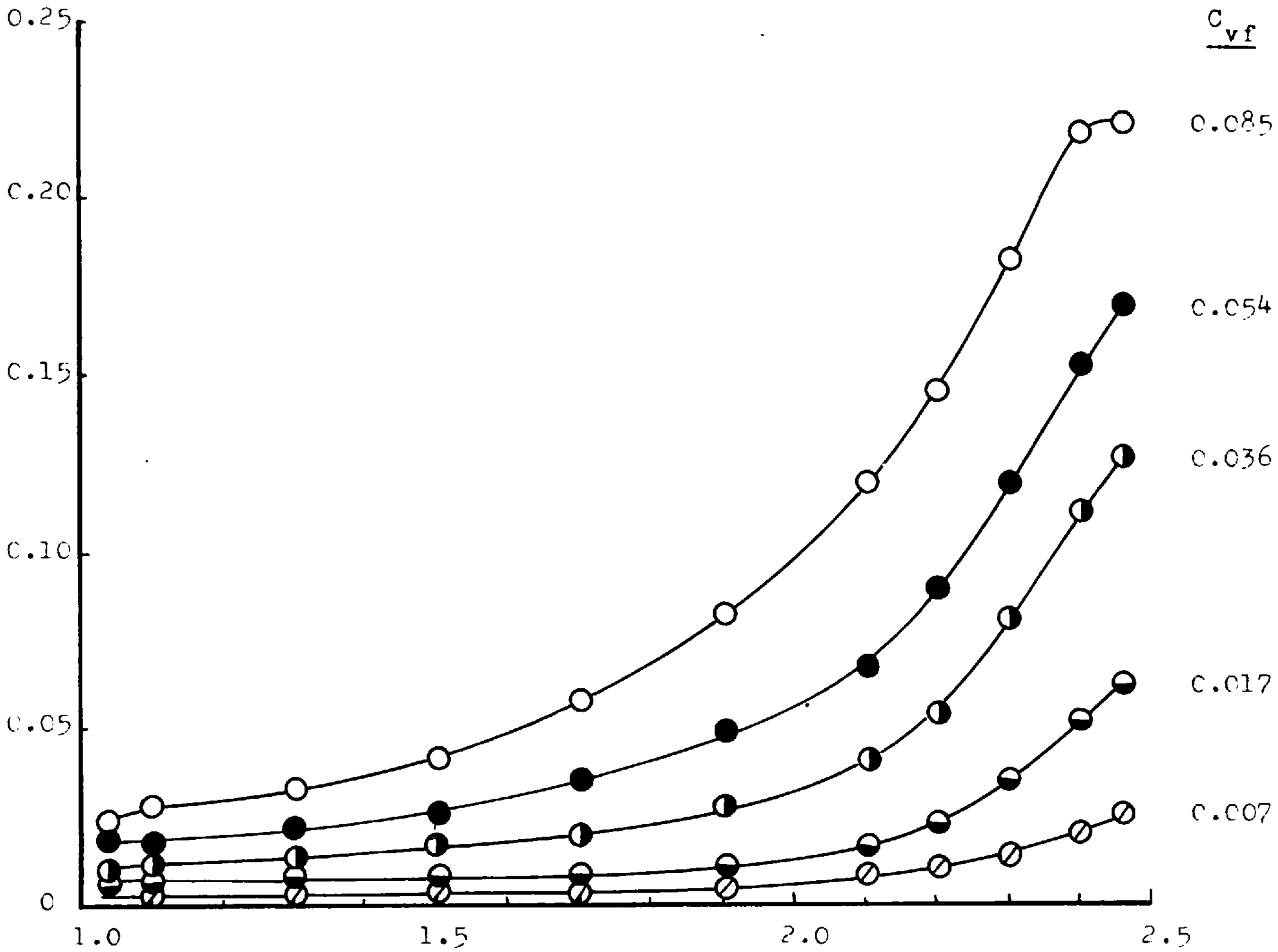

FIGURE B.5.4: Concentration profiles obtained with the Mark 7 cell using glass spheres: size fraction -72 +100 B.S.

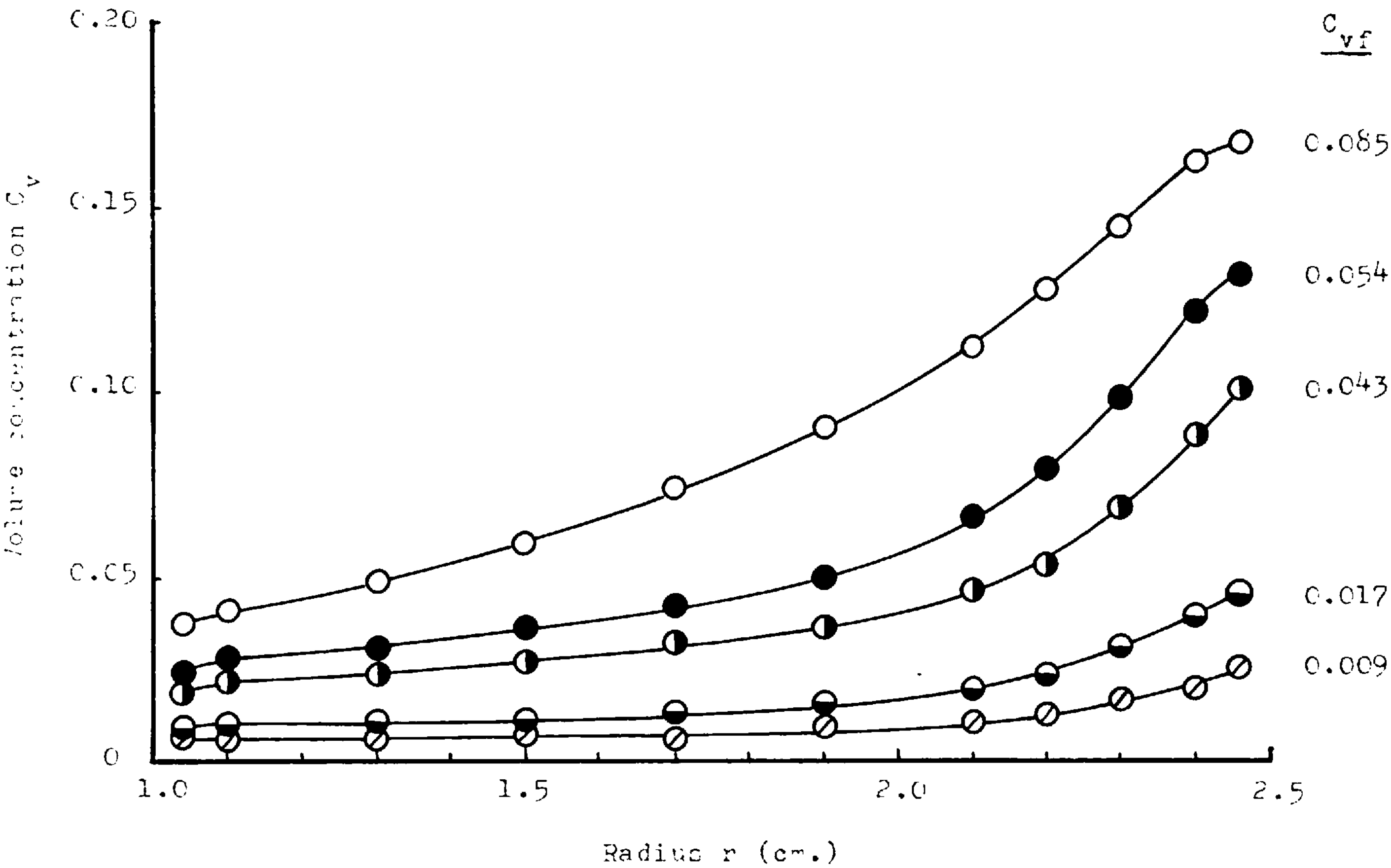

FIGURE B.5.5: Concentration profiles obtained with the Mark 7 cell using glass spheres: size fraction -100 +150 B.S.

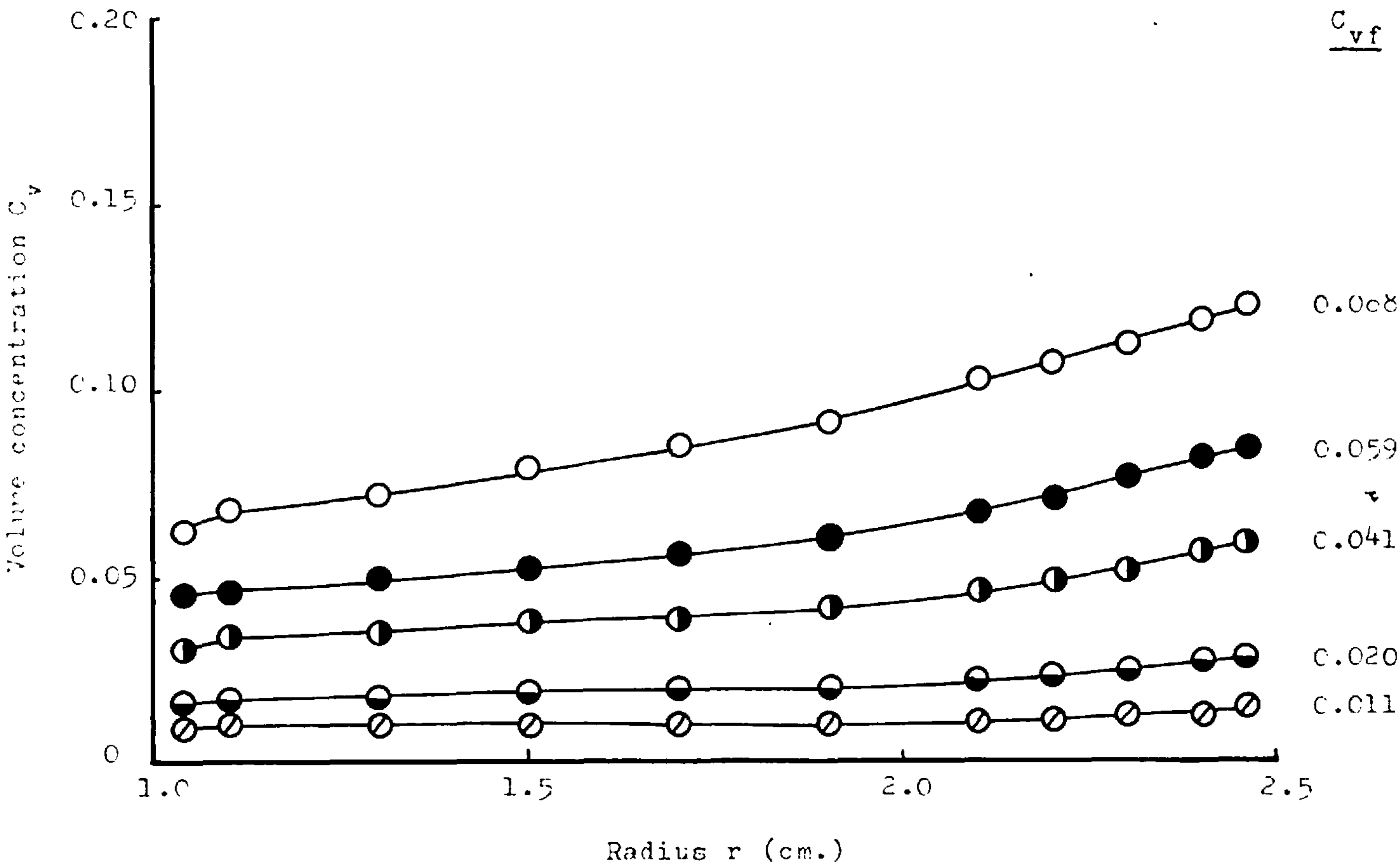

FIGURE B.5.6: Concentration profiles obtained with the Mark 7 cell using glass spheres: size fraction −150 +200 B.S.

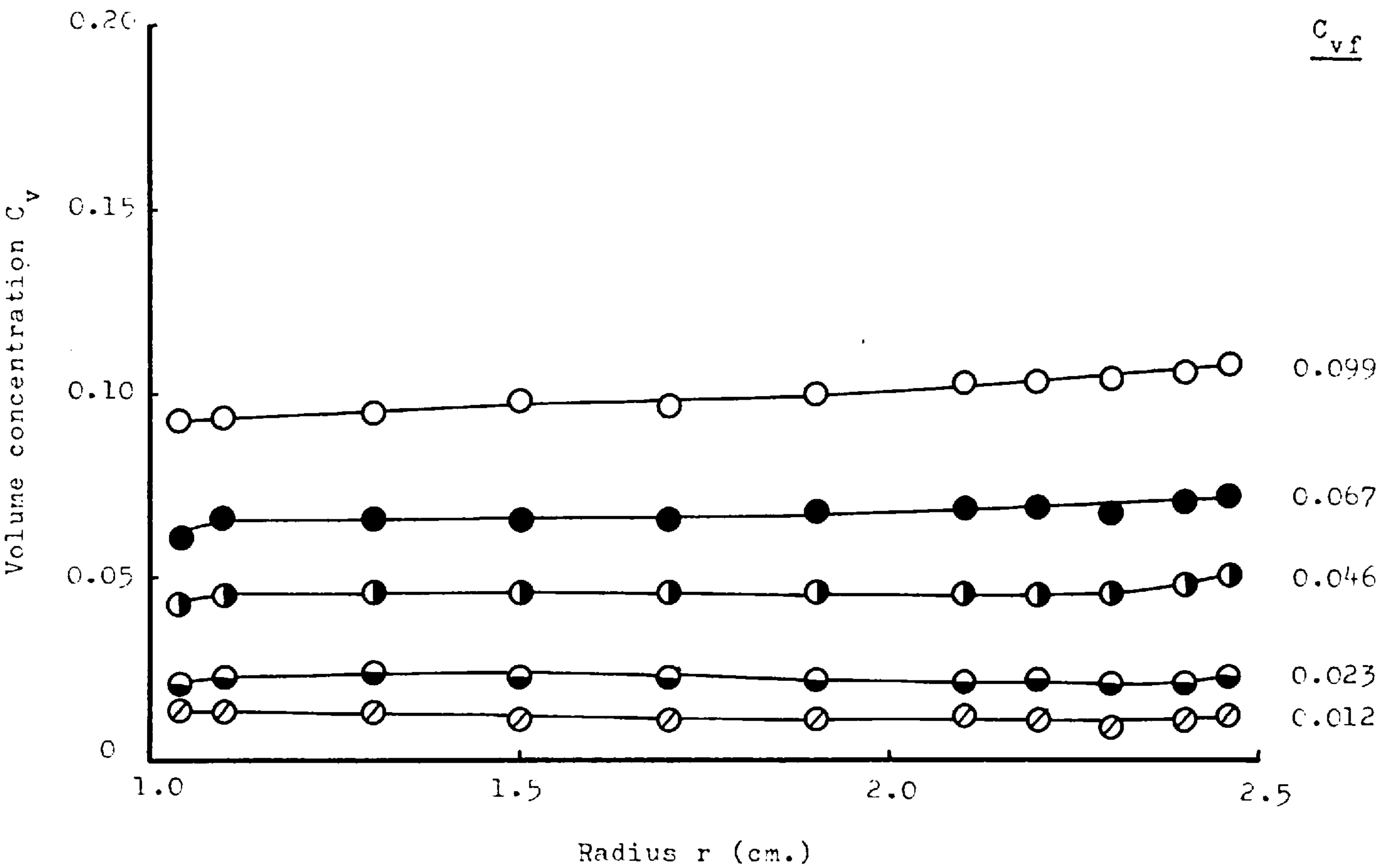

FIGURE B.5.7: Concentration profiles obtained with the Mark 7 cell using glass spheres: size fraction -200 +325 B.S.

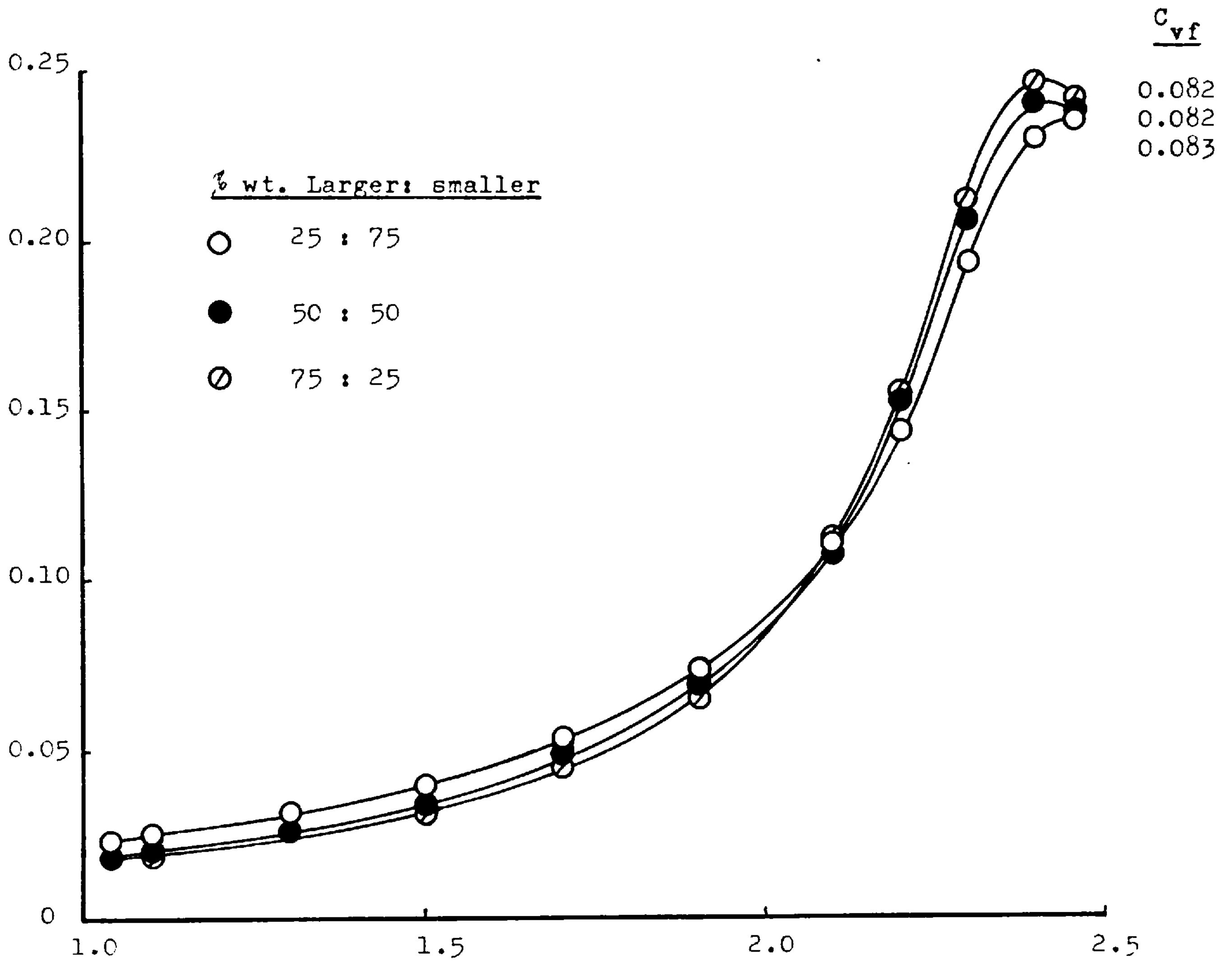

FIGURE B.5.8: Concentration profiles obtained with the Mark 7 cell using glass spheres: size fractions −52 +72/−72 +100

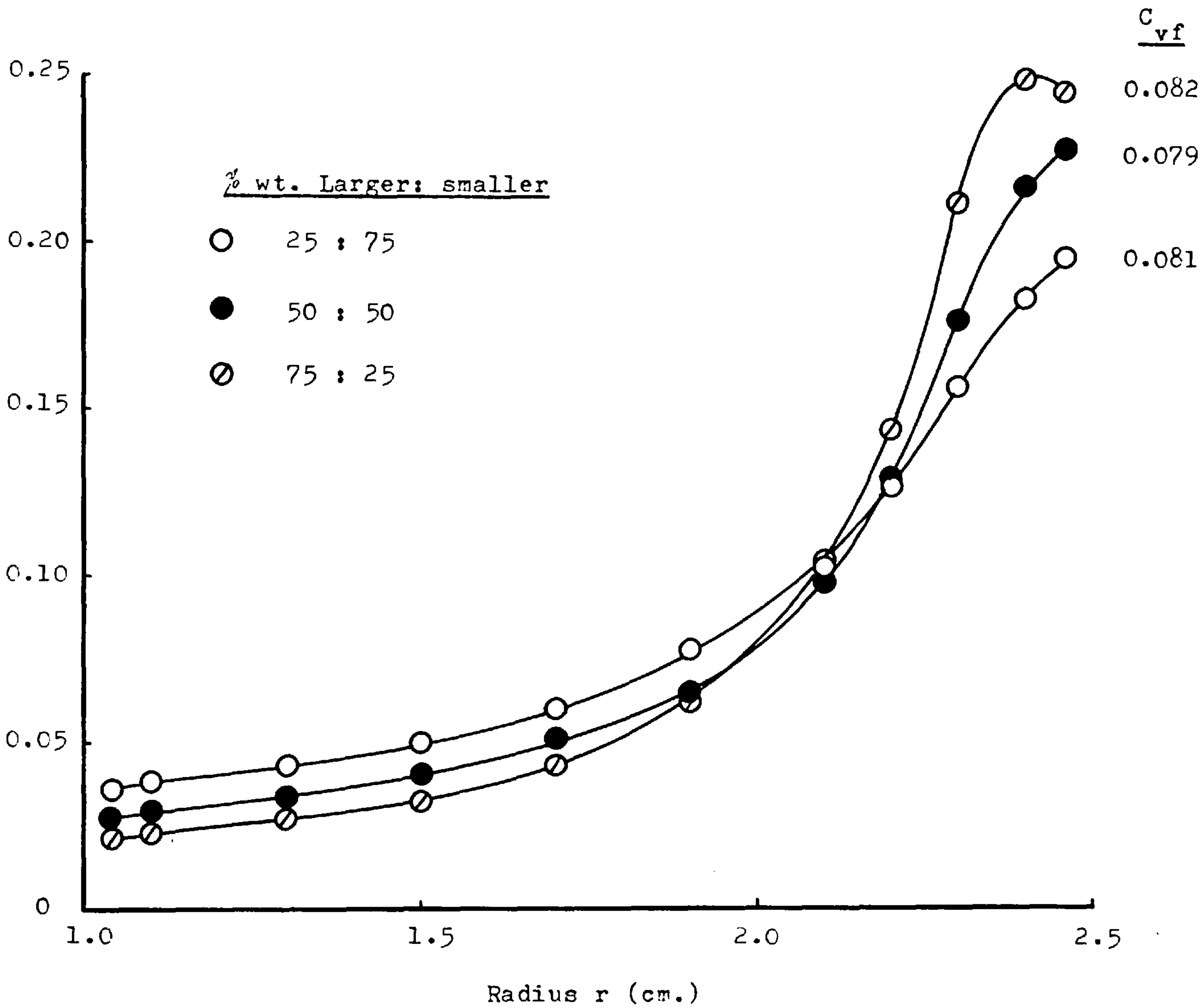

FIGURE B.5.9: Concentration profiles obtained with the Mark 7 cell using glass spheres: size fractions -52 +72/-100 +150

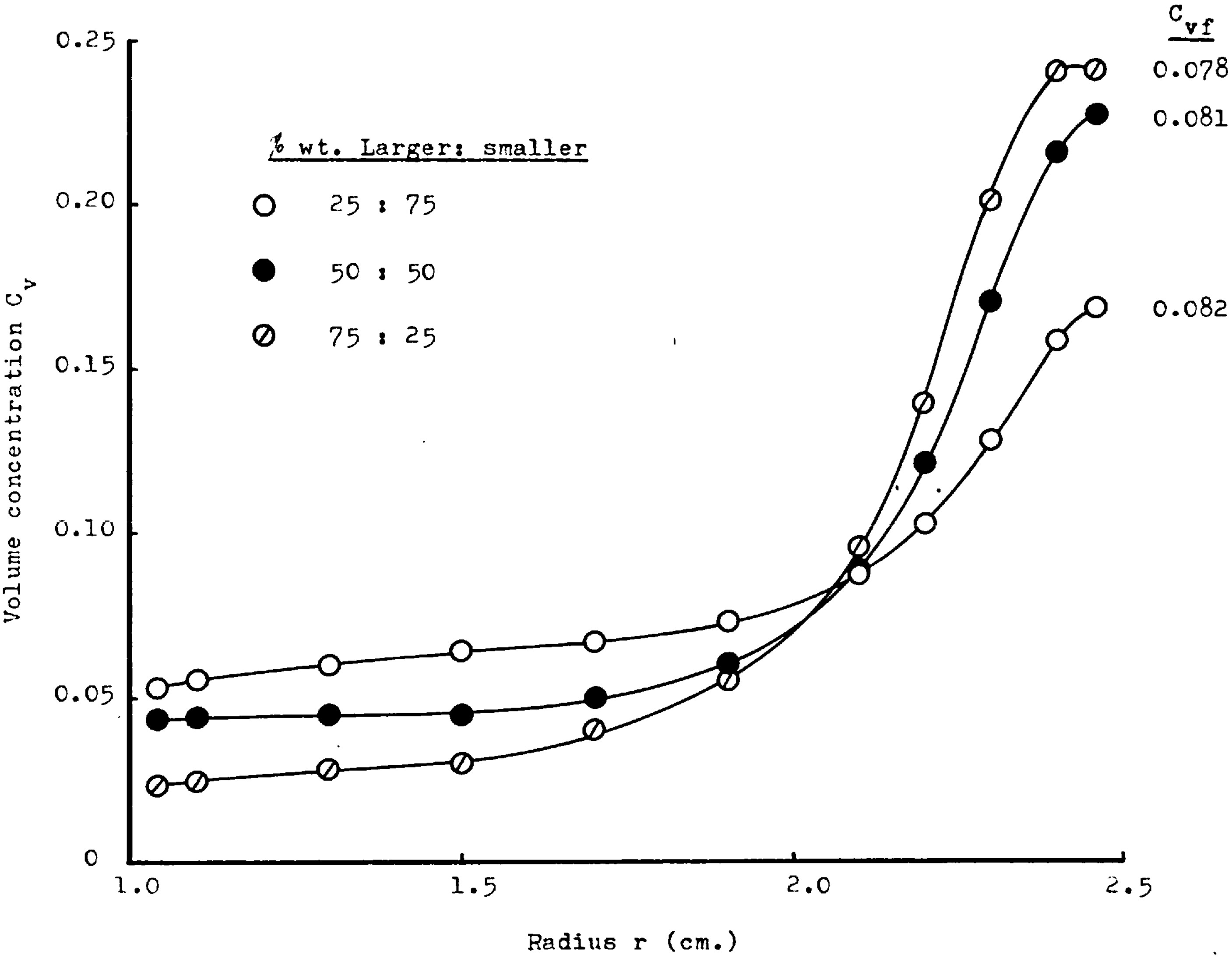

FIGURE B.5.10: Concentration profiles obtained with the Mark 7 cell using glass spheres: size fractions −52 +72/−150 +200

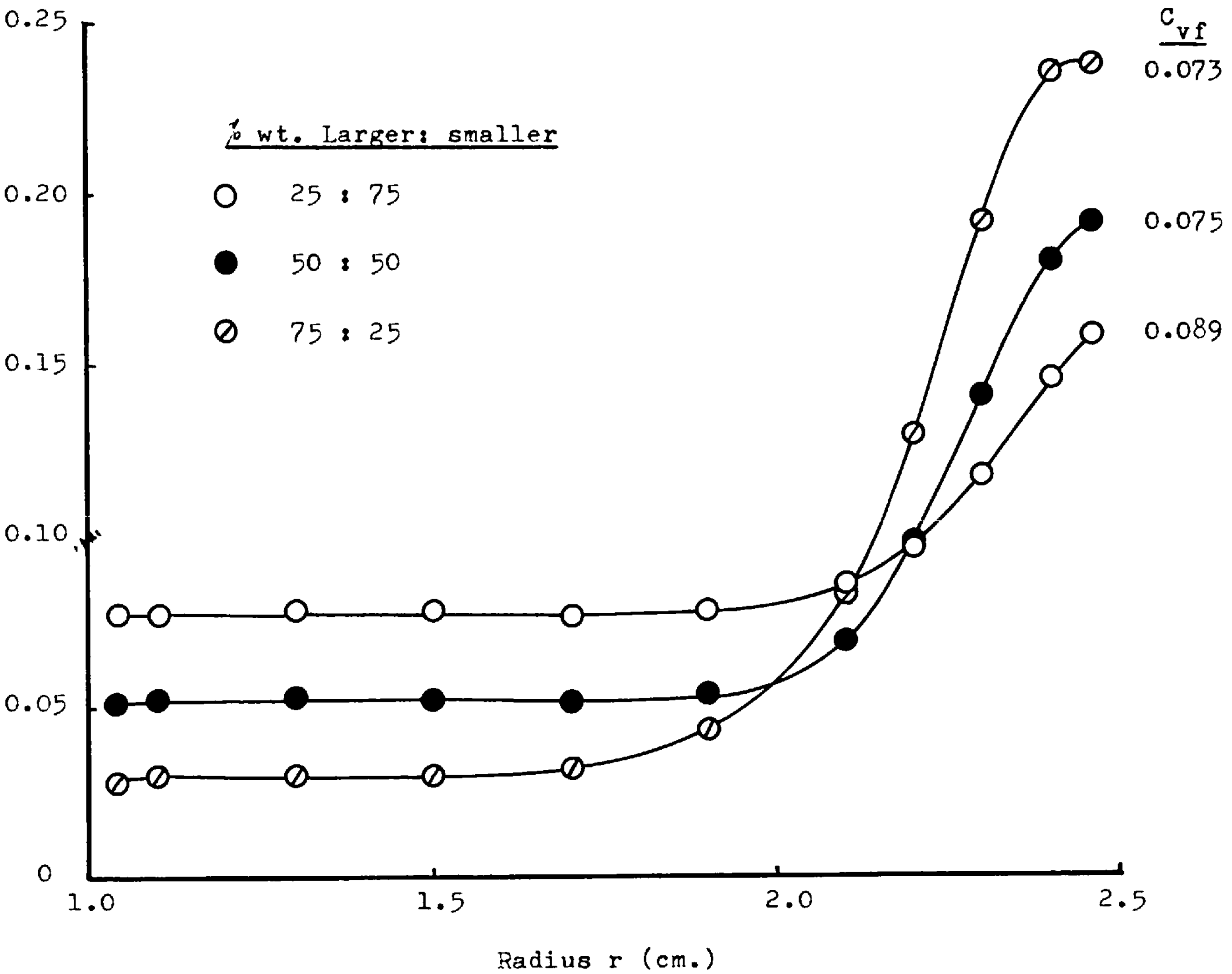

FIGURE B.5.11: Concentration profiles obtained with the Mark 7 cell using glass spheres: size fractions −52 +72/−200 +325

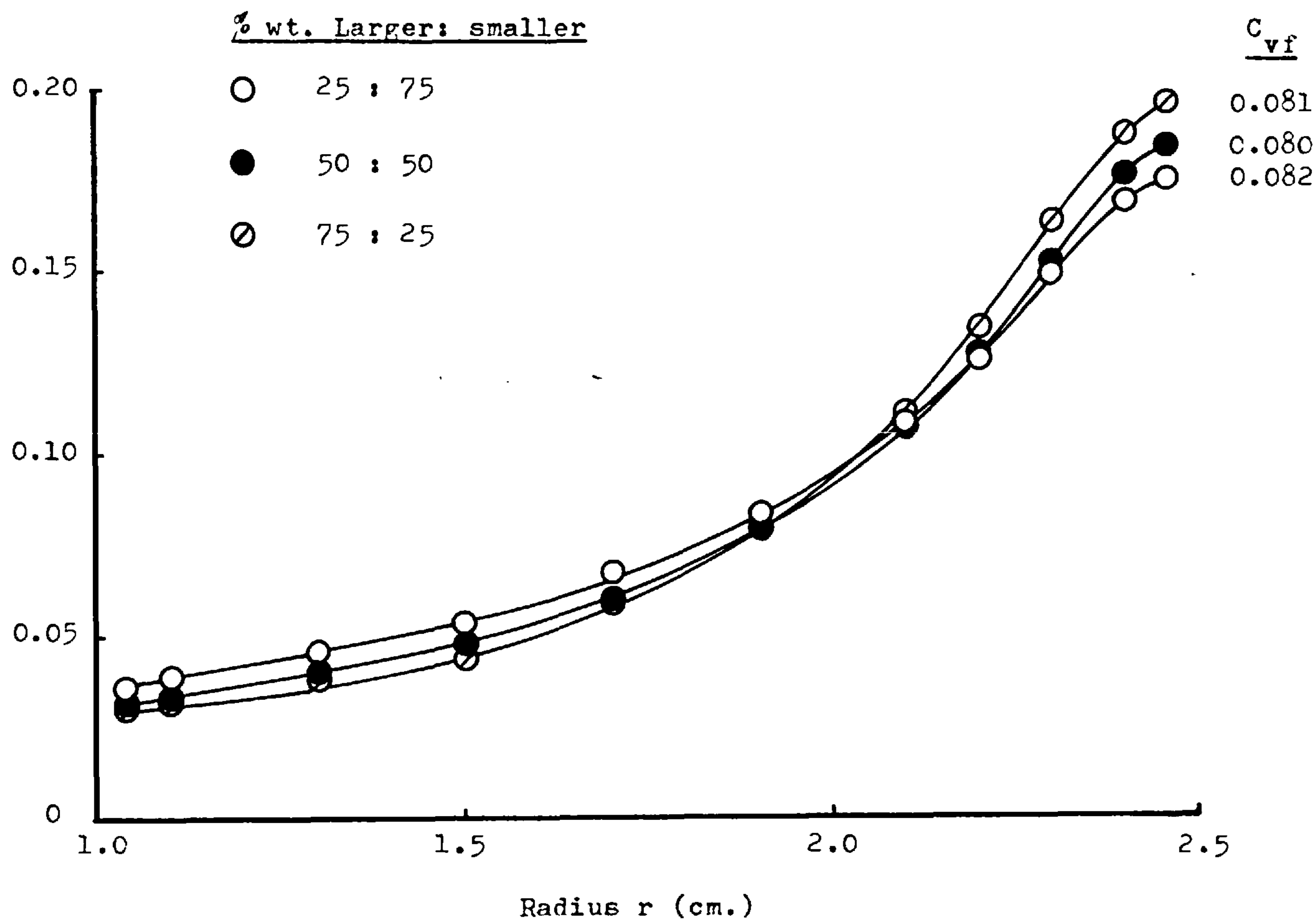

FIGURE B.5.12: Concentration profiles obtained with the Mark 7 cell using glass spheres: size fractions −72 +100/−100 +150

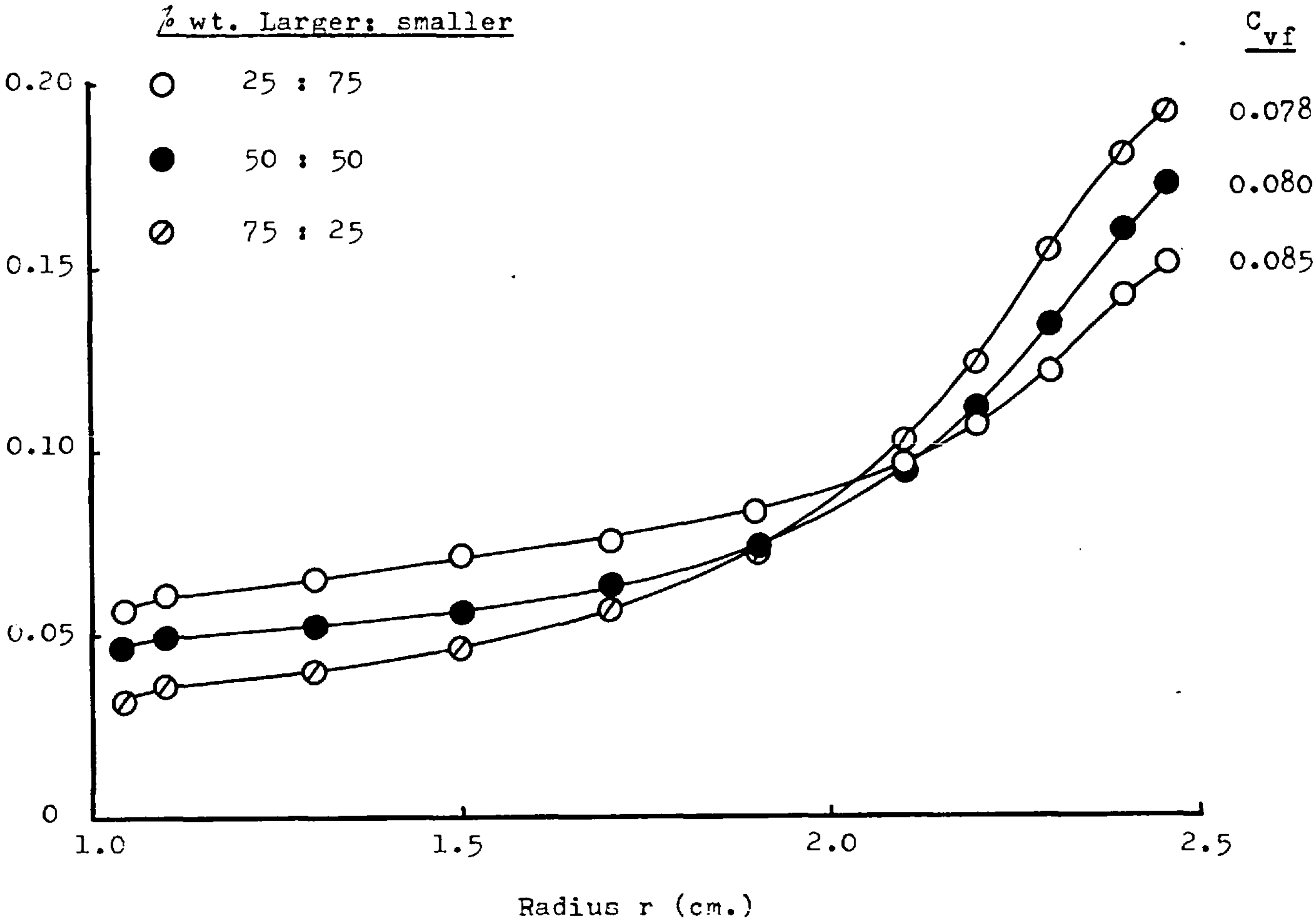

FIGURE B.5.13: Concentration profiles obtained with the Mark 7 cell using glass spheres: size fractions -72 +100/-150 +200

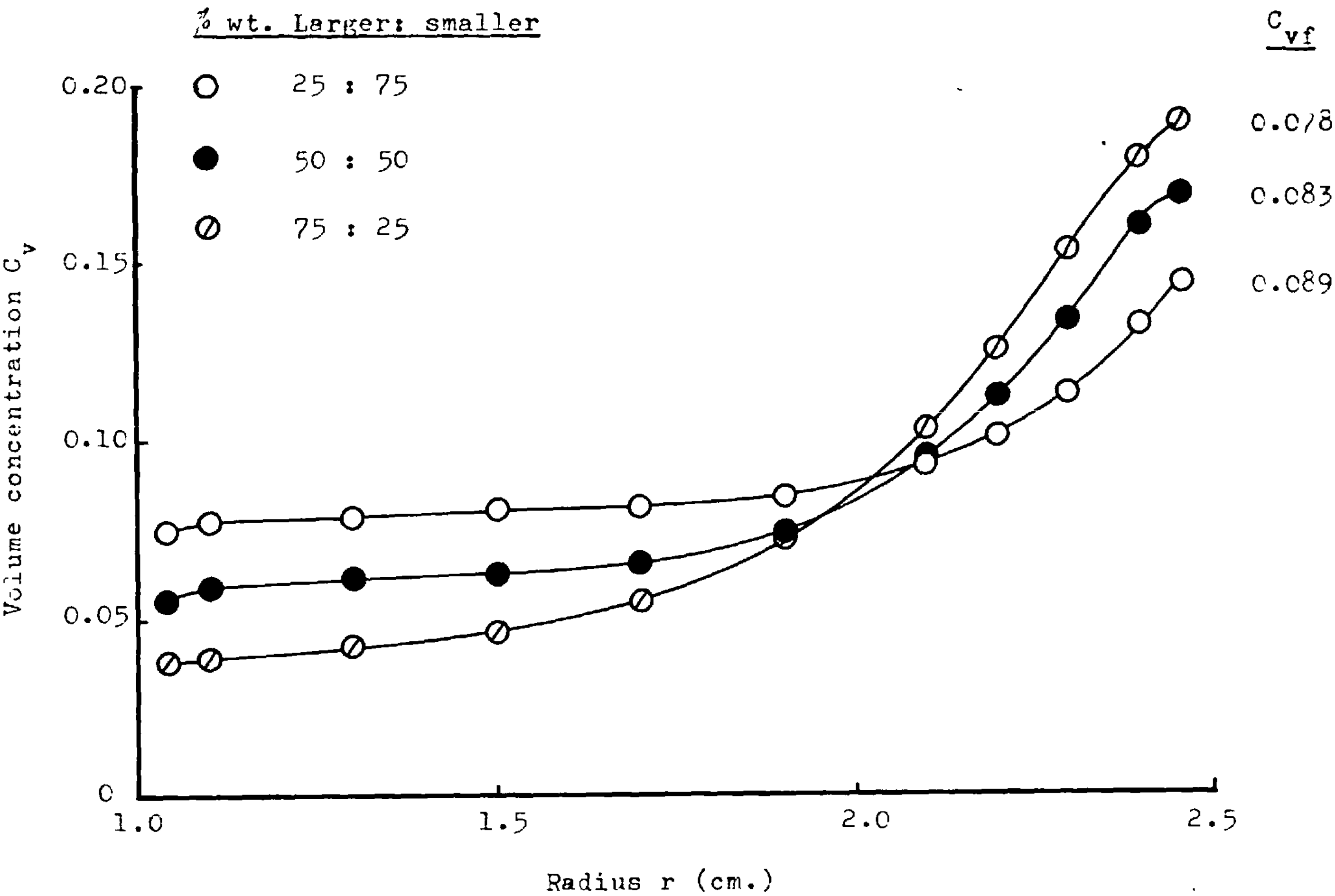

FIGURE B.5.14: Concentration profiles obtained with the Mark 7 cell using glass spheres: size fractions -72 +100/-200 +325

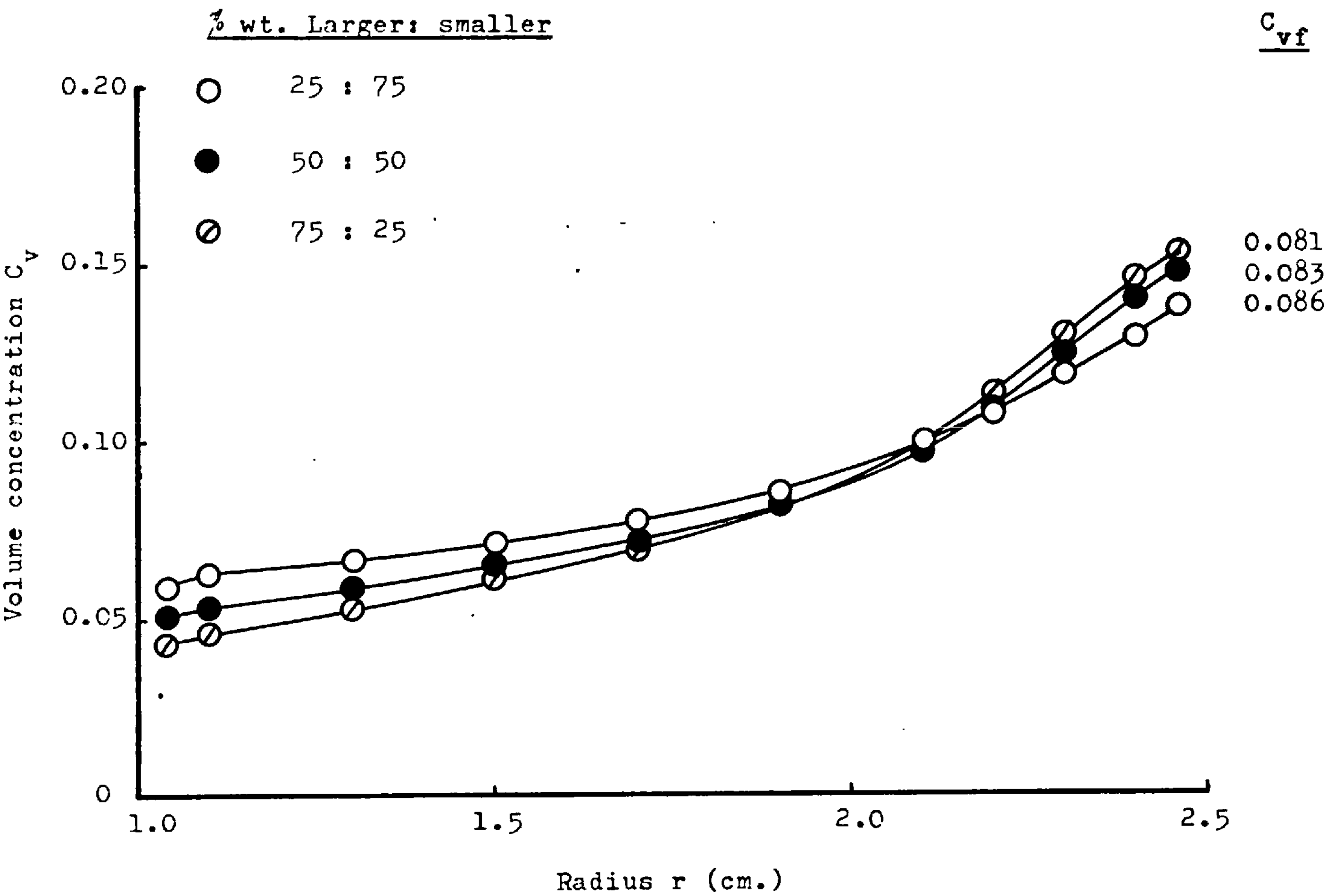

FIGURE B.5.15: Concentration profiles obtained with the Mark 7 cell using glass spheres: size fractions -100 +150/-150 +200

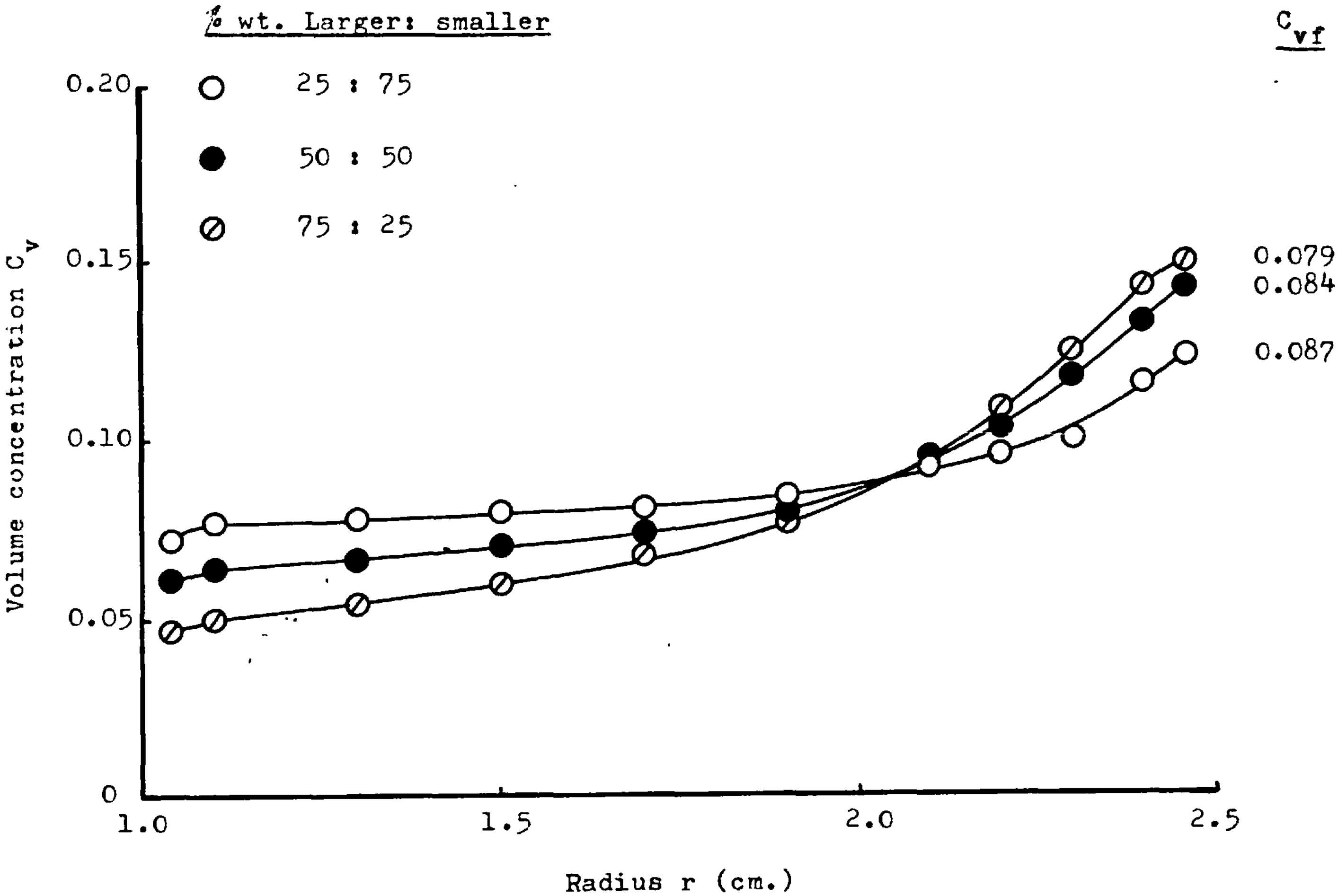

FIGURE B.5.16: Concentration profiles obtained with the Mark 7 cell using glass spheres: size fractions −100 +150/−200 +325

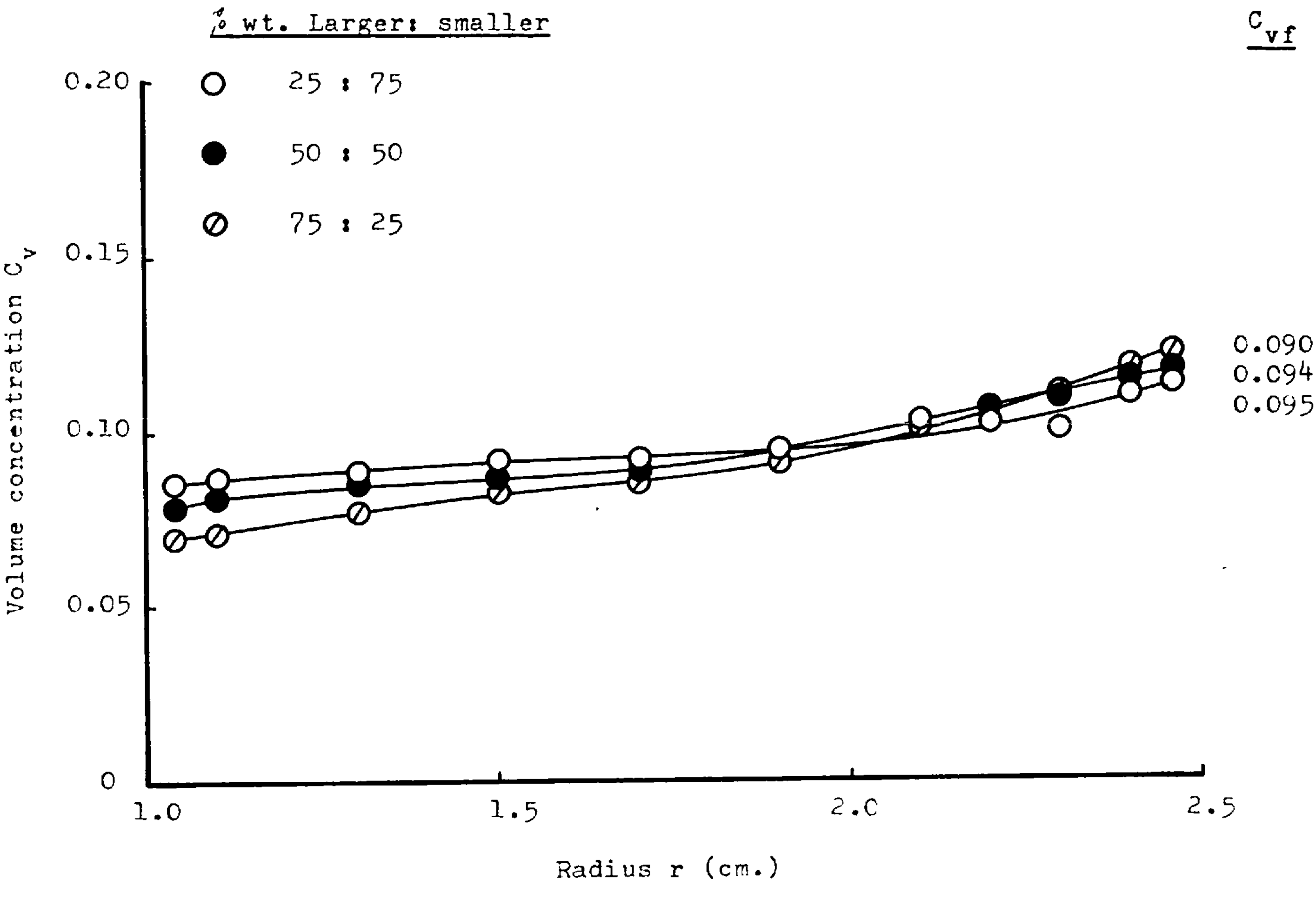

FIGURE B.5.17: Concentration profiles obtained with the Mark 7 cell using glass spheres: size fractions -150 +200/-200 +325

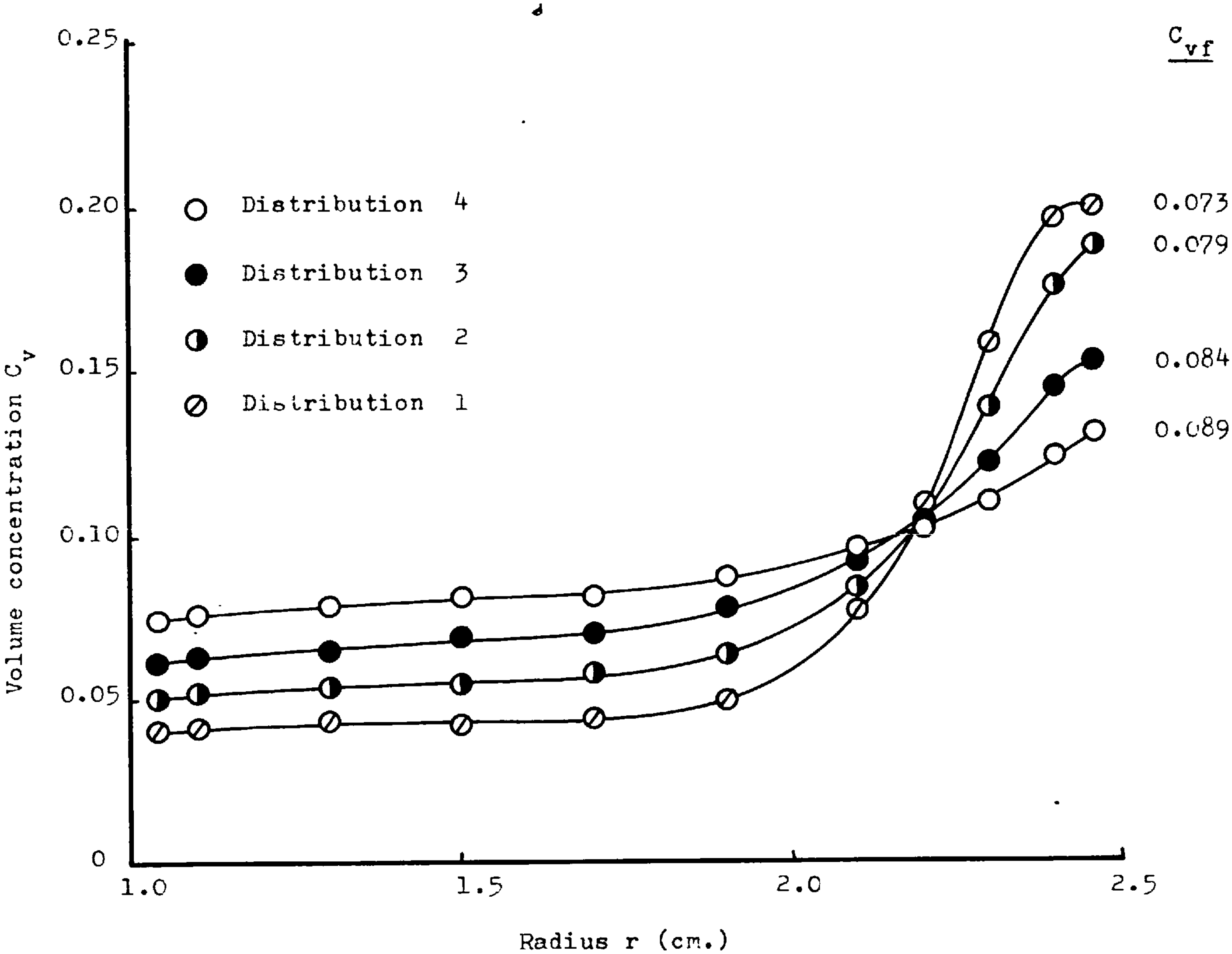

FIGURE B.5.18: Concentration profiles obtained with the Mark 7 cell using glass spheres: size distributions 1, 2, 3, 4.

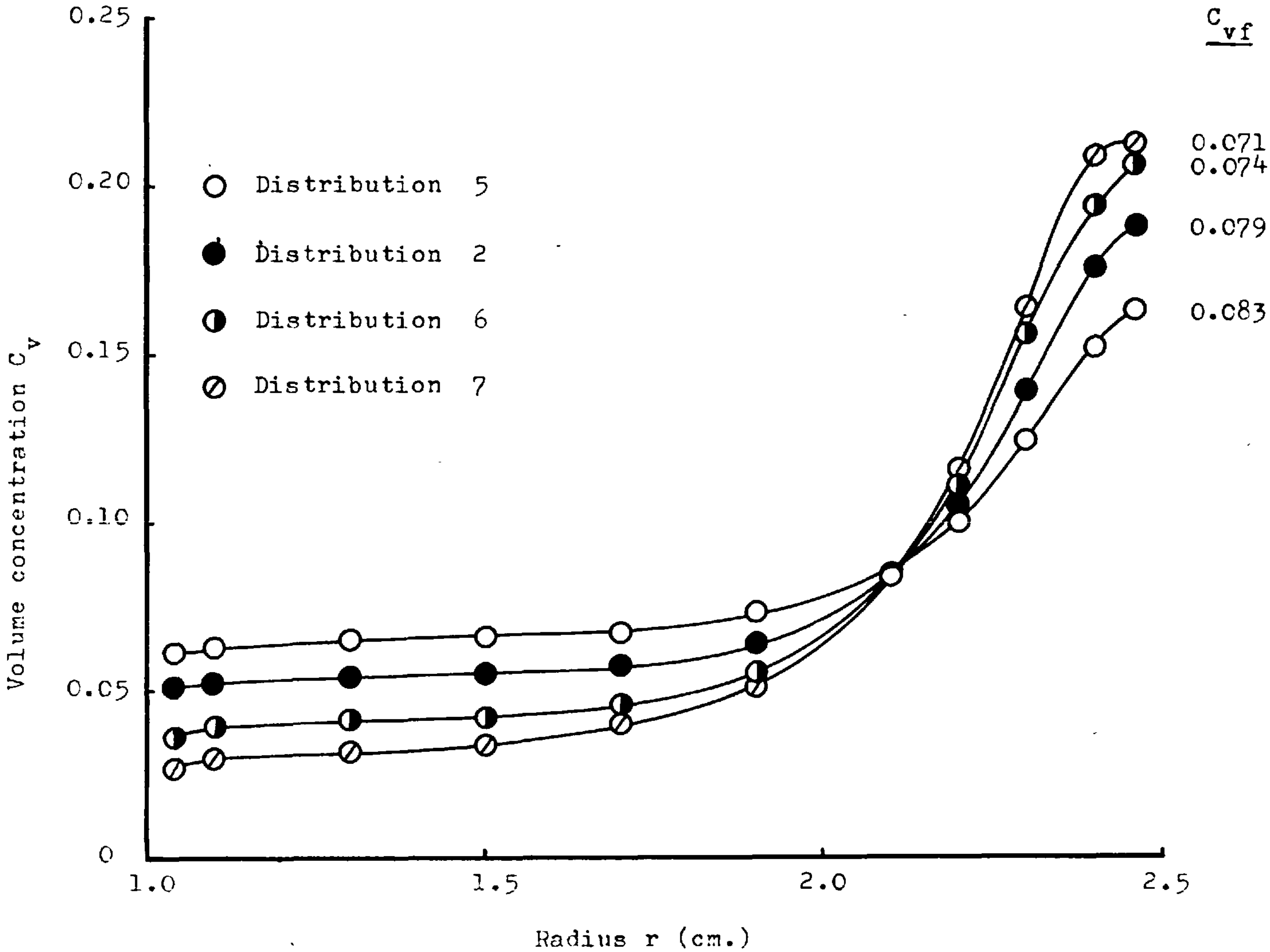

FIGURE B.5.19: Concentration profiles obtained with the Mark 7 cell using glass spheres: size distributions 2, 5, 6, 7.

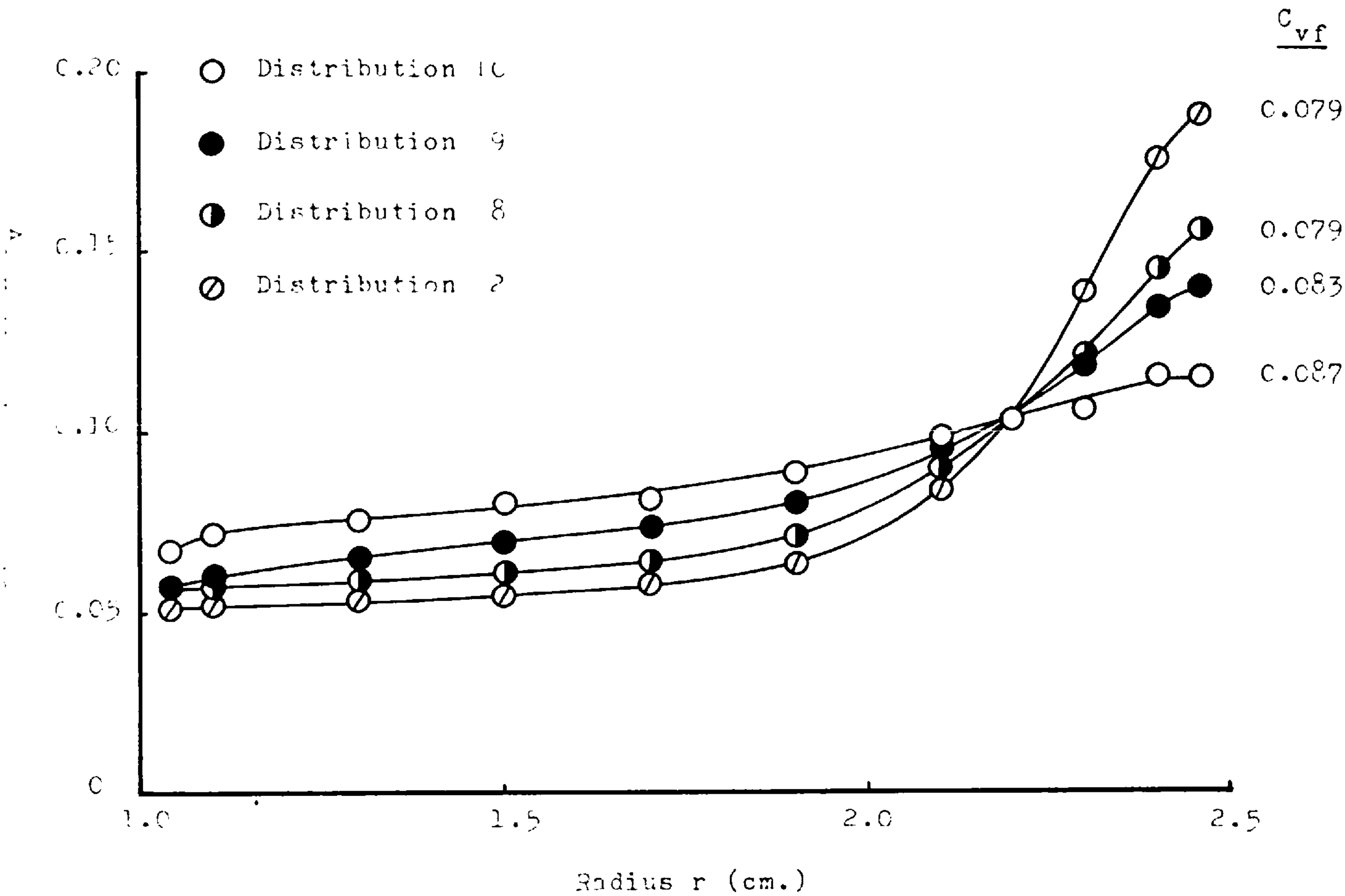

FIGURE B.5.20: Concentration profiles obtained with the Mark 7 cell using glass spheres: size distributions 2, 8, 9, 10.

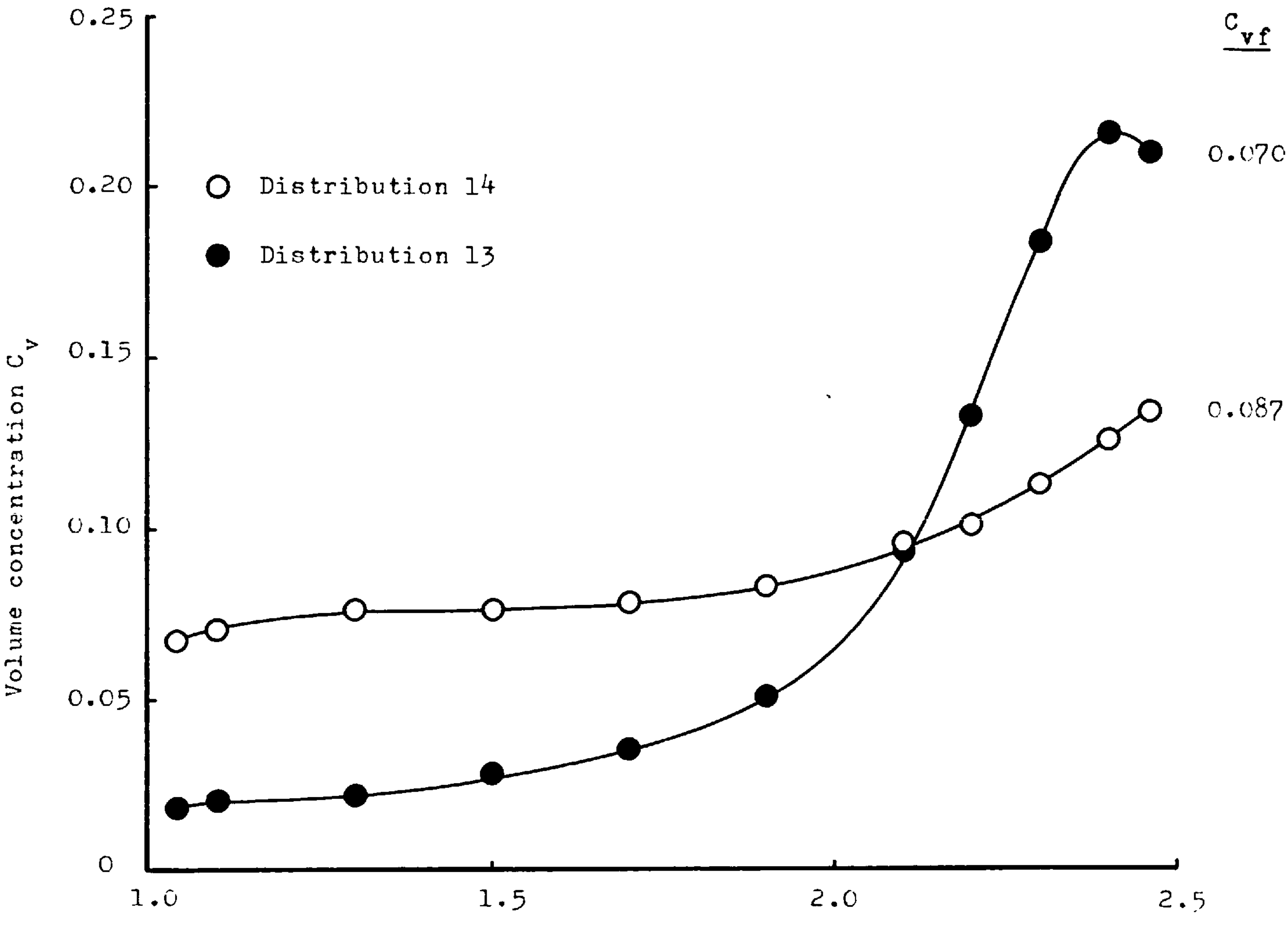

FIGURE B.5.21: Concentration profiles obtained with the Mark 7 cell using glass spheres: size distributions 13, 14.

while near the outer wall both the concentrations and the concentration gradients are high. In view of the high radial velocities obtainable with such coarse particles, the existance of any particles at all in the inner region is surprising, and their presence can only be accounted for in terms of secondary fluid flow, enhanced fluid drag, or boundary layer separation. The secondary fluid flow could act both within and downstream of the helix; in the first instance by reducing or even reversing the particle radial velocities in the zone where the fluid flow is towards the inner wall and, in the second instance, by destroying the concentration gradient when it has passed out of the helix. A reduction or reversal of the particle motion within the helix could only occur if the bulk of the particles was distributed within one of the layers in which the secondary fluid flow was towards the inner wall; the most likely one being that next to the bottom face of the channel, since gravitational forces would tend to concentrate the coarser particles within this layer. Enhanced fluid drag due to turbulence within the fluid is quite likely to occur (section 4.1.2b) though the effects should be less noticeable for the coarser particles. Boundary layer separation would create a region of high turbulence near the inner wall causing a disruption of the tangential flow and a reduction in the particle radial velocities. With the results in their present form, it is not possible to analyse the extent to which these mechanisms might be responsible for the observed effects. This task is performed in Section B.5.3.1.

Another interesting feature of the profiles, obtained at the higher feed concentrations with both -52 +72 and

-72 +100 mesh glass balls, is the peak particle concentration recorded at an equivalent radius of motion of 2.4cm. This could be the result of a high concentration layer at the outer wall, originally created within the helix and subsequently dispersing and moving back towards the centre of the channel. If this is the explanation, however, the profiles obtained at lower feed concentrations should exhibit similar maxima on a reduced scale. Since they do not, it appears much more likely that the mechanism responsible is the particle shearing pressure discussed in Section 4.1.2.c. For a particle size of 235μ travelling at 200cm/sec in a velocity gradient of 500sec^{-1}, it was estimated that the turbulent particle shearing force could equal the centrifugal force at a radius of motion of 2.5cm if the volume concentration of solids rose to about 0.22. In the present instance, the peaks are obtained at a radius of motion of 2.4cm for the two coarsest size fractions whose mean sizes are 181μ and 253μ, the corresponding volume concentrations being 0.22 and 0.19. These results agree sufficiently well with the estimated conditions to suggest that this is indeed the mechanism giving rise to the concentration maxima and the lower concentrations between the maxima and the outer wall of the channel are the result of the shearing force equalling the centrifugal force at these lower concentrations by virtue of the higher velocity gradient near the channel wall.

The profiles obtained for the three finer size fractions show progressively less evidence of radial particle motion until, at -200 +325 mesh B.S, the particle concentration is virtually the same at all points across the channel.

The concentration profiles may also be used to check whether the effect of the concentration of surrounding particles on the radial velocity of a given particle is in agreement with the results obtained by previous workers (Section 3.1.2c). According to the equation quoted, i.e.

$$U = U_T(1 - C_V)^Q$$

if the concentration of particles in the feed to the helix is increased, the radial velocity of the particles should be reduced by a factor $(1-C_V)^Q$, where C_V is the local concentration of particles and Q is a function of the Reynolds number for the particle. For a given increase in the feed concentration of particles, the concentration observed at any particular radius after a radius of motion should therefore comprise a larger fraction of the original feed concentration in regions where C_V decreases with α.

In Figures B.5.22, B.5.23, the results obtained in the regions of maximum concentration change have been examined by plotting the concentrations recorded at r = 1.1cm, r = 2.4cm against the feed concentration for the fine size fractions tested. In the zone near the inner wall (r = 1.1cm, $C_V < C_{Vf}$), it can be seen that changes in feed concentration do not produce any significant change in the radial velocities, as the recorded concentrations for each particle size increase linearly with feed concentration. In the zone near the outer wall (r = 2.4cm, $C_V > C_{Vf}$), the expected type of behaviour does materialise. Increases in feed concentration reduce the radial velocities appreciably for all particle sizes coarser than 150 mesh B.S, as evidenced by the curved plots obtained for these particles.

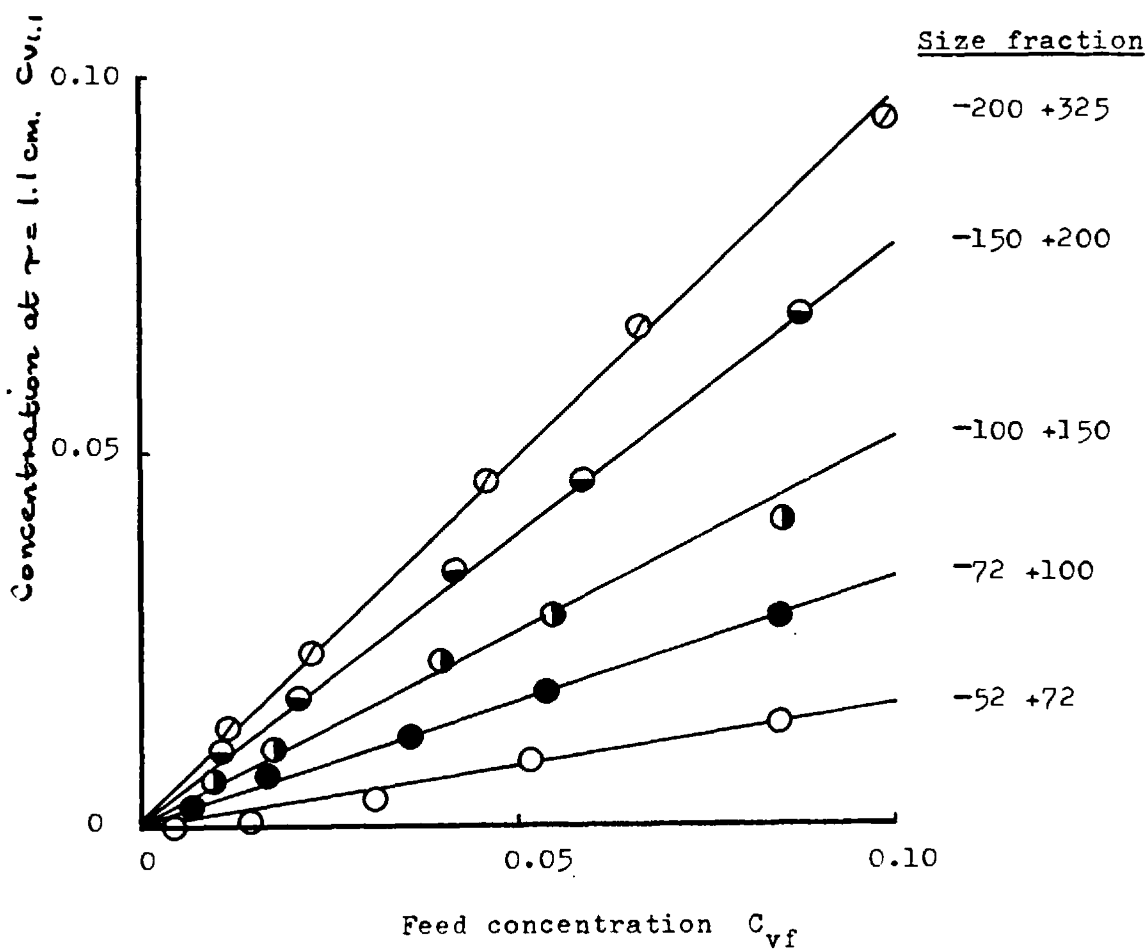

FIGURE B.5.22: Effect of feed concentration (r=1.1cm.)

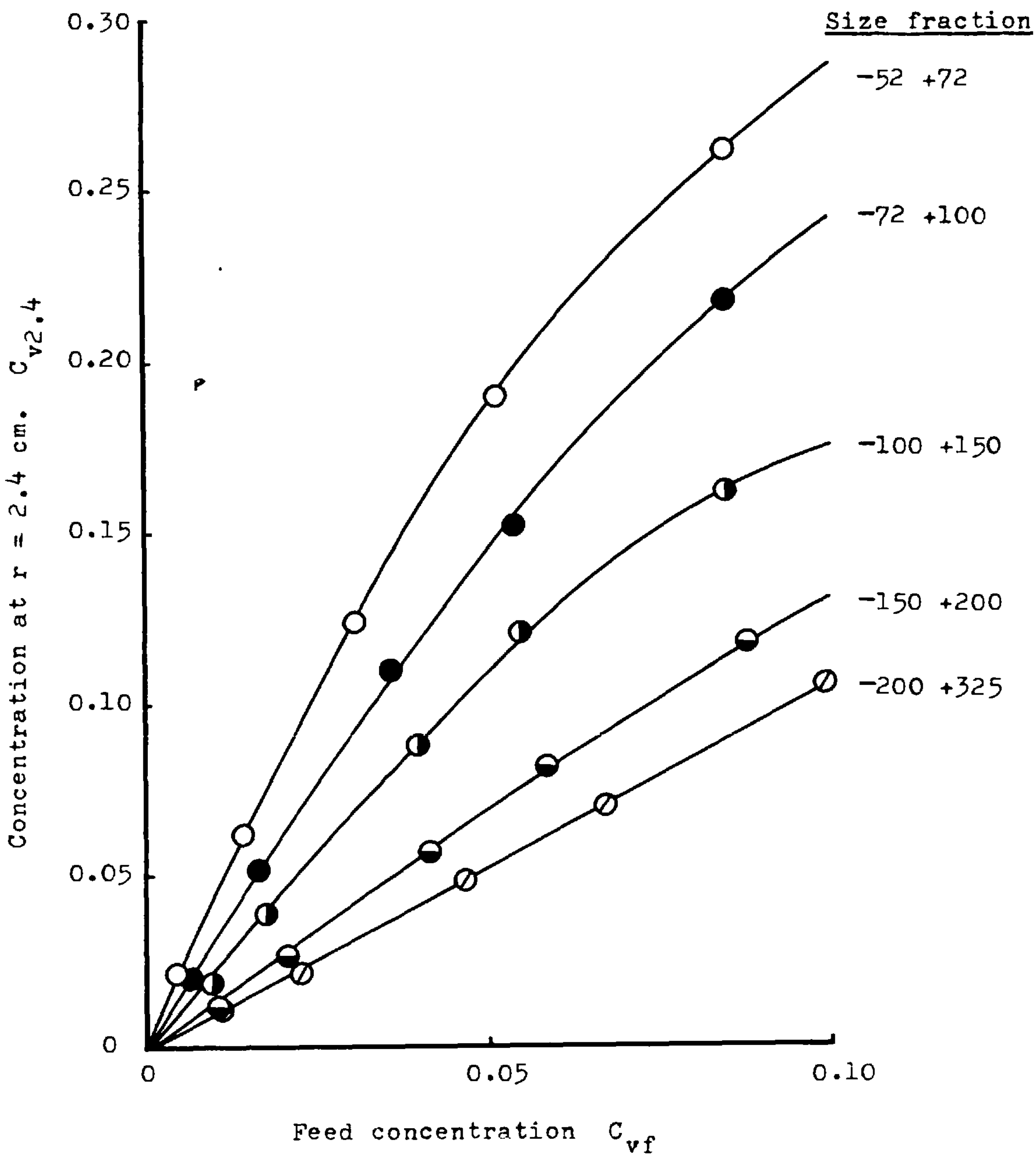

FIGURE B.5.23: Effect of feed concentration (r=2.4 cm.)

5.2.2 Two Size Fractions

Detectably different concentration profiles were obtained for all pairs of size fractions, and the relative positioning of the curves was correct in all cases. The coarsest sample of each pair of size fractions having -52 +72 mesh material as a component displayed a peak concentration similar to that found for these particles in the single size fraction. (Section 5.2.1)

In the previous section, the influence of the volume concentration of particles present on the radial velocities attained by the particles was examined for single size fractions. The main purpose in obtaining the results for pairs of size fractions was to find out whether or not particles of different size interacted with each other when present in varying proportions but at a constant total volume concentration in the feed and, if so, the manner in which the interaction varied with particle size.

The measurements made at r = 1.1cm and r = 2.4 cm. have again been used as the criteria in assessing the degree of interaction. The expected values of C_V for these two positions have been calculated for all samples at the measured feed concentration - assuming no interaction - by reading off the proportionate contributions from Figures B.5.22, B.5.23. The results are given in Table B.5.1 together with the measured values of C_V. Also shown is the % difference in the calculated (no interaction) and measured concentrations, calculated as

$$\%\ \text{Difference} = 100\ \left(\frac{\text{Measured - calculated}}{\text{calculated}}\right)$$

TABLE B.5.1.

Interaction between Size Fractions of Glass Spheres

Pairs of Size Fractions (U.S.Mesh)	Relative Propor-tions Coarse/Fine	C_{Vf}	$CV_{1.1}$ CALC.	$CV_{1.1}$ MEAS.	$CV_{1.1}$ % DIFF	$CV_{2.4}$ CALC.	$CV_{2.4}$ MEAS.	% DIFF
-52+72	25/75	0.0830	0.024	0.025	+4.2	0.227	0.229	+0.9
-72+100	50/50	0.0819	0.020	0.020	Ø	0.236	0.240	+1.7
	75/25	0.0817	0.017	0.019	+11.8	0.246	0.246	Ø
-52+72	25/75	0.0813	0.035	0.039	+11.4	0.184	0.182	-1.1
-100+150	50/50	0.0791	0.027	0.030	+11.1	0.205	0.216	+5.4
	75/25	0.0815	0.020	0.023	+15.0	0.233	0.248	+6.4
-52+72	25/75	0.0817	0.051	0.056	+9.8	0.148	0.158	+6.3
-150+200	50/50	0.0813	0.038	0.044	+15.8	0.184	0.216	+17.4
	75/25	0.0775	0.024	0.025	+4.2	0.229	0.240	+4.8
-52+72	25/75	0.0891	0.069	0.077	+11.6	0.138	0.145	+5.1
-200+325	50/50	0.0754	0.043	0.052	+20.9	0.163	0.180	+10.4
	75/25	0.0734	0.027	0.030	+11.1	0.201	0.236	+17.4
-72+100	25/75	0.0821	0.038	0.039	+2.6	0.173	0.168	-2.9
-100+150	50/50	0.0796	0.034	0.034	Ø	0.183	0.176	-3.8
	75/25	0.0806	0.030	0.033	+10.0	0.198	0.186	-6.1
-72+100	25/75	0.0853	0.057	0.061	+7.6	0.141	0.141	Ø
-150+200	50/50	0.0797	0.044	0.049	+11.4	0.159	0.159	Ø
	75/25	0.0781	0.035	0.036	+2.9	0.181	0.180	-0.6
-72+100	25/75	0.0893	0.073	0.077	+5.5	0.127	0.131	+3.2
-200+325	50/50	0.0833	0.054	0.059	+9.3	0.152	0.159	+4.6
	75/25	0.0783	0.039	0.039	Ø	0.176	0.178	+1.1
-100+150	25/75	0.0858	0.061	0.063	+4.9	0.127	0.129	+1.6
-150+200	50/50	0.0825	0.054	0.054	Ø	0.136	0.140	+2.9
	75/25	0.0809	0.047	0.046	-2.1	0.139	0.146	+5.0
-100+150	25/75	0.0868	0.074	0.077	+4.1	0.109	0.116	+6.4
-200+325	50/50	0.0844	0.063	0.064	+1.6	0.126	0.134	+6.3
	75/25	0.0793	0.050	0.050	Ø	0.139	0.143	+2.9
-150+200	25/75	0.0949	0.088	0.087	-1.1	0.106	0.110	+3.8
-200+325	50/50	0.0937	0.082	0.081	-1.2	0.111	0.115	+3.6
	75/25	0.0898	0.074	0.071	-4.1	0.114	0.118	+3.5

The differences recorded between the calculated and measured concentrations are generally small, the measured values being on average about 4-5% higher than the calculated. The % differences are smaller in the outer region, where the absolute concentrations are higher. This is contrary to expectation since, regardless of the nature of the interaction effects between different particle size groups, it is reasonable to expect a proportionately larger effect in regions of high particle concentration. This by itself throws doubt on the validity of the recorded differences, but the overiding argument in favour of discarding them is the fact that the recorded differences are, on average, positive in both the inner and outer regions. This apparent effect is readily refuted on simple mass transfer considerations since if the particle concentration is lower than predicted in the inner zone it must be higher than predicted in the outer zone. The greater part of the observed differences must therefore be attributed to experimental error, the likeliest cause being inaccurate estimates of the effective feed density (C_{Vf}).

Therefore it must be concluded that, within the limits of accuracy of the observations, no significant interaction takes place between different size fractions.

5.2.3 Size Distributions

The results obtained with size distributions of glass spheres are notable for the constancy of the particle concentrations across the inner region of the channel. If these curves are compared with the ones obtained for the same size distributions of quartz sand (Figures A.3.14 - A.3.17), it can be seen that a measurable concentration gradient was recorded in the inner zone for the latter material. The results obtained for the quartz sand must be treated with reserve, however, since the concentration measurements were less reliable, the flowrate control was unsatisfactory and the made-up size distributions differed considerably from their nominal composition in several cases. (Section A.3.5.2)

The results obtained with two size fractions suggested that no significant interactions occurred between different size fractions, within the limits of detection of the present equipment. This conclusion was checked for the size distribution results by calculating the expected values of C_V for positions r = 1.1, r = 2.4cm. in the same manner employed earlier. The results are given in Table B.5.2.

TABLE B.5.2.

Interaction within Size Distributions of Glass Spheres

SIZE DISTRIBUTION NUMBER	C_{Vf}	$C_{V_{1.1}}$			$C_{V_{2.4}}$		
		CALC.	MEAS.	% DIFF.	CALC.	MEAS.	% DIFF
1	0.0733	0.043	0.041	- 4.7	0.203	0.196	-3.4
2	0.0793	0.050	0.052	+ 4.0	0.183	0.176	-3.8
3	0.0841	0.063	0.063	Ø	0.147	0.145	-1.4
4	0.0894	0.085	0.076	-10.6	0.124	0.124	Ø
5	0.0828	0.059	0.063	+ 6.8	0.165	0.152	-7.9
6	0.0743	0.038	0.039	+ 2.6	0.204	0.194	-4.9
7	0.0711	0.030	0.030	Ø	0.215	0.209	-2.8
8	0.0792	0.056	0.057	+ 1.8	0.150	0.145	-3.3
9	0.0829	0.063	0.060	- 4.8	0.135	0.134	-0.7
10	0.0870	0.075	0.072	- 4.0	0.108	0.115	+6.5
13	0.0703	0.025	0.020	-20.0	0.230	0.216	-6.1
14	0.0867	0.070	0.070	Ø	0.129	0.126	-2.3

Although the results for r = 2.4cm show a more consistent tendency than those found with two size fractions, one observation markedly contradicts the general tendency, and, in any case, the results at r = 1.1cm display a completely random variation. The conclusion that these is no measurable interaction between different particle sizes, therefore, remains unchanged.

5.3 Concentration Variation Near the Inner and Outer Walls

A general analysis of the relationship between the volume concentration and the velocities of the particles in a suspension moving through a helical turn was given in Section 4.3.2, where the continuity equation for the particles was derived. For steady state conditions within the helix, it was shown that

$$\frac{\partial(rUC_V)}{\partial r} + \frac{\partial(VC_V)}{\partial \alpha} = 0 \quad \ldots \quad \ldots \qquad (4.30)$$

In order to obtain some kind of quantitative model as a basis for assessing the particle behaviour in the regions of interest - the zones near the channel walls - it is necessary to simplify equation 4.30 by making suitable assumptions that can be justified by the experimental evidence.

5.3.1. Concentration Variation near the Inner Wall

Most of the concentration profiles obtained with glass spheres display low or even non-existant radial concentration gradients in the zone near the inner wall, a tendency that is particularly noticeable in all the results obtained with full size distributions. (Figures B.5.18 - B.5.21). Since the volume concentration of particles is constant at all positions across the inlet to the helix and appears to have remained independent of r (or nearly so) in the region adjacent to the inner wall, the most obvious simplification to equation 4.30 is to consider C_V as a function of α only.

If the behaviour exhibited by pure fluids (Figure B.2.3) is taken as a guide to what might occur with a suspension, it would appear that the tangential velocity V does not vary to any great extent with α. Also, it should be possible to approximate the velocity distribution by a simple linear model for the region of interest. i.e.

$$V = V_1 + br \quad \ldots \quad \ldots \quad \ldots \quad \ldots \qquad (5.1)$$

where V_1 is the velocity at the inner wall and b is the velocity gradient normal to the wall.

The two major factors determining U are the tangential velocity V and the volume concentration C_V. Since V is considered independent of α and C_V starts at the feed concentration (C_{Vf}) and decreases, it should be possible to treat U as being independent of α and C_V without introducing major errors (Also, see section 5.2.1.)

Taking C_V as a function of α and U as a function of r, equations 4.30 and 5.1 may be combined to give

$$C_V . \frac{d(rU)}{dr} + (V_1 + br) \frac{dC_V}{d\alpha} = 0 \quad \ldots \quad \ldots \qquad (5.2)$$

Integrating with respect to α between the limits C_{Vf} at α=0 and C_V at α gives

$$\ln\left(\frac{C_{Vf}}{C_V} \right) = \frac{\alpha}{(V_1+br)} \frac{d(rU)}{dr} \quad \ldots \quad \ldots \quad \ldots \qquad (5.3)$$

which may be integrated with respect to r between U_1 at r_1 and U_2 at r_2 to give

$$U_2r_2-U_1r_1 = \frac{1}{\alpha}\ \ln\left(\frac{C_{Vf}}{C_V}\right) \left[V_1(r_2-r_1) + \frac{b}{2}\ (r_2{}^2- r_1{}^2)\right]\ \ldots \quad (5.4)$$

As equation 5.4 is only intended to represent the behaviour in one region of the helix, it only has to satisfy the conditions for that region. These were discussed in Section 4.3.2 and the relevant conditions were given in equations 4.32, 4.33: i.e. $C_V=C_{Vf}$ (constant) for all values of r at $\alpha = 0$ and $UC_V = 0$ for all values of α at $r = 1.0$cm. The first condition was applied when integrating equation (5.2), while the second may be applied by putting $r_1=1.0$cm, $U_1=0$ in equation 5.4

$$U_2 = \frac{1}{\alpha}\ln\left(\frac{C_{Vf}}{C_V}\right) \quad \left[V_1\left(1- \frac{1}{r_2}\right) +\frac{b}{2}\left(r_2- \frac{1}{r_2}\right)\right] \qquad \ldots \qquad (5.5)$$

The calibration measurements were made with the centre line of the source at a position on the leadout from the helix equivalent to $r_2 = 1.1$cm. From Figure B.2.3., reasonable values for the tangential velocity equation are estimated as $V_1 = 100$cm/sec and $b = 66.7\text{sec}^{-1}$ for $\bar{V} = 200$cm/sec. Putting these values in equation 5.5 gives for the velocity at $r = 1.1$cm:

$$U_{1.1} \simeq 2.5\ln\left(\frac{C_{Vf}}{C_V}\right) \qquad \ldots \quad \ldots \quad \ldots \qquad (5.6)$$

The radial velocity has been calculated for each size fraction of glass balls using equation (5.6). A feed concentration of $C_{Vf} = 0.085$ was chosen and the appropriate values of C_V were interpolated from Figure B.5.22.

These 'measured values of U have been compared with a set of 'apparent terminal velocities' calculated for the same conditions. Unfortunately, the motion of all the sizes concerned fell within the transitional regime, so the equations developed earlier for the laminar and turbulent regimes (Sections 3.2.1 - 2) could not be used. The velocities were therefore calculated according to the method of Heywood[11] using the arithmetic mean size of each fraction and then corrected for interference effects using equation 3.18 and the data given in Table B.3.1. The measured and calculated velocities are compared in Table B.5.3.

TABLE B.5.3.			
Radial Velocities of Size Fractions of Glass Balls at r = 1.1cm.			
SIZE FRACTION		CALCULATED U_{TER} (cm/sec)	MEASURED U (cm/sec)
B.S.mesh	Mean Aperture (μ)		
- 52+72	253	11.1	4.5
- 72+100	181	7.4	2.8
-100+150	129	4.7	1.6
-150+200	89	2.8	0.63
-200+325	61	1.5	0.06

The measured values of U are substantially lower than the calculated values. There are a number of factors that could be responsible: they are listed below and then discussed in more detail.

(a) Use of the arithmetic mean size in calculations;

(b) Use of apparent terminal velocity in calculations;

(c) Incorrect assumptions regarding the axial velocity profile;

(d) Degeneration of the concentration profile;

(e) Reduction of the measured velocities by secondary fluid flows;

(f) Disruption of the particle motion by boundary layer separation;

(g) Inaccurate concentration measurements due to solids settling out in the circuit during the test runs;

(h) Lift forces or 'Magnus' Effects;

(i) Enhanced fluid drag due to the turbulent axial flow of fluid.

(a) Use of the arithmetic mean size during the calculations was dictated by the lack of knowledge about the behaviour of particles in the transitional regime. What is really required is a mean velocity for the range of sizes present in the size fraction concerned, but this can only be obtained where the dependence of velocity on size is fully identified. The relationships holding within the various regimes are as follows:

$$\begin{array}{lll} \text{Laminar:} & U \propto D^2 & \\ \text{Transitional} & U \propto D^{\bar{n}} & (\bar{n} = \tfrac{1}{2} \rightarrow 2) \\ \text{Turbulent:} & U \propto D^{\frac{1}{2}} & \end{array}$$

The sizes corresponding to the mean velocity for the size fraction $-D_1 +D_2$ would therefore be calculated as

$$\text{Laminar:} \quad \bar{D} = \frac{\Sigma i D^2}{\Sigma i}$$

$$\text{Transitional} \quad \bar{D} = \frac{\Sigma i D^{\bar{n}}}{\Sigma i}$$

$$\text{Turbulent} \quad \bar{D} = \frac{\Sigma i D^{\frac{1}{2}}}{\Sigma i}$$

where i = number of particles of size D.

Since the value of $\bar{n}$ is unknown, the arithmetic mean based on $\bar{n} = 1$ was used in the calculations. The order of error introduced by this assumption can be calculated: assuming size fractions spaced at $\sqrt{2}$ intervals and a uniform distribution of sizes within each size fraction, the maximum error introduced by adopting the arithmetic mean size for the fraction $-\sqrt{2}$ D+D is $\pm$ 0.5%

$$\text{i.e.} \quad \frac{\bar{D}}{D} = 1.206 \pm 0.006 \quad \ldots \quad \ldots \qquad (5.7)$$

The mean size of 253μ calculated for the -52 +72 mesh material could therefore be in error by $\pm$ 1.3μ. Since the screens used in sizing the material were probably only accurate to within 5μ and other sources of inaccuracy contributed much larger errors, this effect can be neglected.

(b) The 'apparent terminal velocity' is obtained by neglecting any relative tangential velocity between particle and fluid and arbitrarily putting $\frac{dU}{dt}=0$ in the equations of motion (3.15a,3.19). The errors introduced in calculating particle tracks are likely to be small for particles exhibiting laminar motion (Section 3.2.1) but may be large for those exhibiting turbulent motion (Section 3.2.2). Since the apparent terminal velocity neglects the initial acceleration period, it must represent an overestimate of the actual velocity. Another consideration relevant to this point was discussed earlier (Section 4.1.2b), namely whether particles could experience ideal forms of fluid drag when moving radially in a fluid medium that is exhibiting turbulent flow in a tangential direction. It seems most unlikely that the finer particles could experience viscous drag in a turbulent fluid, though the coarser particles might concievably encounter an enhanced form of turbulent drag. In general, the vortices present in the fluid must result in an increased resistance to motion for all particle sizes, possibly to the extent of almost totally preventing motion of the smaller particles. It would appear, therefore, that the apparent terminal velocity represents a considerable overestimate of the actual velocity, since it not only neglects the acceleration period but also fails to take fluid turbulence into account. A further effect - the 'Magnus' or lift force - is also ignored in obtaining the apparent terminal velocity, but this is considered separately.

(c) The values assumed for the axial velocities were used in determining both the calculated and measured particle radial velocities. In the transitional region, the apparent terminal velocity, U_{TER}, varies with V^2 at low Reynolds numbers, changing progressively to V at high Reynolds numbers as turbulent behaviour is approached. As the measured velocity U varies (approximately) with V, inaccuracies in the assumed values of V will only affect the finer sizes. The relative differences recorded are largest for the finer sizes, so over estimates of V could be partially responsible for these. However, they do not explain the differences recorded at the coarser sizes.

(d) Degeneration of the concentration profile in the interval between the slurry leaving the helix and entering the measurement zone was discussed in Section 5.5. It was concluded that a significant proportion of the concentration gradient might be lost in this way, and this could contribute noticeably to the difference between the calculated and observed particle velocities, especially for the finer sizes. This has been investigated as follows: the centre of the measuring zone was some five equivalent channel diameters downstream of the exit from the helix and, by analogy with pure fluid behaviour, the helix may be considered to exert an influence as far as 50 equivalent diameters downstream. Assuming a linear rate of remixing of the concentration gradient, this suggests that about 10% of the actual concentration could have been lost by remixing. Applying this correction to equation 5.6:-

$$U \simeq 2.5 \ln\left(\frac{1.1 C_{Vf}}{C_V}\right) \quad \ldots \quad \ldots \qquad (5.8)$$

$$U \simeq 2.5 \ln\left(\frac{C_{Vf}}{C_V}\right) + 0.24 \quad \ldots \qquad (5.9)$$

so that a 10% increase in C_V could reduce the measured value of U by about 0.24cm/sec. This would account for only a small proportion of the difference recorded for the -200 +325 mesh particles and would have no effect on the large differences recorded for the coarse sizes. To account for all the difference at -200 +325 mesh, 75% of the concentration reduction would have to be lost by remixing, while the differences recorded at -150 +200 mesh and above would require correction factors suggesting that >100% of the concentration reduction had been lost. This effect can therefore not be held responsible for the differences recorded in Table B.5.3.

(c) The probable effects of secondary fluid flow of the recirculatory type were discussed in section 4.1.2c and 5.2.1. It seems unlikely that this type of flow would affect the overall motion of the particles unless they were preferentially concentrated in the bottom layer of the channel by gravitational forces. If this effect did occur, however, the velocities of all sizes of particles should be reduced by about the same absolute amount. In fact, the discrepancies vary from 6.6cm/sec. at 253μ down to about 1.5cm./sec. at 61μ, which suggests that secondary fluid flow is not a significant factor.

It is probable that secondary flow provides the main agency for remixing the solids in the region immediately downstream of the helix, but this effect has already been considered.

(f) Separation of the boundary layer would lead to an increase in turbulence near the inner wall and a reduction in the axial or tangential velocity. The consequences of over estimating V have already been discussed and it was concluded that this could only be responsible for differences found with fine particles whose behaviour approached laminar conditions. However, the likelihood of boundary layer separation is difficult to assess even for a pure fluid, since it depends on the aspect ratio of the channel. (Section B.2.3). With appreciable concentrations of particles present, it is at present not possible to estimate whether separation is likely ot occur or how great an effect separation might produce if it did take place.

(g) Substantial losses of material were recorded during most runs conducted using size fractions coarser than 200 mesh B.S. It was inferred that the losses all occurred when the material was initially placed in suspension, since no consistent reduction in the readings at any given position was recorded during the runs and sequential scans conducted on the same samples showed little change. (Section A.4.1.4.) In any case a reduction in the amount of solids in suspension would lead to a lower value of C_V and hence an over estimate of the measured value of U, so this effect cannot be held responsible for the observed effects.

(h) The lift force was discussed in Section B.3.1.1. It was not taken into account in the analysis which followed or in the equation used to calculate the (theoretical) apparent terminal velocity. Since the concentration measurements made at r=1.1cm. were in close proximity to the channel wall, it is likely that a high radial velocity gradient existed within the fluid. The lift force created as a result of this would tend to increase the axial velocity of the particle in question, as illustrated in Figure B.5.24(a), and this would lead in turn to an increase in the radial velocity of the particle. Neglect of the lift force in the calculated values of U shown in Table B.5.3 will, therefore, have led to under estimates of U. As the differences recorded are in the opposite sense, this cannot have contributed to them.

(i) Calculations of the apparent terminal velocities for laminar or turbulent conditions assume that the corresponding ideal types of fluid drag are operative. It is assumed in the derivation of these drag forces that any fluid flow or turbulence present is associated entirely with the relative motion between particles and fluid. In the sizer helix, however, the suspension is flowing axially at a high Reynolds number and must in consequence exhibit a considerable amount of turbulence in addition to and independent of that generated by the particle motion. This inherent fluid turbulence must enhance the drag forces opposing particle motion, possibly, in the case of fine particles that would normally be subject only to viscous drag, to the extent of preventing any effective radial motion. 'Enhanced' drag of this type could well be a major cause of the low recorded velocities.

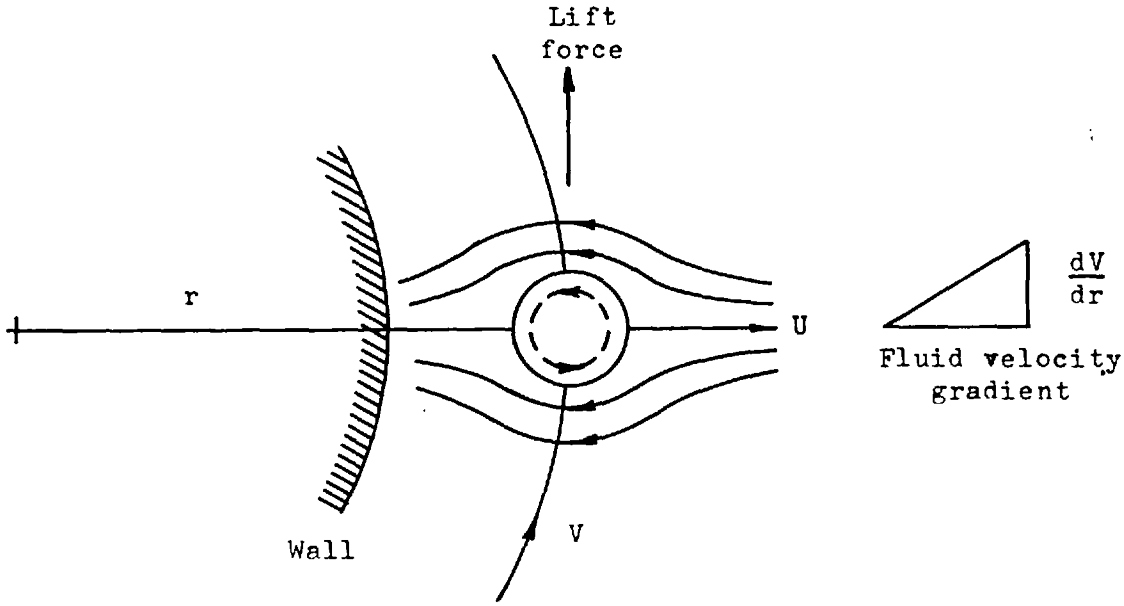

(a) Lift force on particles near the inner wall.

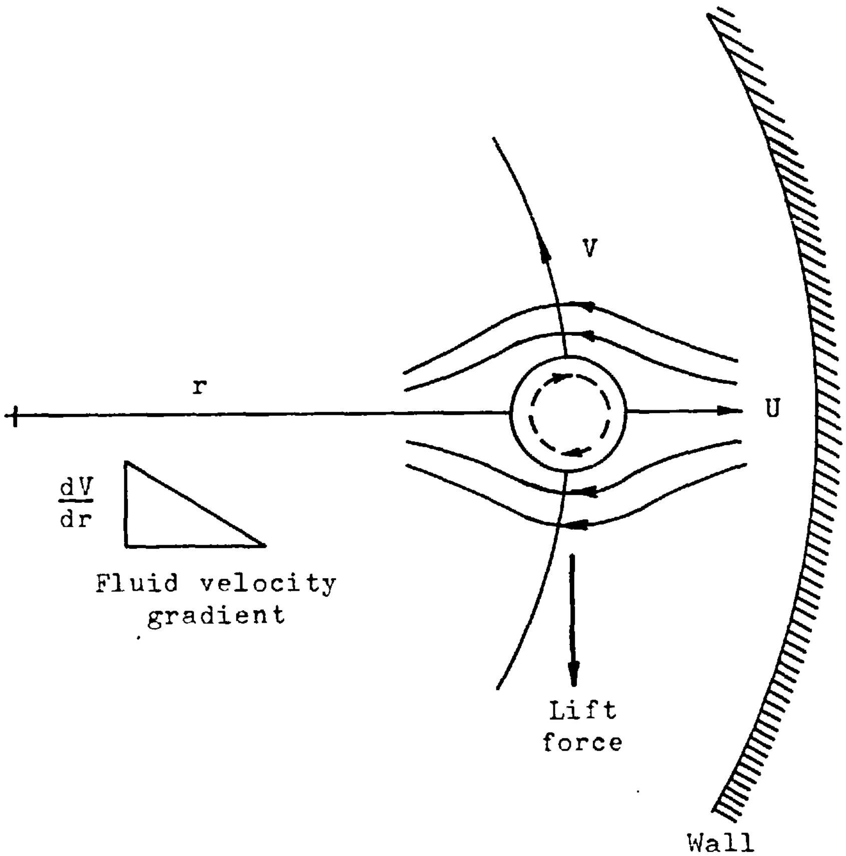

(b) Lift force on particles near the outer wall.

FIGURE B.5.24

5.3.2 Concentration Variation Near the Outer Wall

The particle concentrations rise above the feed concentration in the zone adjacent to the outer wall of the channel, so that the assumption employed in the treatment of the zone near the inner wall - namely that the particle radial velocity U could be considered independent of C_V - becomes untenable. Also, the tangential velocity V may be expected to change noticeably with α (Figure B.2.3) in the region near the outer wall. Since C_V and V are the factors which determine U, it is obvious that any realistic analysis of the behaviour near the outer wall must take account of the fact that U will vary with C_V and V and, therefore, with r and α also.

For steady state conditions within the helix, the continuity equation which must be satisfied has been derived:

$$\frac{\partial(rUC_V)}{\partial r} + \frac{\partial(VC_V)}{\partial \alpha} = 0 \quad \ldots \qquad (4.30)$$

In order to attempt a formal solution of equation 4.30, the relationships between U, V, C_V, r and α must be known in full. This information is not available as yet, and, in any case, the nature of the functions is likely to be such that numerical methods of solution would be required.

The most urgent requirement for practical purposes is some means of estimating the particle velocities under the conditions described above. If it is accepted that the radial motion of particles in a pure fluid environment (C_V = 0) is represented with sufficient accuracy by the apparent terminal velocity (Section B.3.2.3), then the main ways in which this velocity is affected by particle concentration are through interference effects (Section B.3.1.2.c) and particle shearing forces (Section B.4.1.2.d). In combination, these factors are likely to result in marked reductions in the radial velocity of the particles in the zone immediately adjacent to the outer wall where both the concentration of particles and the fluid velocity gradient are high. Over a restricted performance range, it seems reasonable to suppose that the expected behaviour could be described by a simpler relationship than would be apparent from examination of the individual equations. (3.18, 3.29, 4.15, 4.26).

For example, if the radial flux of particles is considered to be constant in this region:

$$UC_V = \varepsilon_k \text{ (Constant)} \quad \ldots \quad \ldots \qquad (5.10)$$

or

$$U = \frac{\varepsilon_k}{C_V} \quad \ldots \quad \ldots \qquad (5.11)$$

Equation 5.11 implies that any increase in C_V causes a direct and proportionate reduction in U. The form of this equation is such that it can only hold over a limited range, since it implies that U becomes infinitely large as C_V approaches zero. Also it assumes that U is independent of V and varies only with r and a because C_V varies with them. This last assumption is not unreasonable, however, since the examples of particle motion calculated earlier (Section B.3) for the case V = constant showed that the dependence of U on r becomes much less marked for r > 2cm. (Figures B.3.6, B.3.9.) In practice V is likely to increase with r (Figure B.2.3) and the variation in U may well be almost non-existant or even in the opposite sense to that shown.) The over-riding argument in this case, however, is that other factors such as the 'interference' and 'Bagnold' effects are likely to control U to such an extent that the dependency of U on r and V is negligable in comparison.

If the continuity equation (4.30) is rederived on the basis that the radial flux ($\mathcal{E}_r$) is constant (i.e. independent of r or α) it states

$$\frac{\partial \mathcal{E}_\alpha}{\partial \alpha} = \mathcal{E}_r \quad \ldots \quad \ldots \quad \ldots \qquad (5.12)$$

On integration and resubstitution for $\mathcal{E}_\alpha$ and $\mathcal{E}_r$ equation 5.12 gives

$$U = \frac{1}{\alpha} (V - V_f \cdot \frac{C_{Vf}}{C_V}) \quad \ldots \quad \ldots \qquad (5.13)$$

The quantities V_f, C_{Vf}, refer to the inlet and V, C_V to the outlet conditions in the helix.

To be acceptable, equation 5.13 must satisfy the conditions stated in equation 4.32, 4.33, i.e. $C_V = C_{Vf}$ (constant for all r) at $\alpha = 0$, and $\mathcal{E}_r = 0$ at r = 2.5cm. for all α. It meets the first but not the second of these conditions: $\mathcal{E}_r$ cannot be zero at r = 2.5cm. as it has been defined as constant for all values of r. In present form, therefore, equation 5.13 would over estimate the radial velocity U at any given radius.

It is possible to devise an approximate model that will satisfy both conditions. The approach is based on dividing the region into two parts: one immediately adjacent to the channel wall which acts as a reservoir and in which the concentration of particles is considered to be constant and an inner part, in which the motion of the particles is governed by the constant flux behaviour already described. The transfer of particles from the constant flux region into the wall reservoir is considered to take place at a velocity dictated by the constant flux equation and the concentration within the reservoir. This model is illustrated in Figure B.5.25.

Consider the flux of particles entering and leaving the reservoir:

Let ε'_r = Radial flux of particles crossing shaded interface along radius at α. ($\varepsilon'_r = UC_V'$, independent of r and α).

C_V' = Concentration within reservoir along radius at α.

V' = Tangential velocity within reservoir, assumed independent of r in this region . (i.e. V' is a function of α only. This assumption is not unreasonable, as the tangential component of the Bagnold shear force must tend to reduce the velocity gradient $(\frac{\partial V}{\partial r})$ in this region.)

ε'_α = Tangential flux of particles entering reservoir ($\varepsilon'_\alpha = V'C_V'$, a function of α).

For steady state conditions within the reservoir:

$$\varepsilon'_r . r_1 \delta\alpha + \varepsilon'_\alpha (r_2 - r_1) = (\varepsilon'_\alpha + \delta\varepsilon'_\alpha)(r_2 - r_1)$$

$$\therefore \left(\frac{r_1}{r_2 - r_1} \right) \varepsilon'_r = \frac{\delta\varepsilon'_\alpha}{\delta\alpha}$$

Taking limits as $\delta\alpha \to 0$

$$\frac{d\varepsilon'_\alpha}{d\alpha} = \left(\frac{r_1}{r_2 - r_1}\right) \varepsilon'_r \quad \ldots \quad \ldots \quad \ldots \qquad (5.14)$$

Integrating between 0 and α and substituting for ε'_α, ε'_r:

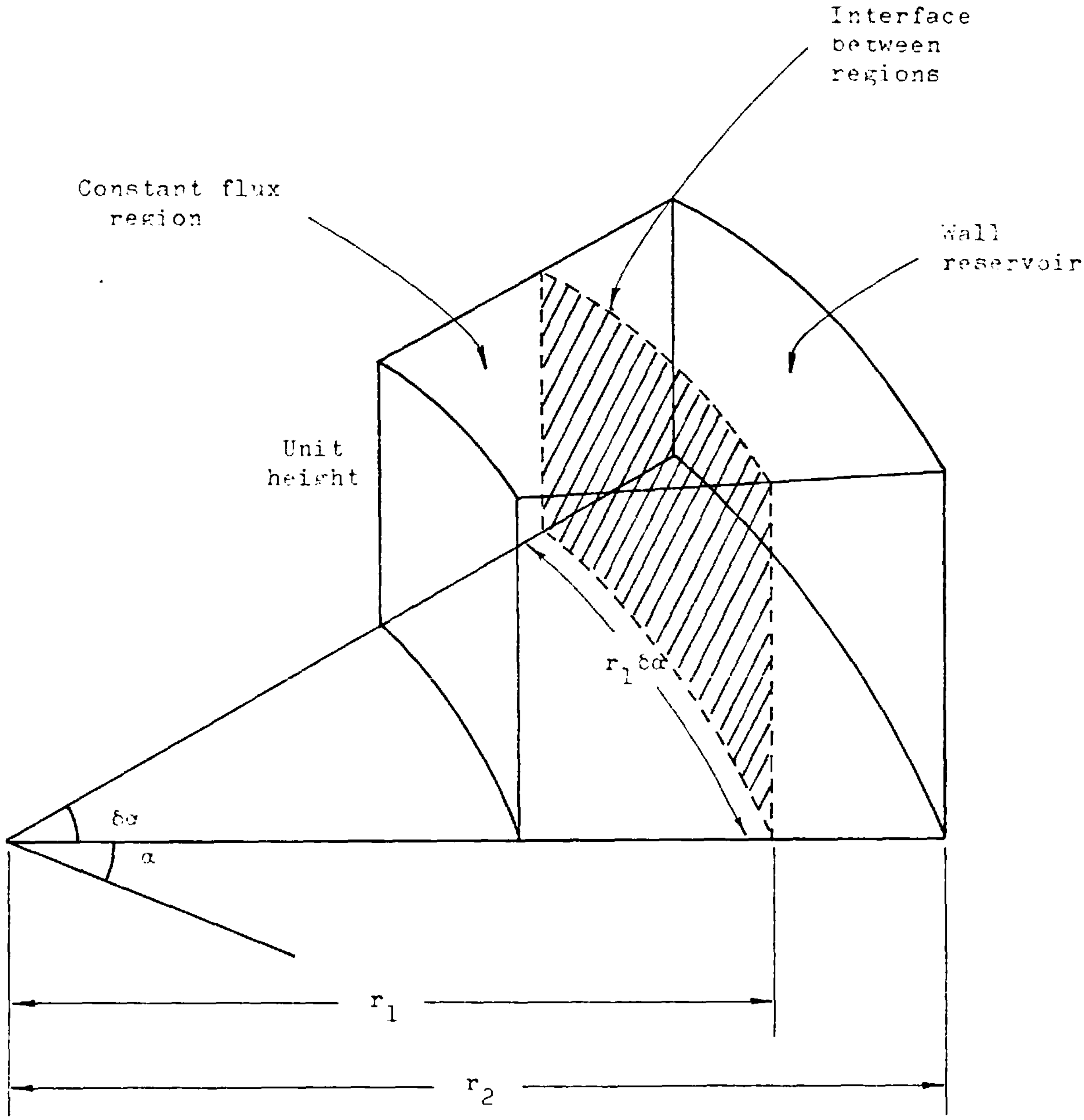

FIGURE B.5.25: Approximate model for region near outer wall.

$$V'C_V' - V'_f C_{Vf} = \left(\frac{r_1}{r_2-r_1}\right) \alpha U C_V'$$

$$\therefore \quad U = \frac{r_2-r_1}{r_1\alpha}\left(V' - V'_f \, \frac{C_{Vf}}{C_V'}\right) \quad \ldots \quad \ldots \qquad (5.15)$$

Equation 5.15 is similar in form to equation 5.13, but can be made to satisfy both the required conditions.

It was assumed in deriving the model that $\varepsilon_r = 0$ at r_2, which satisfies one condition. Rearranging 5.15 in the form

$$C_V' = C_{Vf} \cdot \left[\frac{V'_f}{V' - \dfrac{Ur_1\alpha}{r_2-r_1}}\right] \ldots \quad \ldots \qquad (5.16)$$

and putting $V' = V'_f$ at $\alpha=0$ gives $C_V' = C_{Vf}$, which is the other required condition.

The calibration measurements were made at a position corresponding to r = 2.4 cm., so the velocity $U_{2.4}$ will be calculated from equation 5.15 by putting r_1 = 2.4cm., r_2 = 2.5cm. The exact manner in which V' is likely to change with α is not known, but if the behaviour observed to hold with pure fluids (Figure B.2.3) is used as a guide, it appears that V' will initially (α=0) be less than $\overline{V}$ by a factor of, say, 0.7 - 0.8 and will increase progressively as the suspension passes through the helix, reading perhaps 1.1 - 1.2 $\overline{V}$ if fully developed curved flow is attained. These values relate to the behaviour at the midsection of the channel, however, and when the velocity profile is averaged over the full depth of the channel (Section 4.3.1) they are likely to be reduced somewhat. In any case, it seems improbable that fully developed curved flow is reached under the consitions employed in the present helix. In view of these considerations, it is assumed that V' will change from $0.7\bar{V}$ at $\alpha=0$ to $\bar{V}$ at $\alpha=2\pi$. If the suspension is considered to accelerate at a constant rate of v cm./sec./rad., then V' may be expressed as

$$V' = V'_f + v\alpha \quad \dots \quad \dots \quad \dots \qquad (5.17)$$

when $V'_f = 0.7\times200 = 140$cm/sec, $v = \frac{60}{2\pi} = 9.55$cm./sec./rad.

Alternatively, the treatment used when considering the Bagnold shear forces (Section B.4.1.2.d) could be adopted: namely, to assume that the tangential component of the shear force will minimise the alterations in the axial velocity profile that would otherwise be expected, so that V' may be considered independent of α. However, equation 5.17 is thought to represent a more realistic approach.

Combining equations 5.15 and 5.17 gives

$$U_{2.4} = 1.13 - 0.93 \frac{C_{Vf}}{C_{V'}} \quad \dots \quad \dots \quad \dots \qquad (5.18)$$

The values of $C_{V'_{2.4}}$ corresponding to $C_{Vf} = 0.085$ have been interpolated from Figure B.5.23 and used with equation 5.18 to calculate U. These results have been compared with the apparent terminal velocities, calculated as before by the method of Heywood[11] using, in this case, a mean value for V' of $0.85\bar{V}$ = 170 cm./sec. and a correction for interference effects based on the interpolated values of $C_{V_{2.4}}$. The results are given in Table B.5.4 (overleaf)

TABLE B.5.4			
Radial Velocities of Size Fractions of Glass Spheres at r=2.4cm.			
SIZE FRACTION		CALCULATED U_{TER} (cm./sec.)	'MEASURED' U (cm./sec)
B.S.Mesh	Mean Aperture (μ)		
-52 +72	253	4.8	1.03
-72 +100	181	4.0	0.97
-100+150	129	3.7	0.85
-150+200	89	2.7	0.64
-200+325	61	1.7	0.45

The measured velocities obtained from the two zone constant-flux model are all substantially lower than the apparent terminal velocities, though the proportional variation from size to size is almost the same for both sets of figures. Possible reasons for the differences are listed below and then discussed at greater length. Factors already considered in detail when analysing the results for the zone near the inner wall are only included in summary form.

(a) Use of the arithmetic mean size in calculations;

(b) Use of the apparent terminal velocity in calculations;

(c) Incorrect assumptions regarding the axial velocity profile;

(d) Degeneration of the concentration profile;

(e) Reduction of the measured velocities by secondary fluid flows;

(f) Inaccurate concentration measurements due to solids settling out during the test runs;

(g) Lift forces or 'Magnus' effects;

(h) Inadequacy of the 'two-zone flux' model as a representation of the interference and shearing force retardations.

(a) The use of the arithmetic mean size was shown earlier to have a negligible effect on the calculations.

(b) The apparent terminal velocity was previously shown to be an overestimate of the actual velocity, since among other things, it failed to take into account the period during which the particles are undergoing initial accleration, and neglected the turbulence present in the fluid due to it's axial flow behaviour. These arguments are still relevant, but it is possible that the moderate to high concentrations of particles present near the outer wall (particularly with the coarser sizes) tend to modify the fluid behaviour either by enhancing or diminishing the turbulence. A reduction in the overall turbulence seems the likelier alternative so - on these grounds alone - it might appear that the apparent terminal velocity represents a better estimate of the actual velocities achieved by the coarser particles near the outer wall than it did for the same particles near the inner wall. However this effect is likely to be small in comparison with that arising from the main drawback of the apparent terminal velocity model- namely that it completely neglects the Bagnold effect. The Bagnold effect exerts an influence on the radial motion of the particles in two ways: first, the radial component of the shearing force acts in direct opposition to the force tending to accelerate the particles and second, the tangential component of the shearing force must modify the axial velocity profile of the suspension which, in turn, will affect the accelerative force acting on the particles. The latter effect is considered in more detail in the next section, but it seems likely that the greater part of the differences found in Table B.5.4 is due to the inadequacy of the apparent terminal velocity model in failing to take the radial component of the Bagnold shear force into account.

(c) It was shown in the earlier discussion of the values assumed for V that overestimates of V could lead to values of the apparent terminal velocity that were too large for the finer sizes, but that there should be little or no difference at the coarse sizes. As consistent relative differences were found at all sizes, incorrect assumed values for V' cannot be held responsible for these, although the absolute values of both the calculated and measured particle velocities could well be in error.

The probable axial behaviour of the suspension was deduced by analogy with the data available for pure fluids. Unfortunately, as mentioned in Section (b) above, this approach does not make any overall allowance for the tangential component of the Bagnold shearing force, although one consequence of the force is allowed for in the definition of V'. It has already been shown (Section 4.1.2d) that the 'inertial' type of shearing force is more likely to occur with the high radial velocity gradients existing within the sizer helix. The shearing stress ($\overline{\tau}$) between adjacent layers of particles in the suspension may therefore be obtained from equation 4.23 i.e.

$$p = 0.042 \mathrm{Cos}\alpha \; D^2 \lambda^2 \left(\frac{dV}{dr}\right)^2 \quad \ldots \quad \ldots \quad \ldots \qquad (4.23$$

The relationship between p, $\overline{\tau}$ and the angle of the resultant (α) is given by

$$\frac{\bar{\tau}}{p} = \operatorname{Tan} \alpha \quad \ldots \quad \ldots \quad \ldots \quad \ldots \qquad (5.19)$$

Combining 4.23, 5.19 gives

$$\bar{\tau} = 0.042 \operatorname{Sin}\alpha \; D^2\lambda^2 \left(\frac{dV}{dr} \right)^2 \quad \ldots \qquad (5.20)$$

For spherical particles, Bagnold found an average value of tan α = 0.32, or α = 17.7°. Substituting this average value in equation 5.20 gives

$$\bar{\tau} = 0.0128 \; D^2\lambda^2 \left(\frac{dV}{dr}\right)^2 \quad \ldots \quad \ldots \qquad (5.21)$$

The 'linear particle concentration' (λ) may be related to the more familiar volume concentration of particles (C_V) by means of the expression

$$C_V = \frac{\pi}{6} \left(\frac{\lambda}{1+\lambda}\right)^3 \quad \ldots \quad \ldots \quad \ldots \qquad (5.22)$$

The stress given in equation 5.21 may be compared with the viscous stress generated in water alone with the same velocity gradient i.e.

$$\tau_{H_2O} = n \cdot \frac{dV}{dr} \quad \ldots \quad \ldots \quad \ldots \qquad (5.23)$$

The ratio $\bar{\tau} / \tau_{H_2O}$ has been calculated for all five size fractions over a range of volume concentrations, taking $\frac{dV}{dr}$ = 500 sec.$^{-1}$ and $n = 10^{-2}$ poise. The results are presented in Figure B.5.26. It is apparent that for the conditions assumed, the inertial shear stress can rise to nearly six times the equivalent pure fluid shear stress for the coarsest size fraction, with proportionately smaller increases for the finer size fractions.

The concentrations recorded at an equivalent radius of motion r = 2.40cm. with C_{Vf} = 0.085 were extracted from Figure B.5.23 and used earlier in the compilation of Table B.5.4. These same values may be used to estimate the

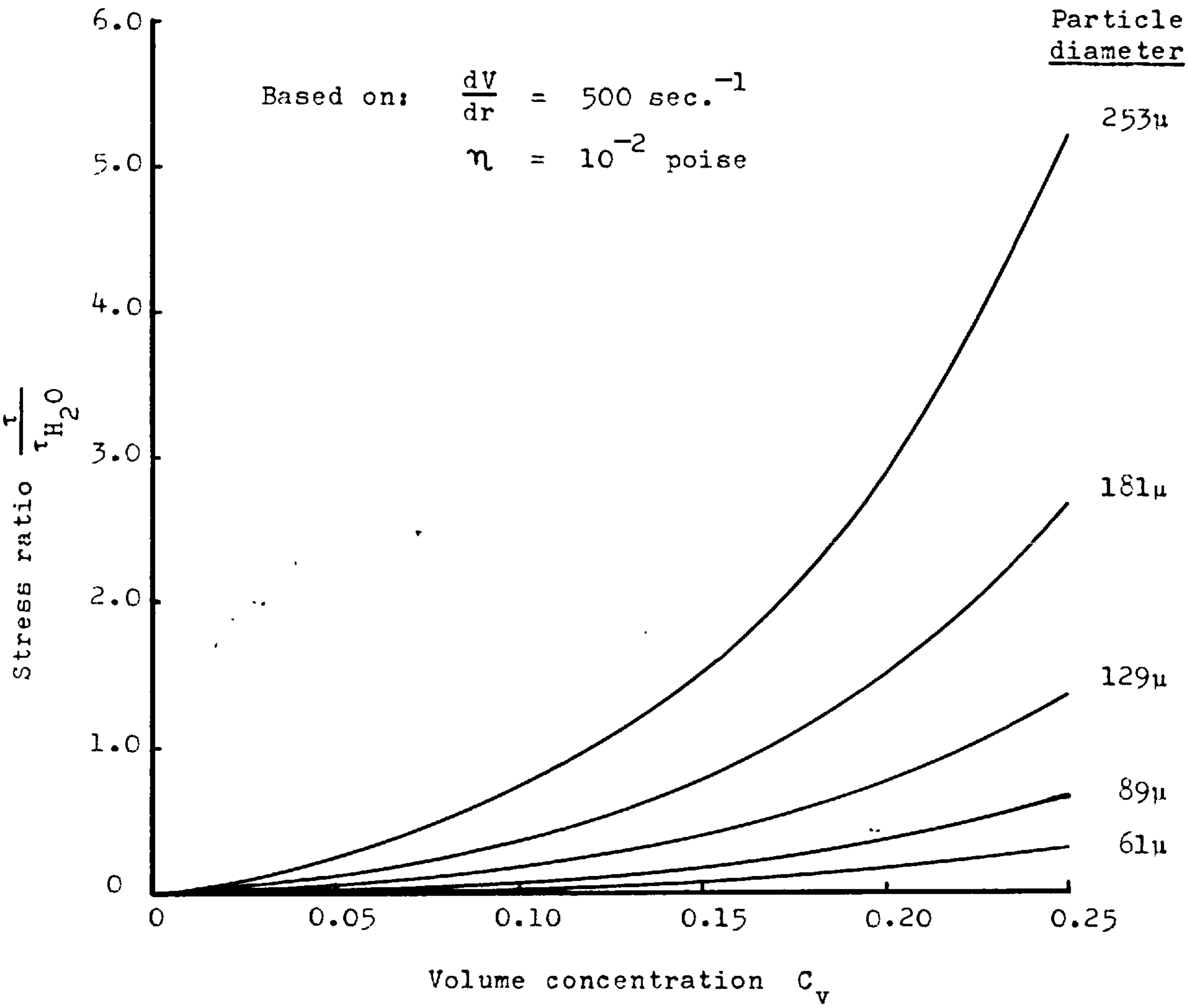

FIGURE B.5.26: Ratio of 'inertial' particle shearing stress to pure fluid shear stress.

magnitude of the ratio $\overline{\tau} / \tau_{H_2O}$ from Figure B.5.26. The results are given in Table B.5.5.

TABLE B.5.5

Ratio of Inertial Particle Shearing stress to Fluid Shear Stress

SIZE FRACTION		$C_{V2.4}$ MEASURED FOR C_{Vf}=0.085	STRESS RATIO $\overline{\tau} / \tau_{H_2}$
B.S. Mesh	Mean Aperture (μ)		
-52 +72	253	0.263	5.90
-72+100	181	0.219	1.90
-100+150	129	0.162	0.45
-150+200	89	0.114	0.10
-200+325	61	0.090	0.04

The increased shearing stress present must result in an overall reduction in the axial velocity of the suspension throughout the region near the outer wall. Measurements of the apparent viscosity of suspensions of -200+325 mesh glass spheres (σ=2.36) made by Clarke[22] with a modified Ferranti viscometer showed that, at a shear rate of 328 sec^{-1}, the apparent viscosity of the suspensions increased at a far higher rate than would be expected from consideration of the Bagnold effect alone. In this work, however, the particles in contact with the outer cylindrical wall of the viscometer were prevented from moving relative to the wall by a system of vertical channels cut into the surface, whereas no such slip-limiting device was employed by Bagnold[17].

Since the radial accelerative force acting on the particles is a function of the axial velocity, the radial velocities of all sizes of particles must also be reduced. This reduction will be very small for the finest size fraction, but could be quite large for the coarsest size fraction. For this reason, the values of V' used in the calculations probably represent over-estimates of the actual velocities, the degree of over-estimation increasing with particle size.

(d) The most likely consequence of degeneration of the concentration profile due to remixing downstream of the helix would be the transfer of some of the high concentration material from the outer wall back towards the centre of the channel. This effect was discussed previously in connection with the behaviour near the inner wall of the channel, where it was concluded that as much as 10% of the concentration difference created within the helix might be lost by remixing. If a correction of +10% is applied to the values of $C_{V_{2.4}}$ used in Table B.5.4, the new values of the measured radial velocity (U_{CORR}) are given by

$$U_{CORR} = U + \frac{0.0081}{C_{V_{2.4}}} \quad \ldots \quad \ldots \quad \ldots \qquad (5.24)$$

Equation 5.24 results in corrections to the measured velocities for the five size fractions 61, 89, 129, 181, 253μ of +0.09, +0.07, +0.05, +0.04, +0.03 cm./sec. These corrections are so small in relation to the existing differences that degeneration of the concentration profile is obviously not a significant factor.

(e) Secondary fluid flow effects were discussed previously in sections 4.1.2.c, 5.3.1.e. It was concluded that secondary flow might have interfered with the radial motion of the finer sizes in the region near the inner wall, as these particles displayed proportionately smaller velocities compared with the apparent terminal velocities.

In the present instance, the measured velocities represent an almost constant fraction of the apparent terminal velocities and as the coarser sizes should be little affected by secondary flow in any case, it seems unlikely that this can be a major contributory factor. This conclusion does not preclude the existance of secondary fluid flow or the possibility of it having an effect in the region near the inner wall, however, since the relatively high concentrations of particles near the outer wall may well interfere with the secondary flow itself - possibly to the extent of causing it to recycle at a smaller radius of motion than would otherwise be the case.

(f) Although losses of material due to settling out during the test runs could cause artificially low measured velocities in the region near the outer wall this is not considered to be a likely explanation, for the reasons outlined earlier. (Section 5.3.1.g)

(g) The lift force was discussed orginally in Section 3.1.1 and also in relation to the behaviour near the inner wall. (Section 5.3.1.h). The anticipated direction of the lift force in the region near the outer wall is illustrated in Figure B.5.24.b. It can be seen that the force will act in a manner calculated to decrease the axial velocity of the particle and, hence, its radial velocity. Since the measured radial velocities are in fact too high, the lift force could well have contributed to this effect.

(h) The constant flux model is intended to take account of two types of retardation: the so-called 'interference' effects (Section 3.1.2.c) and the 'inertial' shearing force (Section 4.1.2.d). If any relative motion between particles and fluid in the tangential direction is ignored, the equation describing the interference effects may be written as

$$U = U_T(1 - C_V)^{\epsilon} \quad \ldots \quad \ldots \quad \ldots \qquad (5.25)$$

in which the exponent ϵ is a function of the Reynolds Number for the particle. The 'inertial' shearing force was calculated in Table B.4.2 as a proportion of the accelerative force for particle sizes corresponding to the limiting conditions for laminar and turbulent motion. The equivalent changes in the apparent terminal velocities may be calculated from this data by making use of equations 3.20, 3.29 (putting $\frac{d^2r}{dt^2}$ and Θ equal to 0 in each case.).

If the reductions in particle velocity caused by these two factors are considered to be additive in effect, the total reduction calculated from equation 4.53 and the data in Table B.4.2 may be compared with that predicted by the constant flux model, which suggested

$$U = \epsilon_k . C_V^{-1} \quad \ldots \quad \ldots \quad \ldots \qquad (5.11)$$

Taking $U = 1$ at $C_V = 0.10$, this comparison has been made for the limiting sizes for laminar (45µ) and turbulent (235µ) motion. The results are given in Table B.5.6. (See overleaf).

TABLE B.5.6.

Comparison between 'Inertial and Interference' velocity reduction and that predicted by Constant Flux Model

VOLUME CONC^{N} C_V	CONSTANT FLUX VELOCITY	LAMINAR MOTION (45μ)			TURBULENT MOTION (235μ)		
		Inertial Redn. (%)	Interfer. Redn. (%)	Net Velocity U	Inertial Redn. (%)	Interfer. Redn. (%)	Net Velocity U
0.100	1	0	0	1	0	0	1
0.125	0.80	2	10	0.88	6	5	0.89
0.150	0.67	4	21	0.75	14	11	0.75
0.175	0.57	6	32	0.62	26	18	0.56
0.200	0.50	10	40	0.50	45	23	0.32

On the basis of these estimates, it would appear that the constant flux model provides a reasonable approximation to the behaviour expected from particles exhibiting laminar or near-laminar motion (i.e. material < 200 mesh) over the concentration range C_V =0.10 to C_V = 0.20 and for particles exhibiting turbulent or near-turbulent motion (i.e. material > 235μ) over the concentration range C_V = 0.10 to C_V= 0.175. For turbulent motion, the reduction in velocity caused by the inertial shear force increases so rapidly when C_V > 0.175 that the constant flux model is no longer applicable.

With this exception the constant flux model appears to give an adequate fit at the two extremes of the transitional regime of particle motion and it follows that it should give as good or nearly as good a fit within the transitional regime itself, since the inertial and interference reductions vary to a large extent in a manner that is compensatory.

The above discussion is necessarily tentative, since most of the calculations depend largely on the values assumed for the axial velocity and velocity gradient, and these are obtained by analogy from pure fluid behaviour without making any allowance for the effect of particles present. (section 5.3.2.c)

In brief, it seems reasonable to consider the constant flux model adequate for all conditions except those involving high concentrations of large particles. In the latter case, the constant flux overestimates the measured velocity by making insufficient allowance for the inertial shearing force. However, as all the differences recorded in Table B.5.4 show measured velocities which are low, the errors introduced by using the constant flux model are clearly small compared with other effects within the system.

5.3.3 Summary and Conclusions

The motion of particle populations in the regions adjacent to the walls of the sizer helix has been analysed in terms of simple models derived from the continuity equation given in Section 4.3. Near the inner wall the experimental evidence indicated that C_V was independent of r, and U was considered to be independent of z and C_V - i.e. a function only of r. The axial velocity distribution was considered independent of z and treated as a linear function of r, these assumptions being based on the evidence available for pure fluids. The continuity equation was solved for these conditions, the form of the solution being such that the radial velocity of the particles at a given radius of motion (1.1c.m.) could be calculated from a knowledge of the initial and final volume concentration of particles recorded at that radius. The 'measured' velocities calculated in this way were all considerably smaller than the apparent terminal velocities obtained using Heywoods method, ranging from about 40% of the terminal velocity at 253μ down to 4% at 61μ. It seems probable that the apparent terminal velocity is mainly in error, since it assumes that particles can undergo ideal types of drag when moving radially in a fluid undergoing turbulent axial flow and, also, neglects the initial acceleration of the particles and the consequences of boundary layer separation, secondary fluid flow and lift forces. The extent to which there individual effects are responsible for the overall discrepancy is at present a matter of conjecture, but it seems unlikely that secondary fluid flow plays a major role.

In the region near the outer wall of the helix, the motion of the particles is governed to a large extent by interference effects and Bagnold shearing forces. A constant flux model was proposed to describe this behaviour, but in order to satisfy the boundary conditions it was necessary to modify the model by dividing the region into two parts: one adjoining the wall which acts as a reservoir and an inner part feeding the reservoir with a constant flux of particles. The concentration and tangential velocity of the particles in the reservoir were considered to be independent of the radius and the tangential velocity was treated as a linear function of α. A new continuity equation was derived and solved for these conditions, making use of the initial and final volume concentrations of particles recorded at r = 2.4cm. as the 'reservoir' concentrations and estimating the tangential velocities from the evidence available for pure fluids. These calculations provided 'measured' values of U corresponding to the final particle concentrations recorded at r = 2.4cm. and the figures were compared with the apparent terminal velocities obtained using Heywoods method and a mean value for the tangential velocity. In all cases the 'measured' values were lower, amounting to some 20 - 25% of the apparent terminal velocities. Most of the differences must be due to the failure of the apparent terminal velocity model in not taking the radial component of the Bagnold shear force into account. Both the measured and terminal velocities quoted are probably inaccurate, since the assumed values of the tangential velocity could be in error by a significant amount due to the effects of the tangential component of the Bagnold forces.

Neither of the proposed models can be made to satisfy all the requirements set out in equations 4.32 - 4.34, since each model is only valid for a given set of conditions that appears to hold for a particular region.

5.4 Calibrations for Glass Spheres

The calibration technique evolved previously for ground quartz (Section A.4.1.6) was entirely empirical in origin and was only suitable for samples whose size distributions could be described in terms of Gaudin - Schuhmann functions.[4] A further disadvantage was that two readings had to be taken for each sample, the calibration plot being based on the difference between the readings. (Figure A.4.10).

The results obtained with size distributions of glass spheres can be presented in the same way (Figure B.5.27),

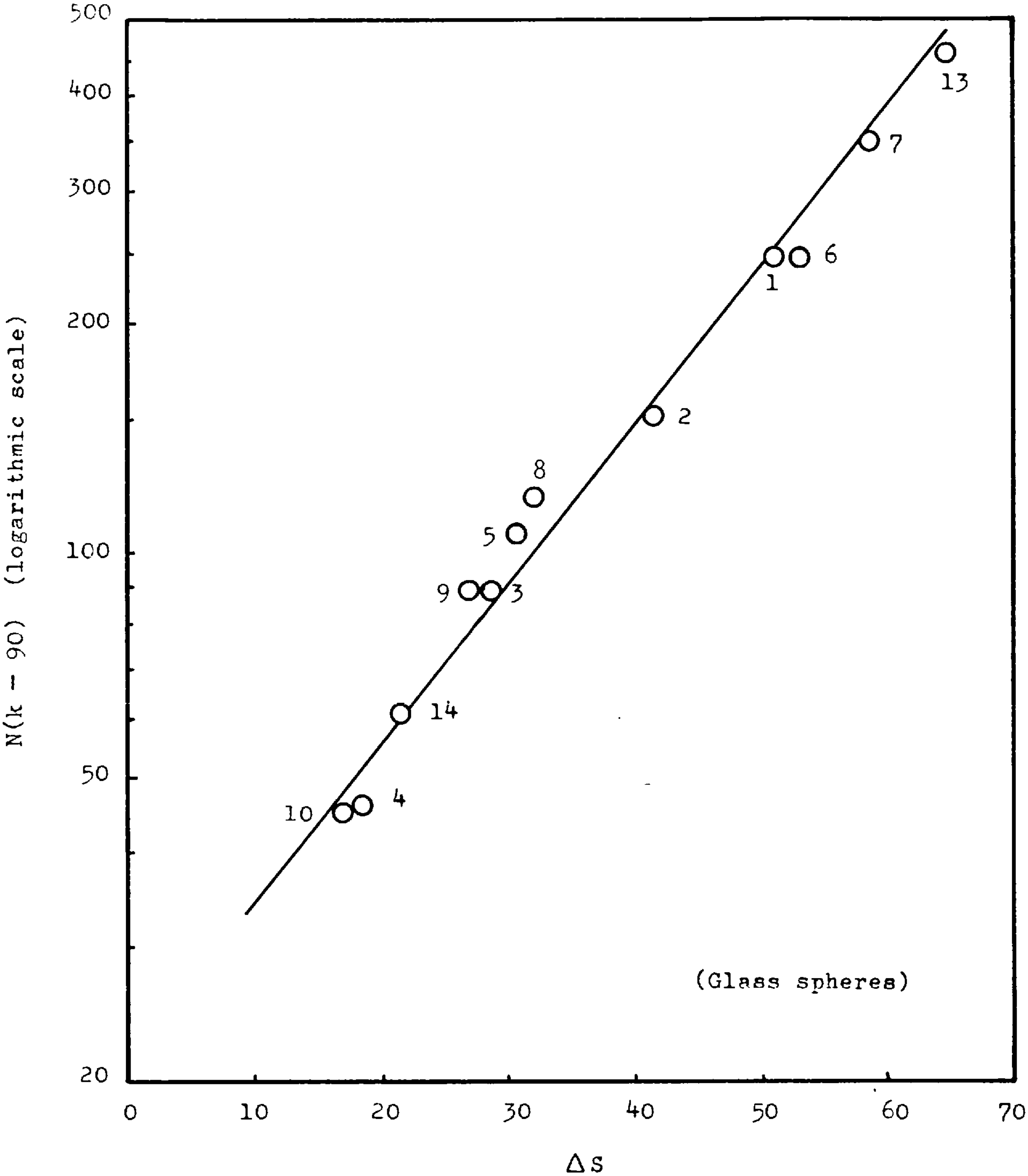

FIGURE B.5.27: Size distribution calibration for Mark 7 cell.

though the correlation is not as good as that obtained with ground quartz. (Figure A.4.10). This type of calibration is limited in scope and it seemed desirable to develop a more general method based, if possible, on one rather than two readings. With this objective in view, the measurements made near the inner and outer walls of the helix were considered separately.

5.4.1 Calibrations based on Measurements made at r = 1.1cm.

The analysis conducted earlier showed that the velocities of individual size fractions could be related to the measured particle concentrations in a simple manner. (Equation 5.5). Making reasonable assumptions about the axial velocity profile, the equations reduced to give

$$U_{1.1} \simeq 2.5 \ln\left(\frac{C_{Vf}}{C_V}\right) \quad \ldots \quad \ldots \quad \ldots \qquad (5.5)$$

From equations 5.4 and 5.5 the velocity of single size fractions ($U_{1.1}$) is directly proportional to the logarithm of the ratio $\left(\frac{C_{Vf}}{C_V}\right)$, so this quantity may be used as a direct representation of the velocity. If the logarithm (to base 10) of the ratio $\left(\frac{C_{Vf}}{C_V}\right)$ is plotted against the (arithmetic mean) particle size (D) for single size fractions, the result is a straight line (Figure B.5.28, circled points), giving the relationship

$$\frac{C_{Vf}}{C_V} = 0.571 \times 10^{0.00405D} \quad \ldots \quad \ldots \quad \ldots \qquad (5.26)$$

If this result is combined with equation 5.5, the velocity of the particles is given by

$$U_{1.1} = 0.0233D - 1.4 \quad \ldots \quad \ldots \quad \ldots \quad \ldots \qquad (5.27)$$

When the concentration is measured for a mixture of size fractions or a size distribution, the value obtained is an average one and it may be related to an average size. Since no interaction was found between particles of the same or of different size (Figure B.5.22, Tables B.5.1, B.5.2), the total concentration obtained with a mixture of particles of different sizes can be computed by summing the partial concentration contributed by each size according to equation 5.26.

Denoting the weight proportion of size D by the symbol M, the total observed concentration is given by

$$\frac{C_{Vf}}{C_V} = \Sigma(M.0.571 \times 10^{0.00405D}) \quad \ldots \quad \ldots \quad (5.28)$$

If the total observed concentration is to be plotted against a mean size, the mean must be calculated from equation 5.28. Denoting this mean by $\check{D}$:

$$0.571 \times 10^{0.00405\check{D}} = \Sigma\,(M\ 0.571 \times 10^{0.00405D})$$

$$\check{D} = \frac{\log[\Sigma M \text{ antilog}(0.00405D)]}{0.00405} \quad \ldots \quad \ldots \quad (5.29)$$

The mean size defined by equation 5.29 has been calculated for all samples that contained more than one size fraction. The measured concentrations have been plotted against this mean size on the same graph as that employed for single size fractions. (Figure B.5.28). Slightly more of the points fall below the original line than fall above it, but the agreement is generally good and confirms the applicability of equations 5.26, 5.29 and the earlier conclusions regarding the lack of interaction between particles in this region.

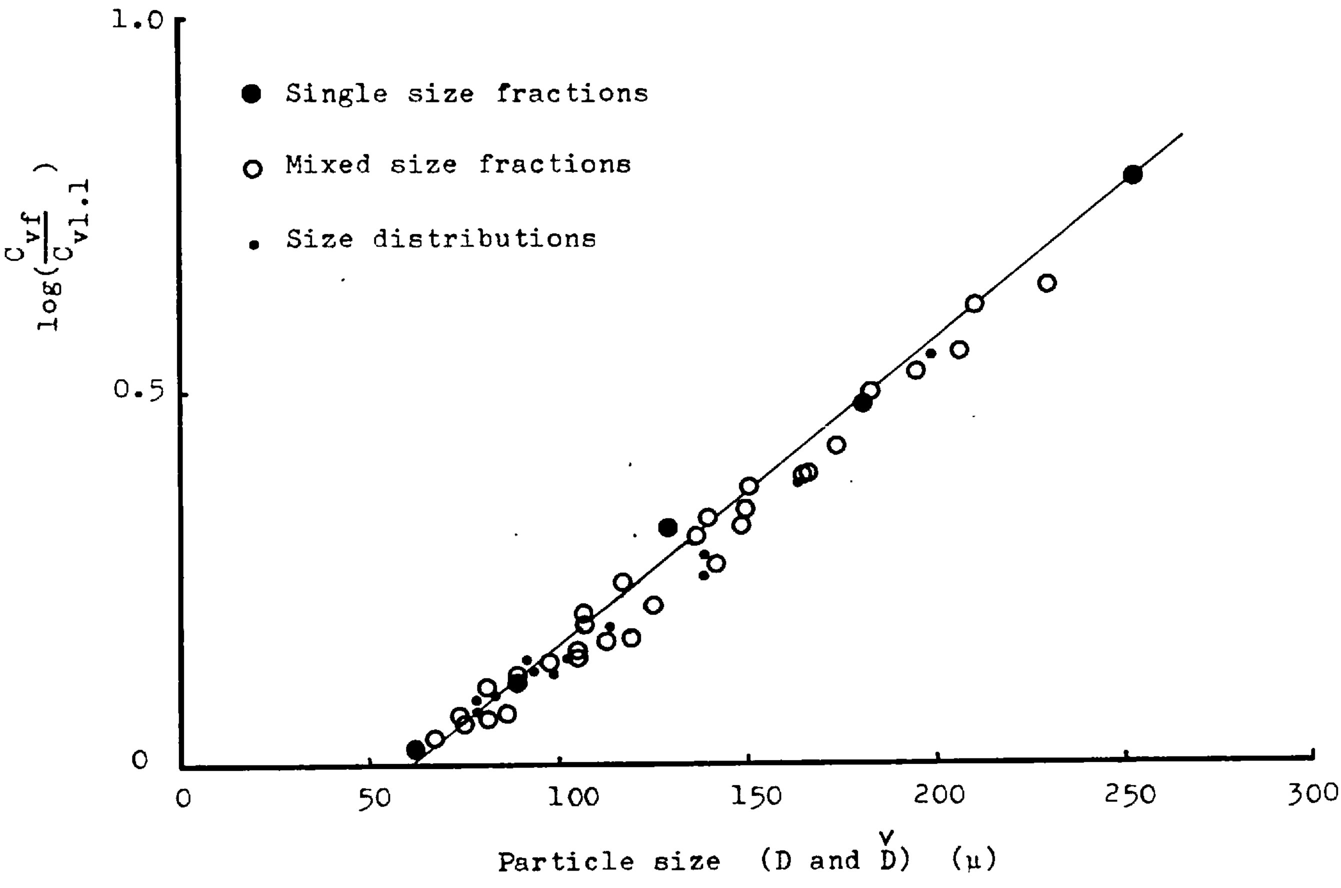

FIGURE B.5.28: Mean size calibration No.1

Inner zone, r = 1.1 cm.

The mean size defined in equation 5.29 is unusual in form and does not lend itself to calculation by integration in the case of the Gaudin-Schuhmann or any other convenient size distribution function. However, the form of this mean, which is the logarithm of the sum of weighted antilogarithms, suggested that the geometric mean (the antilogarithm of the sum of weighted logarithms) might provide a useful approximation. The geometric mean, besides being more familiar, can be calculated without difficulty for most size distribution functions. Denoting the geometric mean by $\hat{D}$, and using the same symbols as before:

$$\hat{D} = \text{Antilog}\left[\Sigma M \log D\right] \quad \ldots \quad \ldots \quad \ldots \qquad (5.30)$$

The geometric mean sizes have been calculated for all the mixed size fraction and size distribution samples used in the testwork. To illustrate the correlation between the two mean sizes defined by equations 5.29, 5.30, they have been plotted against each other in Figure B.5.29. It can be seen that the correlation is extremely good for all samples up to a mean size of 135μ, and for coarser samples only one point diverges from the line by more than about 10μ. In view of this generally good agreement, the use of the geometric mean size ($\hat{D}$) in place of the mean defined by equation 5.29 should lead to an almost identical calibration, with a slightly greater scatter and possibly more of a bias towards the coarser sizes, since in all cases $\hat{D} \geq \check{D}$.

The data used in obtaining Figure B.5.28 have been replotted against the geometric mean size in Figure B.5.30. The scatter is greater, as anticipated, but a mean calibration line can be drawn which will give the geometric mean size, corresponding to a given concentration measurement, to within $\pm$ 10μ for D < 100μ and $\pm$ 20μ for D > 100μ. These

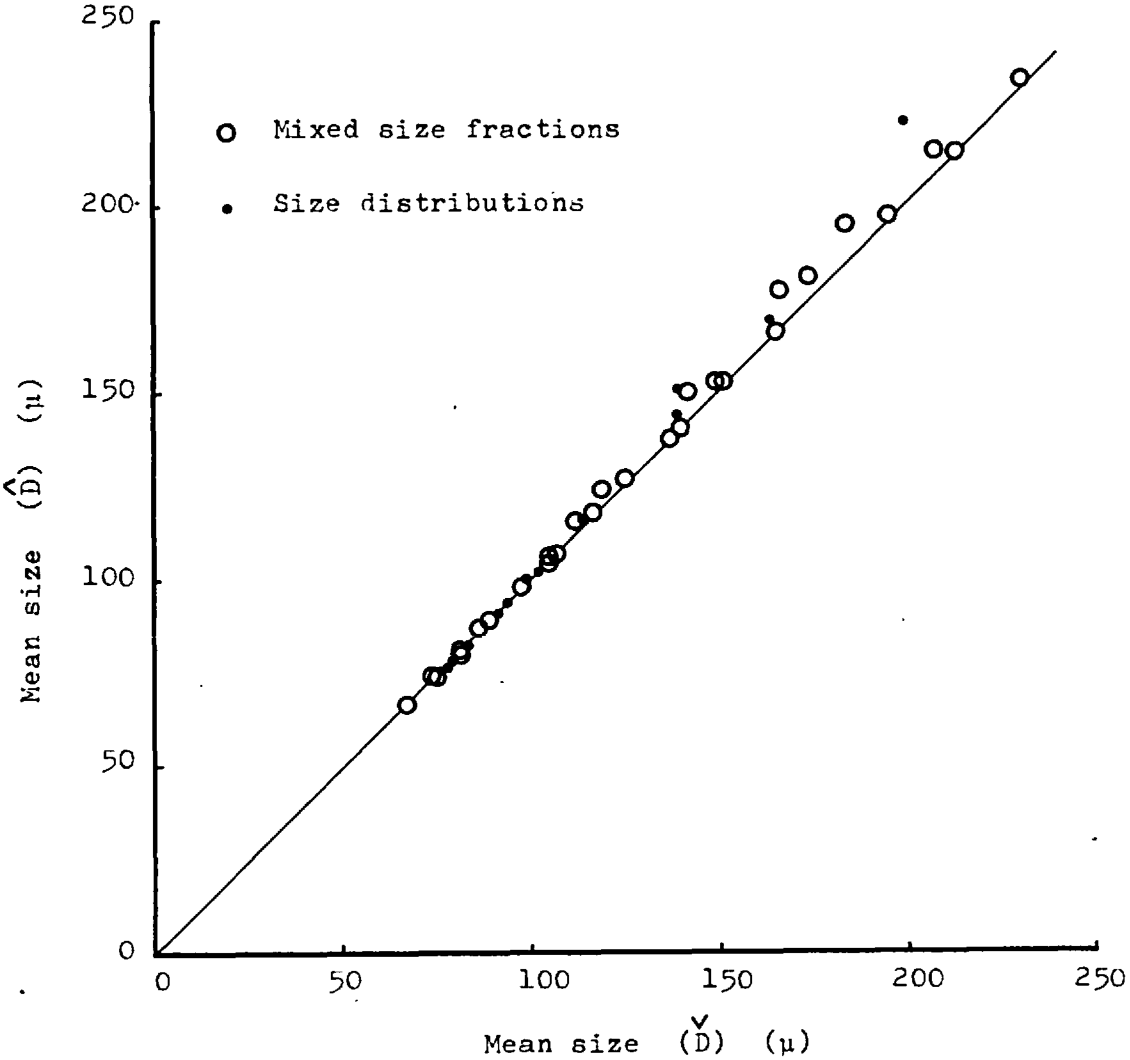

FIGURE B.5.29: Correlation between mean sizes $\hat{D}$ and $\check{D}$

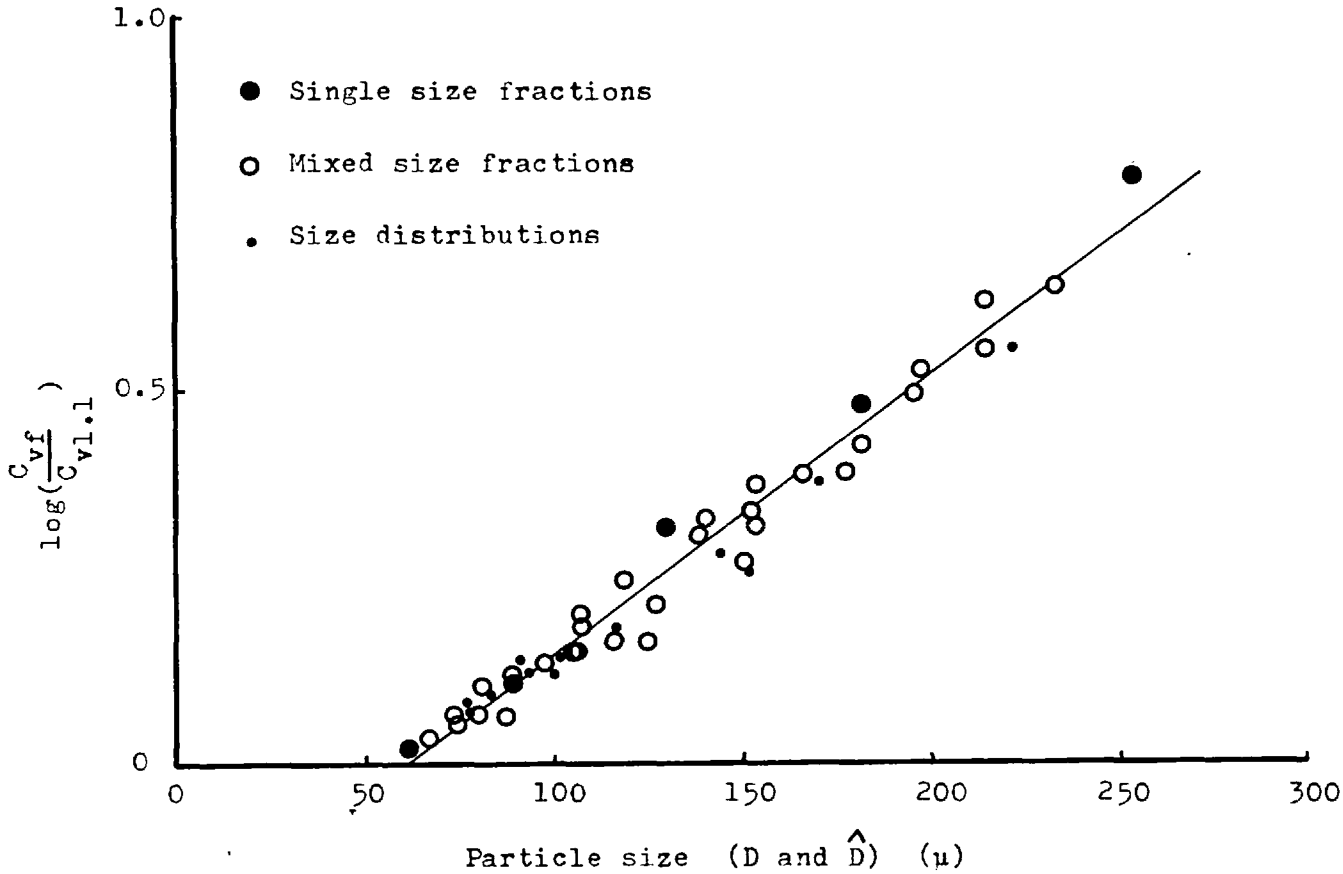

FIGURE B.5.30: Mean size calibration No.2
Inner zone, r = 1.1 cm.

limits are considerably smaller than the normal sieve aperture spacings and should be quite satisfactory for the control of most size reduction processes.

The calibration equation is therefore given by

$$\frac{C_{Vf}}{C_V} = 0.571 \times 10^{0.00405\hat{D}} \quad \ldots \quad \ldots \qquad (5.31)$$

Since no interaction was found between particles, C_V increases linearly with C_{Vf} and equation 5.31 is, therefore, valid for feed concentrations ranging from $C_{Vf} = 0$ to $C_{Vf} \simeq 0.10$.

5.4.2 <u>Calibrations based on Measurements made at r = 2.4 cm.</u>

The model developed for the outer region suggested a simple relationship between the concentration of the particles and their velocity. (Equation 5.15). Making reasonable assumptions concerning the behaviour of the axial velocity profile, the equation reduced to give

$$U_{2.4} = 1.13 - 0.93 \frac{C_{Vf}}{C_V} \quad \ldots \quad \ldots \quad \ldots \qquad (5.18)$$

The velocity of the particles is therefore linearly related to the ratio $\frac{C_{Vf}}{C_V}$. If this quantity is calculated for $C_{Vf} = 0.085$ and plotted against the size (D) for single size fractions, each to a logarithmic scale, the points fall approximately on a straight line. (Figure B.5.31, circled points). The equation of this straight line is

$$\frac{C_{Vf}}{C_V} = \frac{29.5}{D^{0.834}} \quad \ldots \quad \ldots \quad \ldots \qquad (5.32)$$

Combining equations 5.18 and 5.32 gives the velocity in terms of particle size :

$$U_{2.4} = 1.13 - \frac{27.4}{D^{0.834}} \quad \ldots \quad \ldots \quad \ldots \qquad (5.33)$$

The concentrations recorded for mixtures of size fractions or size distributions are average values, and they may be related to average sizes. Unfortunately, although no interaction was found between different sizes of particle in the outer region, a certain amount of self interaction was found at the coarser sizes. (Figures B.5.23) This self interaction created a non-linear relationship between C_V' and C_{Vf}, such that a two-fold increase in C_{Vf} produced a less than two fold increase in C_V'. Strictly speaking, this non-linearity means that the total concentration obtained with a mixture of size fractions cannot be accurately computed by summing the partial concentrations contributed by individual sizes according to equation 5.32, because this equation is only valid at one concentration ($C_{Vf} = 0.085$) and, when applied pro rata to lower values of C_{Vf}, it underestimates the total value of C_V' by a significant amount.

The mean size against which the total concentration should be plotted may be calculated from equation 5.32. Denoting this mean by ($\overset{o}{D}$), it follows that

$$\overset{o}{D} = \left(\Sigma M D^{0.834} \right)^{\frac{1}{0.834}} \quad \ldots \quad \ldots \qquad (5.34)$$

The correlation between $\overset{o}{D}$ and the concentration calculated by summation of equation 5.32 (ignoring the non-linearity) is also illustrated in Figure B.5.31. It is apparent that more points fall below the original line than above it, a tendency caused by the non-linearity discussed above. The correlation is not bad and could provide the basis for a calibration, were it not for the unfamiliar form of the mean defined by equation 5.34 and the difficulties

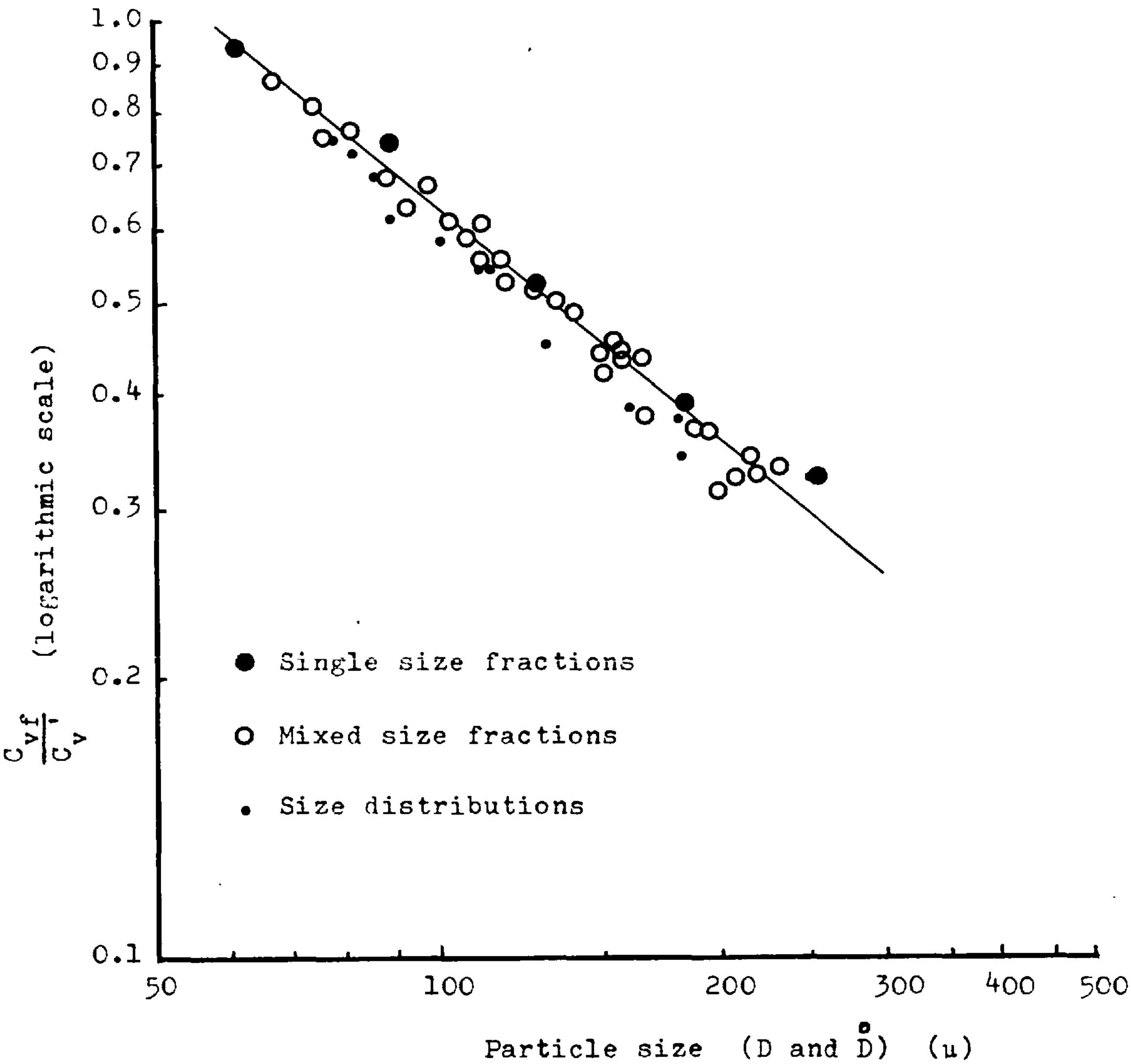

FIGURE B.5.31: Mean size calibration No.3

Outer zone, r = 2.4 cm.

associated with necessary calculations. However, trial calculations revealed that the latter mean differed very little from the arithmetic-weight mean ($\bar{D}$) which is defined as

$$\bar{D} = \Sigma MD \quad \ldots \quad \ldots \quad \ldots \quad \ldots \qquad (5.35)$$

The two mean sizes have been compared in Figure B.5.32 for all the mixed size fraction and size distribution samples used in the testwork. The agreement is good, the arithmetic-weight being in all cases the larger, but never exceeding $\overset{o}{D}$ by more than 5μ.

The data used in constructing Figure B.5.31 have been replotted against the arithmetic-weight mean in Figure B.5.33. It is apparent that the arighmetic-weight mean gives a better fit, as the scatter is reduced and the points are distributed more or less equally about the line. The explanation for this rather unexpected result lies in the fact that the arithmetic - weight mean consistently over-estimates the mean size calculated from equation 5.34 and therefore, when substituted in equation 5.32 it tends to compensate for the non-linear relationship between C_V' and C_{Vf}.

The calibration line in Figure B.5.33 may be used to determine the arithmetic weight mean to within ± 5μ for $\bar{D}$ <100μ and ± 20μ for 100<D<200μ. Above 200μ the scatter of the points is such that $\bar{D}$ may lie within ± 30μ of the line. These limits are comparable with those found for the inner zone calibration.

The calibration equation is its final form becomes:-

$$\frac{C_{Vf}}{C_V'} = \frac{29.5}{(\bar{D})^{0.834}} \quad \ldots \quad \ldots \quad \ldots \qquad (5.36)$$

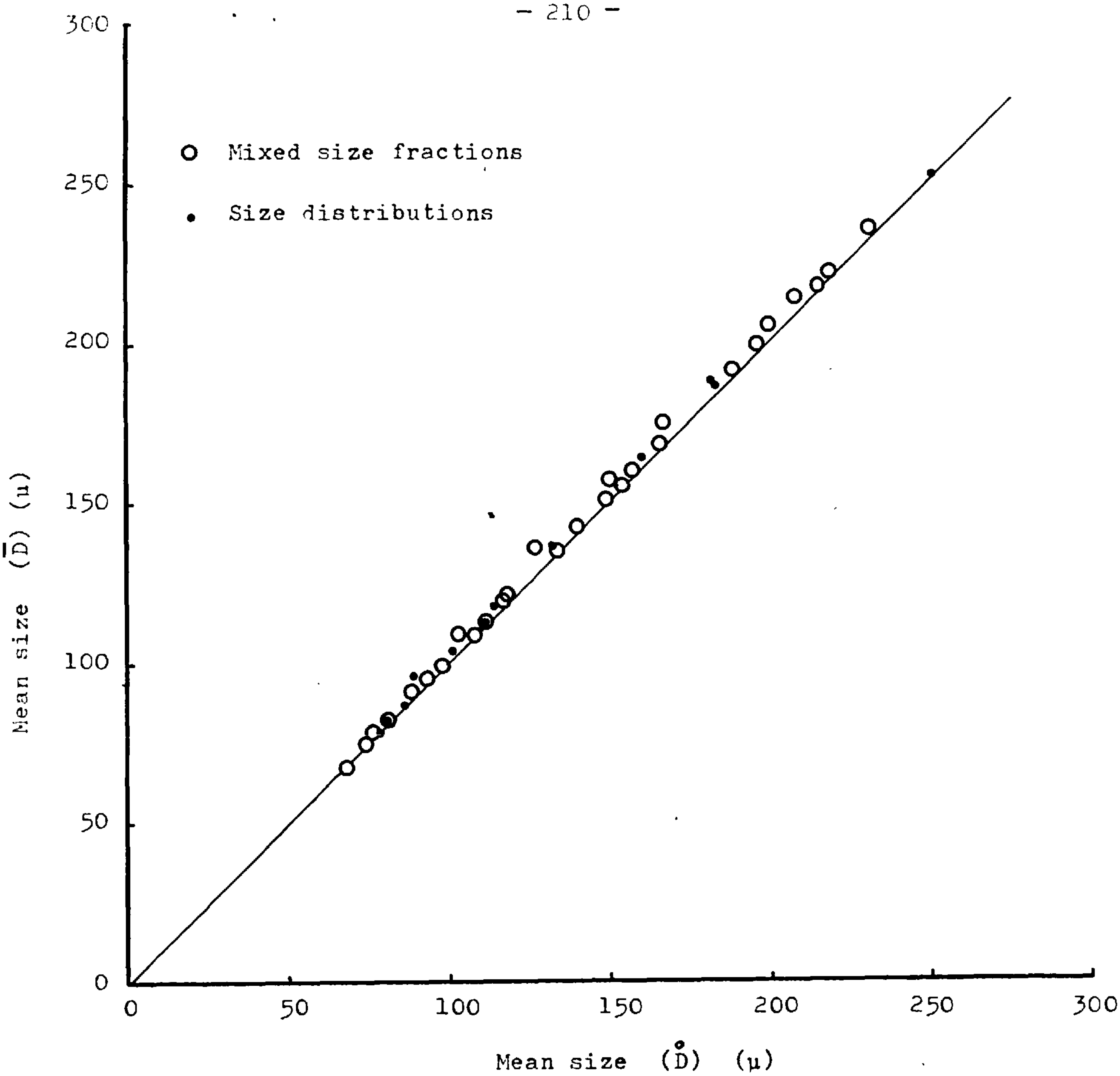

FIGURE B.5.32: Correlation between mean sizes $\bar{D}$ and $\mathring{D}$

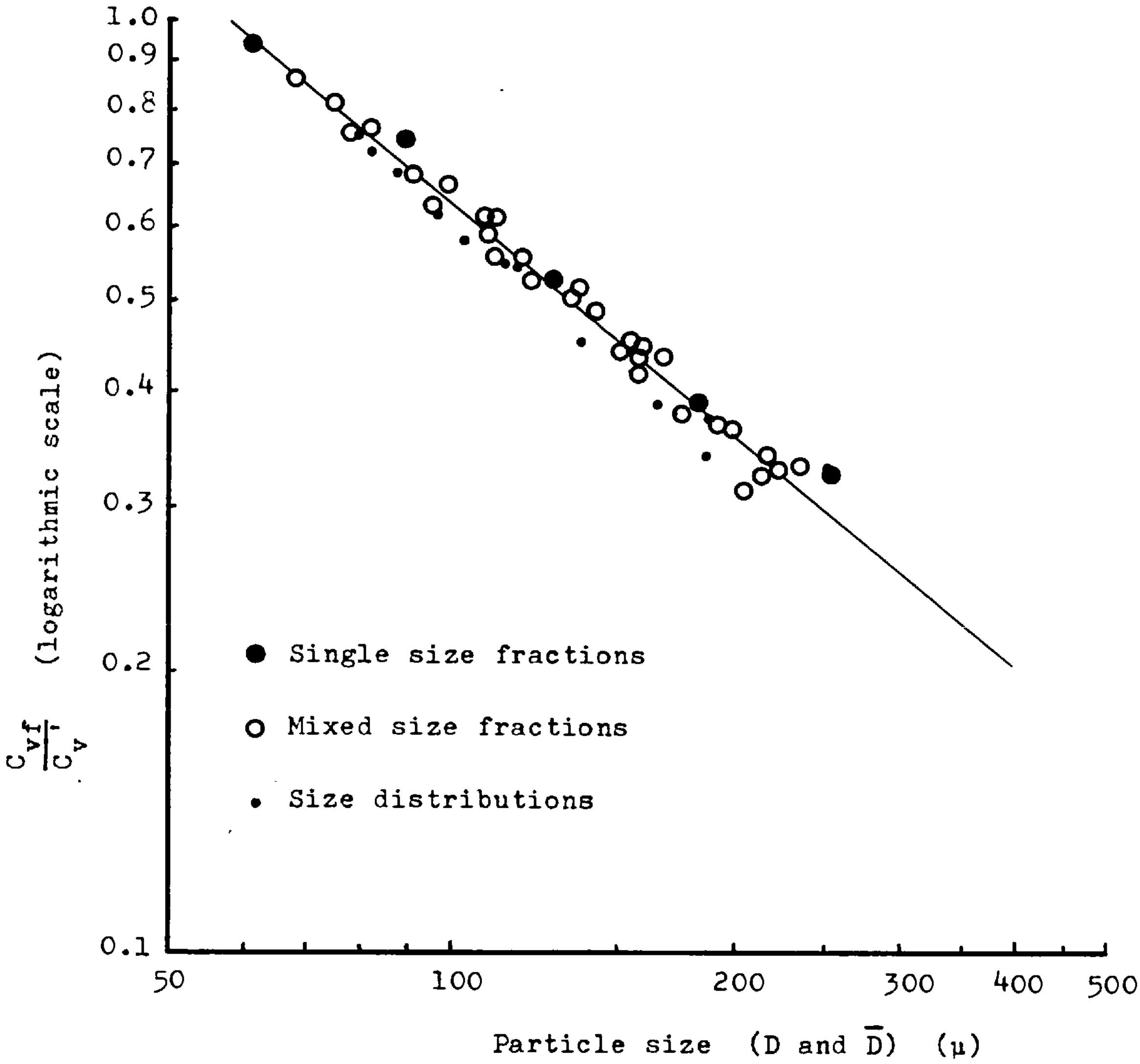

FIGURE B.5.33: Mean size calibration No.4
Outer zone, r = 2.4 cm.

Although a substantial degree of interaction between particles was found at higher feed densities, this effect is compensated by using the arithmetic-weight mean size, as explained above. Equation 5.36 may be considered valid, therefore, over the range $C_{Vf} = 0$ to $C_{Vf} = 0.10$.

5.4.3 Comparison between Old and New Calibration Systems

The measurements conducted on size distributions of glass spheres may be used to obtain an empirical calibration of the type developed originally for ground quartz, as has already been demonstrated in Figure B.5.27. The separate calibrations developed for each measuring position are preferable to the earlier calibration because, in addition to having a more fundamental basis, they can also be applied to any kind of ideal or non-ideal size distribution. However, it is interesting to compare the different calibration techniques with a view to determining the extent to which they agree with one another.

The earlier empirical calibration, which was based on the difference between the wall zone readings, cannot be broken down to give individual calibrations for each zone. However, the individual calibrations can be used to predict the difference reading (ΔS) for each of the twelve Gaudin-Schuhmann distributions that were tested. These values of ΔS may then be plotted against log $M(k-90)$ and, if the calibration systems are equivalent to each other, a straight line should result. This has been done in Figure B.5.34 and it can be seen that, although a mean straight line can be drawn, the correlation is an approximate one only.

5.5 Summary and Conclusions

A comprehensive series of tests was carried out on a new and improved version of the experimental rig.

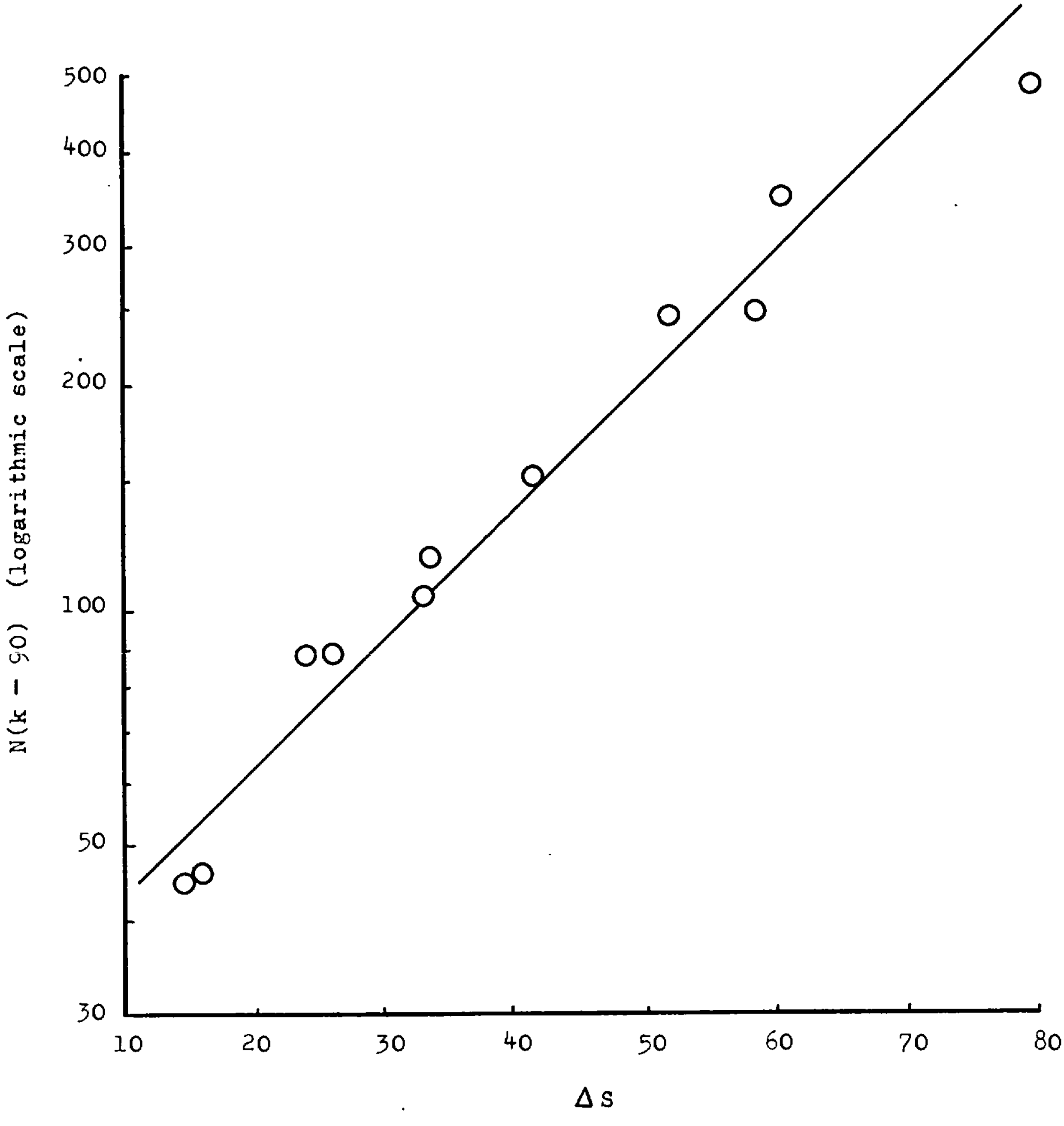

FIGURE B.5.34: Comparison between calibrations

Concentration profiles were determined for single size fractions of glass spheres over a range of feed concentrations, for pairs of size fractions mixed in varying proportions, and for the Gaudin-Schuhmann size distributions employed in the earlier work on ground quartz.

Separate solutions to the continuity equation were developed for the two regions near the walls of the channel, the approach adopted in each case being based on the characteristics of the concentration profiles. Where necessary, reasonable assumptions were made regarding the axial velocity profile and in other instances where experimental data was lacking. The solutions were in the form of equations relating the initial and final concentrations to the radial velocities of the particles. Near the inner wall, the radial velocities were assumed independent of concentration and so the results obtained were valid for the entire retention time in the helix. The velocities near the outer wall were markedly dependent on the concentration and so the results obtained were valid only at the measured final concentrations.

The data obtained for glass spheres were used to obtain individual size calibrations based on concentration measurements made in each of the wall regions. These calibrations were general in nature, since - unlike the earlier empirical calibration - they could be applied to any kind of ideal or non-ideal size groupings and were valid for a range of feed concentrations. A comparison was made between the calibration systems and it was shown that, for Gaudin-Schuhmann type size distributions only, the original calibration system could be reproduced with reasonable agreement by combining the results of the new individual calibrations.

6. REVIEW

6.1 Progress Achieved

The work described in each of the two major parts of this thesis was intended to satisfy a separate and entirely different set of objectives. It seems best, therefore, to review each part separately.

6.1.1 Part A: Development of the Sizing Technique.

The aim of this work was to develop a system capable of performing rapid and frequent measurements of the size distribution of particles in a suspension.

Visual assessment of early test runs, conducted with mixtures of differently coloured size fractions, suggested that the proposed centrifugal system could provide a means of sizing homogeneous materials over a size range which is of considerable interest in the mineral and chemical industries. Measurements of particle concentration carried out on suspensions of ground quartz using a beta-transmission density gauge confirmed this. An empirical calibration based on the Gaudin-Schuhmann function was developed for size distributions of quartz.

When this stage of the work was reached, the basic aim had been realised. However, there were two important restrictions on the performance of the sizer that seriously limited its usefulness. First, the exact form of the force field within the helix and the type of particle motion was unknown, so that deviations from the empirical calibration could not be explained or compensated. Second, the sizer had only been tested on homogeneous materials and there were forseeable difficulties in applying it to materials containing a range of specific gravities. A new stage in the research was planned, therefore, in the hope that it would go some way towards lifting the first of these restrictions.

6.1.2 Part B: Investigation into the Sizing Technique

The aim of this work was to gain an insight into the behaviour of particles within the helix, to determine the forces acting on the particles and, if possible, to construct a theoretical model.

A theoretical and experimental investigation into the behaviour of ideal (spherical) particles within the sizer was carried out. The theoretical study was limited in many instances by the inadequacy of existing models and the lack of experimental evidence regarding the flow behaviour of fluids and suspensions at high Reynold's numbers. The behaviour of particles moving in unbounded radial force fields under conditions of laminar and turbulent motion was calculated approximately, the results being used as a guide in making certain assumptions in the later stages of the analysis. It was found that, in the present stage of development of hydrodynamic theory, the motion of particles within enclosed helical channels could not be predicted from first principles. A continuity equation was derived for the particles, which if solved would permit the calculation of the average velocity of the particles over the full depth of the channel from known or measured values of the particle concentration.

A programme of experimental work was carried out with glass spheres. The results of the theoretical and experimental investigations were used to obtain limited solutions to the continuity equation for the regions adjacent to the inner and outer walls of the helix. The radial velocities of the particles calculated from the solutions to the continuity equation were compared with theoretical estimates of the apparent terminal velocities of the particles and were found to be considerably smaller in all cases.

On the basis of this work, it was concluded that the main factors opposing particle motion were probably enhanced or non-ideal fluid drag forces in the zone near the inner wall and a combination of shear forces and interference effects in the zone near the outer wall. It was thought that lift forces might play a significant role in the outer zone but not in the inner zone and that the type of secondary fluid flow likely to occur in the helix would probably not have contributed significantly to the observed effects. The likelihood of boundary layer separation taking place at the inner wall could not be assessed.

To summarise, the work carried out so far has shed some light on the nature of the forces at work within the sizer helix and has given an indication as to which forces are the more important. The investigation could have been taken further if more information had been available concerning the axial and radial velocity profiles created within helical channels by fluids and suspensions flowing at medium to high Reynold's numbers.

6.2 Future Work

The most immediate objective of future work will be to obtain some of the missing information concerning the flow behaviour of the fluids and suspensions within helical channels. Since the existing helix is far too small to permit determination of the velocity profiles by any of the known techniques, it will be necessary to construct a scaled-up version of the helix and investigate its performances under hydrodynamically similar conditions. Once the changes in the velocity profiles have been determined for various volumetric throughputs, it should be possible to predict the three-dimensional trajectories of individual particles and by summing a large number of trajectories the concentration changes may be predicted. The equations involved are likely to be extremely complicated and difficult to solve, so considerable use of computers is contemplated.

Other interesting but less immediately urgent aspects of the work would include investigations into the effects of changes in the aspect ratio of the channel, the radius of the helix, and the number of turns employed.

The Science Research Council has sponsored a further programme of research along these lines which is currently being carried out. The patents[23] taken out on the sizer have been assigned to the National Research Development Corporation, who have issued a license to manufacture to the firm of Hilger and Watts Ltd.

ACKNOWLEDGEMENTS

The author would like to thank Professor M. G. Fleming in his capacity of both Supervisor and Head of Department for his unfailing support and encouragement throughout the duration of the research. He also wishes to thank his colleagues in the Department of Mining and Mineral Technology: in particular, Mr C. H. J. Beaven and Mr E. Thompson for many helpful discussions and suggestions, and Dr. J. W. Bray for his kindness in finding time to discuss and advise on some of the mathematical aspects of the work.

The support of the Department of Scientific and Industrial Research during the first two years of the research is gratefully acknowledged. Thanks are also due to the Baldwin Instrument Company for lending some of the equipment necessary for the construction and testing of the laboratory prototype and to the National Research Development Corporation for their assistance and encouragement in applying the results of the research to industrial problems.

REFERENCES

1. Holland-Batt A.B., Cohen E.
Unit process Investigations. 1. Grinding, Preliminary Programme. Min. Tech Dept., R.S.M., August, 1963.

2. Holland-Batt A.B., Cohen E.
'The Analysis of a Grinding System as a Unit Process'. Progress Reports 19, 20, 21. Min Tech. Dept., R.S.M. 1963-64.

3. Rhodes, J.R. 'Some Applications of Radioisotopes in Instrument Engineering'. Instrument Practice, May 1962 559-567.

4. Beke, B. 'Principles of Comminution'. Chapter 1, 1964.

5. Hawthorne W.R. 'Flow in Bent Pipes', Proc. Sem. Aero. Sci. 1961.

6. Barua S.N. 'On Secondary Flow in Stationary Curved Pipes' Quart. Jour. Mech. and App. Maths Vol. 16. Part 1, 1963 pp61-77.

7. Detra R.W. Mitt. a.d. Inst of Aerodyn. 1953, No.20 E.T.H. Switzerland.

8. Squire H.B. and Winter K.G. J. Aero. Sci. 18, 1951.

9. Weske, J.R. N.A.C.A. Tech. Note 1471, 1948.

10. Cuming H.G. 'The Secondary Flow in Curved Pipes', A.R.C.R. and M., No.2880, 1955.

11. Heywood, H. 'Calculation of Particle Terminal Velocities' J. Imp. Coll. Chem. Eng. Soc., 4, 1948, 17.

12. Castleman. Nat Adv. Com. for Aeron. (U.S.A.) Tech Note 231.

13. Steinour, H.H. 'Rate of Sedimentation'. Ind. Chem. Eng., Vol.36, 1944.

14. Richardson, L.F. and Zaki, 'The Sedimentation of a Suspension of Uniform Spheres under Conditions of Viscous Flow'. Chem. Eng. Sci. Vol.3 1954.

15. Burgers, J.M. 'Influence of the Concentration of a Suspension on the Sedimentation Velocity'. Proc. Acad. Sci.Amsterdam, Vol. 45, 1942.

16. Orr, C. 'Particulate Technology', Macmillan (1966), 7, 301.

17. Bagnold, R.A. 'Experiments on a Free Dispersion of Large Solid Spheres in a Newtonian Fluid Under Shear'. Proc. Roy. Soc. Series A, Vol. 225, 1954.

18. Lord Rayleigh, 'On the Motion of Solid Bodies through Viscous Liquid'. Phil. Mag. 21, pp697-711. (1911)

19. Maude, A.D., Whitmore, R.L. 'A Generalised Theory of Sedimentation'. Brit. J. App. Phys. 9,481, (1958)

20. Swanson, W.M. 'The Magnus Effect: A Summary of Investigations to Date'. J. Basic Eng., Trans. A.S.M.E. Vol 83 (1961), 461-470.

21. Swanson, V.F. 'The Development of Formula for Direct Determination of Free Settling Velocity of Any Size Particle' Trans A.I.M.E., Soc. Min. Eng., June 1967, 160-166.

22. Clarke, B. 'Rheology of Coarse Settling Suspensions'. Trans Inst. Chem. Engrs., Vol.45, 251-256, 1967.

23. British Patent Application No. 16376/65.

APPENDIX

Finite Difference Solution for Turbulent Radial Motion of a Spherical Particle in a Uniform Tangential Velocity field, in the absence of Secondary Fluid Flow

The basic equation to be solved is of the form

$$\frac{dT}{dr} + aT = \frac{b}{r} \quad \ldots \quad \ldots \quad \ldots \quad \ldots \quad \ldots \qquad (1)$$

where $a = \dfrac{6P}{10D\sigma}$ and $b = \dfrac{2(\sigma - P)V^2}{\sigma}$

Consider a series of successive values of r spaced at equal intervals of h, where h is small. Let T_{n-1}, T_n, T_{n+1}. be the values of T corresponding to r_{n-1}, r_n, r_{n+1} etc.

By definition, $T = f(r)$. Expanding this as a Taylor series in the region of r_n gives:

$$T_{n+1} = f(r_{n+1}) = f(r_n + h) = f(r_n) + hf'(r_n) + \frac{h^2}{2!} f''(r_n) + \text{etc.}$$

$$\therefore T_{n+1} = T_n + h\left(\frac{dT}{dr}\right)_n + \frac{h^2}{2!}\left(\frac{d^2T}{dr^2}\right)_n + \ldots \quad \ldots \qquad (2)$$

$$\text{Also } T_{n-1} = T_n - h\left(\frac{dT}{dr}\right)_n + \frac{h^2}{2!}\left(\frac{d^2T}{dr^2}\right)_n - \quad \ldots \quad \ldots \qquad (3)$$

$$\therefore T_{n+1} - T_{n-1} = 2h\left(\frac{dT}{dr}\right)_n + \text{terms in } h^3 \text{ and above}$$

$$\therefore \left(\frac{dT}{dr}\right)_n = \frac{1}{2h}\left(T_{n+1} - T_{n-1}\right) \quad \ldots \quad \ldots \qquad (4)$$

But from equation (1):

$$\left(\frac{dT}{dr}\right)_n = \frac{b}{r_n} - aT_n \quad \ldots \quad \ldots \quad \ldots \quad \ldots \qquad (5)$$

Combining equations (4) and (5) gives

$$T_{n+1} = \frac{2bh}{r_n} - 2ahT_n + T_{n-1}$$

In the most general form the value of T_n is given as

$$T_n = \frac{2bh}{r_{n-1}} - 2ahT_{n-1} + T_{n-2} \quad \ldots \quad \ldots \qquad (6)$$

Equation (6) shows that once a solution has been initiated, succession values of T may be calculated from those already found.

In order to commence the solution, one boundary value is required; say $T = T_o$ at $r = r_o$. The value of T at r_1 is then guessed (T_1) and equation (6) applied repeatedly to find T_2, T_3, T_4 etc.

The intial guessed value of T_1 contains an unknown error, known multiples (m) of which are present in the later values of T. The significant point is that from equation (6) these increasingly large error multiples are of alternating sign.

The 'error pattern' that is generated as the solution progresses can easily be determined, and by interpolation between successive pairs of large positive and large negative error multiples, the original error in T_1 may be estimated.

A second solution may then be obtained very rapidly indeed, by applying the known 'multiple error' corrections to the first set of values of T. The second solution so obtained is normally of sufficient accuracy.

The error pattern produced by repeated applications of equation (6) is shown overleaf:

r	T + ERROR	ERROR MULTIPLE 'm'	z *
r_0	T_0 + Nil	0	z_0
r_1	$T_1 + m_1E$	1	z_1
r_2	$T_2 - m_2E$	$2(ah)$	z_2
r_3	$T_3 + m_3E$	$[1+4(ah)^2]$	z_3
r_4	$T_4 - m_4E$	$[4(ah)+8(ah)^3]$	z_4
r_5	$T_5 + m_5E$	$[1+12(ah)^2+16(ah)^4]$	z_5
r_6	$T_6 - m_6E$	$[6(ah)+32(ah)^3+32(ah)^5]$	z_6
r_7	$T_7 + m_7E$	$[1+24(ah)^2+80(ah)^4+64(ah)^6]$	z_7
r_8	$T_8 - m_8E$	$[8(ah)+80(ah)^3+192(ah)^5+128(ah)^7]$	z_8
r_9	$T_9 + m_9E$	$[1+40(ah)^2+240(ah)^4+448(ah)^6+256(ah)^8]$	z_9
r10	$T_{10} - m_{10}E$	$[10(ah)+160(ah)^3+672(ah)^5+1024(ah)^7+512(ah)^9]$	z_{10}

*z = Apparent value of T.

If $T \pm m_8E$ are chosen as the interpolation values, then $(T - m_8E) = z_8$ is known directly. $(T + m_8E)$ is found by linear interpolation, which is accurate enough for present purposes.

The required formulae are

$$T + m_8E = \left(\frac{m_8 - m_7}{m_9 - m_7} \right) (z_9 - z_7) + z_7$$

$$T - m_8E = z_8$$

Hence:

$$E = \frac{1}{2m_8} \left[\left(\frac{m_8 - m_7}{m_9 - m_7} \right) (z_9 - z_7) + z_7 - z_8 \right]$$

The error E is then applied to the first set of values of T using the known table of error multiples given above.